Kinetics, Thermodynamics and Habitability of Microbial Iron Redox Cycling

by

Brian St Clair

A Dissertation Presented in Partial Fulfillment
of the Requirements for the Degree
Doctor of Philosophy

Approved March 2017 by the
Graduate Supervisory Committee:

Everett Shock, Chair
Ariel Anbar
Ferran Garcia-Pichel
Hilairy Hartnett

ARIZONA STATE UNIVERSITY

May 2017

ABSTRACT

Many acidic hot springs in Yellowstone National Park support microbial iron oxidation, reduction, or microbial iron redox cycling (MIRC), as determined by microcosm rate experiments. Microbial dissimilatory iron reduction (DIR) was detected in numerous systems with a pH < 4, but was not detected at higher values. Rates of DIR are influenced by the availability of ferric minerals and organic carbon. Microbial iron oxidation (MIO) was detected from pH 2 – 5.5. In systems with abundant Fe (II), dissolved oxygen controls the presence of MIO. Rates generally increase with increased Fe(II) concentrations, but pseudo first order rate constants are not significantly altered by additions of Fe(II). MIRC was detected in systems with abundant biogenic ferric mineral deposition.

The rates of microbial and abiological iron oxidation were determined in a variety of cold (T= 9-12°C), circumneutral (pH = 5.5-9) environments in the Swiss Alps. Rates of MIO were measured in systems up to a pH of 7.4; only abiotic processes were detected at higher pH values. Iron oxidizing bacteria (FeOB) were responsible for 39-89% of the net oxidation rate at locations where biological iron oxidation was detected. Members of putative iron oxidizing genera, especially *Gallionella*, are abundant in systems where MIO was measured. Speciation calculations reveal that ferrous iron typically exists as $FeCO_3^0$, $FeHCO_3^+$, $FeSO_4^0$ or Fe^{2+} in these systems. The presence of ferrous (bi)carbonate species appear to increase abiotic iron oxidation rates relative to locations without significant concentrations. This approach, integrating geochemistry, rates, and community composition, reveals biogeochemical conditions that permit MIO, and locations where the abiotic rate is too fast for the biotic process to compete.

For a reaction to provide habitability for microbes in a given environment, it must energy yield and this energy must dissipate slowly enough to remain bioavailable. Thermodynamic boundaries exist at conditions where reactions do not yield energy, and can be quantified by calculations of chemical energy. Likewise, kinetic boundaries exist at conditions where the abiotic reaction rate is so fast that reactants are not bioavailable; this boundary can be quantified by measurements biological and abiological rates. The first habitability maps were drawn, using iron oxidation as an example, by quantifying these boundaries in geochemical space.

ACKNOWLEDGMENTS

A project of this magnitude benefits from the contributions of many individuals. These contributions can be direct, like sample analysis, logistical planning, instruction and writing. But many of the most lasting contributions are less direct, including discussions on science, sharing of expertise or motivation, and inspiration from friends and colleagues. Direct contributions to this research are acknowledged at the end of each chapter. Those deeply involved in this work and who provided the inspiration for this work are recognized here.

I got my start in research under Dan Davis, at the University of Arkansas. I can trace most of my basic laboratory skills to the members of his lab, especially under the guidance of Nicole Vanderbush and Marilyn Davis. It was my experience in research as an undergraduate that lead to the decision to pursue research professionally. Being accepted to GEOPIG will likely be the most life altering event of my professional career. My advisor, Everett Shock, shaped my professional and personal development in countless ways. I am grateful to have been guided through grad school by such an insightful scientist and mentor, who's drive to understand the interactions of life with the environment will continue to inspire me throughout my career. Many others mentored me along the way, including my committee: Ariel Anbar, who shared his knowledge of isotopes and provided early support; Ferran Garcia-Pichel, who taught me the basics of geobiology; Hilairy Hartnett, from whom I learned firsthand how to perform field experiments, and who pushed me to do my best. Their support and guidance shaped the structure of this work.

The research presented in my dissertation was only possible with hard work of dozens of individuals. Justin Pottenger, initially unimpressed with the working conditions that nature imposes for field work, became an indispensable part of this work. He helped run experiments over five field expeditions between Yellowstone, Switzerland and Southern Arizona. Justin was eventually able to perform my experimental protocol with more patience and precision than I was. Many others in GEOPIG made significant contributions to the planning and execution of this research, including Grayson Boyer, Peter Canovas, Alysia Cox, Randall "Vince" Debes, Jeff Dick, Jeff Havig, Alta Howells, Kristin Johnson, Jordan Okie, Apar Prasad, Panjai Prapaipong and Kirtland Robinson. Kurt Hanselmann at ETH-Zurich shared his deep experience on the geomicrobiology of systems in Switzerland that enabled a successful field campaign, as well as assisted with air transportation logistics. Research in Yellowstone was always enhanced by insight and conversation with Eric Boyd of Montana State University. I am grateful to him and his lab for helping me understand the microbial communities in my study sites. Many others not already mentioned deserve recognition for keeping me balanced, in no particular order Ian Pahk, Jenna Donnateli, Steve Davidowski, Iolanda Klein, Robert Schmitz, Bennett Addison, Dan Mieritz, Adam Monroe, and many others. It was a privilege and honor to work with all these skilled and insightful individuals.

Finally, I thank my family. This includes my parents Kevin and Diana St Clair, who supported and encouraged me to develop my interests and talents; My brothers, Paul and Blake, who's own personal and professional development inspires me; and Alysia Cox, without whom I would be lost. Without their love and inspiration, I would not be writing this dissertation.

TABLE OF CONTENTS

CHAPTER Page

LIST OF TABLES

LIST OF FIGURES

CHAPTER 1

INTRODUCTION

Iron is the 6th most abundant element in the universe and the 4th most abundant element in earth's crust (Fleischer, 1953). It exists in minerals and as aqueous species in two common oxidation state: Fe(II) and Fe(III). Transformations between physical forms and oxidation states can occur spontaneously under many conditions on earth's surface. The process can also be catalyzed by microorganisms for metabolic energy. The process of oxidizing Fe(II) → Fe(III) can be coupled to reduction of molecular oxygen, nitrate, sulfate, and many other inorganic electron acceptors (review by Melton et al., 2014). The reverse reaction, reducing Fe(III) → Fe(II) can be coupled to oxidation of hydrogen, sulfide, or a host of organic compounds (Lovely, 1991). Most sediments and soils host iron metabolizing organisms. Microorganisms are responsible for nearly all the Fe transformations in some environments (see chapters 2 and 3). Microbial lineages across the archaeal and bacterial domains of life retain the ability to oxidize and reduce iron, suggesting the processes evolved early in Earth's history (Weber *et al.*, 2006). A goal of this research was to determine the underlying geochemical conditions that permit or exclude microbes to gain a living by catalyzing iron redox transformations across the many environments in which they are found.

Microbial iron oxidation has been reported at locations as diverse as marine hydrothermal vents (Fleming et al., 2013), cave walls (Kasama and Murakami 2001), acid mine drainage (Druschel et al., 2004), hot springs (Inskeep et al., 2005), and many other locations where reduced iron encounters oxygen the atmosphere. Iron-oxidizing organisms known to live in environments from pH < 2 to > 8, and temperatures from

freezing to boiling. Ferric oxyhydroxide minerals are the most common product at pH > 2, while aqueous Fe^{3+} is the most common product in extremely acidic locations. Iron reducing organisms are found in an even broader range of habitats that iron oxidizers. Isolates have been reported from pH < 2 to > 10. The currently know upper temperature limit for life, 121 °C, is held by a species that uses iron reduction for metabolic energy (Kashefi and Lovely, 2003). Iron commonly comprises 1-2 weight % in sediments, making it the most abundant oxidant in anoxic settings (Nealson and Saffarini, 1994). Reduction of ferric minerals coupled to oxidation of organic compounds is also yields significant energy, especially at low pH (Shock et al., 2010). Microbes take advantage of this abundant energy source; iron reduction can be the primary mechanism of organic carbon oxidation many environments (Slobodkin, 2006). Work in support of this thesis measured rates of iron and carbon transformations in Yellowstone hot springs.

While there is a wide range of habitats that support microbial iron metabolism, the local environment imposes dramatically varying conditions that have consequences for their habitability. The geochemistry (especially pH) determines how much energy can be gained from the catalysis of a specific iron redox reaction. Acidic and hydrothermal environments are limited to lineages that can cope with the conditions. Abiotic iron oxidation can be extremely rapid in circumneutral environments, forcing organisms to compete for available Fe(II). This study measured microbial and abiotic iron oxidation and reduction kinetics across a broad range environments and geochemical conditions. Given the extremes of geochemistry and temperature known to support iron metabolism, a broad goal of this research was to determine the underlying physical chemistry that permits microbes to use this reaction in such diverse environments. This research

combines geochemical data, thermodynamic calculations, and rates of microbial and abiotic process from Yellowstone hot springs, cold springs and lakes in the Swiss Alps, and acid mine drainage to determine how environments provides habitability.

1.1 **Distinguishing Biotic and Abiotic Iron Oxidation at Low Temperatures**

Abiotic ferrous iron oxidation in air is extremely rapid in neutral pH conditions (Stumm and Lee, 1961). The presence of certain inorganic anions, especially dissolved inorganic carbon, can increase abiotic iron oxidation rates relative to dilute solution (Millero, 1985). The underlying mechanism of the enhanced reaction rate involves the formation of ferrous (bi)carbonate aqueous species; these species react spontaneously with dissolved O_2 orders of magnitude faster than Fe^{2+} (King 1998). Despite this rapid abiotic oxidation, microbes are also capable of catalyzing this reaction for metabolic energy (Neubauer et al, 2002). This had led to research to understand the interplay of abiotic and microbial processes in such systems (Melton et al., 2014) has cataloged factors that influence rates in such systems. This pressure from the rapid abiotic iron oxidation rate is widely acknowledged, but it was previously unknown if the abiotic rate can be too fast for biology to compete. A goal of this research is to explore natural systems that exhibit the fastest rates of abiotic iron oxidation to determine if they exclude microbial iron oxidation.

Many circumneutral pH springs and lakes in the Swiss Alps show evidence of iron oxidation (Steiner et al., 2000; Hegler et al., 2012), which is often apparent as red iron staining. Microcosm microbial and abiotic iron oxidation rate experiments were performed at 7 springs and 3 lakes to determine the biological and abiological oxidation rates. Experimental locations were selected to have and wide range of pH and

geochemical compositions that led to large variations in abiotic iron oxidation rates. Analysis showed significant concentrations of dissolved inorganic carbon in many of the spring locations that potentially increase abiotic iron oxidation rates. New estimates of thermodynamic properties of several ferrous (bi)carbonate aqueous species were made that permitted speciation calculations on these systems. Results showed significant concentrations of these aqueous species. Community composition data revealed populations of putative metal oxidizing microbes, especially *Gallionella.* Combining the rate measurements, geochemical data, speciation calculations, and community composition reveals locations where microbes are responsible for most of the observed iron oxidation, and locations where the abiotic rate was too fast for biology to compete.

1.2 Microbial Iron Reduction, Oxidation, and Redox Cycling in Yellowstone National Park

Yellowstone National Park (YNP) is home to more than 10,000 hydrothermal features, the largest concentration on earth (Nordstrom et al., 2006). Underground boiling and phase separation leads to surface features characterized by either liquid dominated chloride-bicarbonate compositions or steam dominated sulfate rich acidic systems (Shock et al., 2010). The two end member fluids, along with shallow groundwater and mixing, combine to create one of the most geochemically diverse locations on earth. In a single thermal area is it possible to find variations of almost any element by up to 5 orders of magnitude. This geochemical diversity has been recognized since the early 1900's, most notably by Allen and Day (1935) (summarized by Shock et al., 2010). This makes YNP a natural laboratory with which to test hypotheses about the interactions between life and their local chemical environment.

Hot springs have dissolved iron concentrations varying by more than 2 orders of magnitude at any given pH, and up to 5 orders of magnitude across all locations (see Fig. 18). Ferric minerals can be observed in hot springs throughout Yellowstone, including acidic locations where abiotic iron oxidation is expected to be non-existent. Iron oxidation has been noted in several pH ~3 hot springs (Macur et al., 2004; Inskeep et al., 2005; Kozubal et al., 2008; 2012). Likewise, evidence of microbial iron reduction has been reported for organisms from a handful of Yellowstone hot springs (Slobodkin et al., 1999; Kashefi et al., 2002; Johnson et al., 2003; Fortney et al., 2016). Calculations of energy available to microbes show that ferrous iron oxidation with oxygen yields sufficient metabolic energy at pH > ~2 (See chapter 4). Ferric mineral reduction with small organic acids yields energy at most locations with pH < ~9 (Windman et al., 2009; my unpublished data). This energetic availability, combined with clues from geochemical data and contextual observations in the field, suggests that geochemical diversity in hot supporting dissimilatory microbial iron metabolism may be much more broad than the locations that have been described to date. Kinetics experiments, analogous to those described in section 1.1, were performed dozens of Yellowstone hot springs. Assays were performed for simultaneously for microbial and abiotic iron oxidation and reduction. Some locations showed evidence of complete redox cycling. These experiments indicate that microbial iron oxidation is more widespread than previously reported. Accompanying geochemical and phylogenetic data from each experiment location suggest the relative rates of processes is broadly influenced by pH, ferric mineral content, organic carbon, and dissolved oxygen. Results indicate there is much yet to be

learned about iron redox metabolism and the organisms use it for metabolic energy in hot spring ecosystems.

1.3 The Construction of Quantitative Habitability Diagrams

Two things must be true for microbes to gain chemical energy from the environment. First, there must be a source of energy. This requires the presence of compounds in different oxidation states that are out of thermodynamic equilibrium with one another. Second, there must be mechanistic difficulties that are keeping those compounds from reacting, which means that the chemical energy cannot dissipate by itself (Shock and Boyd, 2015). Using this energetic reference frame, geochemical habitability can be defined and quantified by the combined presence of thermodynamic and kinetic limitations at diverse environments on the Earth. To demonstrate this point, the kinetic and thermodynamic barriers have been quantified for an iron oxidation reaction by combining rate experiments and geochemical data from the previously outlined chapters, as well as additional field work and literature data.

Microorganisms across the phylogenetic tree of life gain energy by reacting dissolved reduced iron with oxygen to form ferrihydrite in environments with temperatures that from freezing to boiling and pH values between 2 and 7. However, not all combinations of pH and temperature are habitable. In high-pH environments this reaction occurs rapidly on its own, which prevents microorganisms from taking advantage of it (Seto, 2014; chapter 2 of this work). In addition, the pH at which this occurs decreases with increasing temperature. The limitation, where abiotic oxidation is too rapid for biology to compete, is defined at the kinetic boundary. In acidic environments, however, the abiotic oxidation reaction rate is significantly slowed,

allowing microorganisms ample opportunity to catalyze iron oxidation. However, increasing acidity lowers the energy yield, ultimately creating an energy boundary to habitability at the lowest values of pH. Combining such energetic and kinetic boundaries permits habitability to be mapped for individual reactions using geochemical variables that include pH, temperature, and concentrations of reactants and products of the reaction. The first habitability map has been made, showing geochemical combinations that support microbial iron oxidation. Geochemical data from fieldwork at hot springs, acid mine drainage, and cold springs fed by snowmelt were used to calculate energy supplies. Field experiments of biotic and abiotic rates of iron oxidation and reduction were used to determine kinetic limitations. The resulting multi-dimensional habitability maps for several iron oxidation reactions provide a framework for future studies of many other chemolithotrophic metabolic process throughout surface and subsurface environments on Earth, which will quantitatively constrain the discussion of habitability on other planets.

CHAPTER 2

DISTINGUISHING BIOTIC AND ABIOTIC IRON OXIDATION AT LOW TEMPERATURES

2.1 Introduction

Iron oxidizing bacteria (FeOB) catalyze the reaction of Fe(II) with molecular oxygen to gain metabolic energy, generating ferric minerals as a byproduct. The idealized reaction stoichiometry is $Fe(II) + {}^{1}/_{4}\ O_2 + {}^{5}/_{2}\ H_2O \rightarrow FeOH_3 + 2H^+$. Nitrate-dependent oxidation and photoferrotrophy have also been documented, but here the focus is on oxidation via atmospheric or dissolved O_2. Biological iron oxidation has been documented in a wide variety of circumneutral habitats, including iron-rich springs (James and Ferris, 2004; Hegler *et al.*, 2012), the arctic tundra (Emerson *et al.*, 2015), caves (Kasama and Murikami, 2001), ocean seeps (McAlister *et al.*, 2011), and other environments where reduced iron and atmospheric oxygen are out of equilibrium. In the present study, iron springs and iron-cycling lakes in the Swiss Alps with greatly varying compositions were studied to assess kinetics of microbial and abiotic iron oxidation across a wide range of low-temperature geochemical conditions.

In circumneutral environments, abiotic iron oxidation can be extremely rapid. FeOB compete with the abiotic oxidation process for Fe(II), which requires quantification of the relative contributions of FeOB and abiotic rates to place FeOB in their broader biogeochemical context. *In situ* rate measurements of oxidation attributable to FeOB in circumneutral environments are emerging (Kasama and Murikami, 2001; James and Ferris, 2004; Rentz *et al.*, 2007; Ferris *et al.*, 2016). Using literature data, Emerson and Fleming (2010) calculated that FeOB contributed an average of 45% of the net rate of

iron oxidation. This result is based on a limited number of examples, however, and the reported range is from 28-75% (Rentz *et al.*, 2007). Rate measurements of FeOB in pure culture also show competition from abiotic processes (Neubauer *et al.*, 2002; Sobolev and Roden, 2004; Drushel *et al.*, 2008; Eggerichs *et al.*, 2014). Recent studies have cataloged how geochemistry in circumneutral environments affects broader biogeochemical cycling of iron (Eggerichs *et al*., 2014; Melton *et al.*, 2014). A goal of the present study is to determine where the abiotic iron oxidation rate is so fast that biology cannot compete at a bulk level. Field sites have been selected where Fe(II) and oxygen coexist out of equilibrium (at least initially) but the reaction may not provide bioavailable energy owing to the rapid abiotic rate.

Many years of research have resulted in comprehensive descriptions of rates and mechanisms of abiotic iron oxidation, which guided my search for locations with rapid abiotic rates. Stumm and Lee (1961) were the first to quantify rates of abiotic iron oxidation. Their results demonstrated that oxidation rates in dilute solution are extremely sensitive to pH between values of approximately 4-8, with a one pH unit increase leading to more than one order of magnitude increase in the Fe oxidation rate. In this pH range, Stumm and Lee (1961) gave this iron oxidation rate law:

$$-\frac{d[\mathrm{Fe}^{2+}]}{dt} = k[\mathrm{Fe}^{2+}][\mathrm{OH}^{-}]^{2}[\mathrm{O}_{2}] \qquad (1),$$

where brackets indicate concentration, and k is the rate constant. At ambient conditions, rates at pH values less than ~4 and greater than 8 have been shown to be independent of pH (Lowson, 1982; Millero, 1985). Millero (1985) made it clear that this type of dependence of the rates of iron oxidation on pH is driven by iron speciation. Fe^{2+} is the dominant species at low pH values. Hydrolysis becomes significant at pH > 4, leading to

the formation of $FeOH^+$, $Fe(OH)_2^0$ and $FeOH_3^-$ species. The relative abundances of these hydroxide complexes increase and become dominant as pH increases. The oxidation rates of ferrous hydroxide species become orders of magnitude faster with each subsequent association, and are all orders of magnitude faster than the oxidation of Fe^{2+} (Millero *et al*., 1985; Morgan and Lahav, 2007).

Most abiotic iron oxidation rate experiments were performed in dilute solutions, but natural waters contain thousands of solutes and are in contact with minerals. Inorganic solutes can slow or hasten oxidation rates by changing the speciation of Fe(II), with each species having a unique oxidation rate constant (Millero and Izzaguirre, 1989). Organic solutes can both enhance or slow Fe(II) oxidation (Santana-Casiano *et al.*, 2000), with many common organic acid ligands stabilizing Fe(II) in solution. Mineral surfaces can also catalyze oxidation. Ferric mineral products of microbial and abiotic oxidation have both been shown to be autocatalytic (Park and Dempsey 2005; Rentz *et al*., 2007; Ferris *et al*., 2016). Mineral catalyzed oxidation is known as heterogeneous oxidation. The mechanism is thought to involve sorption of Fe(II) to surfaces of ferric mineral products, which lowers the activation energy for Fe(II) oxidation. Geochemical analysis of water and minerals, and subsequent speciation calculations, can indicate which species or minerals are driving abiotic rates in a system. The inherent complexity of factors contributing to abiotic Fe (II) oxidation rates requires that rates in natural systems be measured for a precise value to be obtained.

The sites sampled in this study all contain significant concentrations of dissolved inorganic carbon (DIC), and in most systems bicarbonate or carbonate is the most abundant anion. Millero *et al.* (1995) used equilibrium constants for the formation of

ferrous bicarbonate and carbonate ((bi)carbonate) species from Bruno *et al.* (1992) to calculate the speciation of ferrous iron in natural waters, and determined that complexes include $FeHCO_3^+$, $FeCO_3^0$, $Fe(CO_3)_2^{-2}$, and $Fe(OH)(CO_3)^-$. Experiments by King (1998) quantified the oxidation rates of these individual aqueous (bi)carbonate complexes. King's data are widely used to estimate ferrous iron oxidation rates in (bi)carbonate-rich natural systems. The apparent overall rate can be expressed as a sum of the oxidation rates of the individual aqueous species (King 1998):

$$-\frac{d[Fe^{2+}]}{dt} = k_{app}[Fe^{2+}][O_2] \qquad (2)$$

$$k_{app} = 4(k_1\alpha_{\mathrm{Fe^{2+}}} + k_2\alpha_{\mathrm{FeOH^+}} + k_3\alpha_{\mathrm{FeOH_2{}^0}} + k_4\alpha_{\mathrm{FeCO_3{}^0}} + k_5\alpha_{\mathrm{Fe(CO_3)_2{}^{-2}}} + k_n\alpha_{\mathrm{n}} \ldots)$$

where α is the fraction of the total Fe(II) in solution accounted for by each aqueous species, k is the second-order rate constant for oxidation by oxygen of the specified aqueous species. The individual rates are multiplied by 4 to account for the stoichiometry of 4 moles of Fe(II) per mole of O_2. Speciation calculations can be performed to determine how much of the rapidly oxidizing ferrous (bi)carbonate species are present. It should be noted that there is still some debate on the exact speciation of ferrous iron in bicarbonate media, given the limited experimental data available (Fosbol *et al.*, 2010; Lemire *et al.*, 2014; but see below).

When the concentration of O_2 is constant the rate expression simplifies to the pseudo- first-order expression:

$$-\frac{d\{Fe^{2+}\}}{dt} = k_{ox}[Fe^{2+}] \qquad (3).$$

In this expression k_{ox} is the pseudo-first-order rate constant. This simplified rate expression is commonly reported from field experiments because it encompasses the sum

of all processes and allows rates to be directly compared among systems. It also permits the sum of the abiotic processes to be distinguished from biotic rates. Values measured in this study are reported as k_{ox}.

Taken together, the geochemical data, sediment composition, rate measurements, Fe speciation calculations, and community composition permit an integrated description of iron transformation in cold natural systems. These data can provide a foundation upon which to discuss the habitability of Fe(II) oxidation in various contexts, including active systems, ancient oceans, and extraterrestrial environments.

2.2 Site Descriptions

In September 2015, I sampled springs and lakes in four areas in the southeastern Graubünden Canton in the Swiss Alps: Rablönch, Val Sinestra, Alvanau Bad, and the Jöri lakes (see **Fig 1**). The locations range in elevation from 920 to 2740 meters above sea level. GPS coordinates for each sample location are available in appendix C. Each sample site was selected based on apparent iron redox processes, including abundant reduced iron, significant iron minerals or staining, or preliminary data.

2.2.1 Rablönch

The iron-carbonate spring Funtana Rablönch (official name) is situated on the North side of the Engadin river, 1.6 km east of the town of Scuol, Graubünden Canton, Switzerland. It is located approximately 5 km east of the recently described iron-bicarbonate spring Fuschna (Hegler *et al.*, 2012). The source water emerges into a concrete housing in an agricultural field. A map of the area showing spring features and sampling locations is given in **Fig 2**. The water has minimal contact with the atmosphere before it is piped 24 meters downhill, emerging in a storm drain under an access road. The main outflow

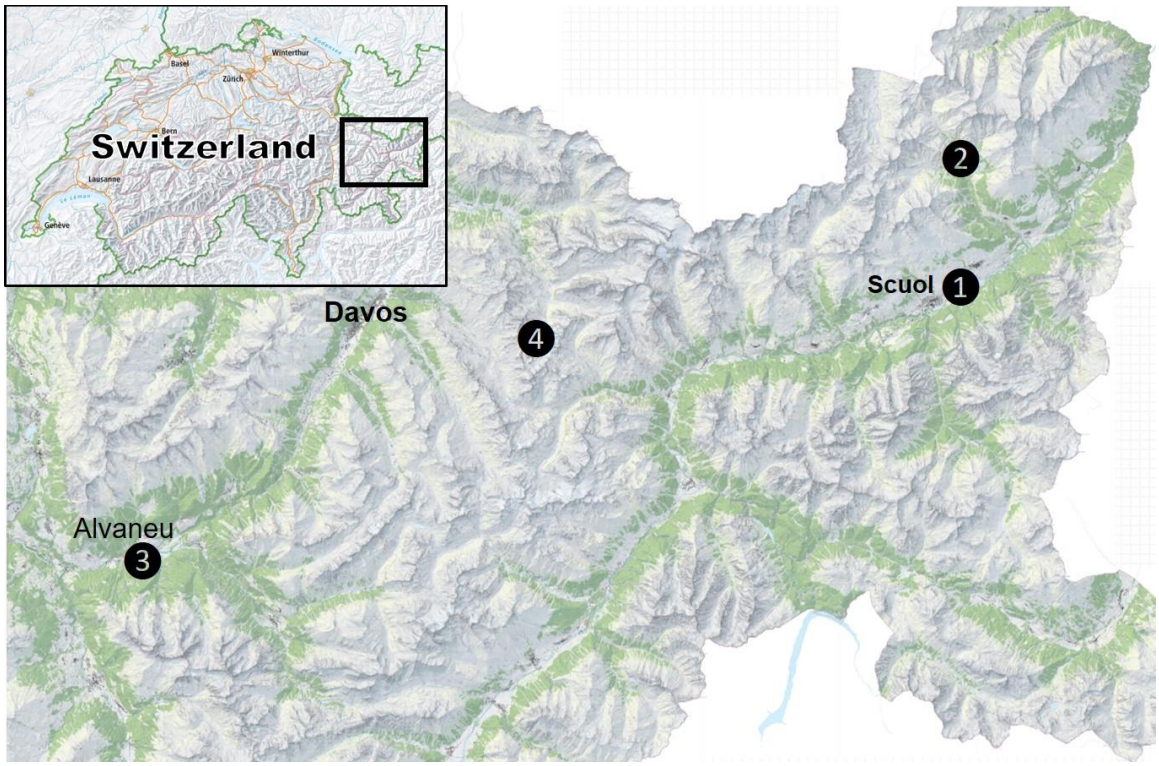

Figure 1 - A map of northeastern Graubünden canton with sample areas indicated by numbers. 1 – Rablönch, 2 – Val Sinestra, 3 – Alvaneu Bad area. 4 - Jöri Lakes. Individual sample information within each area can be found in tables 1-4. GPS coordinates for each sample are located in Appendix C. Inset is map of Switzerland. Map used with the permission of Geodata © Swisstopo.

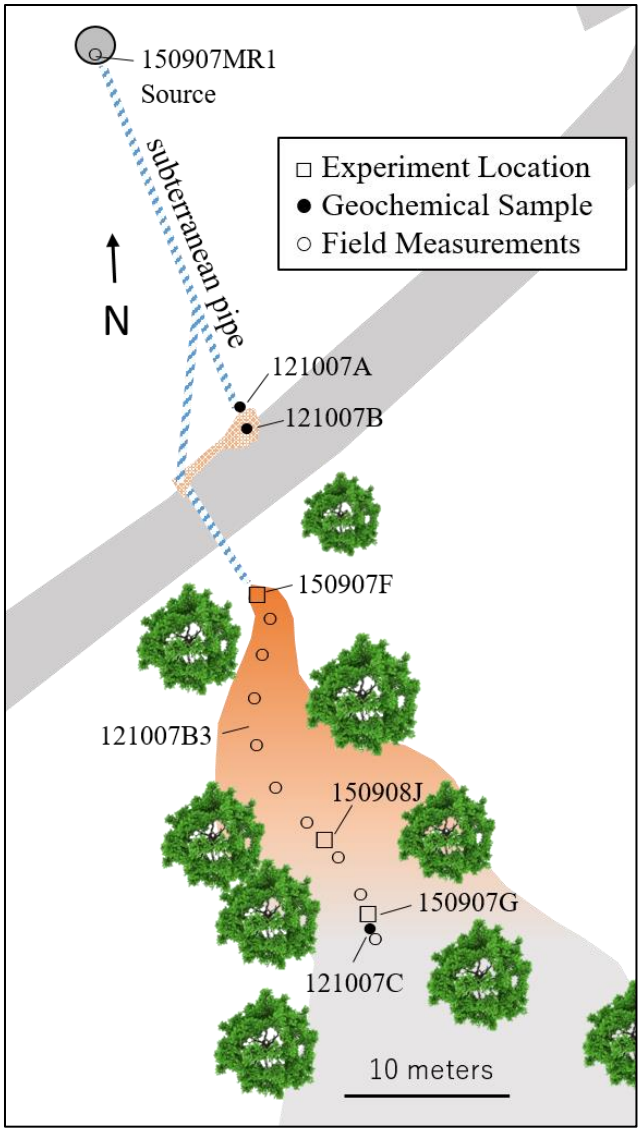

Figure 2 – Map view sketch of Rablönch spring. Features are drawn to scale. The orange-fading-to-grey area is the carbonate terrace; the intensity of the orange indicates visible iron staining. The terrace continues off the diagram to the south for ~30 meters. The grey circle at top left is a concrete housing for the spring source. Blue stippled lines show underground pipes, which at one point go under the road (grey strip). Green symbols are trees. Filled circles with sample IDs indicate locations of samples with complete geochemical data (see methods); filled squares indicate locations of rate experiments; open circles show locations of field measurements only. A profile of the outflow can be found in figure 3.

produces a carbonate terrace composed mostly of calcite stretching approximately 60 meters down the hillside. Iron staining persists approximately 20 meters down the main outflow. The predominant flow was first sampled where it emerges on the downslope side of the road at ~25 L / min. A portion of the spring flow of water is diverted (~2 L / min) to a roadside spigot to allow residents to collect the mineral water. Vibrant iron mats are produced near both outlets. Significant mineral precipitation frequently alters the flow path of the main channel in the carbonate terrace.

Complete geochemical sample suites (see methods) were taken at three points along the main flow path indicated by the sample numbers in Fig 2. Profiles of pH, O_2(aq), Fe(II), conductivity, and temperature along the main flow path are shown in **Fig 3**. The pH increases by two pH units over 20 meters, likely due to CO_2 degassing as suggested by the deposition of calcite. Dissolved oxygen increases steadily until it reaches atmospheric saturation at around 12 meters from the road outlet. Fe(II) steadily decreases from 100 µ*m* near the source to under 2 µ*m* at 20 meters. Conductivity fluctuates, but generally decreases from 1650 µS as calcite precipitates. Additional field data from the Rablönch sample locations can be found in Table 1. Samples taken at the same locations in 2012 and 2015 suggest that the chemical composition of the spring is stable, at least during the Fall season. Oxidation rate experiments were performed in the main outflow in the vibrant iron mat, at a site with moderate iron staining, and at a location just upstream of the point where iron is completely depleted, as shown in Fig 2.

2.2.2 Val Sinestra

The springs at Val Sinestra have high concentrations of iron and arsenic, and the water and sediment have been used historically as folk remedies to treat a wide variety of

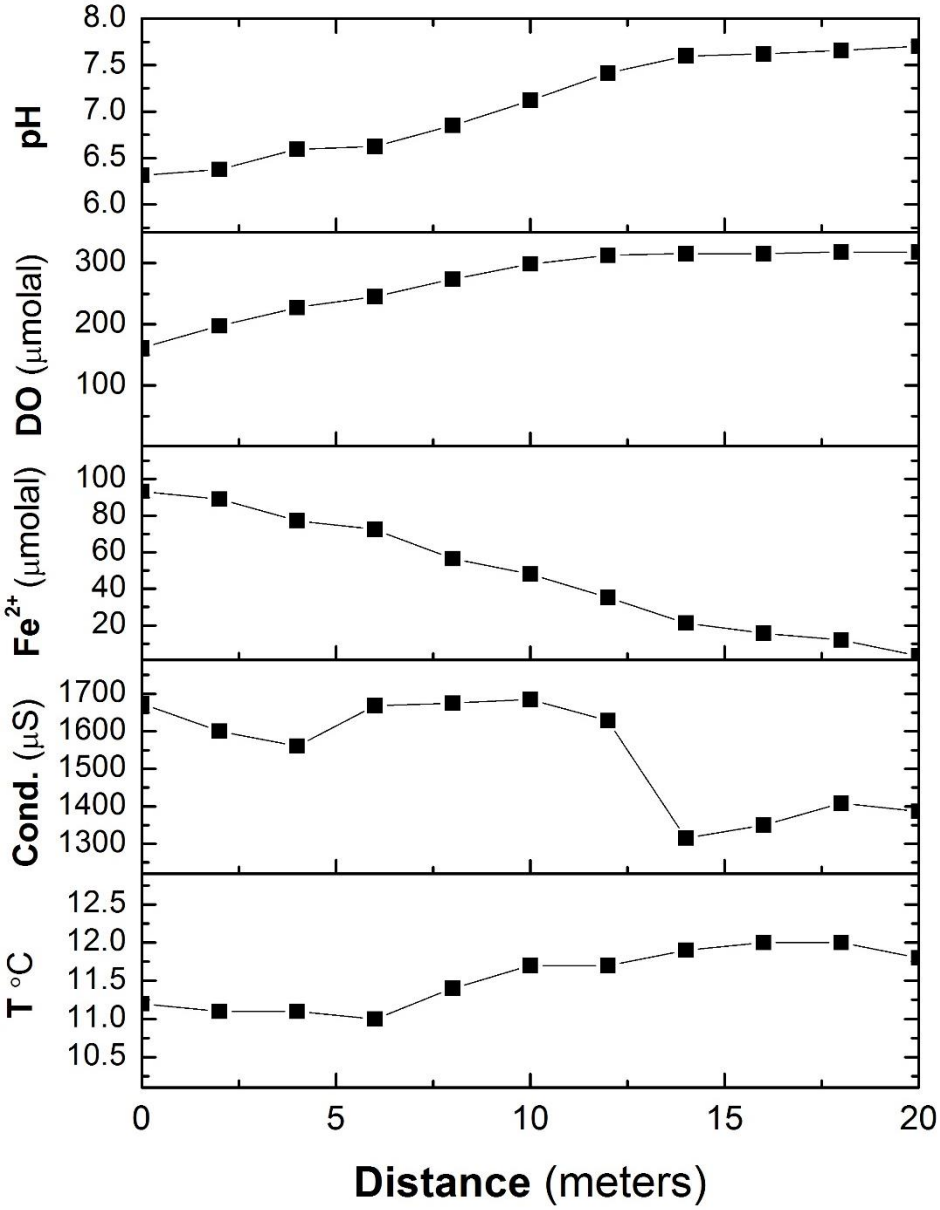

Figure 3 - Profile of field data collected along the Rablönche spring outflow. Distance is measured from site 150907F and proceeds along the main flow path (see map, figure 2). The pH increases substantially down the outflow. The dissolved oxygen increases until it approaches saturation with air around 12 meters. Ferrous iron is simultaneously depleted. The conductivity follows a general downward trend, but exhibits variability. The temperature changes less than 1°C throughout the outflow; which continues for ~10 more meters down the terrace until the water becomes too shallow to make measurements. A table of these values is available in appendix C.

Table 1 – Field measurements from spring sources and outflows

Sample ID	Notes	pH	Cond µS	T °C	O_2(aq) µmolal	Fe^{+2} µmolal
		Rablönch				
150907F[a]	Vibrant iron mat	6.32	1674	11.1	162	93.2
150908J[a]	Iron stained carbonate	7.67	1657	12.7	318	28.3
150907G[a]	Little to no iron staining	7.91	1401	10.7	327	4.2
121007A	Upper roadside pipe	6.30	2070	10.7	<6	60.5
121007B	N side of road iron mat	6.30	2070	10.5	121	59.7
121007C	Outflow of 121007B	7.90	1888	9.7	309	8.8
150907MR1	Source (in housing)	5.99	1795	11.1	3.4	93.2
150907MR2	Same site as 121007A	6.09	1790	11.2	7	ND
150907MR3	Same site as 121007B	6.36	1755	11.3	94	ND
121007B2	Same site as 150907F	6.59	2070	10.7	211	ND
121007B3	Mid channel iron mat	7.18	2050	10.8	277	ND
		Val Sinestra				
150906B[a]	Conradins spring*	6.62	5140	7.9	103	
121017E	Same site as 150906B	6.68	6960	7.4	106	22
150906C[a]	under trap door	6.11	2886	8.6	1.4	166
150906D	Ulrichs spring* pool	7.00	6510	8.7	159	1.4
150906MR2	Ulrichs spring* source	6.38	6780	8.9	8	141
121017MRA	Same site as 150906D	6.49	8700	8.8	BDL	ND
150908H		6.28	2892	8.5	105	152
121017F	Same site 150908H	6.31	3930	8.4	60	115
121017G	Conradins spring*	6.60	3940	8.3	156	157
150906MR1	Same site as 150906B	6.77	2175	9.1	206	0.9
121017MRB	Water from Pump	6.32	3910	7.9	210	ND
150908I	La Brancia Creek	8.27	257.4	5.3	319	BDL
		Alvaneu Bad area				
150905A[a]	Arvadi Spring	7.93	1118	7.8	314	2.5
150911T[a]	Eisenquelle	7.34	1502	7.9	5	5

Sample IDs in bold have complete geochemical suites, non-bolded IDs only have field data. Field measurements of outflows channels indicated in the maps (figs 2 and 4) are depicted in figures 3 and 5, and are available in appendix 3.
[a] indicates iron oxidation experiment location.

ailments. A grand hotel, clinic and bathhouse were built on the site, which was in use from the early 1800s until the closure of the hotel in the mid-1900s. Recent renovations for tourism have led to the site being reopened, though the springs are no longer a draw and remain inaccessible to the public. The source water of the springs is still located in the now dilapidated bathhouse, but have returned to a more natural state having been largely undisturbed for many decades. The volume of outgassing CO_2 is significant and can build up in the enclosed space, as evidenced by the numerous dead birds and mice in the structure. Extreme caution should be used when sampling these springs to avoid the risk of asphyxiation. There are four spatially distinct sources of water, that were also found to be compositionally different (see Table 1). Three of the springs precipitate a calcite layer on the water surface. The sediment in each spring is a deep orange color. Only one of the sources flows at a high enough rate to produce an outflow, as shown in the map of the area in Fig 4. This spring (sample number 150906C) is located under a trap door and flows 20 meters through an underground pipe to an outlet on the bank of La Brancla creek, a tributary of the Engadin river. The outflow creates an orange iron-arsenic microbial mat that stretches for twelve meters before flowing into the creek.

Samples were taken at each of the sources, as well as in the outflow. The field data profile for this outflow can be seen in Fig 5; note the break in scale between the source and the next sample more than 20 m downstream beyond the pipe. As at Rablönch, the pH increases down the outflow, although the increase is considerably smaller. O_2 increases down the outflow but never reaches saturation. The Fe(II) concentration is greater at Val Sinestra than at Rablönch, and its gentle decrease down the outflow is consistent with the slower abiotic oxidation rate in the lower pH outflow.

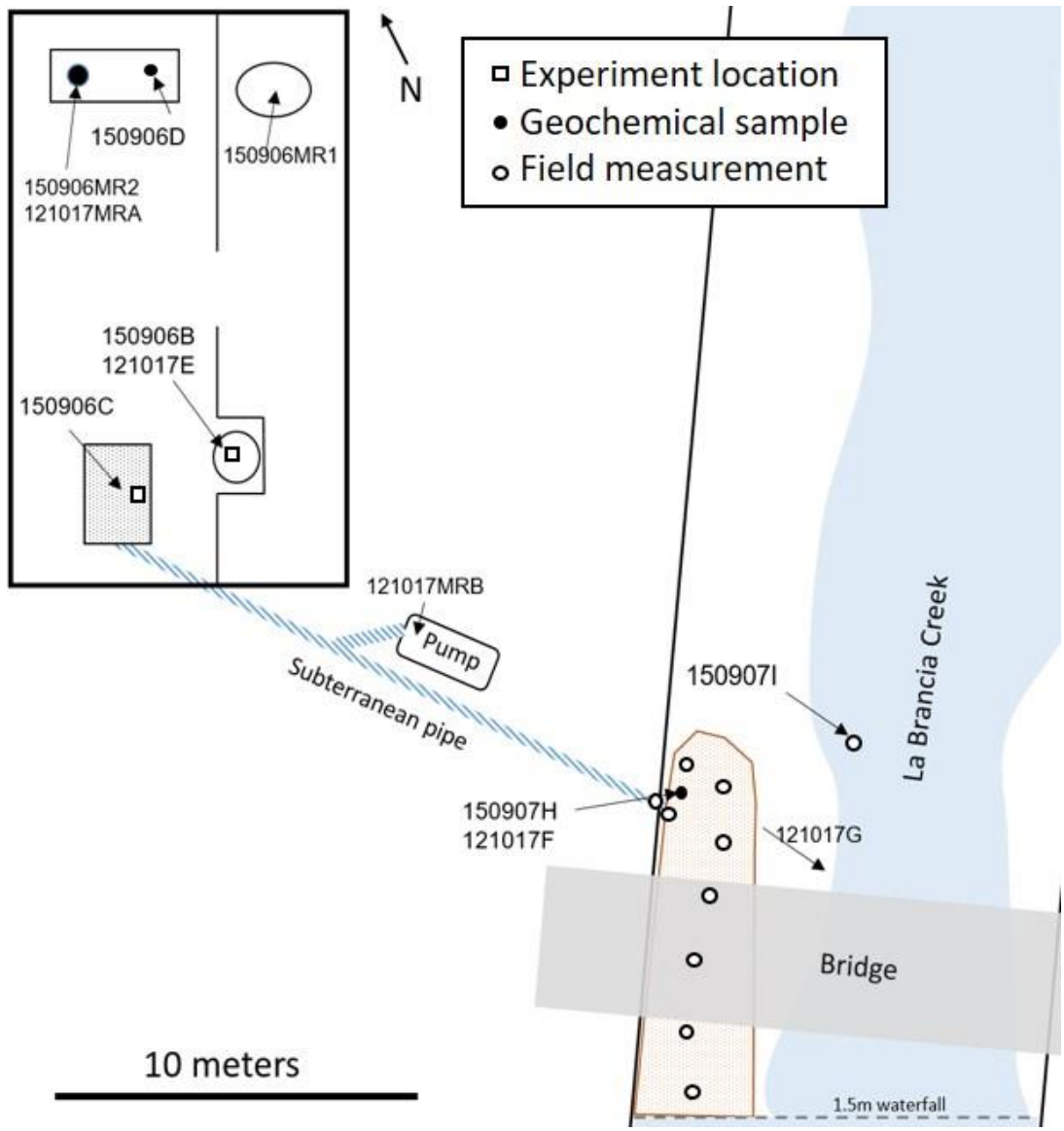

Figure 4 – Map view of the Val Sinestra area. The top left rectangle represents the dilapidated bath house, which is drawn to scale. Springs are drawn as circles and squares, with sample locations indicated with symbols analogous to figure 2. Locations of complete geochemical sample suites are labeled with the sample number. The orange area represents an iron mat located in the riverbed. The hashed line indicates an underground pipe that brings spring water from the bathhouse to the riverbed. A profile of the outflow from 150906C through the iron mat can be found in figure 5. The iron mat terminates abruptly when it falls down a short waterfall into the creek.

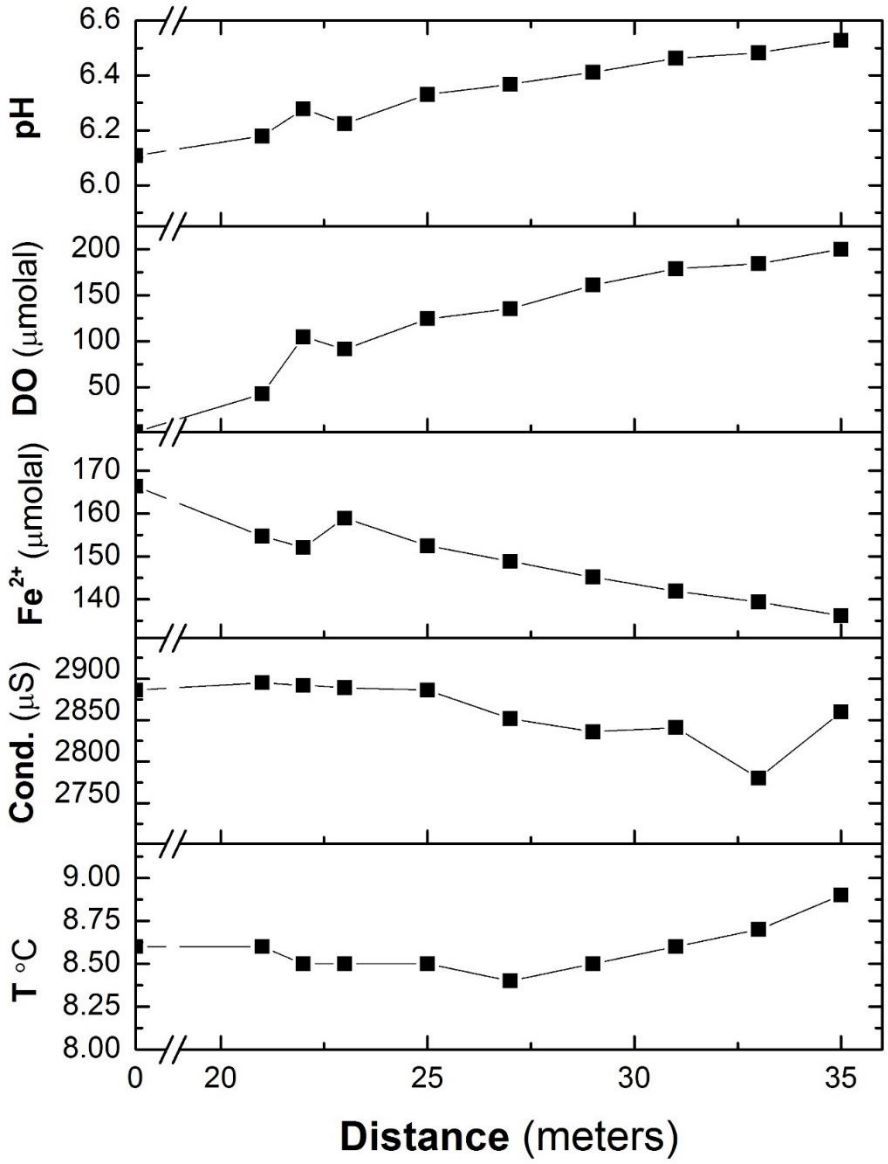

Figure 5 - Val Sinestra outflow profile – Distance is measured from the source in the bathhouse 150906C (see map). The break in the distance scale corresponds to the underground pipe. The majority of the accessible outflow is located in the channel of the river. The pH increases with distance from the source. Dissolved oxygen increases as air infiltrates the water. The water never quite gets to saturation with the air despite the relatively long outflow distance. Fe(II) decreases consistently along the outflow. Conductivity is stable between the source and the start of the outflow, but begins to decrease consistent with mineral precipitation. The temperature does not change appreciable over the distance of the outflow path.

2.2.3 Alvaneu Bad area

There are several iron and sulfide rich springs in the Alvaneu Bad area. The springs are spread over approximately a kilometer along the base of a steep mountain. The outflows of the springs drain into the Albula River east of the town of Filisur and south of Alvaneu. Sampling took place at two iron springs, Arvadi and the aptly named Eisenquelle. Arvadi spring is a mix of two separate springs located along a walking path next to a golf course. The source waters are contained in a locked utility building. The water is piped through a half meter diameter drainage pipe for more than 50 meters which allows interaction with the atmosphere. The pseudo-source emerges in a 4 meter diameter pool designed to look like a natural spring. The water is fully oxygenated at this point, with only minor amounts of iron remaining. The spring also contains apparent dissolved sulfide (as indicated by precipitated sulfur and sulfide smell), which was not measured due to technical difficulties in the field. The sediment in the spring is mostly calcite with visible ferric minerals and flocculent elemental sulfur. A profile of pH, oxygen, temperature and conductivity taken down the outflow from the pseudo source show little change in composition over 15 meters (data not shown). An Fe-oxidation experiment was performed close to the pseudo-source.

Eisenquelle is an iron spring approximately 1.3 km West of the town of Filisur, Graubünden Canton, Switzerland. This spring emerges from the base of a steep mountain and produces a vividly colored iron mat. Filamentous photosynthetic biomass is found along the length of the spring and is coated in iron oxyhydroxides, similar to the description of iron-encrusted photosynthetic biomass from Mori *et al.* (2015). The flow merges with a mountain stream less than a meter from the source. Iron oxide is visible as

the merged waters flow ~12 meters into the Albula river. A rate experiment was conducted at the spring source.

2.2.4 Jöri Lakes

The Jöri Lakes are a series of 24 lakes and ponds located at an average of 2600 meters above sea level in the Vereina valley, 10 km southeast of Davos, Switzerland. The retreating Jöri glacier has increased the number of lakes from 13 in the early 1900's to 21 in 1999. The original 13 lakes are numbered (I – XIII) as outlined by Kreis (1921); the numbering was expanded to XXI by Hinder *et al.* (1999b). Several more lakes have formed over the last 17 years, including lake XXII described here. A map of the area is shown in Fig 6. More complete descriptions of the Jöri catchment can be found in Kreis (1921) and Hinder *et al.* (1999a, 1999b).

All of these lakes are completely covered by ice during the winter, which permits anoxic regimes that facilitate redox cycling (Hinder *et al.*, 1999b), and several show evidence for iron cycling (Steiner *et al*., 2000). We observed ferrous iron in waters and sediment, as well as iron mineral staining on rocks and sediments. The snowmelt fed lakes are extremely dilute, and conductivities ranged from 6-50 µS/cm. Field data collected in this area can be found in Table 2.

2.3 Methods

2.3.1 Geochemistry

Complete geochemical suites were collected to provide geochemical context for each rate experiment, and include field measurements, water chemistry and sediment characterization. Field measurements include pH, temperature, conductivity, dissolved oxygen, and ferrous iron. Water samples were analyzed for major ions, dissolved organic

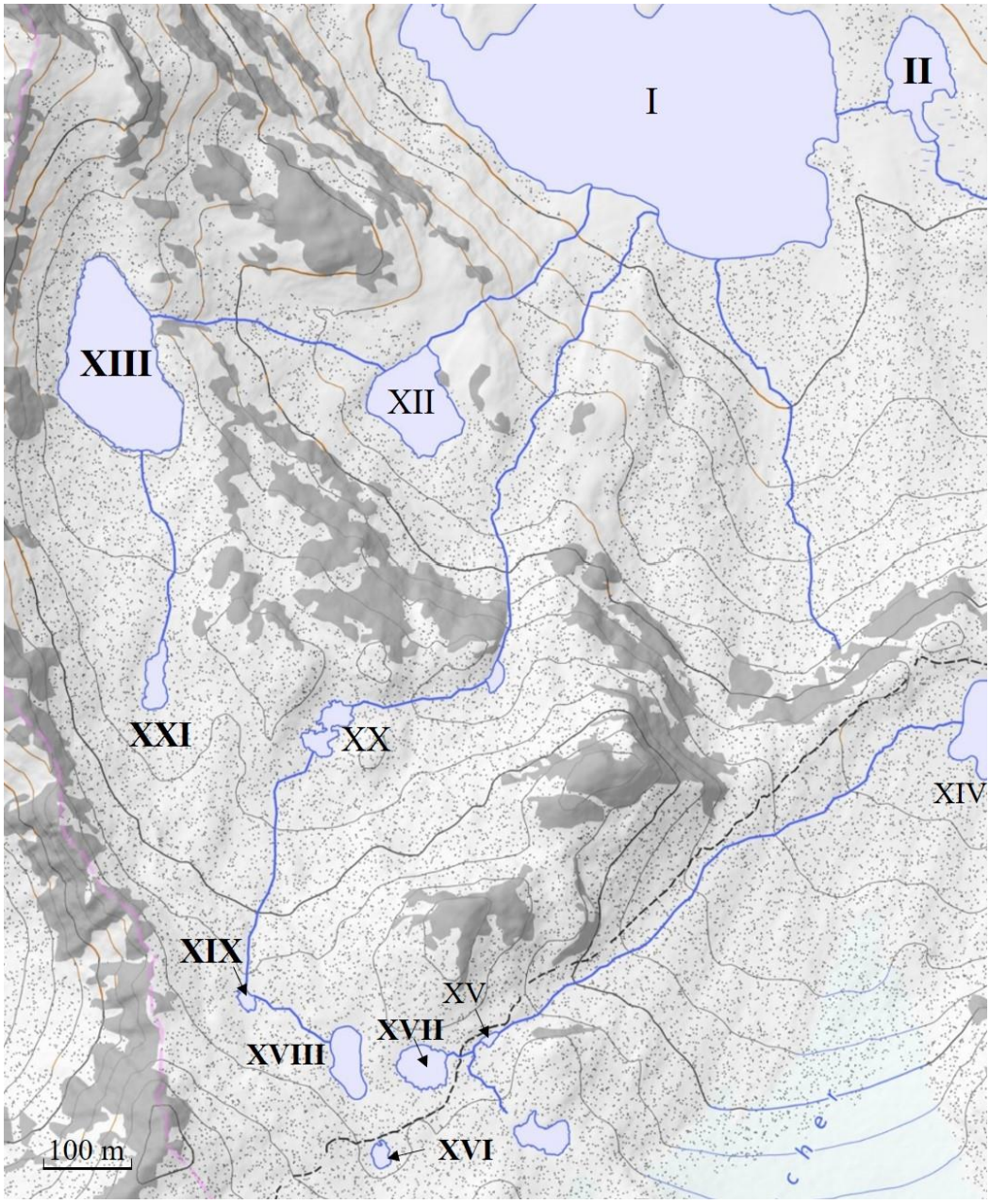

Figure 6 – A topographical map of the western Jöri lakes catchment. Roman numerals designate lake numbers from previous publications (Kreis, 1921; Hinder et al., 1999b). Bolded numerals indicate sample locations. Lakes II, XII, XIII have abundant iron staining on rocks. Map used with the permission of Geodata © Swisstopo

Table 2 – Jöri Lake Field Measurements

Sample ID	Lake number	pH	Cond µS / cm	T °C	O_2 µmolal	Fe^{+2} µmolal
150909K	XIII	6.64	7.1	9.7	293	0.4
150909L	XIII Outflow	7.08	6.8	9.9	293	0.2
150909N[a]	XIII 10 meter depth	5.76	14	7	218	15.6
150910P	Snow above XIII	6.69	4.6	8.5	251	ND
150909M[a]	XXI	9.03	25.6	8.1	336	BDL
150910O[a]	II	6.98	30.7	7.2	320	BDL
150910Q	XIX	7.36	28.8	6.6	321	BDL
150910R	XVIII	7.18	29.1	6.5	321	0.4
150910S	XVI	8.94	33.5	3.8	343	BDL

All samples have complete geochemical suites. Major ion data corresponding to these samples is in table 4.
[a] indicates iron oxidation experiment location.

carbon (DOC), dissolved inorganic carbon (DIC), trace elements, $\delta^{18}O_{water}$, $\delta^{2}H_{water}$, and small organic anions. Sediments were analyzed for mineral composition by X-Ray Diffraction (XRD) and sediment iron.

Temperature, pH, conductivity and dissolved oxygen were measured with portable meters in the field. The pH meters were calibrated daily at ambient temperatures. Dissolved oxygen was measured using a fluorescence method with a detection limit of 15 parts per billion (ppb) and a resolution of ± 4 ppb (Fibox 4 meter and optical probe, PreSens Inc., Germany).

Water was collected into a 1L Nalgene bottle for experiments and geochemistry simultaneously using either a 140 mL syringe or a polypropylene dipper. All collection tools were acid washed prior to the trip and rinsed with spring water between samples. Samples were filtered through 1.2 µm and 0.8/0.2 µm polyethersulfone (PES) syringe filters (Acrodisc® 32 mm PF Syringe Filter with Supor filters®) rinsed with 20 mL of water before collection. Aliquots were collected in the order listed here to minimize contamination. Water isotope samples were collected in 40 mL square glass vials with no headspace. Samples for cations and anions were collected in separate 30 mL high density polyethylene (HDPE) bottles that had been HCl rinsed, and then triple rinsed with 18.2 MΩ.cm ultrapure water. The cation bottle was treated with 1 mL of 6 N methanesulfonic acid. 5-10 mL of headspace was left to allow for expansion during sample freezing on the evening of collection. Dissolved inorganic carbon (DIC) samples were collected in 40 mL brown borosilicate vials with butyl rubber stoppers. Dissolved organic carbon (DOC) samples were collected in the same type of vials, with Teflon-lined silicone stoppers and 1 mL of concentrated H_3PO_4. The DIC and DOC samples were filled completely to

eliminate head space and quickly sealed to prevent degassing. Trace elements were collected in HCl-rinsed 60 mL HDPE bottles containing 800 µL of trace-metal-free concentrated nitric acid. Organic acid samples were collected last in precombusted brown borosilicate glass vials with deionized-water-rinsed Teflon caps. Field blanks were collected with the same sampling equipment and methods with 18.2 MΩ.cm deionized water brought to the field in HCl and water rinsed 1L HDPE bottles.

Water Analyses – Water isotopes ($\delta^{18}O$, $\delta^{2}H$) were determined with an Off-Axis Integrated Cavity Output Spectroscopy (Los Gatos Research) using methods previously outlined (Meyer-Dombard 2014). Cations (Na^{+}, K^{+}, NH_4^{+}, Ca^{+2}, Mg^{+2}), anions (SO_4^{-2}, Cl^{-}, Br^{-}, F^{-}, NO_3^{-}, NO_2^{-}) and small MW organic anions (formate, acetate, lactate) were measured using ion chromatography (IC). Cations and anions were determined on two Dionex DX-600 IC systems using suppressed conductivity detection by methods previously described (Fecteau, 2016). Briefly, the anion system used S11-HC/AG11-HC columns, a potassium hydroxide eluent generator, and a carbonate removal device. The cation system used CS-16 and CG-16 columns and cations are eluted isocratically with 19 mM methanesulfonic acid (MSA). Organic anions were determined on a Dionex ICS-1500 system using an ICE-AS6 ion exclusion column and 0.4 mM heptafluorobutyric acid eluent. DIC and DOC were determined by methods previously outlined (Havig et al., 2011; Schubotz et al., 2013; Meyer-Dombard et al., 2014).

Samples for ferrous iron were taken directly with a 3 mL syringe and immediately filtered through a 0.2 µm PES filter into a 5 mL plastic vial containing 100 µL of 10 g/L 1,10-phenanthroline monohydrate in 0.1M glycine/HCl buffer adjusted to pH 2.3. Laboratory experiments showed this method preserved ferrous iron for later measurement

for up to 2 months. The method did not reduce ferric ions, or oxidize ferrous iron. Measurements were accurate even in with ratios of up to 100:1 Fe^{3+}/Fe^{2+}, which can cause issues with some photometric methods. This method has been tested and used in several harsh natural systems, including acidic hot springs and acid mine drainage (see chapters 3 and 4). The detection limit is 0.006 mg Fe / L, with a total uncertainty of +/- 0.01 mg/L for a field measurement.

Sediment samples were collected with a variety of cleaned Teflon spoons, scoops, and tweezers that were sterilized with ethanol between samples. Each sample was collected into a new 100 mL sterile sample cup. Aliquots for DNA and RNA were transferred into 1.8 mL cryovials and immediately frozen on dry ice. Samples for XRD and reducible iron were placed in 5 mL cryovials and also frozen on dry ice in the field. Larger pieces of sediment were placed into sterile whirlpak bags and frozen later in the day.

2.3.2 Sediment Analysis

Carbon content and isotopic composition of sediments was determined by Elemental Analysis – Isotope Ratio Mass Spectrometry (EA-IRMS) on a Costech elemental analyzer and a Thermo Delta plus Advantage IRMS (Havig et al., 2011). Samples were prepared by drying sediments at 50°C overnight, grinding to a fine powder, and drying again overnight. Total carbon samples were prepared by weighing ~100 mg of sediments in tin capsules to the nearest microgram. Organic carbon analyses were prepared the same way, except they were repeatedly acidified with high purity 3 M HCl (OmniTrace ®) in silver capsules.

Mineral composition of sediments was analyzed by powder X-ray Diffraction (XRD). Sediment samples were frozen in the field on dry ice to minimize redox processes. In the lab, samples were dried at 50°C overnight before being powdered using an agate mortar and pestle. Approximately 200 mg were mixed with isopropanol and applied to quartz zero background slides. Mineral identification was performed by XRD using Cu Kα radiation from 4° to 90° 2Θ, with a step size of 0.016° and rate of 0.850 s/step with a Siemens D5000. The XRD system was run at 40 kV and 40 mA. Resulting diffractograms were analyzed using the JADE XRD software.

Sediments were characterized for their poorly crystalline ferric mineral content by the method outlined by Lovely and Phillips (1989), which allows for rapid quantification of minerals that are available to microbial iron oxidizers. Ferrous iron in sediments was measured by adding approximately 100 mg of freshly weighed sediment to 5 mL of 0.5 M HCl (OmniTrace). Samples were vortexed and allowed to sit for one hour. Iron was measured using the ferrozine method in HEPES buffer (Lovely and Phillips, 1989). The total iron content of the sediments, including amorphous ferric minerals and Fe^{3+}, were determined by the same method, except a solution of 0.25 M hydroxylamine and 0.25 M HCl was used to reductively dissolve minerals. Ferric iron was then determined by subtracting the measured Fe(II) from the total iron.

2.3.3 Rate Experiments

Experiments were designed to measure the rates of biological and abiological iron oxidation reactions *in situ*. Microcosm experiments (60 mL) were performed using sediment and sample water at the field site. Two procedures were used, with the choice determined by the anticipated duration of the experiment. The standard protocol was used

in systems where ferrous iron was not anticipated to be depleted for at least 20 minutes. Typically, 10 grams of sediment and 40 mL of spring water were combined in a 60 mL serum bottle. Each assay included an *in situ* rate (unamended), an added Fe(II) treatment, and a killed control. Rates were measured in triplicate. The experimental treatment included addition of either 1 mg/L Fe(II) (as $FeSO_4 \bullet 7\ H_2O$) to samples from springs with native concentrations less than 0.5 mg/L, or 3 mg/L Fe(II) to all other systems. This range in Fe(II) allowed an assessment of maximum metabolic capacity of each system and better resolution of rate constants. Killed controls were fixed with 6 mM sodium azide that had the pH matched to the spring. These killed controls had the same amount of added Fe(II) as the experimental bottles. In cases where the rates were so fast that iron was depleted within minutes, filtered spring water was used as an abiotic control. Measurements of ferrous iron concentration were assayed by the sampling method outlined above at a time interval appropriate for the pH value. The interval was around 30 minutes for springs with pH <7, 10 minutes for springs with pH 7-7.5, and 1 minute for springs with pH > 7.5. These short durations were intended to prevent large changes in the microbial community from occurring over the duration of the experiment.

An alternate protocol was used in systems where ferrous iron was expected to be fully depleted in the experiments in less than 20 minutes. Modifying the protocol permitted more accurate rate measurements at these kinetic extremes. The often low concentration of Fe(II) coupled with the duration of experiment setup times during which microcosm water is equilibrating with the atmosphere can create variations in reaction progress and pH before data collection can begin. This can lead to large uncertainties that interfere with distinguishing rates among treatments. To compensate, all treatments

included added ferrous iron and replicates were performed sequentially to minimize equilibration time. Water was drawn directly from the sample location with a syringe and immediately added to a serum vial. Reagents were added immediately. Time was measured from the moment iron was added. Treatments included added Fe(II) and a filtered-sterile control, each with 3 replicates. The experimental treatment was unmodified from the standard procedure described above. The filtered treatment consisted of 0.2 µm filtered water from the natural system with 1 mg/L added Fe(II) (as $FeSO_4$). Results of several iterations of various sample protocols revealed that filter sterilization is the most representative of *in situ* abiotic rates *in situ*ations where abiotic oxidation is extremely rapid. The primary objective of this treatment is to minimize oxidation of components in the sample fluid and maintain the system pH by minimizing degassing and precipitation. A major drawback is that any mineral catalysis is unmeasured. Test experiments show that addition of sodium azide requires several minutes of equilibration before measurements of Fe(II) and pH are reliable, even when the pH of the azide solution is matched to the pH of the system. While azide is effective at killing FeOB, questions remain about its (and other fixatives) effect on the measured rate during iron oxidation experiments.

2.3.4 Community Composition

DNA extraction from sediments was performed in Prof. Eric Boyd's laboratory at Montana State University, using methods analogous to Boyd et al. (2007) and Coleman et al. (2016). Briefly, approximately 250 mg of thawed sediment or mat sample was used for DNA extraction using a DNA extraction kit (MP Biomedical FastDNA spin kit for soils). DNA was quantified with the Qubit DNA assay kit and a Qubit 2.0 fluorimeter

(Life Technologies). PCR was performed using universal 16s rRNA primers 515F (GTGCCAGCMGCCGCGGTAA) and 806R (GGACTACHVGGGTWTCTAAT). ~1 ng of purified genomic DNA was subjected to PCR in triplicate using an initial denaturation at 94°C (4 min), followed by 35 cycles of denaturation at 94°C (1 min), annealing at 55°C, primer extension at 65°C (1.5 min), and a final extension step at 65°C (20 min). The PCR mixture contained 2 mM $MgCl_2$, 200 µM each deoxynucleotide triphosphate, 0.5 µM each forward and reverse primer, 0.4 mg/ml bovine serum albumin, and 0.25 units of Taq DNA polymerase in PCR buffer (all reagents: Invitrogen) for a total volume of 50 µL. 4µL of each PCR product was run on a 2% agarose gel to ensure amplification. Triplicate PCR products were then pooled and purified using the Wizard PCR cleanup system (Promega) per the instructions, yielding a final volume of 50 µL. DNA was quantified again using the Qubit system. PCR products were sent to the MrDNA lab (Molecular Research LP, Shallowater, TX) for sequencing using the Illumina MiSeq system with 30,000 reads per assay.

2.4.5 Speciation Calculations

Speciation calculations were performed with compositional data from each system. Thermodynamic data used for these speciation calculations were taken from Helgeson *et al*. (1978), Shock *et al*. (1989, 1997), Shock and McKinnon (1993), Sverjensky *et al*. (1997), Shock (2009), together with estimates obtained in this work as described in appendix A. Briefly, thermodynamic properties of $FeHCO_3^+$, $FeCO_3^0$, $Fe(CO_3)_2^{-2}$, $NaCO_3^-$, $NaHCO_3^0$, KCO_3^-, $KHCO_3$, $NH_4CO_3^-$ and other relevant carbonate and bicarbonate aqueous species were estimated using the methods of Shock and Helgeson (1988), Shock *et al*. (1989), Shock and Koretsky (1995), Sverjensky *et al*.

(1997), and Murphy and Shock (1999). Equilibrium constants for these species at 25°C and 1 bar reference conditions were obtained from the literature (see appendix A for references). The thermodynamic properties were used to generate equilibrium constants at appropriate temperatures calculated with the revised Helgeson-Kirkham-Flowers equation of state (Shock *et al*., 1992) using the CHNOSZ software package (Dick, 2008). Geochemical speciation calculations were conducted with the EQ3/6 software package (Wolery and Jarek, 2003) using a thermodynamic database consistent with the references above, and an extended Debye-Hückel equation for activity coefficients (Helgeson, 1969). See appendix A for details.

2.5 Results and Discussion

2.5.1 Rate Experiments

Experiments to determine the rate of biological and abiotic iron oxidation were performed at ten locations. The systems chosen for these experiments vary dramatically in geochemical composition, but all showed evidence that they support iron oxidation. A primary objective of the experiments was to determine the conditions that favor biological oxidation, as well as the conditions that exclude biology. Biological oxidation was detected at six locations; exclusively abiotic oxidation was detected at four locations. Abiotic rates ranged from inconsequential, to oxidation too fast for biology to compete. Results show pH and DIC as major determinants of biological iron oxidation activity. The standard experiment protocol allowed the measurement of three rates: the *in situ* rate, the abiotic rate, and an potential rate amended with added Fe(II), each determined in triplicate. An example of data collected during a field experiment at 150907F, an iron mat at Rablönch is shown in Fig 7. Changing concentrations of Fe(II) over the duration of the

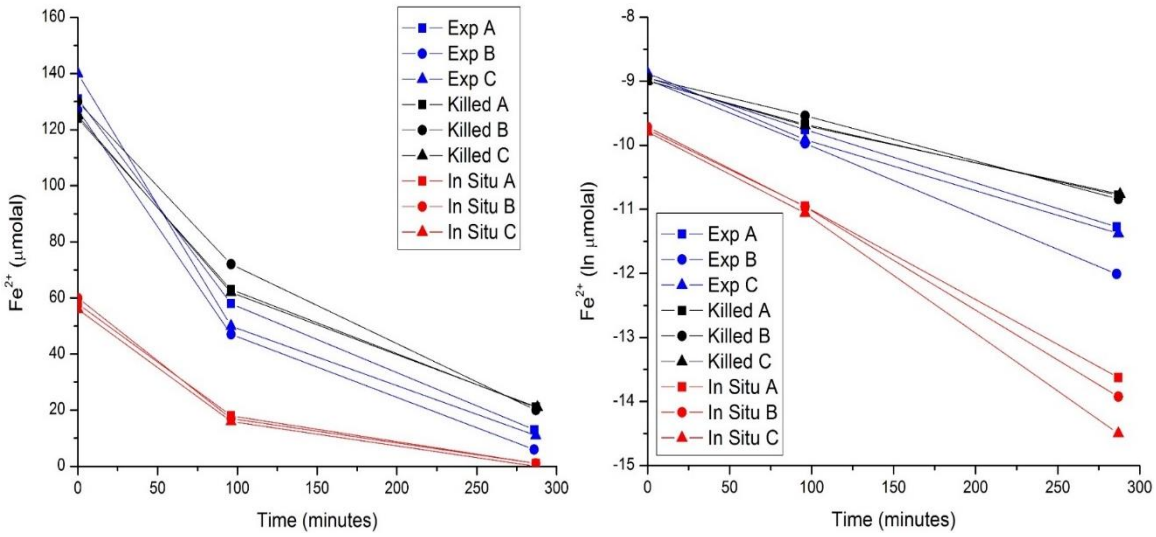

Figure 7 – Representative iron oxidation experimental results (150907F) for a Rablönche iron mat, using the standard rate experiment protocol; additional plots can be found in Appendix B. Blue, black, and red points represent experimental, killed, and *in situ* rates, respectively. Plot 7a shows data as collected during field experiments. The experimental (blue) and killed (black) points both have added ferrous iron, which is why the initial concentration is higher than the *in situ* (red) points. Plot 7b shows the same data plotted on a natural log scale, revealing the first-order kinetics of the reaction.

experiments are shown in Fig 7A. The *in situ* measurements (red points) have an initial iron concentration equal to that found naturally in the springs and Fe(II) is depleted to close to the detection limit after ~275 minutes. This near complete Fe(II) depletion means the measured rate is a minimum value, as the time at which the experiments become fully depleted is unknown. The results from these *in situ* treatments are indicative of the total rate of iron oxidation in the spring, including all biotic and abiotic processes. The experimental measurements (blue points) have ~56 µmolal Fe(II) added to assess the maximum capacity of the system to oxidize iron. In this case, the replicates start near 130 µmolal and decrease to 20 µmolal after ~275 minutes. The black points indicate the results of experiments on killed controls to determine the abiotic rate. The treatments are identical to the experimental measurements, except that 6 mM azide is added to inhibit growth. The initial concentrations are also close to 130 µmolal, but are depleted to only 30 µmolal after ~275 minutes. The differences in rates between the black and blue points are attributable to FeOB in the sediment.

The experimental data are plotted as the natural log of the Fe(II) concentration in Fig 7b. The linearity of the plots in Fig 7b reveal pseudo first order kinetics for these field experiments; the slopes of the lines yield rate constants for the oxidation reactions, k_{ox}. The rate constant is the most comparable measurement of rates among replicates and between systems, as it is independent of the initial concentration of Fe(II). The faster rate constants in the *in situ* and experimental treatments compared with the killed controls indicates rates are enhanced by iron oxidizers. Rate measurements from all standard protocol experiments, including rate constants, rates, and half-lives, can be found in the

upper part of Table 3, and plots analogous to Fig 7 for all standard protocol experiments are collected in Appendix B.

*In situ*ations where ferrous iron is depleted in less than 20 minutes, the standard protocol is not sufficient to resolve differences in rates between treatments. In such systems a modification of the experimental protocol was implemented to attempt to distinguish biotic rates from the rapid abiotic process. An example of data from a spring (150907G) obtained using the modified protocol is shown in Fig 8. The plots are analogous to those in Fig 7, but note the much shorter duration. The experimental treatment (blue points) have sediment, water, and an additional ~56 µmolal Fe(II). The filtered treatment (black points) have only filtered spring water and added ~56 µmolal Fe(II). In this example, biological iron oxidation was not detected in the experiments that include sediments, leading to the conclusion that the observed rate is dominated by abiotic processes. The filtered, abiotic, oxidation rate actually exceeded that of the experimental treatment. While the exact cause for this is unknown, possibilities include desorption of Fe(II) from the sediments or increased chelation from organic compounds in the sediment. The extremely rapid chemical oxidation means any increase to the rate by heterogenous oxidation by ferric minerals is negligible.

Rate data from all modified protocol experiments (type 2) can be found in the lower part of Table 3, including rate constants, half-lives, and initial rates for each replicate. The abiotic component of the rate is included in the experimental and *in situ* treatments. Minimum rates are reported for Jöri Lake 20 (150909M) and Arvadi spring (150905A), because extremely rapid abiotic oxidation in these systems caused the concentration of ferrous iron to be depleted to close to the detection limit by the time the

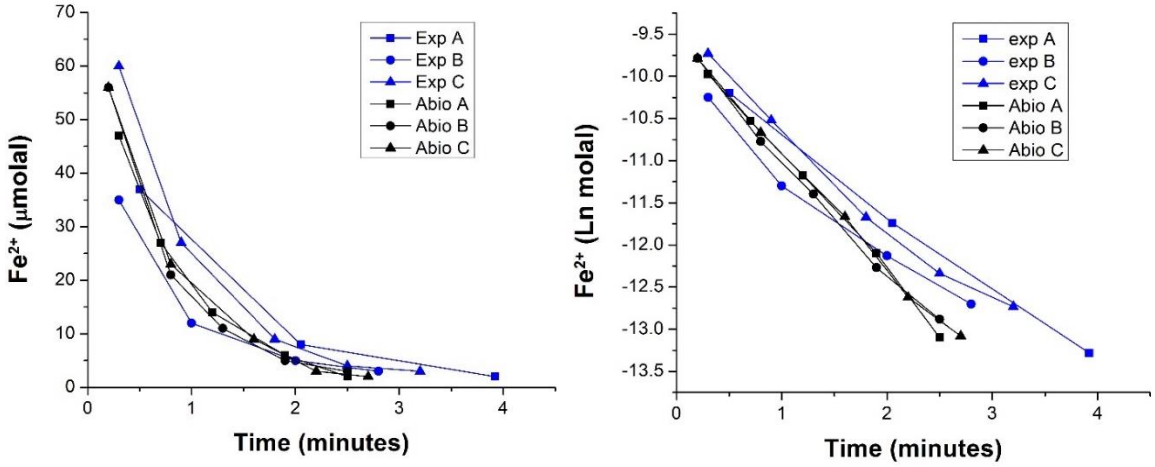

Figure 8 – Representative iron oxidation experimental results (150907G) for an outflow at Rablönche, using the modified rate experiment protocol. Blue points represent the experimental rates, while black points indicate the abiotic (filtered) rates. Plot 8a shows data as collected during field experiments. Both data sets have added ferrous iron (see text). Note the short duration of each experiment. The experimental and abiotic rates are nearly indistinguishable, suggesting biological iron oxidation is not present. Plot 8b shows the same data plotted on a natural log scale, revealing the first order kinetics of the reaction.

Table 3 – Results of *in situ* rate experiments. Results calculated using equation 3. Rate constants, k, and rates calculated from experimental data

				Experimental				In Situ				Killed or Filtered			
				k	half life	Rate	Average Rate	k	half life	Rate	Average Rate	k	half life	Rate	Average Rate
	Sample ID	Sample Name	Replicate	min^{-1}	minutes	$\mu mol\ min^{-1}$	$\mu mol\ min^{-1}$	min-1	minutes	$\mu mol\ min^{-1}$	$\mu mol\ min^{-1}$	min^{-1}	minutes	$\mu mol\ min^{-1}$	$\mu mol\ min^{-1}$
Experiment Type 1	150906B	Conradins/Val Sin	A	0.015	45	0.38	0.33	0.0149	47	0.08	0.08	0.0065	107	0.093	0.12
			B	0.012	57	0.32		0.0162	43	0.08		0.0072	96	0.111	
			C	0.012	58	0.28		0.0168	41	0.07		0.0079	88	0.154	
	150906C	Trap Door	A	0.002	428	0.16	0.14	0.0007	950	0.04	0.04	0.0002	2888	0.023	0.03
			B	0.001	578	0.12		0.0006	1216	0.03		0.0003	2567	0.026	
			C	0.001	506	0.15		0.0007	937	0.04		0.0004	1980	0.032	
	150907F	Rablönche OF4	A	0.011	65	0.45	0.42	0.0185	37	0.34	0.29	0.0061	114	0.243	0.25
			B	0.011	65	0.43		0.0136	51	0.26		0.0062	112	0.256	
			C	0.009	81	0.39		0.0148	47	0.27		0.0066	105	0.264	
	150911T	Eisenquelle Source	A	0.043	16	0.64	0.43	*	*	*	*	0.0107	65	0.137	0.28
			B	0.032	21	0.33		*	*	*	*	0.0129	54	0.275	
			C	0.025	27	0.32		*	*	*	*	0.0192	36	0.424	
	150909K	Jöri Lake 13	A	0.003	215	0.06	0.05	0.0013	533	0.003	0.01	0.0001	5332	0.002	0.01
			B	0.002	330	0.04		0.0018	394	0.010		0.0002	3014	0.006	
			C	0.003	261	0.05		0.0041	169	0.009		0.0004	1733	0.007	
	150910O	Jöri Lake 2	A	0.011	65	0.10	0.08	0.0033	209	0.007	0.00	0.0006	1195	0.009	0.03
			B	0.010	72	0.07		0.0084	83	0.004		0.0025	274	0.044	
			C	ND	ND	ND	ND	0.0057	123	0.003		0.0031	224	0.051	
				Experimental				**Filtered**							
Experiment Type 2	150907G	Rablönche OF6	A	1.080	0.6	12.9	15.88	1.413	0.49	7.324	8.62				
			B	0.901	0.8	10.2		1.365	0.51	9.160					
			C	1.282	0.5	24.5		1.331	0.52	9.379					
	150908J	Rablönche OF5	A	0.706	1.0	15.5	8.90	0.791	0.88	19.240	18.85				
			B	0.585	1.2	6.2		0.761	0.91	17.413					
			C	0.630	1.1	5.0		0.707	0.98	19.885					
	150909M	Jöri Lake 20	A	3.9*	0.18*	N/A#		3.9*	0.18*	N/A#	N/A#				
			B	3.9*	0.18*	N/A#		3.9*	0.18*	N/A#					
			C	3.9*	0.18*	N/A#		3.9*	0.18*	N/A#					
	150905A	Arvadi Spring	A	3.3*	0.21*	8.1*	8.1*	3.3*	0.21*	8.1*	8.1*				
			B	3.3*	0.21*	8.1*		3.3*	0.21*	8.1*					
			C	3.3*	0.21*	8.1*		3.3*	0.21*	8.1*					

a. Indicates minimum rate (see text). N/A indicates not applicable.

third data point was taken (typically less than one minute). While both the experimental and filtered treatments both showed minimum rates, biological oxidation is presumed to be excluded in the bulk system by the lack of bioavailable ferrous iron (see below).

Taken together, the rate experiments show that opportunities for biological Fe oxidation in specific settings are fundamentally determined by the geochemistry of those systems, especially the pH. Results show that FeOB are responsible for the majority of the iron oxidation in systems with pH < 7, while the extremely rapid chemical oxidation in systems above pH ~7.4 effectively preclude FeOB. Results summarized in Fig 9 allow comparison of iron oxidation rate constants found in the live microcosms (red dots) with the abiotic oxidation rates as found in the azide killed and filtered treatments (black squares). The faster of the experimental or *in situ* treatment set is used as the "live" microcosm value (values used are bolded in table 3). The values obtained by both treatments is typically similar, as anticipated from the reactant independent rate constants. The rates in Fig 9 are averages of each three replicates with error bars showing one standard deviation. It can be seen that the abiotic rates measured in these systems increase dramatically as pH increases, consistent with speciation models discussed below, and exceed the rate of iron oxidation in the live microcosm treatments at pH ≥ 7.7. Below this pH, the oxidation rates of the experimental treatments fall in a relatively consistent range, suggesting that FeOB communities have a maximum physiological capacity to oxidize iron. At higher pH, the abiotic rate becomes so rapid that it appears to exclude biology.

It should be noted that the live microcosm rates shown in Fig 9 do not have the abiotic contributions subtracted. Therefore, it is the difference between the two points

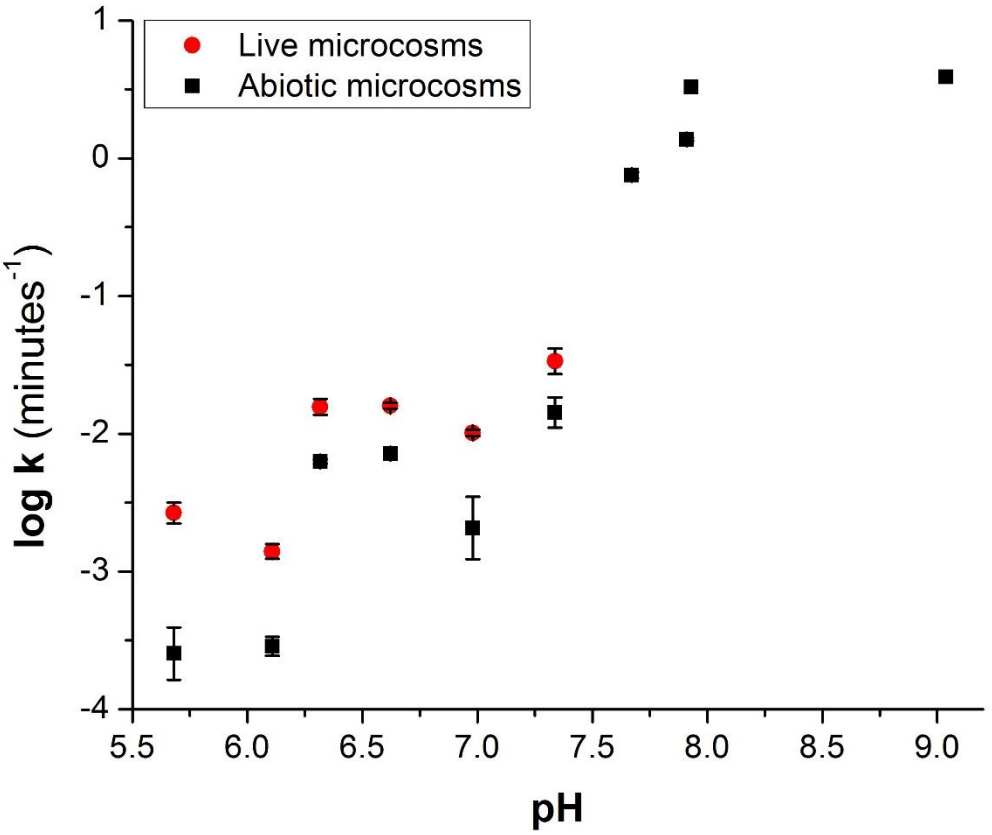

Figure 9 – Live microcosms (red) and abiotic microcosms (black) oxidation rates in Swiss springs and lakes. Reported values are the average of 3 replicates. Error bars signify ± one standard deviation. Live microcosm rates reported here are those measured in the field and do not have the abiotic contribution subtracted. The contribution of FeOB to the rate is the difference between each pair of red and black points. Note that experimental oxidation falls within approximately one order of magnitude of rate constant. A biological contribution to the iron oxidation was not detected above pH 7.4.

that represents the rate of oxidation by FeOB. This difference, represented as the percentage of iron oxidation attributable to biology is shown in Fig 10. The rates used to calculate these percentages are the initial instantaneous rates (found in table 3), as these are most indicative of rates in the natural systems. Since the biotic rate is relatively consistent among systems, as inferred by the rough similarity of iron oxidation in experimental treatments, the abiotic rate dictates how much iron is available to FeOB. Considering that the solubility of Fe(II) is so low at pH > 8, and the abiotic oxidation rate so fast, the maximum attainable flux of Fe(II) is unlikely to support FeOB.

2.5.2 Speciation

The geochemical composition of a natural system can determine the form that ferrous iron takes in solution, and ultimately dictate abiotic iron oxidation rates. As an example, increasing concentrations of bicarbonate were found to significantly increase the abiotic iron oxidation rate even while keeping pH constant (Ghosh, 1974; Millero *et al*., 1989). These observations led to the hypothesis that a ferrous bicarbonate or carbonate complex aqueous species was responsible for the increased rates. Speciation of ferrous iron in bicarbonate media was determined by Bruno *et al*., 1992, which led to quantification of the rate constants for individual chemical species (King, 1998). Taken together, these results explain the observed differences in abiotic rates in the springs and lakes sampled in this study.

Dissolved inorganic carbon (DIC) as bicarbonate and carbonate form the most abundant anions in the spring and lake samples in this study (table 4), as illustrated by the plot of total DIC concentration against the conductivity of the water samples shown in Fig 11. Conductivity is a close proxy for total dissolved ionic species, and the

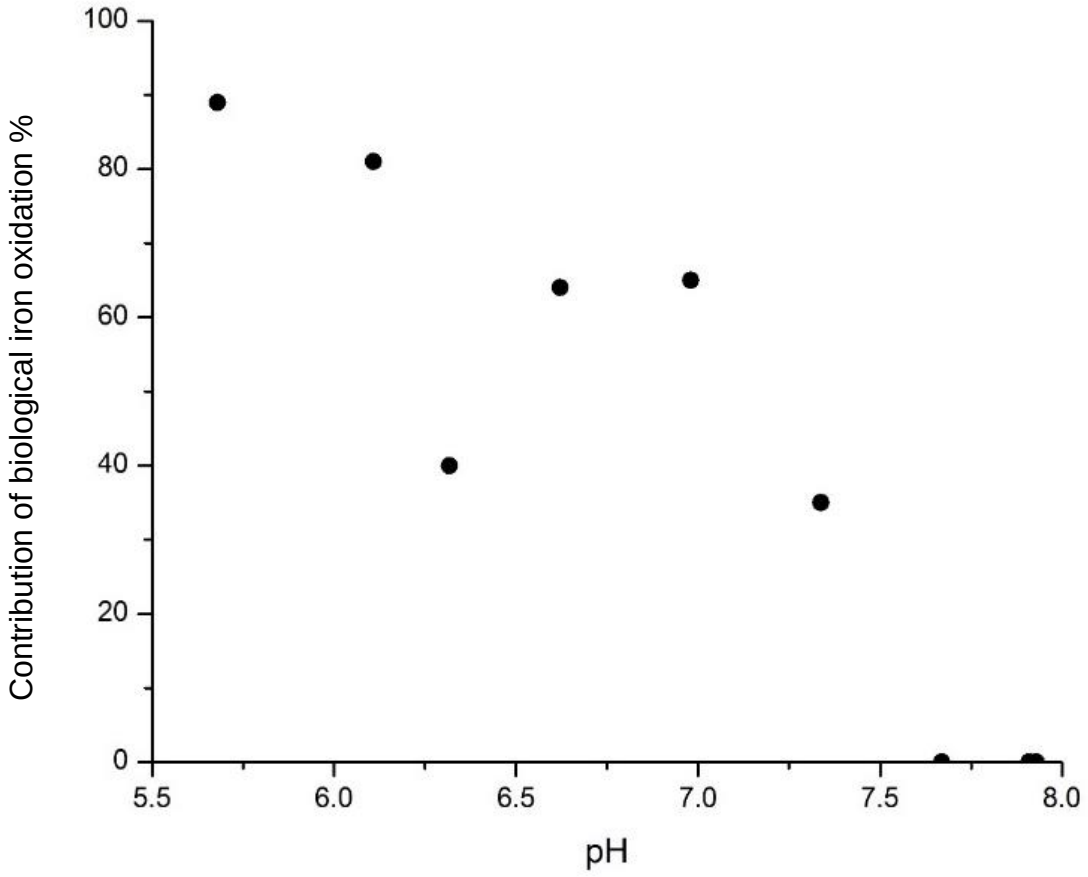

Figure 10 - The percentage of oxidation attributable to biology plotted against the pH of each system. Percentages calculated from average rate constants of triplicate experiments reported in table 5 and shown in Fig 9. The faster of the *in situ* or experimental treatment is used. Environments at pH 7.4 and below support biological oxidation, whereas systems at higher pH values have such high abiotic rates that biological iron oxidation was not detected. One result of 0% biological contribution at pH 9 is not depicted.

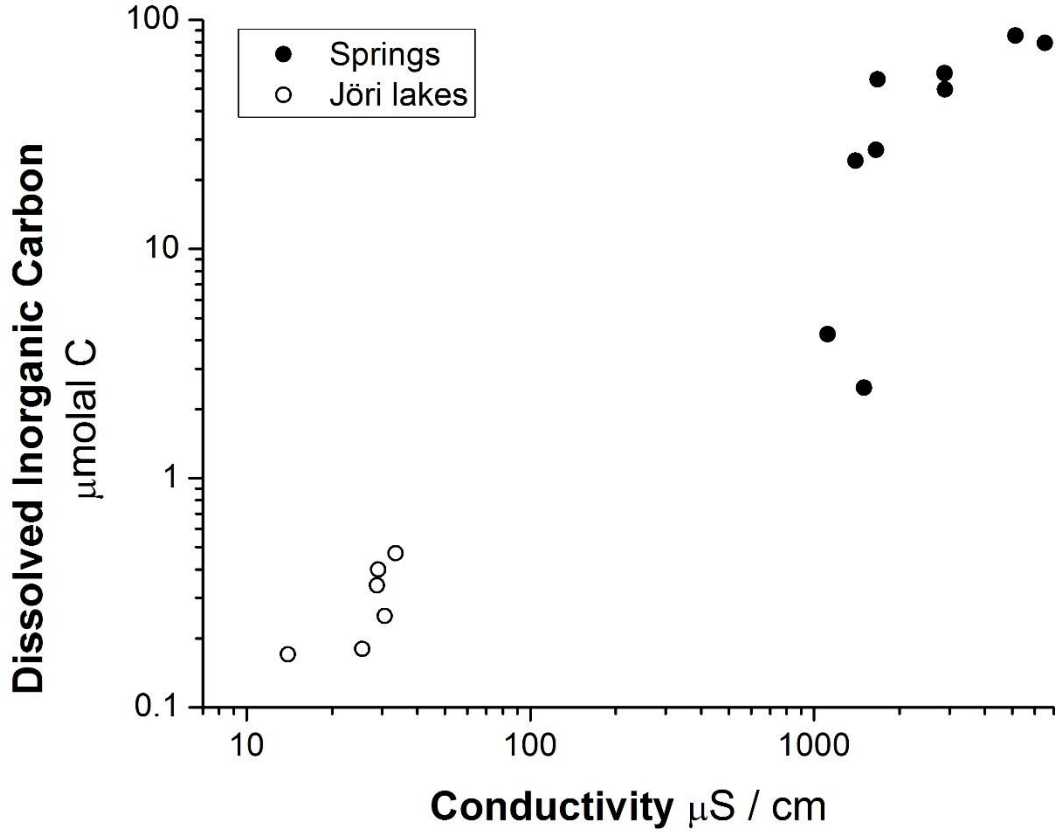

Figure 11 – Dissolved Inorganic Carbon (DIC) in Swiss lakes and springs plotted against measured conductivity. Weathering of local carbonate rocks makes bicarbonate and carbonate abundant ions in solution, and as a result DIC increases nearly linearly with conductivity.

approximately linear distribution of points in Fig 11 suggest that conductivity is determined by the abundance of bicarbonate and carbonate dissolved in the water. These solutes likely reflect weathering of the abundant carbonate minerals in the region. Local geology determines the second most abundant anion in these waters, which is typically either sulfate or chloride. The resulting bicarbonate rich waters dictate the aqueous ferrous iron speciation.

Oxidation rate constants of individual aqueous ferrous species have been determined in the laboratory at a variety of conditions (King, 1998; Santana-Casiano *et al*., 2005; Song *et al*., 2014). While the laboratory conditions differ from the composition of the natural systems studied here, the fact that there are orders-of-magnitude differences among the rate constants remains relevant. Oxidation of aqueous ferrous carbonate complexes can greatly increase overall iron oxidation rates compared to dilute solutions at the same pH. This is especially true for the $Fe(CO_3)_2^{-2}$ species, which, despite its fleeting abundance, is often responsible for the majority of the observed rates. In contrast, ferrous sulfate and chloride aqueous complexes slow the overall rate of abiotic iron oxidation to rates similar to or slightly slower than the rate of oxidation of Fe^{2+}.

In the present study, new estimates of standard state thermodynamic properties of aqueous carbonate and bicarbonate complexes permit speciation calculations at a wide variety of temperatures and pressures. The methods by which these estimates were made are outlined in appendix A. Predicted equilibrium constants for carbonate and bicarbonate complexes, together with the analytical data for major ion concentrations,

pH, and DIC abundances (Table 4[1]) allowed speciation calculations. The samples for geochemical analyses were taken at the locations where water was taken for rate experiments, and as close as possible in time to the start of the corresponding experiments.

A Bjerrum diagram, calculated with thermodynamic data from Appendix A, depicting the speciation of Fe(II) species at 25°C in a solution containing millimolar total carbonate is shown in Figure 12, where it can be seen that Fe^{+2} is the most abundant species at pH < 7. The carbonate species $FeCO_3^0$ and $Fe(CO_3)_2^{-2}$ become dominant between pH 7-9 and >9 respectively. The bicarbonate species becomes significant around a pH of 7, but is never the most abundant species. The hydroxide species $FeOH^+$ and $Fe(OH)_2^0$ that dominate circumneutral ferrous speciation in dilute solution are several orders of magnitude less abundant than the inorganic carbon species.

Speciation calculations were performed for each of the carbonate springs, as summarized in Figure 13, which shows the calculated percentages for each species. Fe^{+2}, represented by black bars, is typically the most abundant species in springs with pH < ~7. The $FeHCO_3^+$ species is calculated to compose up to 25% of the Fe(II) in springs between pH 6-7, and is a minor component at higher pH values. The abundance of $FeCO_3$ (aq) increases dramatically from a few percent at pH 6 to become the most abundant species at pH > 7.5. Owing to the DIC concentrations, $Fe(CO_3)_2^{-2}$ is a minor contributor

[1] : Note that two values of DIC are reported in Table 4 for some samples. In these cases, the values reported in parenthesis are the measured values, while accepted values were recalculated from considerations of charge balance. The reported values are the result of charge balancing, when initial charge imbalance was greater than 10%. The extremely high concentrations led to small amounts of precipitate remaining after analysis suggesting the calculated values are more accurate.

Table 4 – Major Ions, dissolved inorganic carbon, and dissolved organic carbon in samples. Data used to calculate speciation of Fe(II). Units are in µmol / kg of solution, except DIC values reported as mmol C / kg, and DOC are reported as µmol C / kg. Isotopic composition of DIC and DOC is reported as $\delta^{13}C$ VPDB (‰). Isotope values of DIC and DOC reported in italics were dilute and have errors of ± 2‰ . ND is not determined

area	Sample ID	F^-	Cl^-	Br^-	SO_4^{-2}	PO_4^{-3}	NO_2^-	NO_3^-	Li^+	Na^+	NH_4^+	K^+	Mg^{+2}	Ca^{+2}	DIC	$\delta^{13}C$ DIC	DOC	$\delta^{13}C$ DOC
Alvaneu Bad	150905A	83.4	16.3	BDL	8352	0.16	BDL	0.12	1.35	71.2	2.02	27.3	3023	7012	4.24	-3.6	25	-24.5
	150911T	74.6	21.5	BDL	13784	BDL	BDL	0.33	1.07	90.1	2.21	18.4	4661	9644	2.48	-2.7	17	-22.6
Val Sinestra	150906B	27.4	27378	139.2	4064	20.20	1.15	98.75	1350	49879	356	1669	4374	14963	85.3 (66.4)	4.1	133	ND
	150906C	21.4	12574	63.5	2076	BDL	BDL	2.45	445	16876	150	557	2001	7656	58.55 (49.4)	1.7	100	ND
	150906D	41.9	37966	198.9	5565	BDL	BDL	57.99	1805	67070	517	2225	5118	16697	79.1 (55.5)	5.9	117	ND
	150908H	19.8	12699	66.7	2103	0.07	0.04	1.96	621	23218	189	768	2722	9484	49.6 (45.7)	2.4	58	-26.5
Rablönche	150907F	8.9	907	1.55	491	BDL	BDL	1.06	31.8	2519	23.2	110	1789	11071	55.0 (35.1)	3.7	67	ND
	150907G	16.2	980	0.989	494	BDL	0.05	2.16	32.8	2534	18.6	113	1786	9963	24.3 (15.1)	8.1	50	-21.8
	150908J	7.9	978	0.70	478	BDL	0.07	2.64	32.4	2559	18	112	1821	10953	27.1 (16.5)	8.0	75	-15.9
Jöri Lakes	150909K	7.5	2.45	BDL	10.0	BDL	BDL	0.32	0.031	11.9	1.34	2.43	4.63	25.1	0.08 (0.05)	*-3*	92	-20.6
	150909L	7.6	1.21	BDL	9.9	BDL	BDL	0.10	0.0115	9.54	1.14	2.08	3.86	21.6	0.04	*2*	67	-18.5
	150909M	4.2	2.16	BDL	38.0	BDL	0.074	24.18	0.0274	20.5	1.21	4.7	24.4	74.3	0.18	*-11*	50	-20.5
	150909N	7.1	2.41	BDL	9.1	BDL	BDL	0.34	0.0137	11.4	5.96	4.73	5.48	28.6	0.17	*-8*	117	-25.8
	150910O	19.7	2.07	BDL	64.6	BDL	0.0304	16.72	0.0497	17.1	1.06	5.9	15.9	74.5	0.25	-5.5	42	-25.7
	150910P	0.0	0.98	BDL	0.8	BDL	BDL	15.15	0.0014	0.72	8.78	0.268	0.19	5.26	BDL	BDL	25	-21.8
	150910Q	4.9	2.47	BDL	36.9	BDL	0.07	27.31	0.0288	22.3	0.998	5.23	21.7	78.1	0.34	-8.0	42	-19.4
	150910R	7.8	3.27	BDL	16.4	BDL	0.051	25.39	0.0504	38.5	2.31	10	36.9	148	0.40	-5.6	83	-23.2
	150910S	11.7	2.14	BDL	17.9	BDL	0.04	54.12	0.036	48.6	2.01	9.19	38.1	184	0.47	-6.3	42	-23.8

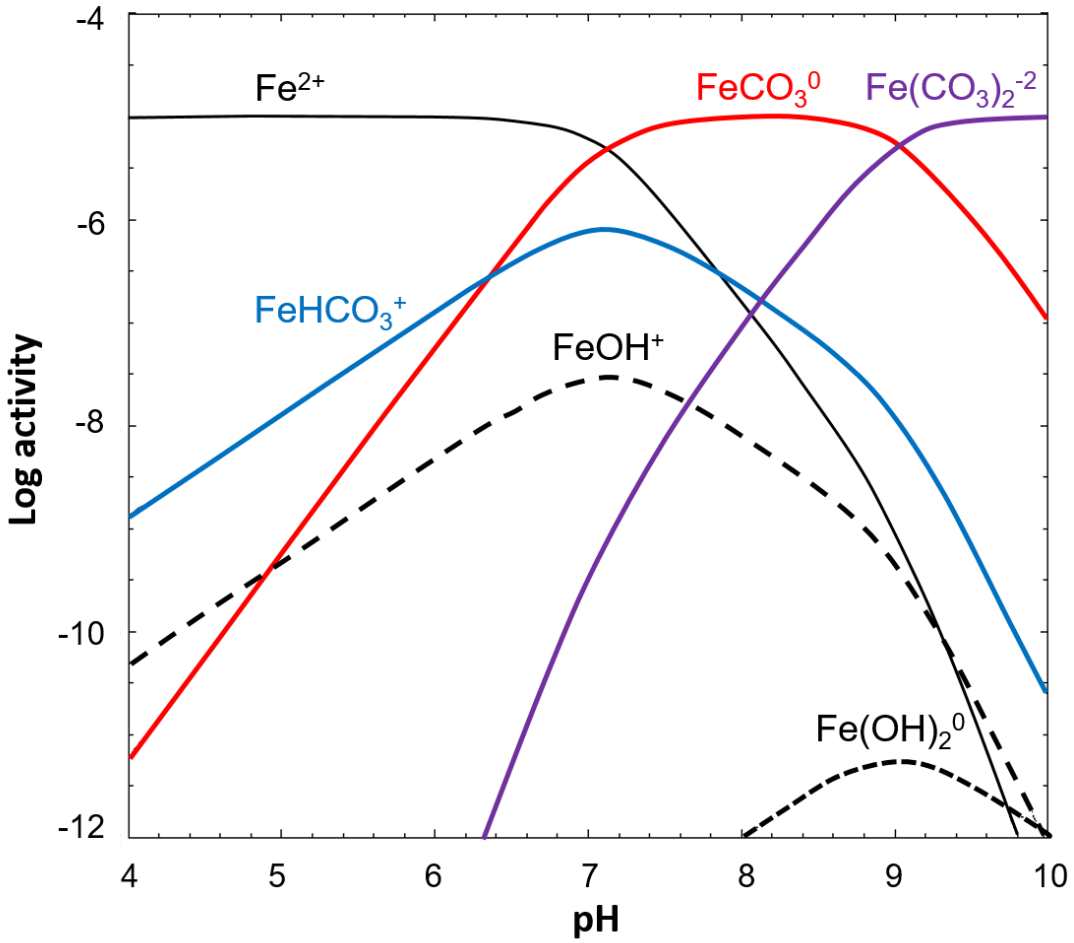

Figure 12 - A Bjerrum diagram showing the speciation of Fe(II) in aqueous solution at 25°C, containing 10-3 M total Fe(II) and 10-3 M total CO_3^{-2}. Equilibrium constants taken from literature values reported in Appendix A. This plot was calculated using the CHNOSZ software package (Dick, 2008), together with a modified database developed in this study (see Appendix A).

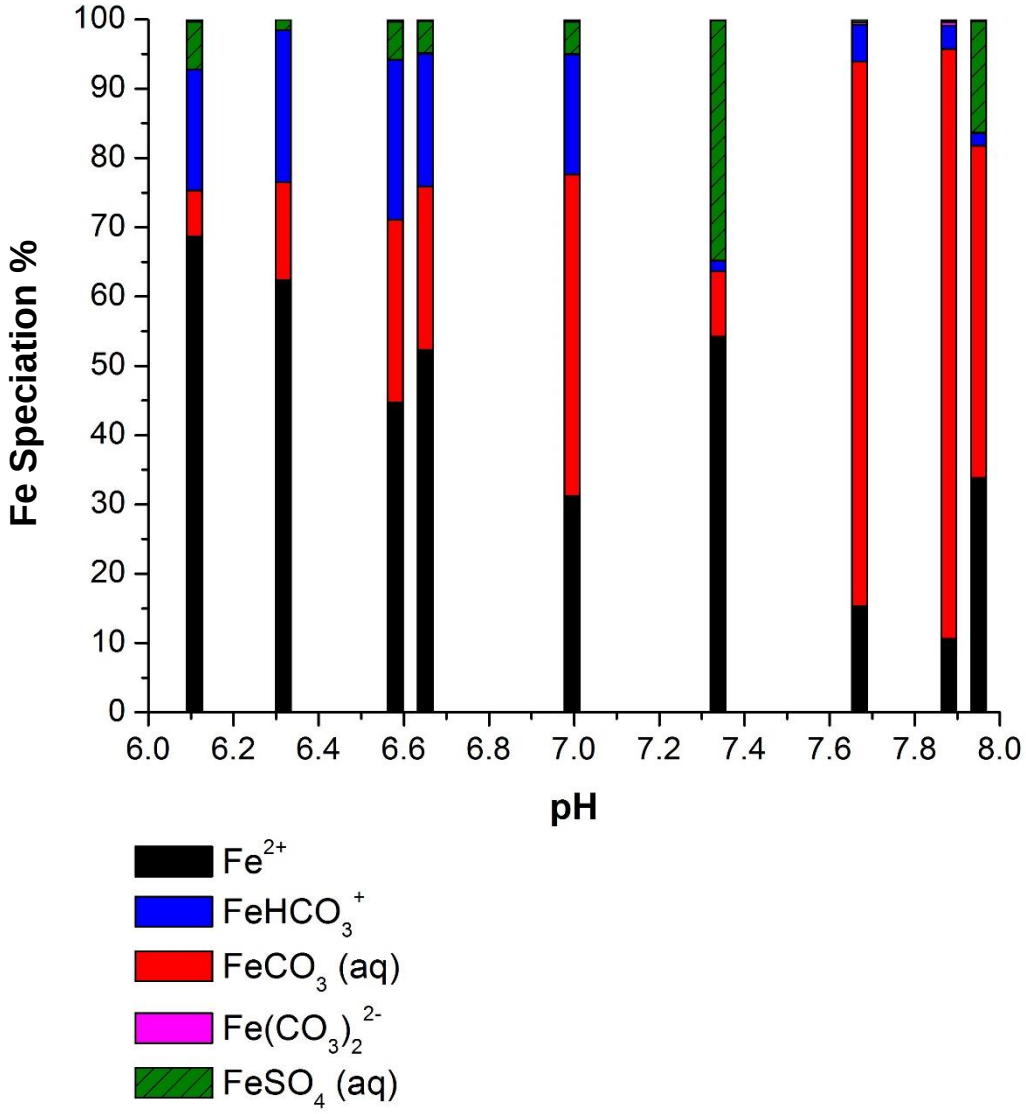

Figure 13 - The speciation of Fe(II) in iron springs. Pairs of springs at pH values of both 6.6 and 7.9 have been offset on the plot to allow all four speciation results to be visible. Black, blue, red, purple, and green bars represent Fe^{+2}, $FeHCO_3^+$, $FeCO_3^0$, and $Fe(CO_3)_2^{-2}$, and $FeSO_4^0$. The springs below pH 6.6 are composed mostly of Fe^{+2}, while $FeHCO_3^+$ is found at 15-25% in this range. $FeCO_3^0$ becomes abundant at pH 7 and above. Springs with relatively high concentrations of sulfate show minor concentrations of $FeSO_4^0$. Other species are present in fleeting amounts and can be found in Appendix C.

to Fe(II) speciation at pH values greater than 7.5 Despite this feeble presence, this species can increase the rate substantially (King 1998). In addition, $FeSO_4$(aq) is a minor contributor to the speciation of Fe(II) in most samples. The dominant speciation of Fe^{2+} and $FeSO_4$ (aq) in the spring at pH 7.3 results from a relatively low DIC content.

The Jöri lake systems are extremely dilute, and the majority were below the detection limit for Fe(II). Speciation calculations were only possible on 3 samples (not shown), yielding results showing abundant $FeOH^+$, $FeOH_2$ and Fe^{+2}. It can be assumed that the other lakes samples would be speciated in similar ways given their similar compositions. Iron oxidation in the lake sediments is likely happening deeper in the sediments than in the springs, as evidenced by visible bands of iron oxide approximately at approx. 3 cm depth in Jori Lake 2, and pore water compositions reported by Steiner *et al*., 2004. Sediment pore waters are likely to speciate quite differently. The lack of anions to form complexes means that speciation and rate would be similar to that found in laboratory experiments of dilute solutions (such as Stumm and Lee 1961; Millero *et al*., 1985).

Overall the speciation results represent an additional layer of information for explaining the observed oxidation rates. As an example, they show that ferrous iron speciation in the springs is dominated by ferrous (bi)carbonate complexes and Fe^{+2}. As a result, the speciation results help to demonstrate that laboratory studies on oxidation rates for individual aqueous species can be relevant to natural ferrous iron containing systems with relatively abundant DIC.

2.5.3 From Subsurface Geochemistry to Community Composition

Surface microbial community compositions reflect subsurface geochemistry and sediment processes. Isotope studies have revealed the source of water rich in DIC that

leads to the observed geochemical composition of springs in the region (Wexsteen *et al*., 1988; Bissig *et al*., 2006; Strauss *et al*., 2016). Likewise, a study of metals in the Jöri lakes provides a framework for iron cycling based on a redox gradient in the sediments (Steiner *et al*., 2000). These studies lay the background for detractingly linking the observed microbial community's metabolic activity to subsurface processes.

The isotopic composition of the water suggests extensive water rock interaction in the source water of springs, but meteoric water in the lakes. Figure 14 shows the H and O water isotopic composition of springs, lakes, and fresh water in the area. Global and local meteoric water lines are included for reference. Note that the Jöri lakes samples (black squares) fall close to these lines. The dilute nature of the lakes combined with the isotopic information support a conclusion that the lakes are composed of minimally reacted meteoric water. This contrasts with most of the mineral springs (open squares), which show an oxygen enrichment, or a deuterium depletion, relative to both water lines. These isotopic compositions are interpreted to result from deep water-rock interactions.

The sources of water and CO_2 in the springs of the lower Engadin region, which includes Rablönch and Val Sinestra, were investigated by Wexsteen *et al*. (1988) who determined that the source of CO_2 is ultimately from metamorphic reactions deep in the subsurface. In their model, the CO_2 rises and infiltrates a carbonate rich aquifer, which results in DIC-rich water with high conductivity. They showed that dozens of mineral springs in the area can be grouped based on their anion and water isotope composition. Some springs fall close to the LMWL, but the most mineralized springs are enriched in ^{18}O. Evaporation could generate the observed $\delta^{18}O$ values, but Wexsteen *et al*. (1988) suggest this is unlikely due to current and past conditions in the region, and conclude that

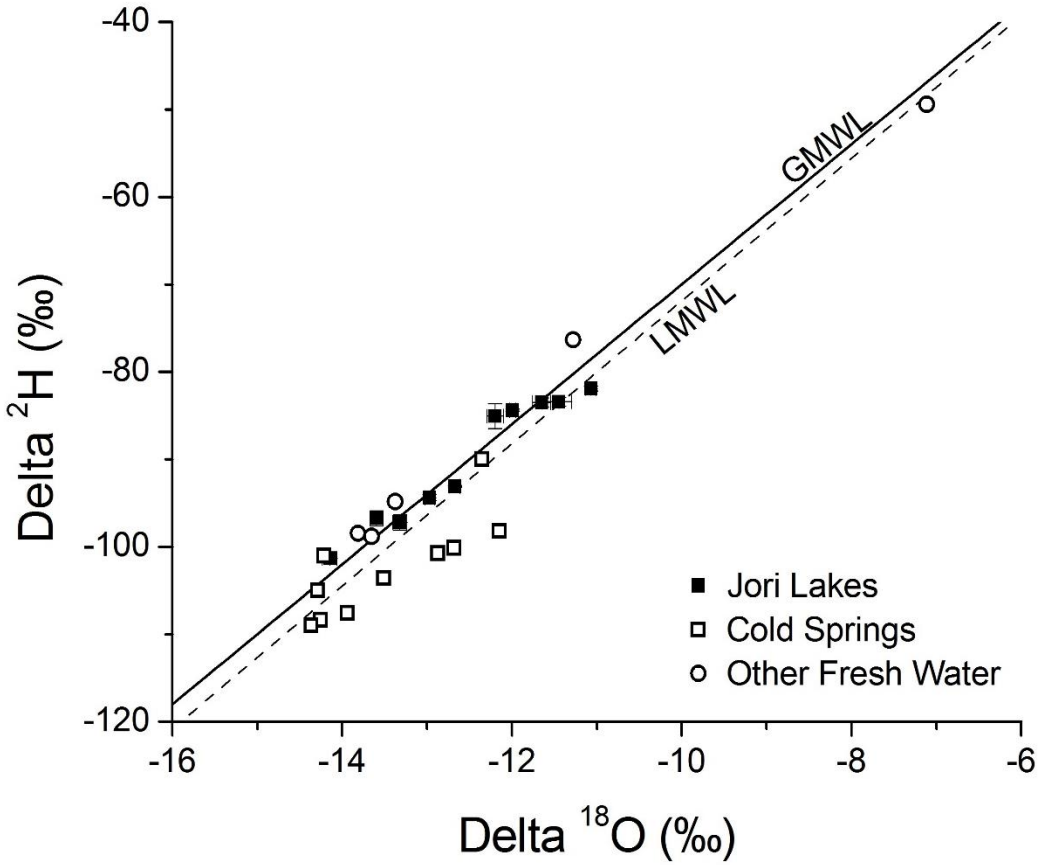

Figure 14 - δ^2H vs. δ^{18}O of all samples taken in this study, including Jöri lakes (black squares), cold springs (empty squares), and other fresh water (circles) from the region; reported in per mil (‰) vs. VSMOW. The Global Meteoric Water Line (GMWL), as reported by Craig (1961), and a Local Meteoric Water Line (LMWL) reported by Strauss et al. (2016) are included for reference. Samples from the Jöri lakes plot along these lines, consistent with meteoric recharge. Many of the cold springs plot to the right of the LWML, which can be caused by either an enrichment towards higher ^{18}O/^{16}O ratios or a depletion in ^{2}H, and are interpreted as resulting from water-rock interaction (see text). Fresh water samples include piled snow, creeks, rivers, and rain.

water-rock reactions are the most plausible explanation for the observed $\delta^{18}O$ values. This is consistent with my observations of higher concentrations of DIC leading to depleted 18O values, as shown in Figure 15. Bissig *et al*. (2006) constructed a conceptual model of groundwater and gas fluxes in the region, leading to the conclusion that there are two end-member sources of water: the DIC-rich aquifer and shallow groundwater. Rablönch and Val Sinestra area springs are composed predominantly of the deeper aquifer end-member fluid.

Sediments – Most microbes, including the majority of FeOB, are found in the sediments in these springs and lakes. Characterizing the sediments for organic carbon and iron content permits estimates of the biomass content and identity and extent of mineral product formation. Results of sediment analysis, including minerals (XRD), total and organic carbon (EA), and their isotopic composition (IRMS) are given in Table 5.

Cold spring sediments primarily contain carbonate minerals, and calcite and dolomite are the most common phases identifiable by XRD. Ferric minerals were not identified by XRD, despite the deep red staining observed in the springs. The organic carbon content of the springs is typically low, with values ranging from 0.09 – 0.25%. The organic C is always isotopically light, -23.4 to -29.5. Most springs do not have much plant debris, so these values may be indicative of microbial biomass. One exception is Arvadi at 0.92% organic C, which contains abundant decaying forest debris. All the springs have significant total carbon contents as expected from XRD results, with values ranging from 2.7 – 11.5 % C by dry weight. If the assumption is made that all the inorganic C is carbonate, then carbonate makes up 14-57% of the total weight of the sediments.

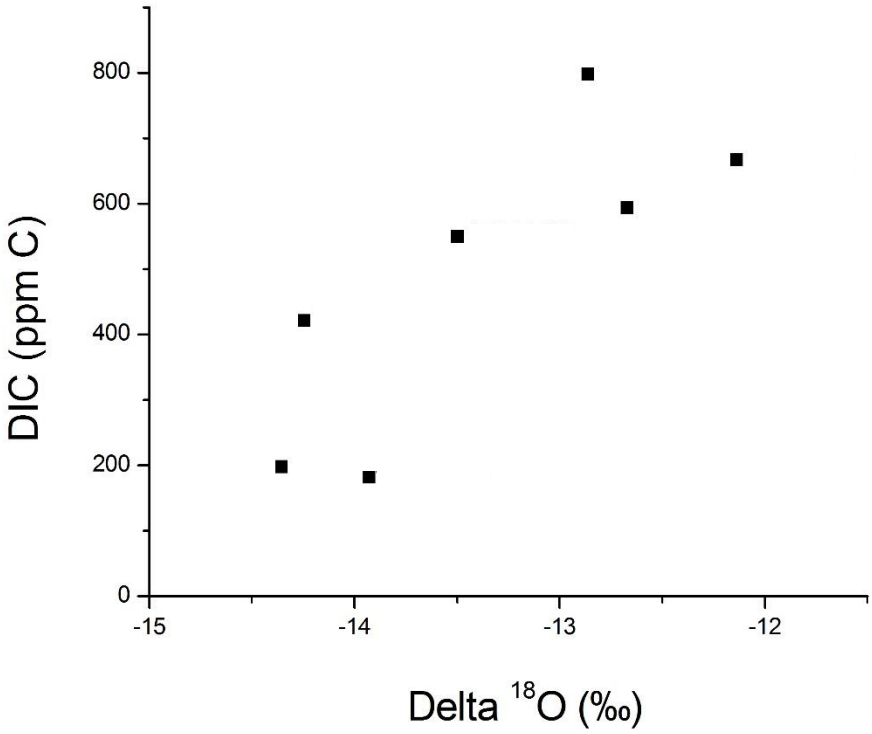

Figure 15 - Concentration of dissolved inorganic carbon (DIC) vs. δ18O of cold springs. The slope is suggestive of subsurface water-rock interaction, most likely interaction with carbonate minerals.

Table 5 – Sediment carbon and mineral content

Sample ID	Name	Organic Carbon	$\delta^{13}C$ v PDB	Total Carbon	$\delta^{13}C$ v PDB	Minerals
150905A	Arvadi	0.92%	-29.5	8.0%	6.94	Calcite, Dolomite, Quartz
150911T	Eisenquelle	0.12%	-27.1	8.1%	-0.07	Quartz, Dolomite, Calcite
150906B	Conradins	0.15%	-27.6	5.7%	2.14	Calcite
150906C	Trap Door	0.25%	-23.4	2.7%	-0.57	Quartz, Calcite, Clinochlore, Illite
150908H	River Outlet	0.13%	-23.9	5.0%	1.51	Quartz, Calcite
150907F	Rablönch OF4	0.12%	-26.2	8.2%	2.35	Dolomite, Calcite, Quartz
150908J	Rablönch OF5	0.09%	-28.2	11.3%	7.89	Calcite
150907G	Rablönch OF6	0.09%	-24.0	11.5%	8.83	Calcite
150909K	Lake XIII	2.47%	-23.7	ND	ND	Quartz, Illite
150909L	Lake XIII Outflow	0.53%	-18.6	ND	ND	Quartz, Albite
150909M	Lake XX	1.27%	-22.8	ND	ND	Quartz, Clinochlore, Muscovite
150910O	Lake II	0.37%	-16.4	ND	ND	Quartz, Illite, Clinochlore
150910Q	Lake XIX	0.22%	-14.7	ND	ND	Quartz, Illite, Clinochlore
150910R	Lake XVIII	0.10%	-18.1	ND	ND	ND
150910S	Lake XXII	0.58%	-20.6	ND	ND	ND

Organic carbon measured by acidifying dry sediment samples to remove inorganic carbon. Organic carbon is generally indicative of microbial biomass in the system, with the exception of Arvadi, which had abundant plant organic matter in the sediment. Total carbon is measured on unacidified samples and contains organic and inorganic carbon. Minerals were identified by XRD. No iron minerals were identified despite often intense iron staining. Samples were frozen prior to analysis to minimize redox processes or other alteration.

Jöri lake sediments contain only quartz and other silicate minerals. The organic carbon content of the lake sediments ranges from 0.10-2.47%, which is considerably larger than that of the spring sediments. These lakes are situated several hundred meters above the treeline, with only sparse seasonal plants dotting the landscape. This suggests that the source of organic carbon is from autotrophic biomass, although atmospheric deposition is also a possibility. The water in lake XIII, with the highest organic sediment C, is dense with phototrophic biomass. The isotopic composition of the biomass in the lakes is heavier than that in the iron springs, possibly a result of the autotrophic process. Total C measurements were not made in lake sediment samples.

Ferric minerals are apparent in iron springs by red staining. The amount of iron present as ferric minerals was measured by reductive dissolutions with hydroxylamine and HCl, as well as Fe(II) in sediments determined by HCl extraction (after Lovely and Phillips 1989). These iron values, along with determined water content, are shown in Table 6. All spring sediments at Alvaneu Bad and Val Sinestra showed relatively large concentrations of Fe(II). Given the strong drive towards oxidation, these relatively high values suggest biological reduction is occurring in the sediments. Sites at Rablönch did not contain large concentrations of Fe(II). The amorphous ferric mineral content of all the springs ranged from 0.33 to 13.5% Fe by dry weight.

Lake sediments have much lower total iron concentrations. Lakes XIII and II, where iron oxidation was detected, have higher concentrations of Fe(II) in the sediments that the other lakes. The high concentration of Fe(II) is likely indicative of iron reducers in the sediments, and the source of Fe(II) for oxidation. The ferric mineral content of the samples is below the detection limit of the reductive dissolution method, which is

Table 6 – Sediment Iron composition of Swiss springs and lakes

Sample ID	Name	Fe(II) dry weight %	ΣFe(III) % dry weight	Water %
150905A	Arvadi Spring	0.18	1.98 ± 0.19	62
150911T	Eisenquelle Source	0.12	0.35 ± 0.02	22
150906B	Conradins/Val Sin	0.3	13.53 ± 0.35	71
150906C	Trap Door	1.0	5.03 ± 1.04	75
150908H	River Outlet	0.25	2.11 ± 0.44	28
150907F	Rablönch OF4	0.05	4.32 ± 0.2	32
150908J	Rablönch OF5	0.12	1.24 ± 0.28	49
150907G	Rablönch OF6	0.05	0.33 ± 0.04	56
150909N	Lake XIII	0.18	BDL	68
150909L	Lake XIII Outflow	0.03	0.02 ± 0.02	26
150909M	Lake XX	0.01	0.02 ± 0.004	37
150910O	Lake II	0.09	BDL	41
150910Q	Lake XIX	0.01	BDL	21
150910R	Lake XVIII	0.01	0.01 ± 0.001	15
150910S	Lake XXII	0.02	0.03 ± 0.001	37

0.0005%. Despite this lack of detection, a lightly stained 1 cm band of apparent ferric minerals was observed at 3 cm depth in lake II. Since oxidation was detected it is likely that these lakes have active redox cycles. Other lakes in the area (table 6) have relatively small sediment concentrations of Fe(II) and ferric minerals, and are less redox active.

2.5.4 Composition to communities

The preceding discussion provides a framework for linking microbial communities to subsurface geochemistry. Higher concentrations of DIC correlate with enriched ^{18}O, as shown in figure 15. This is consistent with studies of the lower Engadin region springs, which includes Rablönch and Val Sinestra, by Wexsteen *et al*. (1988) and Bissig *et al*. (2006). These studies linked higher DIC and ^{18}O enrichment to significant subsurface water-rock interaction. Isotopic data reported by Strauss *et al*. (2016) shows less oxygen depletion for many samples from many of the same region and locations, inconsistent the other studies and our data. The springs with the highest conductivity, as well as the highest concentrations of iron and DIC, are found at Val Sinestra and Rablönch. These locations support the fastest rates of microbial iron oxidation and, as discussed next, contain the largest percentage of putative iron oxidizers.

Small sub-unit ribosomal RNA (16S rRNA) gene sequencing shows putative iron oxidizers are present in every system. The dominant FeOB genus in almost every system is *Gallionella*, which ranges from 1.2–45% of the total community. The relative percentage of organisms putatively involved in iron oxidation reactions are shown in Figure 16. The data are presented in order of decreasing conductivity, which is indicated above each bar. In general, the higher the conductivity, which isotopic and geochemical data suggest is a proxy for water-rock interaction, the more putative iron oxidizers are

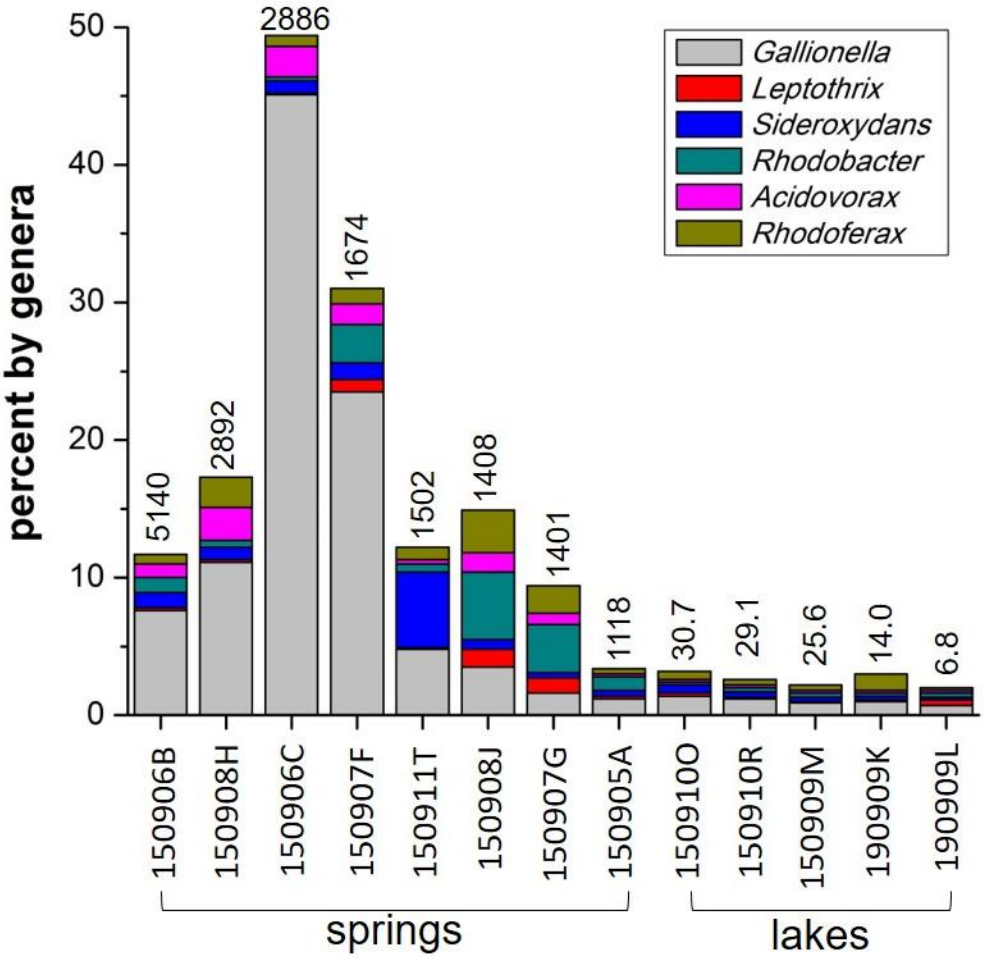

Figure 16 – Microbial community members potentially involved in iron redox cycling in Swiss springs and lakes. Samples are arranged left to right from highest to lowest conductivity, in µS/cm, which is reported above each column. Putative iron oxidizing genus Gallionella dominates the iron mats. The rest of the community, including putative iron reducers and phototrophs, can be found in Appendix C.

present in the system. In addition to *Gallionella*, other genera present include *Rhodobacter*, *Leptothrix*, *Acidovorax*, *Sideroxydans*, *Rhodoferax*, and *Ferrovum*. Note that not all cultured representatives of these genera are known to oxidize iron. In comparison with the spring communities, lake samples show lower percentages of all putative FeOB. *Gallionella* are still the largest percentage of apparent FeOB in these systems, with a range between 0.74-1.35%. Data on the rest of the microbial population at the class level can be found in Appendix C.

The usually prolific genus of FeOB *Leptothrix* is poorly represented in all systems (0.11-1.31%). The pH, O_2 and Fe(II) niches of *Gallionella* and *Leptothrix* overlap, but optima are not the same (Eggerichs *et al.*, 2014). *Gallionella* sequence percentages in these systems are shown in Figure 17 plotted against pH, dissolved oxygen, ferrous iron, and conductivity. It can be seen that *Gallionella* achieve their greatest percentages between pH 6.0-6.5, consistent with the optimum range of pH 6.3-6.6 described by Kucera and Wolfe (1957). In figure 17b there is a positive linear trend of *Gallionella* percentage with Fe (II). Concentrations of Fe(II) higher than 100 µm lead to percentages between 7.5-45%. Percentages as high as 5% can be found at concentrations of Fe(II) as low as 5 µmolal. Bulk dissolved oxygen concentrations close to saturation appear to limit *Gallionella* (fig 17c). The optimal habitat range of dissolved oxygen is reported by Hanert (1981) as 5.6-56 µm. Our findings show no apparent issues with Gallionella growing at O_2 concentrations as high as 160 µm. It should be noted that our data report bulk geochemical composition, and samples for sequencing consist of approximately the top centimeter of sediment. The actual geochemical concentrations experienced by the organisms could vary from the bulk composition. Regardless it seems that in this case

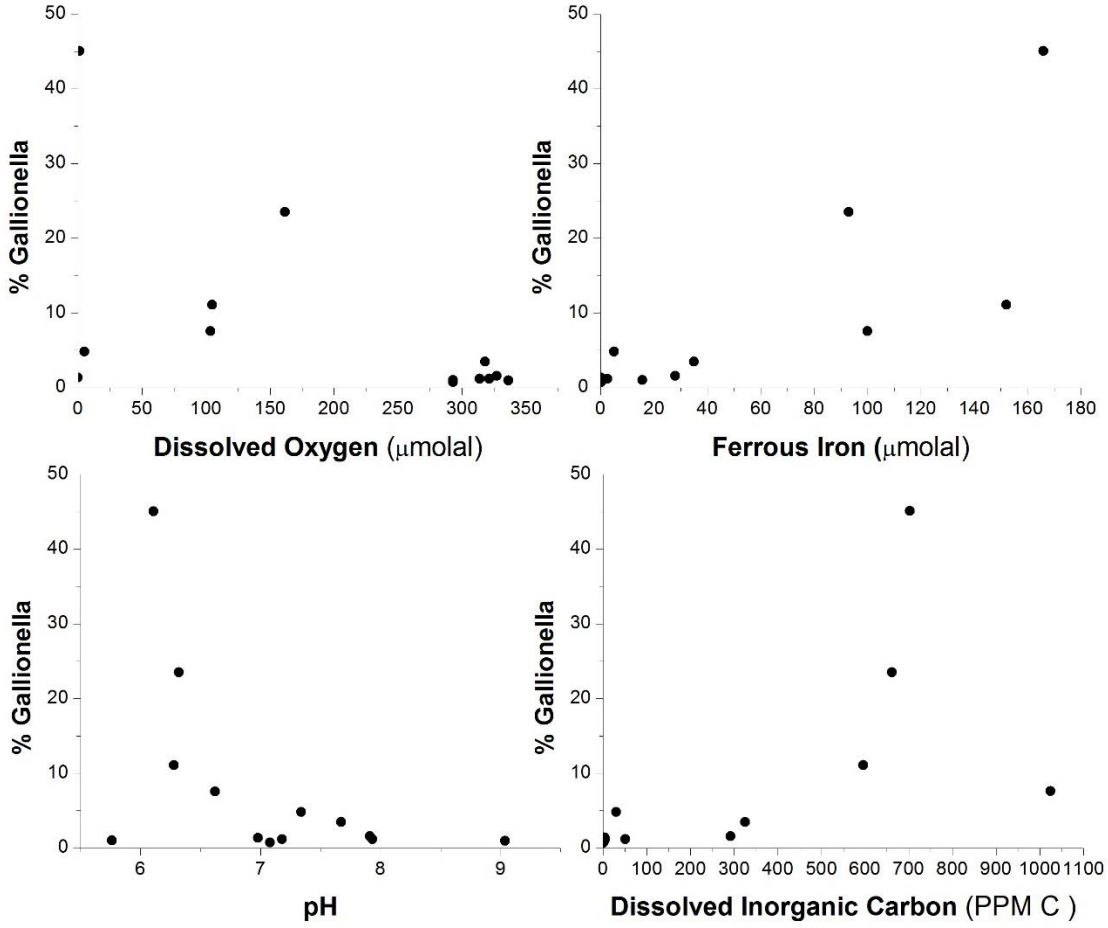

Figure 17 – Presence of *Gallionella* in the sediment, as % of total community, plotted against geochemical variables. *Gallionella* are most abundant between pH 6-7, at concentrations of Fe(II) >50 µmolal, and at bulk oxygen concentrations below ~200 µmolal. Higher DIC concentrations also lead to higher abundances of *Gallionella*, likely corresponding to increased water-rock reaction leading to higher concentrations of Fe(II).

pH, Fe(II) and O_2 should be sufficiently variable to permit both *Gallionella* and *Leptothrix* to flourish.

Fleming *et al.* (2014) identifies low DOC (dissolved organic carbon) as a primary determinant of ecological niche of *Gallionella*, while *Leptothrix* thrive in high DOC, high Fe(II)/Mn(II) environments. As discussed above, all sample sites in this study have low concentrations of DOC, with the highest concentration reaching only 1.7 ppm C. Efforts were made in this study to measure formate, acetate, lactate and propionate, but showed that these organic acids were all close to or below the detection limit (~25 ppb). The organic acid abundance of springs can be found in Appendix C.

Phototrophs - Several of these systems have evidence for oxygenic phototrophic organisms. The water column at Jöri Lake XIII is thick with apparent phototrophic material. The spring Rablönch and the outflow at Val Sinestra show apparent phototrophic biomass in low flow regions at the edges of the flow channel. This was also reported at the nearby Fuschna spring in Hegler *et al.* (2012). In Eisenquelle, long strands of phototrophic biomass were colonized by FeOB. The location of the sampling and experiment close to the source was well below saturation with oxygen, but it is likely that the increased delivery of oxygen further down the channel speeds up the abiotic process. Oxygen bubbles generated by this biomass show evidence of becoming encrusted with ferric minerals and lithified over time.

While it is apparent that FeOB and phototrophs can coexist, ferrous iron has been shown to cause oxidative stress and inhibit growth of cyanobacteria at concentrations as low at 10 µmolal (Shcolnick *et al.*, 2009). Swanner *et al.* (2015) hypothesize that oxygen production during the Archean was modulated by fluxes of Fe(II) in the oceans. This is

partly based upon field observations that modern cyanobacteria are absent in natural systems with concentrations of Fe(II) above ~55µm. Our sequencing results show cyanobacteria present as 1.7% of the biomass in the main flow channel in Rablönch, which has a Fe(II) concentration of 93 µm. Sampling from 2012 suggests the concentration of Fe(II) is consistent at this location. Samples at higher values of Fe(II) show insignificant percentages of cyanobacteria. This finding does not contradict the hypothesis of Swanner *et al.* (2015), but does show cyanobacteria in circumneutral environments tolerating higher concentrations of Fe(II) than previously reported.

Microenvironments - Many authors have recognized that FeOB must compete with the rapid abiotic oxidation rate for available Fe(II) (e.g. Emerson and Moyer, 1997; James and Ferris 2004; Druschel *et al*., 2008; Melton *et al*., 2014). Here we have characterized rates in 10 geochemically variable systems to determine conditions that favor microbial oxidation, and conditions where the abiotic iron oxidation rate excludes the biotic process. Cold systems with large concentrations of DIC appear to support microbial iron oxidation below pH values of 7.4. While this does not completely rule out biological oxidation at higher pH values, it does indicate that biological iron oxidation is not a contributor to the bulk iron oxidation rate at high pH. It is possible that FeOB occur in microenvironments or oxidize iron at rates below the detection limits of the experiments. In most experiments, the difference in the rate of biological and abiotic oxidation must be greater than 0.1 µM/min for the standard protocol or 0.05 µM/minute for the modified protocol to determine that biology is enhancing the rate. Given that these are natural systems that experience variability, and that experiments are being done in

remote locations, the threshold for determining that biology is a major contributor to the rate varies slightly between experiments.

Microenvironments of elevated Fe(II) and low levels of oxygen that exist in layers buried in iron mats may extend the pH range of FeOB greater than that observable by microcosm experiments with bulk sediment and water. Microbial iron reduction almost invariably accompanies iron oxidation (Roden 2012; Ionescu *et al*., 2015). Biological reduction of the biogenic ferric minerals within iron mats may permit low numbers of FeOB in systems where a biological rate was not detected. Our reported values of Fe(II) were sampled in the water right above the mat, but sediments at many locations showed higher concentrations of Fe(II) (table 6). Our sequencing results often showed low abundances of putative metal reducers such as *Geobacter*. Indeed, Hegler *et al.* 2012 determined that iron reduction was happening *in situ* at an iron mat very similar (and geographically close) to Rablönch. Sequencing results and visibly apparent photosynthesis imply local oxygen concentrations may also vary significantly from bulk values. The decay of organic matter in the mats may also allow for chelated ferrous ions to persist and extend its bioavailable tenure. Given these caveats, biological iron oxidation may well occur at pH values greater than those detected during our experiments, but it is unlikely to be a significant biogeochemical process.

2.5 Concluding Remarks

Microbial iron oxidation has long been known to compete with rapid abiotic oxidation in cold circumneutral systems. However, as shown in this study, there are conditions where the abiotic reaction is too fast for biology to compete. Microcosm experiments reported here provide biotic and abiotic oxidation rates at a variety of pH

and other conditions and revealed geochemical conditions that exclude microbial iron oxidation. In the cold (8-12°C), high DIC systems, biological iron oxidation was only detected up to pH 7.4. Comparing relative biotic and abiotic rates suggests that the maximum pH for bulk iron oxidation at the conditions studied is around 7.5. At higher pH values, ferrous iron is oxidatively precipitated within seconds by abiotic processes, rendering it unavailable to FeOB. The underlying cause for the abiotic rate being expedited is the change in speciation of Fe(II) in solution. More reactive aqueous species form at higher pH values, especially the (bi)carbonate complexes that form in the presence of dissolved inorganic carbon, as revealed by new thermodynamic estimates. The iron oxidizing microbial communities are composed predominantly of the genus *Gallionella*. The abundance of *Gallionella* in each system is dictated by oxygen, Fe(II), and pH, and largely agrees with published data on geochemical niches of the genus. Taken together, these data provide an inventory of magnitudes of biotic and abiotic oxidation transformations of iron in these systems, provide a geochemical explanation for the observed rates, and describe the communities that oxidize iron.

The kinetic challenge faced by iron oxidizing microbes in circumneutral environments undoubtedly extends to all temperatures where iron oxidation is physiologically possible. Circumneutral iron oxidation has been studied extensively at low temperatures, but reports from higher temperature are scarce. Rate measurements in such systems are nonexistent. This is due in part to fact the iron-rich circumneutral systems at elevated temperatures are uncommon. Iron oxidizing microbes have been isolated from mesophilic (Clark and Norris, 1996) and thermophilic (Kozubal *et al*., 2012) acidic systems. It is likely that iron oxidizing microbes also inhabit circumneutral

environments at higher temperatures. Abiotic rates in such systems are undoubtedly also dictated by pH and chemical speciation. This implies there is a continuous boundary to the habitability of the iron oxidation reaction in pH and temperature space that is determined by the rate at which biology cannot compete. Extreme kinetic dissipation rates exist for numerous other solutes at conditions common on Earth's surface. Quantification of these rates relative to the rate catalyzed by the microbial community can inform discussions of the contribution of these reactions to habitability on Earth and beyond.

2.6 Acknowledgements

Many people share credit for the development and refinement of the field and analytical methods used in this paper. Justin Pottenger and Randall "Vince" Debes traveled to Switzerland to perform sampling and experiments. Kurt Hanselmann provided us with expertise guidance in the area, as well as supported air transportation. Kris Fecteau performed the ion chromatography analyses. Grayson Boyer and Natasha Zolotova helped analyze DIC, DOC, and sediment C on the IRMS. Eric Boyd and Melody Lindsay at Montana State University provided lab space and advice for the molecular biology work. This work could also not have been done without logistical assistance in Switzerland. Daniel Montluçon at ETH Zurich helped us obtain compressed gas and chemicals prohibited by commercial air travel, as well as provided lab space to prep reagents. Alysia Cox helped collect samples during the preliminary sampling trip in 2012. This work was funded by the National Science Foundation (EAR-1529963).

CHAPTER 3

MICROBIAL IRON REDUCTION, OXIDATION, AND REDOX CYCLING AT YELLOWSTONE NATIONAL PARK

3.1 Introduction

The hydrothermal ecosystems at Yellowstone National Park offer some of the most diverse microbial habitats in the world. In a single thermal area it is possible to encounter pH from <2 to >9, and variations of most elements on the periodic table by up to six orders of magnitude. Large disequilibria are created when the reduced hydrothermal fluids interact with the oxygen-rich atmosphere and oxic groundwater. As a consequence, many locations provide sufficient, quantifiable energy to sustain life from reactions involving the oxidation or reduction of iron (Shock et al., 2010; Canovas & Shock, in press). Iron is present in these systems in both mineral and dissolved forms, the speciation and oxidation state of which are influenced by the pH, ion abundance and identity, and biotic and abiotic rates of reaction. The concentrations of total and ferrous iron can be found in Fig. 18, which shows variations of 2 orders of magnitude at a given pH value. Acidic systems contain more total and ferrous iron than neutral or alkaline systems. This research was carried out across geochemically diverse hot springs to determine how pH, oxygen, organic carbon, and other variables influence biotic and abiotic redox transformations of iron.

3.1.1 Iron Reduction

Dissimilatory iron reduction (DIR) is a microbial metabolism coupling organic carbon or hydrogen to the reduction of ferric minerals or soluble Fe(III). The process has

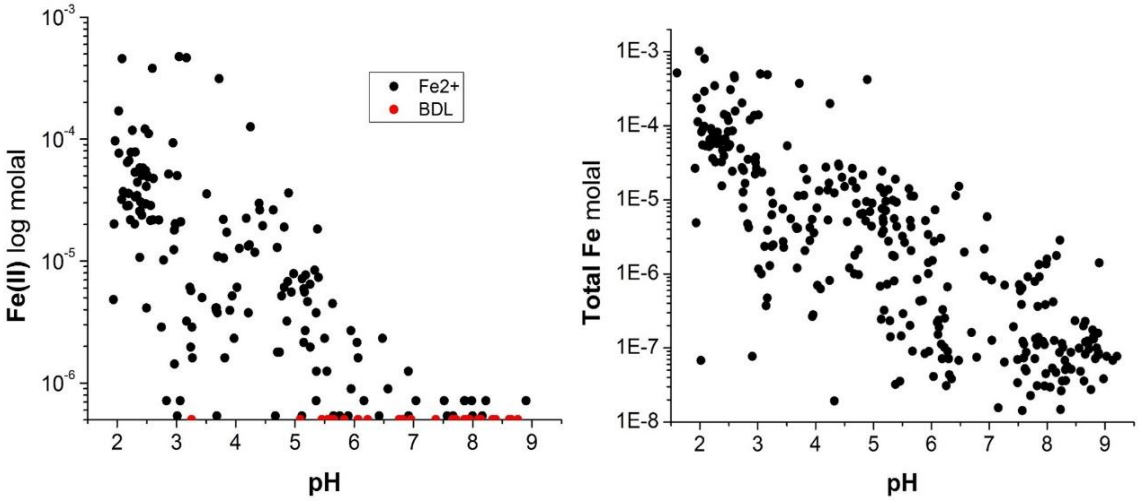

Fig 18 – Ferrous (L) and total (R) iron in Yellowstone hot springs. Ferrous iron was measured in the field with a portable spectrophotometer; total iron was determined in the lab by inductively coupled plasma – mass spectrometry (ICP-MS). Many locations at pH > 5 have concentrations of ferrous iron below the detection limit (BDL, red points).

been documented for dozens of species of bacteria and archaea, as reviewed by Weber *et al*., 2006. Many iron reducing organisms have been isolated from hot springs ecosystems around the world, including from Yellowstone (Slobodkin et al., 1999; Kashefi et al., 2002; Johnson et al., 2003; Fortney et al., 2016). Many organisms classified as heterotrophs have been found to be capable of DIR in low oxygen environments (Johnson and McGinness, 2001; Johnson and Bridge, 2002). Organic acids are commonly used by iron reducers as a carbon source (summarized by Slobodkin, 2005). Individual isolates have been found that can both oxidize and reduce iron, depending on the oxygen concentration in the medium (Bridge and Johnson 1999). Given this evidence for widespread iron reduction, rate measurements of iron reduction by microorganisms in hot springs will constrain the rates and geochemical distribution of these organisms in Yellowstone hot springs. Experimental locations were selected that have a wide variety of pH values, dissolved and ferric mineral content, and concentrations of organic acids and other dissolved organic carbon (DOC).

Investigations of ferric mineral transformations in the laboratory yield insight into our observations from natural systems. Abiotic transformations of ferric minerals include dissolution through protonation, dissolution through organic complexation, and reductive dissolution. Reductive dissolution is the fastest of these three, and lower pH values generally increase the rates these processes (Schwertmann 1991). Reductive dissolution can be coupled to sulfide oxidation (Poulton 2003), and to small organic compounds like ascorbate, oxalate and citrate (Singh et al., 2005 Debnath et al., 2010). At a given pH, the rate of reductive dissolution of 2-line ferrihydrite is about an order of magnitude faster than that of lepidocrocites and 6-line ferrihydrite, and two orders of magnitude faster than

that of goethite dissolution (Larsen and Postma, 2001). Abiotic reductive dissolution of ferric minerals follow the rate law described by Christoffersen and Christoffersen (1976):

$$J = \frac{-dm}{dt} = km_0 f\left(\frac{m}{m_0}\right) g(C) \qquad \text{(eq. 1).}$$

Where J is the overall rate of dissolution (mol/s), m is the amount of undissolved minerals (mol), t is time (s), k is the rate constant (s^{-1}) , and m_0 is the initial mass of minerals. The term $f\left(\frac{m}{m_0}\right)$ is a function of the remaining mineral mass, and g(C) is a function of solution composition. Given the complexity of the g(C) term for hot springs, our approach was to quantify the J term directly by linear fitting of rates over the length of the experiment. Note that the relative abiotic reductive dissolution rates between ferric minerals may affect interpretation of results of this study, as synthetic 2-line ferrihydrite (prepared according to the method of Schwertmann and Cornell, 2000) was used in some treatments. Efforts were made to quantify the total abundance of ferric minerals in order to estimate rate constants.

3.1.2 Iron Oxidation - Microbial iron oxidation is a metabolism involving the oxidation of soluble Fe(II) with oxygen or other electron acceptors. Thermophilic iron oxidizing microorganisms have been isolated from Yellowstone hot springs, including archaea described by Kozubal et al. (2012), and bacteria have described by Holanda et al. (2016). In acid chloride sulfate springs (pH ~2.5 – 3.5), the process is often visibly apparent as red ferric mineral staining (Inskeep et al., 2004; Macur et al., 2004). Less is known about thermophilic iron oxidation at pH < 2.5 and > 4. A goal of this study is to measure rates of biological and abiotic iron oxidation in hot springs across the pH spectrum to determine geochemical controls on the process.

Abiotic Oxidation – Abiotic oxidation may constrain thermophilic iron oxidation at pH values greater than 5 due to the increasing rate of abiotic oxidation at higher pH values. Iron oxidizing bacteria at ambient temperatures face competition from abiotic processes at neutral pH values (Chapter 2 and references therein), and thermophilic organisms may face the same constraint. Rates and mechanisms of abiotic iron oxidation are well understood at low temperatures. The abiotic rate of iron oxidation is dictated by pH (Stumm and Lee, 1961; Singer and Stumm, 1970). The rate expression determined by Stumm and Lee 1961 is

$$-\frac{d[\mathrm{Fe}^{2+}]}{dt} = k[\mathrm{Fe}^{2+}][\mathrm{OH}^{-}]^{2}[\mathrm{O}_{2}] \qquad \text{(eq. 2).}$$

When oxygen is not limiting, and is constant, the rate law can be simplified to the pseudo first order equation:

$$-\frac{d\{Fe^{2+}\}}{dt} = k_{ox}[\mathrm{Fe}^{2+}] \qquad \text{(eq. 3).}$$

Measurements of k_{ox} at 25 °C have been reported by Singer and Stumm (1970) and Millero, et al., (1985). The rate constant for abiotic oxidation of Fe^{+2} at 25°C is small and independent of pH under acidic conditions. With increasing pH above ~ 4, the rate constant increases and becomes second order in OH^{-} concentration by about pH = 4.5. The underlying mechanism involves the chemical speciation of Fe^{+2}, which becomes dominated by aqueous hydroxide complexes at higher pH values (Millero, 1985). These complexes react orders of magnitude more quickly with oxygen than Fe^{2+} (aq), and their increasing abundance with increasing pH is consistent with the observed rate increases (Millero et al., 1985). Speciation calculations indicate that ferrous hydroxide complexes are more abundant at higher temperatures for a given pH value. This suggests that the

speciation at high temperatures may produce rates faster than anticipated an Arrhenius relationship between rate constants and activation energies. We have made measurements of abiotic rates in the lab, analogous to those by Stumm and Lee (1961) and Singer and Stumm (1970), to better constrain the contribution of the abiotic rate in hot spring systems.

3.1.2 Redox Cycling - Experiments at many locations featured *simultaneous* oxidation and reduction experiments. It is becoming increasingly apparent that iron reducers often accompany iron oxidizers where biogenic iron oxyhydroxides are accumulating. Complete iron redox cycling has been demonstrated in lower temperature environments. Blöthe and Roden (2008) and Hegler et al. (2012) describe biological iron oxidation and reduction in low temperature circumneutral sites, while Brock and Gustafson (1976) and Bridge and Johnson (1999) describe the ability of organisms classified as sulfur and iron "oxidizers" to reduce ferric iron. Moran et al. (2016) demonstrated that an autotrophic iron oxidizing isolate from a Yellowstone hot spring excretes formaldehyde, thereby providing a link between the autotrophic iron oxidizers and heterotrophs such as iron reducers. Given the emerging evidence for complete biological redox cycling, experiments at many locations were designed to detect both microbial oxidation and reduction.

3.2 Methods

3.2.1 Site Selection

Sites for oxidation and reduction experiments were chosen to encompass a broad range in pH and other geochemical variables. Sites had either abundant Fe(II), ferric mineral staining, or had been previously reported to support iron cycling. Sites between pH 4 and 6 with abundant Fe(II) were of particular focus, as these sites have abundant

energy available for oxidation but no such sites have yet been identified that support biological iron oxidation.

3.2.2 Geochemistry and Sampling

Geochemical sampling accompanied each experiment using methods previously outlined (section 2.2). Briefly, portable meters were used to measure pH, temperature, dissolved oxygen (in some locations), and conductivity. Portable spectrophotometers were used to measure ferrous iron, dissolved oxygen (in some locations), total sulfide, and dissolved silica in the field. Samples for laboratory analysis were taken in the order listed to minimize contamination; $\delta^{18}O_{water}$ and $\delta^{2}H_{water}$, cation and anion abundance, dissolved inorganic carbon (DIC), dissolved organic carbon (DOC), trace metals, and low MW organic acids. Sediment samples for XRD and sediment reducible iron were taken in 5 mL vials and frozen at -20 °C within a few hours. Samples for molecular biology were collected into a single use sterile sampling cup using a variety of sterile sampling implements. These samples were immediately distributed to 2 mL cryogenic vials containing 0.8 mL of sucrose lysis buffer (Mitchell and Takacs-Vesbach 2008) and frozen in the field on dry ice. Samples were stored at liquid nitrogen temperature until laboratory storage at -80 °C.

3.2.3 Field Rate Experiments

To assay biological iron **oxidation**, microcosm incubations were performed using sediment and spring water sampled from hot springs close to the time of the geochemical samples. Typically, 10 grams of sediment and 40 mL of spring water was combined in a 60 mL serum bottle. The bottles were crimp sealed, with ~15 mL of air in the headspace. Each assay included an amended live treatment (added $FeSO_4 \bullet 7\ H_2O$, 1-10 mg/L Fe(II)

final concentration), live unamended treatment, and killed controls (added $FeSO_4 \bullet 7 H_2O$ to same final concentration as amended live treatment, 5mM sodium azide, matched to within 0.5 pH unit of the system); each treatment measured in triplicate. Method improvements over time resulted in minor changes to the protocol between field seasons. Differences were 2% glutaraldehyde was used in the killed control in experiments with sample IDs beginning with 12 or 13, and higher concentrations of Fe(II) were added to the live amended treatment in sample IDs beginning with 13. Table 7 is a summary of the experimental parameters. Rates were determined by monitoring Fe(II) concentrations over the duration of the experiments, typically 3-5 hours. Assays were measured with the modified 1,10 phenanthroline method previously described in section 2.3.

Assays for biological iron **reduction** are similar to those described for oxidation. Added Fe + C, added C, unamended, and killed control incubations were performed at each location. Sediment and water were added to serum bottles as quickly as possible for each spring, minimizing interactions with the air. The reagents were added for each treatment, and the bottles were immediately crimp sealed the headspace purged with nitrogen for 5 minutes. Synthetic 2-line ferrihydrite (Schwertmann and Cornell, 2000) was added to the Fe + C treatment and the abiotic control. Formate, lactate, acetate, and propinoate (FLAP), as sodium salts, were added to a final concentration of 200 μ*mol*. The pH of the reagents was within 0.5 pH units of the measured pH in the spring. This was accomplished by taking several sets of analyzed reagents at different pH values to the field. Killed controls duplicated these Fe + C bottles, but were killed with 5 mM sodium azide. All assays were performed in triplicate. Ferrous iron was monitored over the experimental duration of two to five hours.

Table 7 – Microcosm Rate Experiment Parameters

Reduction	Treatment	Iron source	Carbon Source	Fixative	Headspace
	Added Fe + C	100 mg ferrihydrite[a]	200 μM FLAP[b]	--	N_2
	Added C	--	200 μM FLAP[b]	--	N_2
	Unamended	--		--	N_2
	Killed	100 mg ferrihydrite[a]	200 μM FLAP[b]	6mM azide	N_2
Oxidation	**Treatment**	**Iron source**		**Fixative**	**Headspace**
	Added Fe	50-250 μM Fe(II) aq		--	Air
	Unamended	--		--	Air
	Killed	50-250 μM Fe(II) aq		6mM azide	Air

[a] ferrihydrite is synthetic 2-line ferrihydrite (method of Schwertmann and Cornell, 2000)
[b] FLAP – Formate, lactate, acetate, propionate, as sodium salts

Given the complex hot spring compositions, iron reduction rates are presented as μmols of iron reduced per gram of wet sediment per minute (analogous to Hegler et al., 2012). The measured concentrations were divided by the remaining volume of sample water in the microcosm to determine the number of μmols reduced. These values were plotted over the duration of the experiment and the slope determined by a linear fit. The mass of wet sediment added in the field (typically 10 g) is then considered. Since 3 mL is drawn at each sampling time, this volume is not negligible. I assumed that the microbial community is not greatly perturbed during a minimal sediment handling period and that any observed rates reflect the ability of the community to reduce iron *in situ*. The microcosm bottles are swirled gently to equilibrate the reagents and iron within the sediment with the overlying water.

3.2.4 Laboratory abiotic iron oxidation experiments

Laboratory experiments were conducted to determine the abiotic rates of Fe(II) oxidation at temperatures relevant to Yellowstone hot springs. Abiotic oxidation experiments were performed analogously to those of Stumm and Lee 1961 and Singer and Stumm 1970, but in unbuffered, dilute solution. One liter of 18.2 MΩ.cm ultra-pure water (Barnstead inc.) was used in all experiments, with trace grade HCl or NaOH used to adjust the pH. Iron stock solutions of ferrous sulfate heptahydrate (ACS grade, Sigma-Aldrich) were made fresh daily in 0.01M HCl. The starting solution was allowed to equilibrate with air by bubbling with filtered air for ~30 minutes before the start of the experiment. The reaction vessel was surrounded by a well-thermostated water bath (± 0.2 °C). The pH reported is measured after Fe(II) has been added and equilibrated. Rate data is available in appendix B.

3.2.5 Sediment Analyses

Sediment carbon and sediment reducible iron were determined as outlined in section 2.3. Briefly, carbon content and isotopic composition of sediments was determined by Elemental Analysis – Isotope Ratio Mass Spectrometry (EA-IRMS) on a Costech elemental analyzer and a Thermo Delta plus advantage IRMS. Samples were dried, ground to a fine powder, and dried again. Total carbon measurements were made by weighing sediments in tin capsules to the nearest microgram. Organic carbon analyses were prepared the same way, except they were repeatedly acidified with high purity 1M HCl. Sediments were characterized for their poorly crystalline ferric mineral content by the method outlined by Lovely and Phillips (1989), which allows for rapid quantification of minerals that are available to microbial iron oxidizers. Ferrous iron in sediments is determined by adding approximately 100mg of fresh weighed sediment to 5mL of 0.5 M HCl (trace grade). Fe(II) is determined using the ferrozine method. The total iron content of the sediments, which includes amorphous ferric minerals and Fe^{3+} were determined by the same method, except a solution of 0.25 M hydroxylamine and 0.25 M HCl was used to reductively dissolve minerals. Total ferric iron was determined by subtracting the measured Fe(II).

3.2.6 Community Composition

DNA was extracted and sequenced according to methods previously outlined in section 2.3, except different PCR primers were used to better resolve bacterial and archaeal communities. Extractions were performed in Prof. Eric Boyd's laboratory at Montana State University. Briefly, Approximately 250 mg of thawed sediment or mat sample was used to extract DNA using following the standard protocol of a DNA

extraction kit (MP Biomedical FastDNA spin kit for soils). PCR was performed using archael and bacterial 16s rRNA primers. The archaeal primers were 344F (ACGGGGYGCAGCAGGCGCGA) and 915R GTGCTCCCCCGCCAATTCCT. Bacterial primers were 1100F (YAACGAGCGCAACCC) and 1492R (GGTTACCTTGTTACGACTT). DNA was subjected to PCR in triplicate using an initial denaturation at 94°C (4 min), followed by 35 cycles of denaturation at 94°C (1 min), annealing at 61°C for archael primers and 55°C for bacterial primers, primer extension at 65°C (1.5 min), and a final extension step at 65°C (20 min). The PCR mixture was the same as previously described. 4µL of each PCR product was run on a 2% agarose gel to ensure amplification. Triplicate PCR products were then pooled and purified using the Wizard PCR cleanup system (Promega) per the instructions, yielding a final volume of 50 µL. DNA was quantified again using the Qubit system. PCR products were sent to the MrDNA lab (Molecular Research LP, Shallowater, TX) for sequencing using the Illumina MiSeq system with 30,000 reads per assay.

3.3 Results and Discussion

3.3.1 Iron Reduction

Assays for microbial iron reduction were performed at 27 hot spring locations in Yellowstone. Biological iron reduction was detected at 19 sites. Field data accompanying each of these sites is shown in Table 8. The experiments were designed to distinguish between locations where DIR is occurring *in situ*, and sites where DIR is inducible with the addition of either ferric minerals or organic anions. The pH and temperatures of sites where iron reduction was detected is depicted in Fig. 19. Black circles are locations where iron reduction was determined to be happening *in situ*. Green and red circles

Table 8 - Field data from locations where iron oxidation and iron reduction experiments were performed

Sample ID	pH	Cond. µS / cm	Temp. °C	Fe(II) µm	Oxygen µm	ΣSulfide µm	Latitude x (12T)	Longitude y (UTM)	Elevation m
120713SH	2.16	5810	79.3	290	41	28.4	540859	4944563	2389
120714TN	2.82	4707	67.1	132	69	0.1	523030	4952609	2291
120718SJ	3.16	3879	61.7	24	106	0.6	522517	4952715	2297
120721SA	2.25	3715	64.6	46	31	14.2	521449	4960847	2275
120722SK	1.94	6700	87.7	47	41	6.8	518485	4949604	2279
120723TM	1.78	13350	82.2	49	murky	0.6	541822	4950862	2373
130711SD	3.17	4140	84.8	26	12	8.8	522522	4952733	2293
130711SE	3.29	1460	63.1	36	44	0.5	522521	4952728	2293
130712TF	2.79	4135	87.0	145	24	0.5	523025	4952606	2285
130714SX	2.73	9960	89.8	279	22	3.8	545156	4957169	2518
130716SC	5.37	3270	60.1	1	8	BDL	544512	4939797	2400
130716SF	3.77	2612	39.5	43	91	3.3	544526	4939794	2399
130717SJ	1.99	6890	66.3	260	murky	35	540881	4944597	2378
130718SP	2.68	2995	57.9	240	94	7	545158	4957166	2519
130720TV	2.18	6370	68.2	235	20	61	542027	4951114	2660
130720TY	2.53	1000	82.6	13	murky	213	541755	4950850	2367
130721SC	1.99	2813	76.6	9	18	4	518373	4949607	2283
130721SF	2.60	2872	87.9	82	19	4	518479	4949604	2272
130722TK	3.78	314	86.0	66	2	5.5	515148	4928548	2275
130722TM	3.69	458	63.4	3	44	ND	515138	4928591	2268
130723SS	3.11	4501	61.1	26	34	0.7	522862	4953168	2284
130723SV	3.69	ND	68.9	27	ND	0.3	523040	4953343	2293
140724TB	4.61	272.6	71.8	6	56	3.9	515127	4928547	2287
140724TD	4.80	254	61.8	1	47	14.9	515148	4928520	2286
140726TM	2.40	2112	81.2	15	12	33.8	541752	4950852	2367
140726TO	1.76	8530	77.4	6	21	19.9	541760	4950862	2373
140730TG	5.24	321	77.0	37	murky	17.4[a]	515125	4928564	2279
140730TI	3.68	266	85.8	3	ND	ND	515134	4928565	2278
140731FG	5.97	1154	51.4	125	132	BDL	520497	4950777	2251
140731FH	6.07	1209	54.0	108	94	BDL	520463	4950765	2246
140802TR	2.04	2800	89.9	54	20	4.5	522549	4952701	2286
140803FI	2.84	4050	89.3	18	12	7.7[a]	522986	4953361	2280
140803FL	3.80	2208	38.6	6	ND	ND	522549	4952701	2286
140804FM	3.50	1878	82.2	20	26	0.9[a]	522542	4952726	2286
140805SX	4.44	427	54.9	19	9	4.8	515111	4929725	2263
140805SY	4.34	532	81.7	4	66	2.5	515018	4929816	2259
150717FB	3.40	3320	68.9	21	38	BDL	522515	4952712	2283
150718FC	2.09	2530	88.6	28	20	4.4	518477	4949606	2276
150720FH	3.57	3700	85.5	26	11	1.9	522516	4952712	2283
150728FQ	3.36	1560	25.4	10	184	0.5	522657	4952811	2270

ND – not detected

BDL – Below detection limit

Murky – samples for dissolved oxygen are necessarily unfiltered. Murky indicates that a measurement was attempted but that the sample did not give a result.

a. Estimated from alternate sample at same location

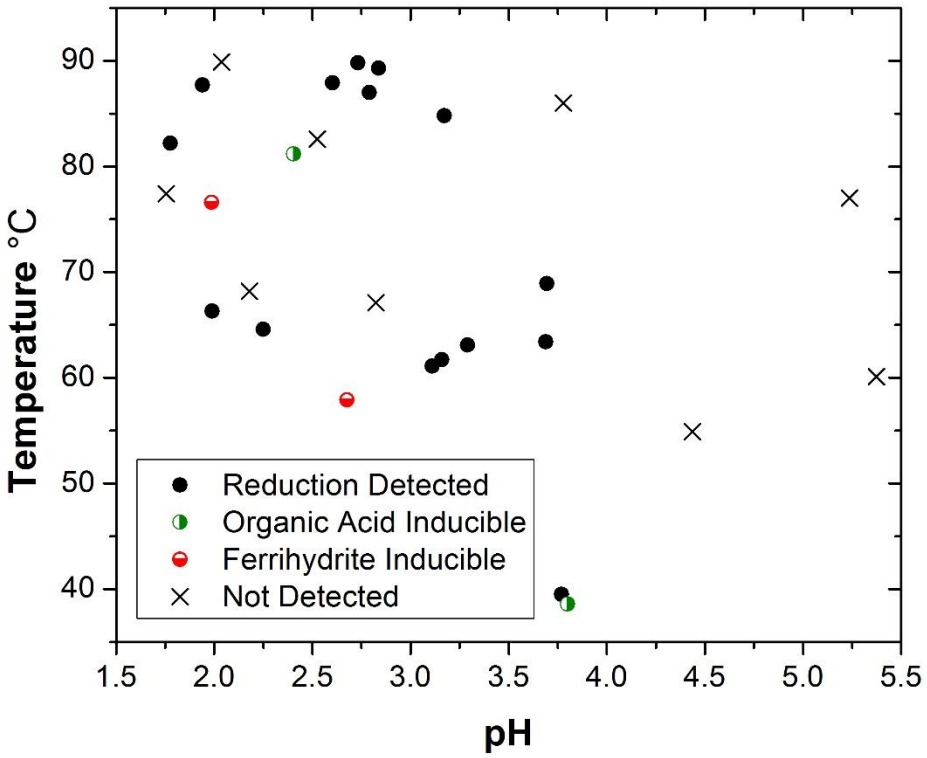

Fig 19 – The pH and temperature of hot springs where biological iron reduction was detected. Black circles indicate biological reduction was occurring *in situ*; green and red circles indicate that biological reduction was induced with organic acids or ferrihydrite, respectively. Black x's indicate that iron reduction was not detected. Biological iron reduction was detected only at pH < 4.

indicate locations where iron reduction was induced with organic acids or ferrihydrite, respectively. Iron reduction was detected in acidic systems below pH 4.

Iron reduction rate experiments have three treatments, added Fe + C, added C, unamended, and abiotic. The iron addition is synthetic 2-line ferrihydrite, and FLAP stands for 200 μM formate, lactate, acetate, and propionate (as sodium salts). In many cases rates were greatly enhanced by the addition of either ferrihydrite or organic acids. Abiotic corrected rates are depicted in Fig. 20. Corrected rates of biological reduction are determined by subtracting the abiotic contribution measured from the abiotic treatment. For correcting the added Fe + C treatment, the average abiotic rates are directly subtracted. For unamended and added C treatments without added ferrihydride, estimates of the abiotic rate are made by the abiotic fraction determined between the added Fe + C and the abiotic treatments. This fraction is then subtracted from the added C and unamended treatments. Each set of bars shows the average of 3 replicates for each biological treatment. The rates are normalized to the amount of wet sediment added in the field, typically 10g. Locations where only one or two treatments are shown indicate that only those treatments showed evidence of biological iron reduction. The unamended (red bars) are indicative of iron reduction happening *in situ*. Most, but not all, sites where biological iron reduction was detected showed some signal of *in situ* iron reduction. Even though biological reduction was detected, rates are generally enhanced by the addition of FLAP (green bars) or ferrihydrite and FLAP (blue bars). Rates measured in each reduction experiment are listed in table 9.

The biological reduction rates are happening in addition to any abiotic reduction present in many locations. Measured abiotic rates are depicted in Fig. 21a. The abiotic

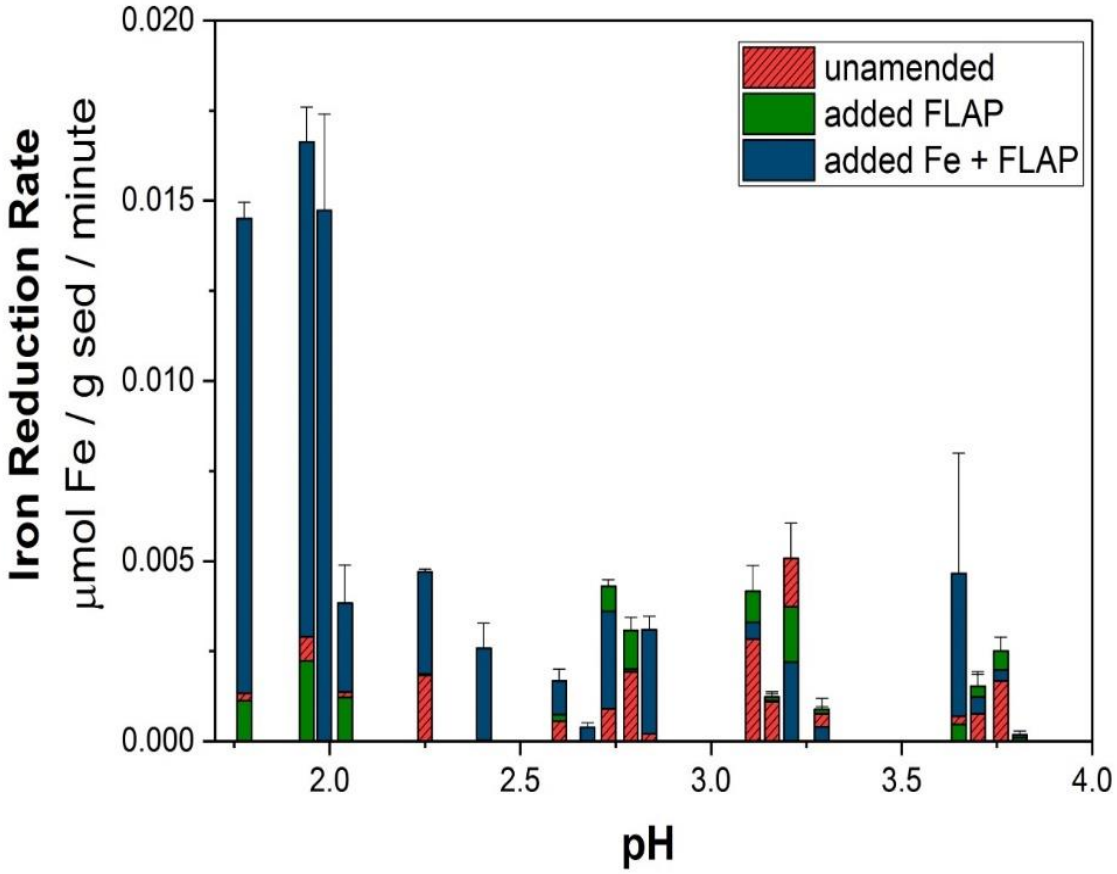

Fig 20 – Rates of biological iron reduction in hot springs. Red, green, and blue bars indicate unamended, added C, and added Fe/C treatments, respectively. Error bars indicate the standard deviation of 3 replicates. Biological iron reduction was not detected above pH 3.8.

Table 9 – Measured rates of iron reduction. The added Fe + C, unamended, and added C treatments do not have the abiotic contribution subtracted.

Sample ID	Added Fe / C nm / g sed / sec	Unamended nm / g sed / sec	Added C nm / g sed / sec	Killed nm / g sed / sec
120714TN	BDL	BDL	BDL	BDL
120718SJ	1.1 ± 0.2	1.1 ± 0.1	1.2 ± 0.1	0.5 ± 0
120721SA	4.7 ± 0.1	1.8 ± 0.01	1.9 ± 0.1	2 ± 0.2
120722SK	16.6 ± 1	2.9 ± 0.1	2.2 ± 0.2	11.9 ± 0.5
120723TM	14.5 ± 0.5	1.3 ± 0.1	1.1 ± 0.1	9.1 ± 2
130711SD	2.2 ± 0.8	5.1 ± 1	3.7 ± 0.3	2.7 ± 0.4
130711SE	0.4 ± 0.1	0.8 ± 0.2	0.9 ± 0.3	0.3 ± 0
130712TF	2 ± 0.6	1.9 ± 0.4	3.1 ± 0.4	0.9 ± 0.1
130714SX	3.6 ± 0	0.9 ± 0.3	4.3 ± 0.2	BDL
130716SC	BDL	BDL	BDL	0.02 0.1
130716SF	2 ± 0.4	1.7 ± 0.2	2.5 ± 0.4	0 ± 0.1
130717SJ	3.8 ± 1.1	1.4 ± 0.6	1.2 ± 0.2	1.7 ± 0.6
130718SP	0.4 ± 0.1	BDL	BDL	0.2 ± 0.1
130720TV	2.2	BDL	BDL	2.2 ± 1.6
130720TY	BDL	BDL	BDL	BDL
130721SC	14.7 ± 2.7	BDL	BDL	BDL
130721SF	1.7 ± 0.3	0.6 ± 0.1	0.7 ± 0.2	BDL
130722TK		BDL	BDL	BDL
130722TM	4.7 ± 3.4	0.7 ± 0.6	0.5 ± 0.2	BDL
130723SS	3.3 ± 0.7	2.8 ± 0.4	4.2 ± 0.7	0.1 ± 0.1
130723SV	1.2 ± 0.7	0.8 ± 0.2	1.5 ± 0.3	BDL
140726TM	3.7 ± 0.7	BDL	0.4 ± 0.04	1.2 ± 0.2
140726TO	9	BDL	BDL	9 0.6
140730TG	BDL	BDL	BDL	BDL
140802TR	9	BDL	BDL	9 0.5
140803FI	3.1 ± 0.4	0.2 ± 0.2	BDL	BDL
140803FL	0.2 ± 0.1	BDL	0.1 ± 0.1	BDL
140805SW	0.8	BDL	BDL	0.8 0.3

BDL – Below detection limit

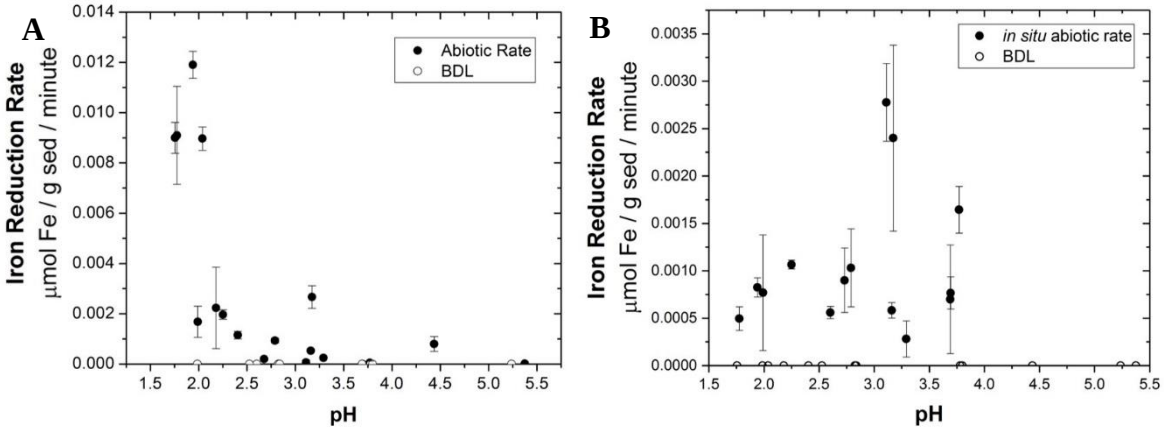

Fig 21 – Rates of abiotic iron reduction in hot springs. 4a – Measured rates of abiotic reduction in amended abiotic reduction experiments (see table 3). 4b – estimated *in situ* abiotic reduction rates. Values are estimated by applying the percentage of the rate determined to be abiotic between the added Fe/C and killed treatments in Table 3 to the unamended treatment.

treatment also included 100 mg addition of ferrihydrite and FLAP, analogous to the live Fe + C treatment, but killed with 5mM sodium azide. Abiotic iron reduction rates are generally quite slow compared to biotic iron transformations at pH values > ~2.5. At extremely low pH springs, however, abiotic rates may rival or exceed the biological rates. Not all extremely acidic springs have fast abiotic rates, suggesting that the type and concertation of available reductants at each location may control the rate. The estimated *in situ* abiotic rates are depicted in Fig. 21b. These values are estimated by applying the percentage difference between the added Fe / FLAP treatment and the killed control to the unamended treatment. The fastest rates are in the pH ~3.3 region. This is likely due to those locations having abundant ferric minerals (Table 10). The lowest pH values no longer show the fastest rates, and many are even below the detection limit. This is a consequence of the scarce nature of ferric minerals per gram of sediment in these systems.

Biological iron reduction was often detected or induced in systems that lacked significant amounts of ferric minerals. Several lines of evidence suggest that regular exogenous input may be responsible for organisms in these springs retaining the ability to reduce iron. Acidic hot springs are typically located in local topographic minima, and have dissolved host rock and soil. Rain events that occur regularly throughout the summer wash in soil from areas surrounding the springs. Instead of becoming more dilute after a rain event, solute concentrations often increase. Several select solutes measured before and after rain storms can be found in Table 11. After one rain storm, the total iron measured in one Washburn hot spring increased more than 4 orders of magnitude. Increases in ferrous iron and DOC were noted as well. The source of increased Fe(II)

Table 10 – Sediment and soil ferric mineral and organic carbon content. Total carbon was only determined on samples at pH > 4. Error reported for organic carbon mass and δC content is standard deviation of 3 replicates. Samples that do not report an error are single measurements. ΣFe(III) is indicative of all hydroxylamine reducible ferric iron in sediment samples. Soil samples have the same units as sediment samples.

Sample ID	pH[a]	Water	Σ Fe(III) mg Fe / g wet sed	Total Carbon mg C / g dry sed	Organic Carbon mg C / g dry sed	stdev	$\delta^{13}C$ VPDB (‰)	stdev
			Sediment Samples					
120714TN	2.82	40	13.86	--	2.06	--	-19.9	--
120718SJ	3.16	29	7.04	--	ND			
120721SA	2.25	38	0.15	--	1.53	0.07	-21.6	0.3
120722SK	1.94	12	0.003	--	0.42	0.04	-21.2	0.5
120723TM	1.78	34	0.19	--	2.56	--	-16.1	
130711SD	3.17	20	0.08	--	0.80	0.02	-22.0	0.1
130711SE	3.29	53	7.04	--	3.48	0.08	-14.8	0.4
130712TF	2.79	28	8.39	--	1.24	0.09	-21.7	0.3
130714SX	2.73	44	0.33	--	1.93	0.09	-24.5	0.4
130716SC	5.37	ND	0.47	--	ND			
130716SF	3.77	ND	0.11	--	ND			
130717SJ	1.99	54	0.07	--	3.91	0.71	-24.0	0.7
130718SP	2.68	56	0.23	--	3.34	0.19	-24.1	0.2
130720TV	2.18	32	0.16	--	1.71	--	-19.2	--
130720TY	2.53	15	0.02	--	0.33	--	-20.2	--
130721SC	1.99	14	0.01	--	0.44	0.06	-21.7	0.6
130721SF	2.60	13	0.13	--	0.29	--	-16.3	--
130722TK	3.78	31	0.05	--	1.71	--	-19.2	--
130722TM	3.69	74	0.76	--	14.37	0.16	-21.2	0.3
130723SS	3.11	59	8.31	--	12.57	0.06	-21.1	0.0
130723SV	3.69	39	11.74	--	8.83	0.10	-17.4	0.3
140724TB	4.61	42	0.84	1.28	1.22	0.74	-23.6	0.2
140724TD	4.80	ND	ND	--	ND	--	--	--
140726TM	2.40	21	0.01	--	0.85	0.20	-19.6	0.1
140726TO	1.76	19	0.05	--	0.72	0.08	-16.1	0.3
140730TG	5.24	38	0.04	9.00	8.23	2.39	-22.4	0.1
140730TI	3.68	27	0.32	--	0.91	0.18	-22.3	0.1
140731FG	5.97	48	3.20	7.00	4.94	0.07	-20.9	0.1
140731FH	6.07	42	1.34	--	6.83	1.52	-20.2	0.2
140802TR	2.04	12	BDL	--	0.24	0.26	-19.5	0.3
140803FI	2.84	25	0.04	--	1.15	0.39	-22.3	0.1
140803FL	3.80	33	7.40	6.49	6.09	0.19	-22.2	0.0
140804FM	3.50	18	3.98	--	1.57	0.20	-17.2	0.2
140805SW	4.44	56	0.48	12.67	12.37	0.55	-20.3	0.1
140805SX	4.34	18	0.09	1.11	0.36	0.29	-24.2	0.5
150717FB	3.40	37	1.77	--	2.62	0.04	-19.89	0.1
150718FC	2.09	15	BDL	--	ND	--	--	--
150720FH	3.57	28	BDL	--	0.81	0.01	-19.91	0.06
150728FQ	3.36	58	1.12	--	6.12	0.08	-17.63	0.20
			Soil samples					
Area			Σ Fe(III)		Organic C		$\delta^{13}C$	
Sylvan			12.2		1.05	--	-24.92	--
Sylvan			14.8		1.17	--	-25.78	--
Sylvan			7.83		1.42	--	-17.59	--
Norris					4.05	--	-20.72	--
Geyser Cr.					7.36	--	-25.56	--
Geyser Cr.					6.18	--	-25.72	--
Geyser Cr.					9.36	--	-26.28	--
Forest Sp.			12.6		5.07	--	-18.12	--
Forest Sp.			14.95		2.01	--	-24.89	--

[a]pH of overlying water

Table 11 − Hot spring composition before and after rain events. Before and after samples were taken on the same day, except 120713SH and 120715TU, which were taken 3 days apart. The third sample reported for Geyser Creek was taken 2 hours after raining had stopped. DOC is dissolved organic carbon.

area	Sample ID		DOC µmol C			Fe(II) µM		Fe_t µM	
	Before	After	before	after	3rd	before	after	before	after
Crater Hills	120713SH	120715TU	125	3083	--	290	1105	--	--
Crater Hills	120713SJ	120713SL	92	1675	--	--	--	--	--
Norris	140803FI	140803FO	83	83	--	18	43	--	--
Rabbit Crk.	140805TJ	140805TP	183	283	--	--	--	--	--
Geyer Crk.	140729TY	140729TD	83	208	250	9	21	--	--
Washburn	090726JA	090726LA	--	--	--	--	--	0.2	444.0

could be from biological or abiotic reductive dissolution of introduced minerals. Field sampling schedules cannot be planned around rain events, and samples were often taken as afterthought. This resulted in incomplete data collection compared to a standard sample, as reflected by the incomplete data available in table 11. To better constrain potential input from rain events, soil samples were taken in thermal areas within a few meters of the hot springs. Organic carbon and ferric mineral contents of these soils are shown in table 10.

3.3.2 Discussion of Microbial Iron Reduction in Hot Springs

Microbial iron reduction was unexpectedly not detected above a pH value of 4, despite isolates (see review by Slobodkin, 2005) that suggest DIR is occurring at higher pH values in hot springs. The chocolate pots hot springs show evidence of DIR (Wu et al., 2013; Fortney et al., 2016). Two reduction experiment performed at the chocolate pots were inconclusive (sample IDs 140731FG, 140731FH). The issue with those experiments was caused by rapid abiotic precipitation during the brief handling period. Despite rendering the microcosms anoxic as rapidly as possible with nitrogen, ferrous iron was still being depleted over the duration of the experiment. This suggests that a modified experimental protocol further minimizing sample water contact with air may be required to detect iron reduction in circumneutral systems.

The combined rate and geochemical data permit generalizations to be made about certain springs types. One common type of spring in which iron reduction is inducible, but not likely occurring all the time is the frying pan type spring. Frying pan springs are extremely acidic shallow pools that are the composed largely of condensed steam. The pH is typically less than 2.2, and can be as low as 1.6. These systems typically have high

fluxes of volcanic gases, often preventing dissolution of atmospheric O_2. The acidic nature of the systems dissolves the surrounding rocks and leaves the springs sitting in local topographical minima. Ferric minerals are non-existent in the sediments of these springs (Table 10, locations with pH < 2.2). However, biogenic ferric minerals sometimes form around the edges of such systems where atmospheric O_2 is able to dissolve. These minerals can be transported into the low-lying springs during rain events, which both induces DIR (Fig. 20) and undergoes rapid abiotic reductive dissolution (Fig. 21a). The rapid reductive dissolution likely prohibits biological iron reduction from occurring except after overland flow delivers fresh iron containing material into the spring. Despite Fe(II) being abundant, microbial iron oxidation is not typically present due to the low oxygen concentrations (as discussed below). Other spring types where iron reduction commonly occurs is pH ~ 3 outflows that are rich in biogenic iron oxides. These iron mat type systems generally appear to be carbon limited as evidenced from the increased rate in the added C treatments (Fig 20, green bars at locations with pH between 2.7 – 3.2). Other spring types support iron reduction as well, but our data does not support generalizations about reduction in other spring types.

3.3.3 Iron Oxidation

Microbial iron oxidation in Yellowstone is often apparent as iron staining. This is especially true under acidic conditions where abiotic precipitation is extremely slow. The biogeochemistry of microbial iron oxidation in acid-chloride-sulfate springs at the Norris Geyser Basin has been described (Macur et al., 2004; Inskeep et al., 2004, Inskeep and McDermott 2005, Kozubal et al., 2008; 2012; Bernstein et al., 2013). These studies have documented various aspects of iron oxidation in springs with a pH of ~3. Such locations

feature extensive outflow channels that permit the infiltration of atmospheric O_2. What is less evident, is the extent to which iron oxidation occurs at other pH values and in larger pools. Our experiments include some of these studied Norris Geyser Basin locations, but also expand geographically and on the pH and temperature range.

Iron oxidation was detected in 18 of the 33 locations where rate experiments were performed. Fig. 22 shows the pH and temperature distribution of these experiments. Iron oxidation was detected from pH ~2 to 5.5 and from 25 to 88 °C (black circles). This expands the range from the acid-chloride-sulfate springs previously reported in Inskeep et al., 2004 and Kozubal et al., 2012 (empty circles), to include other system types. The pH and temperature of locations where biotic oxidation was not detected (x's) reveal clues to the geochemical controls on microbial iron oxidation. At higher pH values, the rate of abiotic oxidation becomes fast enough to potentially limit the amount of bioavailable Fe(II). At the lowest pH values, energy yields from oxidation to ferric minerals becomes limited (Shock et al., 2010). There are other locations in the middle of the diagram where iron oxidation was not detected, yet are surrounded by detections. A closer look at the geochemistry of these systems reveals that some other component, typically a lack of dissolved oxygen, dictates biology in these locations (as discussed in section 3.3.6).

As one can see from figure 22, iron oxidation was not detected at pH values exceeding 5.5. It is well established that the abiotic rate of reaction increases dramatically with pH (Stumm and Lee, 1961; Singer and Stumm 1970a, Millero et al., 1985). Half-lives of the abiotic reaction are minutes under neutral conditions, and seconds under alkaline conditions. Iron oxidizers living in cold circumneutral systems must contend with this abiotic rate for available Fe(II) (see chapter 2). The distribution of detections in

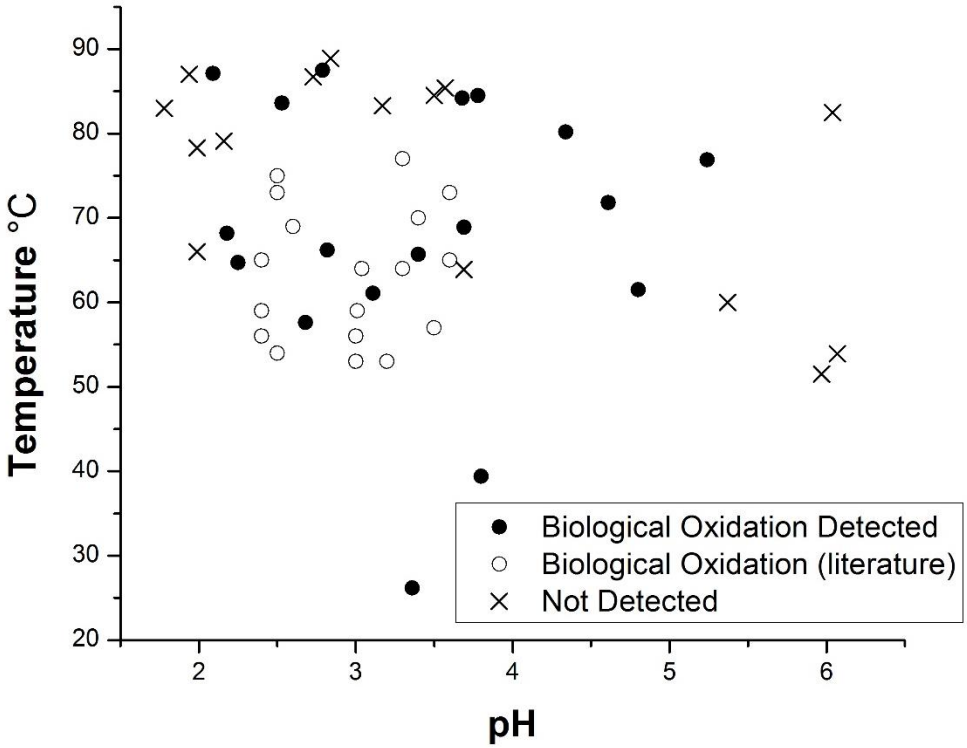

Fig 22 – Temperature and pH distribution of biological iron oxidation in Yellowstone hot springs detected with microcosm experiments. Biological oxidation was detected from pH ~2 to ~5.5, and from 25 to 87 °C. Literature detections are inferred from community composition and isolates from studies of iron stained mats by Macur et al., 2004; Inskeep et al., 2004; and Kozubal et al., 2012.

figure 22 suggest that thermophilic organisms living at pH values higher than 5 may also have to compete with the abiotic rate. The high temperature pH ~ 5 systems are the least acidic high temperature iron oxidation systems described.

3.3.4 Abiotic Oxidation

Laboratory experiments quantifying abiotic rates provide context for observations of iron oxidation in natural systems. Fig. 23 shows abiotic rate constants for the reaction Fe(II) + O_2 → products. As shown by existing rate data from 25 °C, the pseudo-first order constant exhibits a strong dependence of the rate on pH. In acidic conditions, the rate is independent of pH but proceeds extremely slowly. A rate constant of 10^{-7} min^{-1} has a half-life of over 13 years. At pH values > 4 the rate increases dramatically. Under neutral conditions the log pseudo first order rate constant is around -1, which translates to a half-life of 7 minutes. The observed rate increase with pH is a result of the changing speciation of Fe(II). Ferrous hydroxide species appear and then dominate speciation as pH increases. These species have orders of magnitude faster rate constants than Fe(II) (Millero et al., 1985; 1989).

Given the changing speciation, differences in oxidation rate constants between species, and changing pH of neutrality with increasing temperature, analogous experiments at higher temperatures are necessary to establish the pH at which abiotic oxidation potentially outcompetes the biotic reaction in hot spring ecosystems. Figure 23 also depicts my higher temperature measurements. Data for 50, 70 and 90 °C show that rates increase about an order of magnitude for every 15 °C temperature increase. The slopes of the lines in the pH dependent zone become slightly shallower, indicating the Fe(II) species rate increases more, relative to the $FeOH^+$ and $Fe(OH)_2$ aq species.

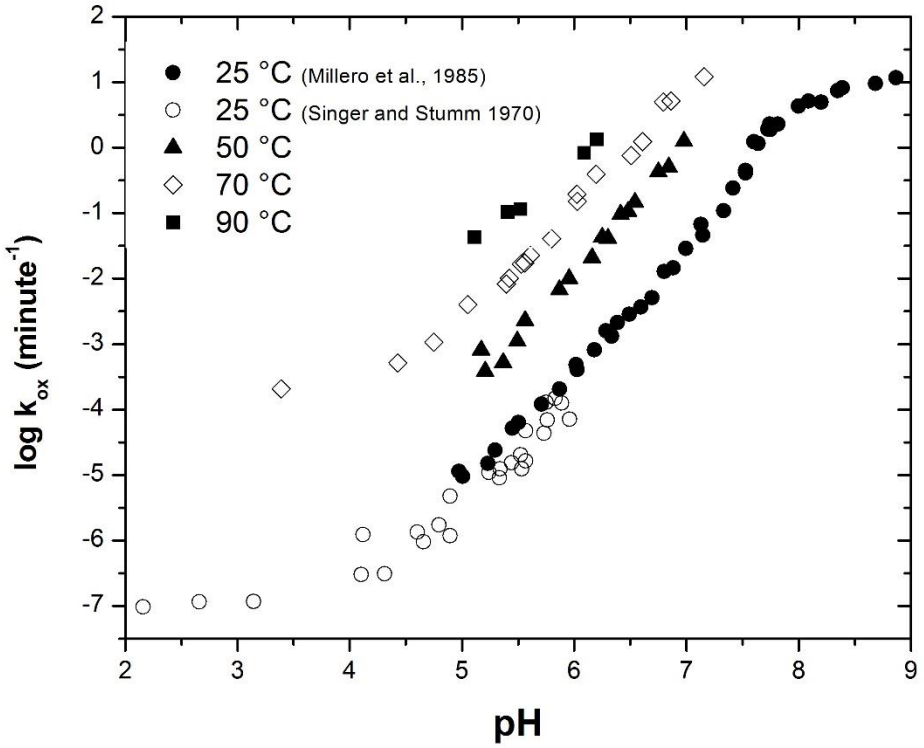

Fig 23 - Pseudo first order rate constant for the reaction Fe(II) + O_2 → products from 25 °C to 90 °C, as determined by laboratory experiments in dilute solution, using Eq. 3. At 25 °C, the observed rate is independent for pH values less than 4, or greater than 8. While the higher temperature measurements do not cover enough of the pH range to show the same sigmoidal shape, the parallel nature of the slopes in the pH dependent region imply the slopes will follow similar trajectories. The temperature contours show that for any given value of the rate constant there is a ~2 pH unit decrease from 25°C to 90°C. This suggests that the kinetic boundary will be at increasingly lower pH values for high temperatures. Data for this plot is tabulated in appendix E

Critically, as temperature increases, the pH that produces a given rate constant drops. This implies that hot springs with pH values around 6 may have rates of abiotic iron oxidation too fast for biology to compete, consistent with observations in figure 22.

Because of the complexity of factors affecting rates in natural systems, the abiotic rate must be measured individually for each location. This is especially true in locations with large accumulations of ferric oxyhydroxides, which sorb Fe(II) and increase the rate of oxidation. Figure 24 shows the measured, abiotic, pseudo first-order rate constants as determined in the field, analogous to laboratory rates in Figure 23. Error bars are relative error calculated from the standard deviation of 3 replicate measurements. Empty circles depict locations where the abiotic rate was below detection. Detection limits were between log k values of -3.8 and -4.2, depending on the duration of the experiment and starting concentration of Fe(II). This puts the detection limit half-life from a few days to weeks. Acidic conditions exhibit the slowest oxidation kinetics, as anticipated from figure 23. Considering that chemical abiotic rate constants at 70 °C are no higher than log k_{ox} of -4, detecting any abiotic rate at all below pH 3 suggests that factors other than chemical oxidation increase the rate. This can include catalysis by ferric minerals or photooxidation. Above pH 5 the rate can be so fast that measurements are difficult. The locations with the two fastest rate constants are minimum rates, as Fe(II) was depleted by the time the second measurement was made.

3.3.5 Biological Rates in Microcosm Experiments

Biological iron oxidation was detected in 18 hot springs in seven thermal areas. Results as both rate constants, analogous to Figs. 23 and 24, and rates are depicted in figure 25. Depicted values have had the abiotic contribution subtracted. The measured

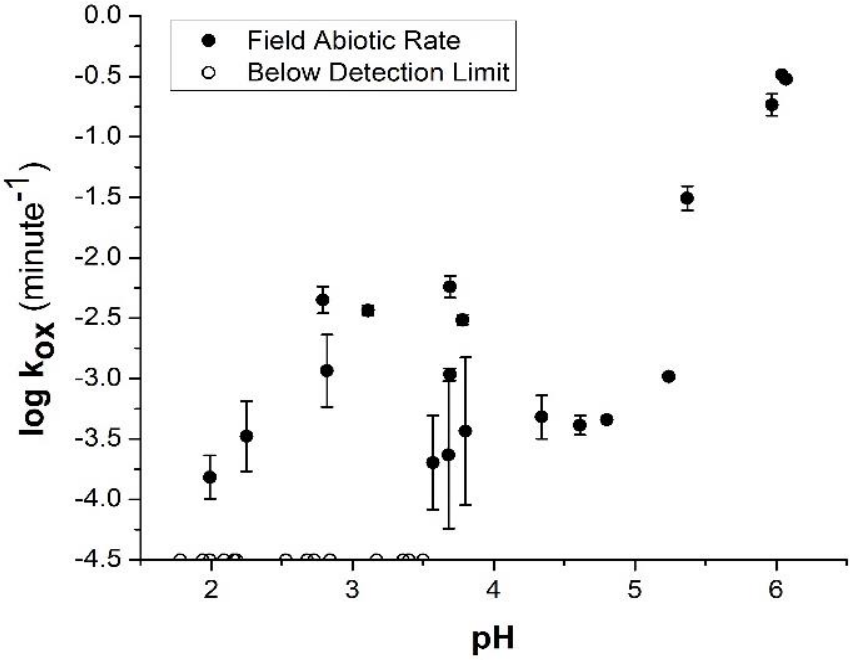

Fig 24 – Rate constants for abiotic oxidation determined in the field. Values were determined using Eq 3. Empty circles depict abiotic oxidation rates below the detection limit (BDL) of around log k = -4, but varies slightly between experiments. Error bars show relative error calculated from the standard deviation of 3 replicate experiments.

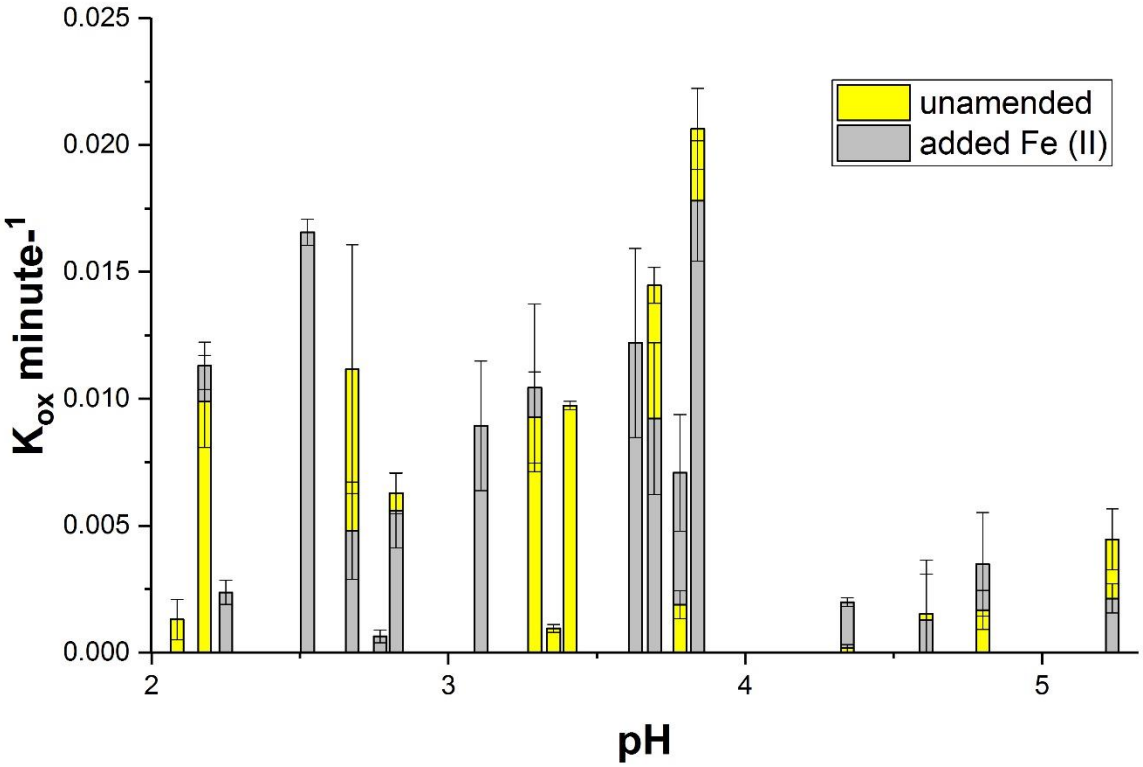

Fig 25 – Rate Constants of Biological Iron Oxidation. Abiotic contributions have been subtracted. Unamended treatments are indicated with yellow bars, while added Fe(II) treatments are shown with grey bars. Error bars represent the standard deviation of three replicates.

rate constants only vary by ~1.5 orders of magnitude (fig 25). Most of the systems that are considered iron mats (pH 2.5 -3.8) have log rate constants around -2 min^{-1}. This suggests these values are typical systems where iron oxidation metabolism is dominant. The measured rate constants drop to ~ -2.5 at pH values greater than 4. This is possibly due to the increasing abiotic rate consuming the available Fe(II).

Rates can be calculated from rate constants using Eq. 2. To determine the rates in experimental treatments, the starting concentration used is the average of the initial iron measured in the microcosms (shown in table 12) multiplied by the abiotic-subtracted rate constants from Fig 25. Similarly, *in situ* rates are calculated by using the measured Fe(II) in each system (table 8) by the measured unamended rate constant from Fig 25. To compare rates of oxidation and reduction, these rates are then divided by volume of the microcosm (40 mL) and normalized to the amount of sediment. Calculated biotic rates, as μmol Fe(II) oxidized / gram wet sediment / minute are shown in Fig 26. The decreasing rates with pH are a result of the decreasing Fe(II) found at higher pH values. The distribution of points does show as much as 2.5 orders of magnitude difference in rates at a given pH value.

3.3.6 Other Geochemical Variables Affecting Microbial Iron Oxidation

While biological oxidation was detected across many diverse systems in Yellowstone, many locations where ferrous iron was abundant did not yield biotic rates. Instead oxygen controls the presence of iron oxidizers in such systems. To determine what concentrations of oxygen are required for microbial iron oxidation, we turn to natural systems that display gradients in oxygen along outflow channels. Microbial iron cycling can be found in hot springs throughout Yellowstone National Park, where the

Table 12 – Rates of iron oxidation in Yellowstone Hot Springs. K_{ox} is calculated with eq 3.

Treatment :	added Fe(II)			unamended		killed
Sample ID	k_{ox} min^{-1}	Fe_i µM	log bio rate µmol/g sed/min	k_{ox} min^{-1}	log bio rate µmol/g sed/min	k_{ox} min^{-1}
120713SH	BDL	---	---	BDL	---	BDL
120714TN	0.0056 ± 0.00147	367	-2.08 ± 0.11	0.0063 ± 0.00082	-2.47 ± 0.06	0.0012 ± 0.0008
120721SA	0.0024 ± 0.00048	225	-2.74 ± 0.09	0.0027 ± 0.00048	-4.58 ± 0.24	0.0003 ± 0.0002
120722SK	BDL	---	---	BDL	---	BDL
120723TM	BDL	---	---	BDL	---	BDL
130711SD	<0.0002	---	---	<0.0002	---	0.0002 ± 0.00018
130711SE	0.0104 ± 0.0033	50	-2.53 ± 0.14	ND	---	BDL
130712TF	0.0006 ± 0.00025	313	-2.22 ± -0.17	0.0051 ± 0.00025	-3.53 ± 0.24	0.0045 ± 0.0011
130714SX	BDL	---	---	BDL	---	BDL
130716SC	<0.031	---	---	<0.031	---	0.0311 ± 0.00705
130716SF	BDL	---	---	BDL	---	BDL
130717SJ	<0.0002	---	---	<0.0002	---	0.0002 ± 0.00006
130718SP	0.0048 ± 0.00192	280	-2.34 ± 0.17	0.0112 ± 0.0049	-1.97 ± 0.19	BDL
130720TV	0.0113 ± 0.00093	423	-1.72 ± 0.04	0.0113 ± 0.00093	-2.03 ± 0.08	BDL
130720TY	0.0262 ± 0.00052	189	-1.7 ± 0.01	0.0262 ± 0.00052	0 ± 0	BDL
130721SC	BDL	---	---	BDL	---	BDL
130722TK	0.0071 ± 0.0023	80	-2.79 ± 0.14	0.0102 ± 0.0023	-5.24 ± 0.13	0.0031 ± 0.0002
130722TM	<0.0011	---	---	<0.0011	---	0.0011 ± 0.00013
130723SS	0.0089 ± 0.00255	191	-2.17 ± 0.12	0.0126 ± 0.00255	-3.9 ± 0.06	0.0037 ± 0.0003
130723SV	0.0092 ± 0.00299	243	-2.05 ± 0.14	0.0145 ± 0.00071	-2.81 ± 0.02	0.0057 ± 0.0012
140724TB	0.0013 ± 0.0018	23	-3.83 ± 0.61	0.0015 ± 0.00211	-4.37 ± 0.6	0.0004 ± 0.00007
140724TD	0.0035 ± 0.00204	11	-3.88 ± 0.25	0.0039 ± 0.00204	-5.08 ± 0.2	0.0005 ± 0.00001
140730TG	0.0021 ± 0.00057	49	-3.49 ± 0.12	0.0045 ± 0.0012	-3.3 ± 0.12	0.001 ± 0.00003
140730TI	0.0122 ± 0.00373	50	-2.62 ± 0.13	bdl	---	0.0002 ± 0.0003
140731FG	<0.18	---	---	<0.0011	---	0.1838 ± 0.03838
140731FH	<0.3	---	---	<0.0011	---	0.3
140803FI	BDL	---	---	BDL	---	BDL
140803FL	0.0178 ± 0.00237	24	-2.78 ± 0.06	0.0206 ± 0.00159	-3.31 ± 0.03	0.0004 ± 0.0005
140804FM	BDL	---	---	BDL	---	BDL
140805SW	BDL	---	---	BDL	---	BDL
140805SX	0.002 ± 0.00017	28	-3.68 ± 0.04	0.0025 ± 0.00017	-5.56 ± 0.38	0.0005 ± 0.0002
150717FB	ND	---	---	0.0097 ± 0.00017	0 ± 0	BDL
150718FC	ND	---	---	0.0013 ± 0.0008	-3.61 ± 0.27	BDL
150720FH	BDL	---	---	BDL	---	BDL
150728FQ	ND	---	---	0.0009 ± 0.00016	-4.44 ± 0.07	BDL

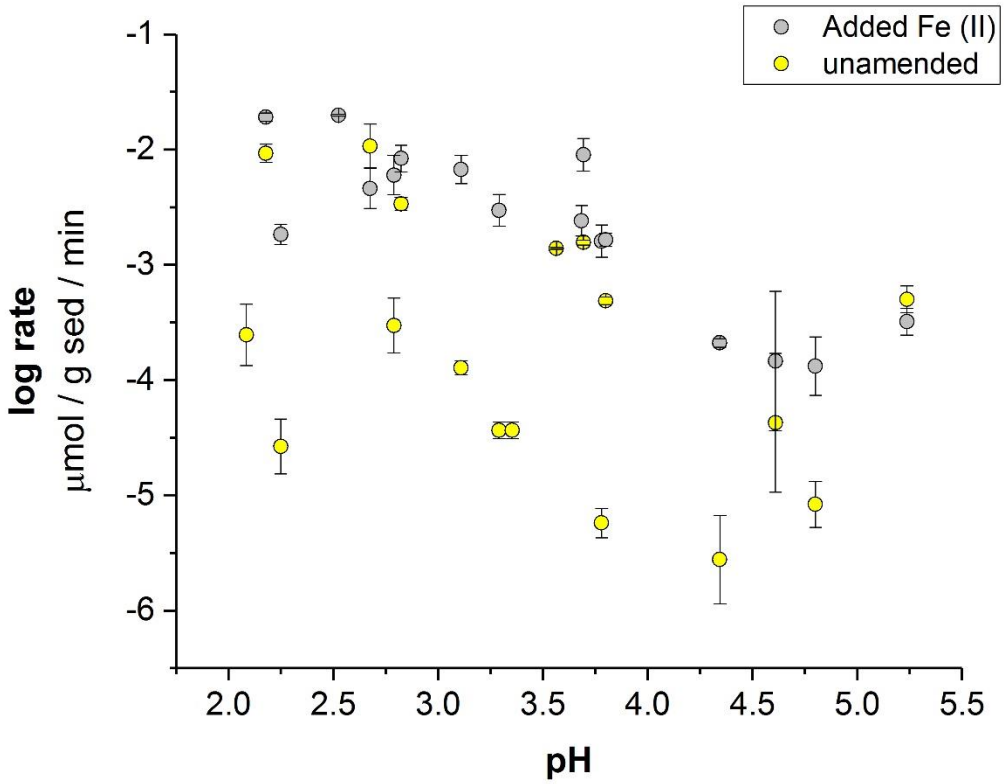

Fig 26 – Rates of biological iron oxidation. Rates determined from the added Fe treatment are shown as grey circles, unamended biological rates are shown as yellow circles. Both rate values have the abiotic contribution subtracted. The generally decreasing rates with pH is a result of the lower concentrations of Fe(II) present in those hot springs.

process is often visibly apparent as red iron oxyhydroxide staining. The point sources of springs that lead to the formation of these mats are typically below the detection limit (<0.16 μM) in oxygen and devoid of iron staining. As the shallow undersaturated water flows away from the source, atmospheric oxygen dissolves in the water. The sudden appearance of iron minerals along the outflow channel permits hypotheses about minimum oxygen values to be tested. The geochemistry and development of iron mats in acidic (pH < 3.8) hot springs were initially described by Macur et al., (2004) and Inskeep et al., (2004), who showed a succession of inorganic substrate utilization by microbes in these systems. Sharp boundaries can be observed between host sediments and sediments rich in biogenic ferric mineral deposits (Fig 27). These mats can be separated into two groups: high sulfide / S^0 depositing springs (Fig 27 a,b), and low sulfide springs (Fig 27 c,d). Measurements of numerous solutes, including oxygen, sulfide, and iron, were made on outflow channels of the springs containing apparent iron metabolism. A highly sensitive dissolved oxygen meter with a detection limit of 0.16 μM was used to make these measurements. The ferric mineral products can all be presumed to be biogenic because of the extremely slow abiotic rate in these locations. Additionally, the lack of visibly observable ferric minerals on one side of the boundary can confidently exclude biological iron oxidation because of extensive mineral and microbial community characterization by Macur et al., (2004), Inskeep et al., (2004), Kozubal et al., (2012), as well as our own data.

Dissolved oxygen concentrations dictate the location of biogenic mineral accumulations in the outflow. The occurrence of acidic hot spring iron mats only at concentrations of dissolved oxygen greater than 20 μM was noted by Kozubal et al.,

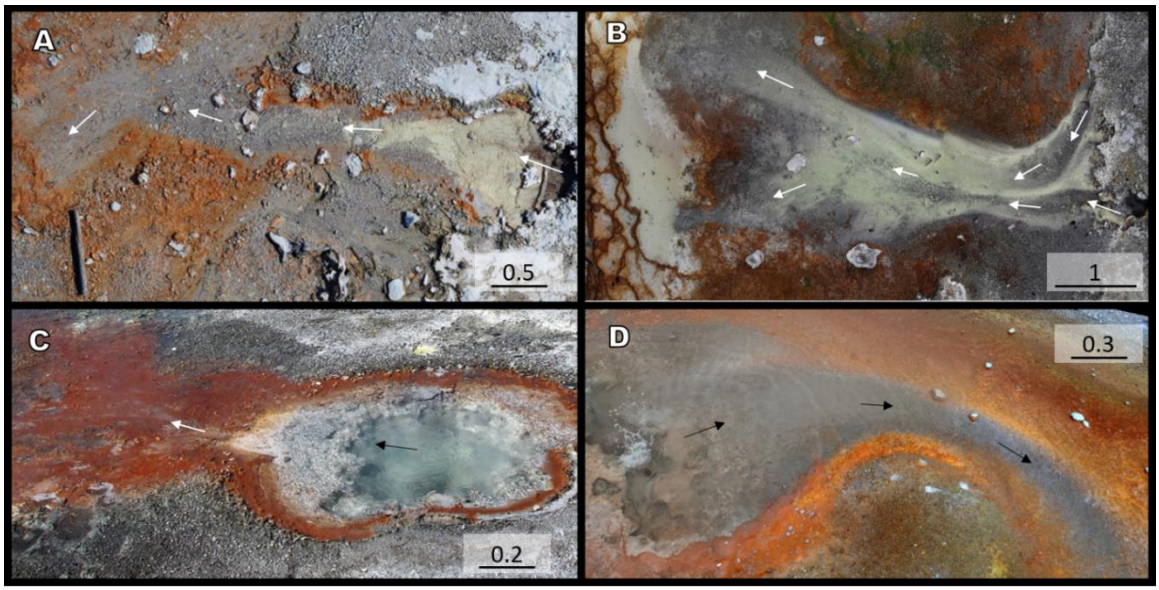

Fig 27 – Photographs of hot springs showing sharp boundaries between red ferric mineral deposition zones and zones devoid of staining. Arrows indicate predominant flow direction. Scale bars indicate distance in meters. Samples IDs for each location are as follows a. 140725FA; b. 130723SS; c. 130723ST; d. 140803FK.

(2012). To determine a universal minimum concentration of dissolved oxygen required to support a community of iron oxidizers that can accumulate ferric minerals, measurements of dissolved oxygen were made across these boundaries at more than two dozen geographically diverse hot springs throughout Yellowstone. Results shows that > 8 µM dissolved oxygen was required for visible iron oxidation products to occur. These data are shown in Figure 28. Black X's indicate ferric mineral products were not observed. Bolded black X's indicate iron oxidation was not observed during a rate experiment. Observation of ferric minerals as shown as empty circles, while microbial iron oxidation detected in rate experiments is shown on the figure as filled circles. It should be noted that while source compositions of these particular systems are relatively stable year to year, small variations in solute concentration and temperature may be observed across the boundary.

The boundaries of iron mats are also influenced in several locations by the concentration of total dissolved sulfide. Kozubal et al. (2012) observed that the iron oxide depositional zone begins at concentrations of total sulfide < 5-10 µm. Experiments with enrichment cultures and occasional field observations of iron oxides forming on sulfur rich biofilm streamers show that sulfide is not toxic to iron oxidizers (data not shown), but rather inhibits the accumulation of dissolved oxygen. Microbial and abiotic sulfide oxidation, leading to visible sulfur precipitation, together with degassing of hydrogen sulfide, contribute to keeping oxygen levels low (Xu et al., 1998; Macur et al., 2004). Our data concur with these references. Only where sulfide concentrations fall below ~5 µM are iron mats able to form. Figure 29 demonstrates that oxygen begins to accumulate only when sulfide is depleted. The only location where iron oxides were observed at high

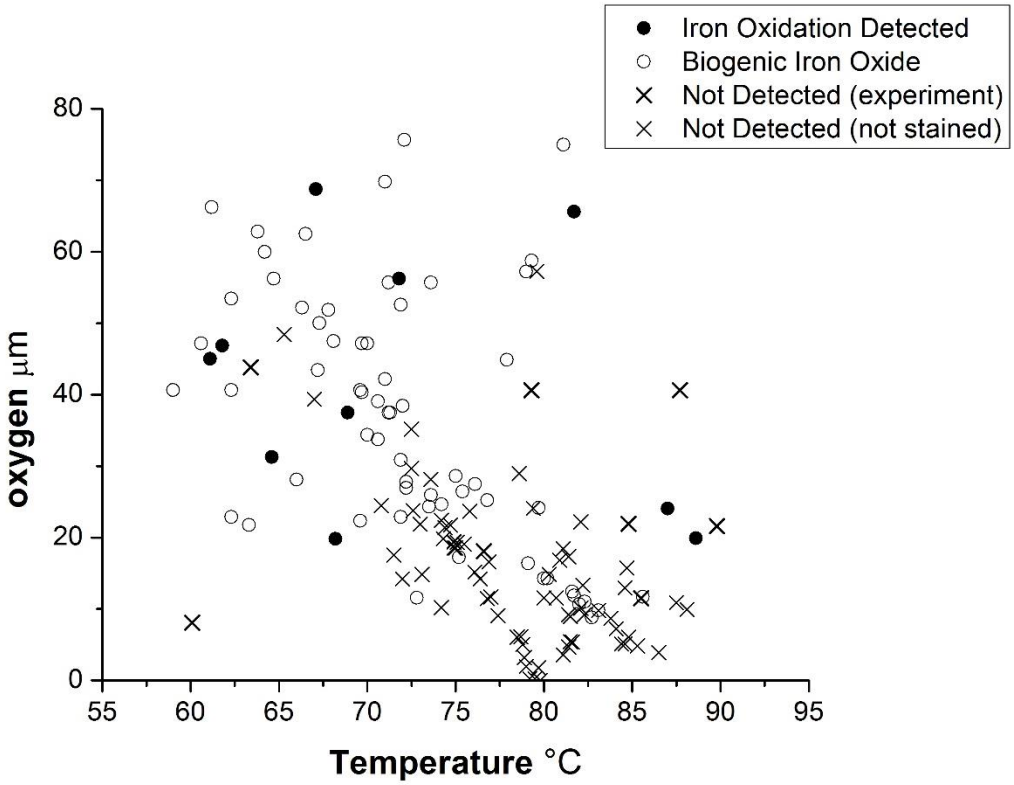

Fig 28 – The temperature and oxygen concentrations supporting and prohibiting accumulation of apparent biogenic iron oxides in outflow channels of acidic hot springs at Yellowstone National Park. Ferric minerals are considered detected when there is red iron staining like that shown in fig 27. The black x's indicate that ferric minerals were not observed, while bolded black x's depict locations where a rate experiment did not produce evidence of biological iron oxidation. Biogenic ferric minerals were never detected when concentrations of oxygen were <8 μM.

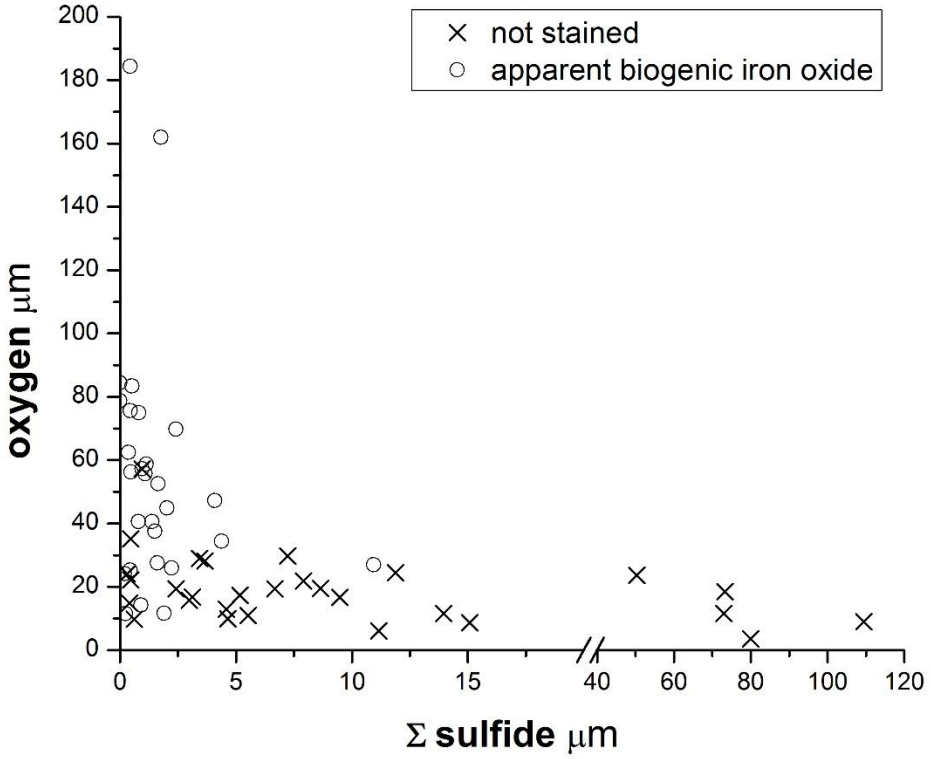

Fig 29 – The presence of apparent biogenic iron oxides in outflow channels at Yellowstone National Park, analogous to figure 28. Total sulfide appears to limit accumulation of dissolved oxygen at concentrations greater than ~5 μM. Apparent biogenic minerals are rarely detected at concentrations of sulfide exceeding 5 μM, or concentrations of oxygen below ~ 20 μM in high sulfide systems.

concentrations of sulfide was an outflow channel with a small point source titrating sulfide into the already oxygen rich water. This was one of only a handful of locations where sulfur deposits and ferric minerals both exisisted. Enrichment cultures of iron oxidizers, however, grow easily at levels exceeding 100 µM sulfide. Formation of biogenic iron oxides occurs at highly consistent concentrations of dissolved oxygen and sulfide in Yellowstone hot springs, and can even serve as visible indicators of the abundance of these geochemical constituents.

3.3.7 Discussion of Iron Oxidation

Microbial iron oxidation is at its optimum at pH ~3. The lower the pH, the less energy is available for iron oxidation to ferric minerals. At pH > 4, however, measured concentrations of Fe(II) are lower as abiotic oxidation begins to compete for available Fe(II). At pH values greater than ~6, abiotic oxidation is so fast that biological oxidation was not detected. This means that hot springs with pH between 2.7 and 3.3 are in the goldilocks zone for thermophilic iron oxidation. Hot spring in this pH range can often have abundant iron oxidizing organisms. The Norris Geyser Basin (NGB) has many hundreds of such hot springs. These systems are found through most acidic thermal areas in Yellowstone, although in lesser numbers than NGB.

Hot springs with a pH between 4-6 with abundant Fe(II) are relatively uncommon, but a few dozen have been identified in Yellowstone. Some support microbial iron oxidation while others have abiotic rates too fast for biology to compete. Many such systems are located in the south Rabbit Creek thermal area. Here relatively dilute, low conductivity water supports microbial iron oxidation. Many small hot springs are iron stained, yet it is not possible to visually determine which support microbial

oxidation and which are just the result of abiotic oxidation. Rate experiments have differentiated the processes in a few locations, with pH ultimately determining which locations support microbial iron oxidation. The chocolate pot springs (sample IDs 140731FG, 140731FH) are notable examples of locations where abiotic oxidation is generally too fast for biology to use the iron oxidation reaction. Out experiments show no difference between killed and live experiments. This does not suggest that biological iron oxidation is completely impossible, but rather it is not happening at the bulk level. Microenvironments no doubt exist in such systems that permit a few organisms to use the reaction.

In hot springs with pH < 2.5, ferric mineral staining is rarely observed. When it is present, ferric minerals are generally observed around the periphery and splash zone of hot springs rather than in the pool sediments. In the water and sediments of such pools, Fe^{3+} ions are the likely product of microbial iron oxidation. Biological oxidation was only detected down to pH 2.2 (Fig 22). Extremely acidic hot springs often contain little to no measurable dissolved O_2. This may explain the lack of observations at these pH values.

Abiotic oxidation rates at pH < 4 show a ~2.5 order of magnitude variation for any given pH value. Abiotic iron oxidation rates are affected by chemical composition, photochemistry, mineral abundance and identity, and other factors. To attempt to clarify some factors contributing to abiotic rates, attempts were made to measure photo oxidation and reduction by using UV transparent glass bottles (data not shown). Some locations showed enhanced oxidation, while others showed photoreduction. No obvious variable was found to predict photochemical enhancements. This inherent complexity of abiotic rates in natural systems means that abiotic oxidation must always be measured.

Method development lead to changing fixatives for abiotic controls to minimize experimental artifacts. I determined that 5 mM sodium azide (matched to within 0.5 pH units to spring) is the best choice of fixative for rate experiments in hot springs. Glutaraldehyde was initially used in some experiments during one field season (sample IDs starting with 13), but the measured abiotic rate in some (but not all) locations was anomalously rapid. This enhancement of the abiotic iron oxidation rate was not observed in dilute solution laboratory oxidation experiments. This suggests that abiotic fixatives in complex media may interact with either iron or the colorimetric method used to quantify it.

There is abundant energy from the oxidation reaction even with dissolved O_2 as low as 1 µM. Iron oxidizing bacteria at low temperatures can grow on oxygen concentrations as low as 1 µM (Druschel et al., 2007). Thermophilic iron oxidizing microbes were not observed to grow below 8 µM dissolved O_2. This observation suggests several possible hypotheses, including this is a physiological (enzymatic) minimum, energetic minimum, or competition from other metabolisms prevents iron oxidation at lower values. The energetic costs of being an autotrophic iron oxidizer in acidic conditions are relatively high. Isolation and laboratory experiments may resolve the reason for this apparent minimum value.

3.3.8 Complete redox cycling

Rate measurements provide evidence of complete microbial redox cycling at 6 hot springs. All location featured large accumulations of biogenic ferric minerals in shallow outflow channels or at the edges of pools. The measured rates from these location are depicted in Figure 30. Colors of bars are indicative of the treatment, following color

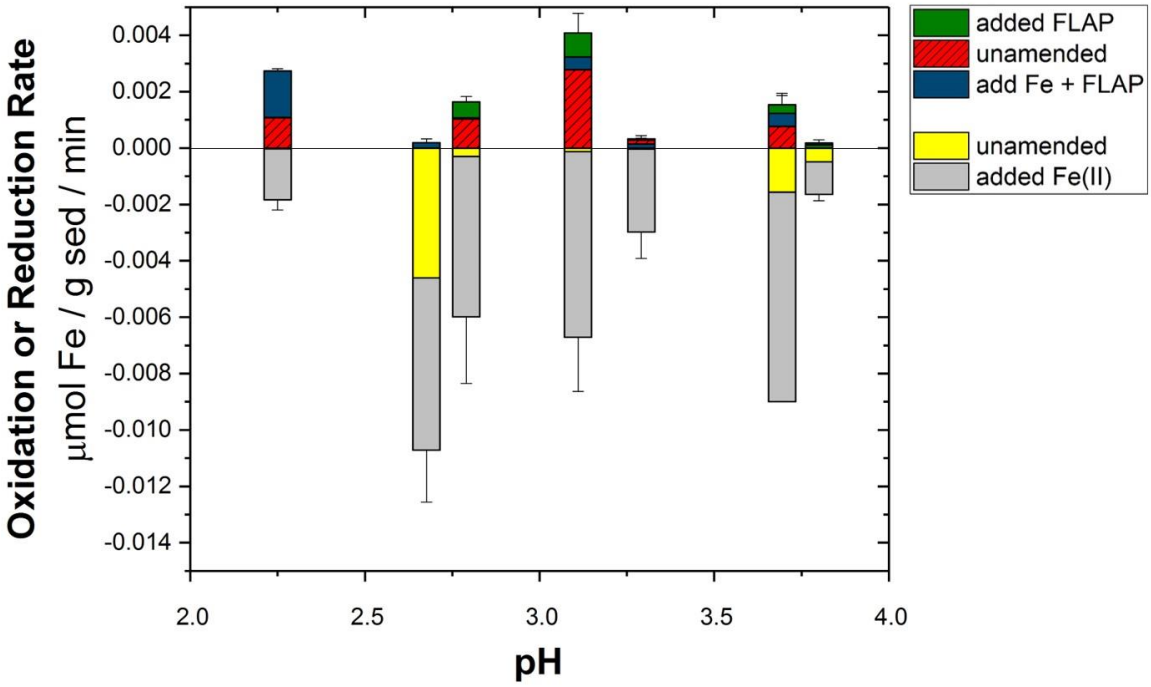

Fig 30 – Rates of complete redox cycling in Yellowstone hot springs. Positive values represent reduction, while negative values represent oxidation. Values are reported as µmol of iron reduced or oxidized, per gram of sediment, per minute. Treatments are indicated by color schemes from Figs. 20 and 25. Error bars represent standard deviation of 3 replicates. Complete redox cycling was observed at 7 locations from pH 2.25 to 3.8.

schemes in Figures 20 and 25. Positive bars indicate reductions and negative bars indicate oxidation. Rates of reduction can exceed oxidation in amended treatments in some locations. The presence of ferric minerals implies that the rate of oxidation is overall faster *in situ*.

Several lines evidence permit a conceptual framework for redox cycling in such systems. Accumulating ferric minerals bury organisms that have latent iron reduction pathways. The ability to reduce ferric iron is a widely-retained ability among thermophilic organisms of many lineages (Johnson and McGinness, 2001; Johnson and Bridge, 2002). The now anaerobic environment features decaying obligate heterotrophs to provide a source of organic carbon. Measurements of oxygen profile into high temperature iron mats by Bernstein et al. (2013) showed that oxygen drops below 3 μM at ~7 mm depth. Many of these iron mats have low DOC in the overlaying fluid, but relatively high sedimentary organic C content (Table 10). The organisms become surrounded by ferrihydrite, which is a high-energy oxidant at low pH values. The combined presence of iron oxidizers and reducers is likely routine in hot springs with large accumulations of ferric minerals.

3.3.9 Microbial composition of springs

Iron Oxidation - Rate measurements remain the most reliable way to determine if biological iron oxidation is occurring at a location, but community sequence data can suggest lineages that may be responsible for the process. Community composition was determined by amplifying and sequencing 16S genes with both bacterial and archaeal specific primers. Putative iron oxidizing bacteria were not identified. In locations where iron oxidation was detected, a combination of 4 archaeal genera make up the majority of

the reads. These include: *Thermofilum*, *Aciduliprofundum*, *Sulfolobus*, and *Vulcanisaeta*. These results are similar to the communities observed by Kozubal et al., 2012, in iron oxidizing hot springs. This study presents a larger range of pH and temperatures for iron oxidation in Yellowstone, yet the community composition is quite similar. *Ferroplasma cyprexacervatum*, an organism commonly associated with mine drainage, was 44% abundant in sample 130718SP. This location in an outflow at the Washburn thermal area was the only location to feature this putative iron oxidizer.

A largely unexplored geochemical region for iron oxidation is mid temperature mild acidic systems. This is partly because locations with these properties are uncommon on earth's surface. Two such samples (150728FQ & 140804FL) show archaeal 16S sequences are dominated by the *Aciduliprofundum* genus. Sequence reads show the organisms are closely related to *Aciduliprofundum sp. epr07_39*, which is a member of the novel Euryarchaeota lineage DHVE2 (deep-sea hydrothermal vent euryarchaeotic 2). These organisms have been shown to comprise as much as 15% of acidic deep sea hydrothermal vent populations (Reysenbach et al., 2006). In our Yellowstone samples these organisms comprise as much as 74% of the archaeal sequence reads. One location dominated by *Aciduliprofundum* is in the Norris Hot Spring basin (150728FQ), where several acidic hot spring outflow channels converge. Each of the source springs have apparent biogenic iron minerals that continue out into the merged channel. The water is a cool 25 °C at pH 3.36. The measured biotic iron oxidation rate at this location is similar to that of other iron mats in the same area that have much higher temperatures (~65 °C). While its likely these *Aciduliprofundum* species are involved in iron transformations, neither isolates nor target genes exist that currently permit this conclusion. Relatively

rapid biological oxidation was detected at this location, while abiotic oxidation was below the limit of detection. Bacterial species from this location do not show any putative iron oxidizers. While the *Aciduliprofundum* are dominant in low temperature outflows, they are also as high as 58 % of sequences at 71 °C in sample 140724FB. Biological iron oxidation was also detected at this sample location. Lists species level archaeal and bacterial community data from most experimental locations are location in Appendix D.

Bacteria involved in iron oxidation were not identified. This presents a significant unresolved question about species distribution in intermediate pH and temperature locations. The condition in outflow channels far downstream from hot sources have can have similar pH, temperature, and metal concentrations to acid mine drainage (AMD). Communities in these cool outflow channels do not resemble AMD. The bacterial communities at the highest temperatures and lowest concentrations of dissolved oxygen typically have large populations of organisms implicated in hydrogen metabolism, such as *Hydrogenobaculum* and *Sulfurihydrogenibium*. Most other locations have significant populations of heterotrophs and fermenters. Some iron mats have significant populations of cyanobacteria. These organisms may provide a symbiotic relationship with iron oxidizing organisms. Bacteria in all locations are shown in figure 31, while archaea are shown in figure 32.

3.4 Concluding Remarks

Rate measurements presented here represent a framework for future work. Microbial iron reduction was only detected at pH < 4, but there are no apparent geochemical barriers that may exclude DIR from higher pH values. In many locations, microbial iron reduction was inducible or enhanced with ferric minerals or organic

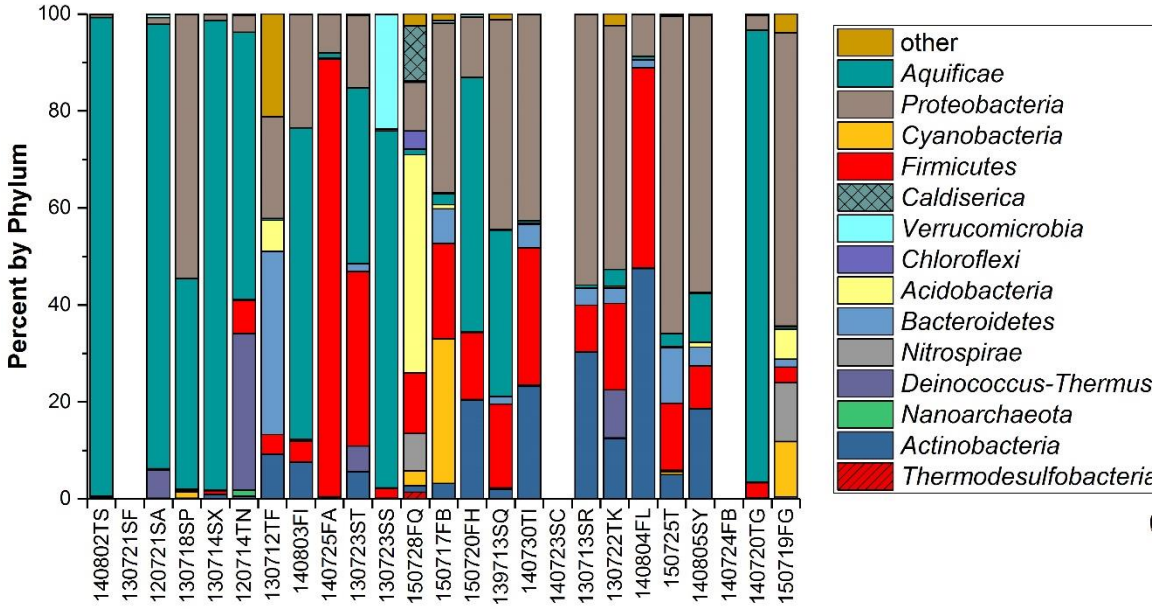

Fig 31 – Phyla of bacteria present in experimental locations.

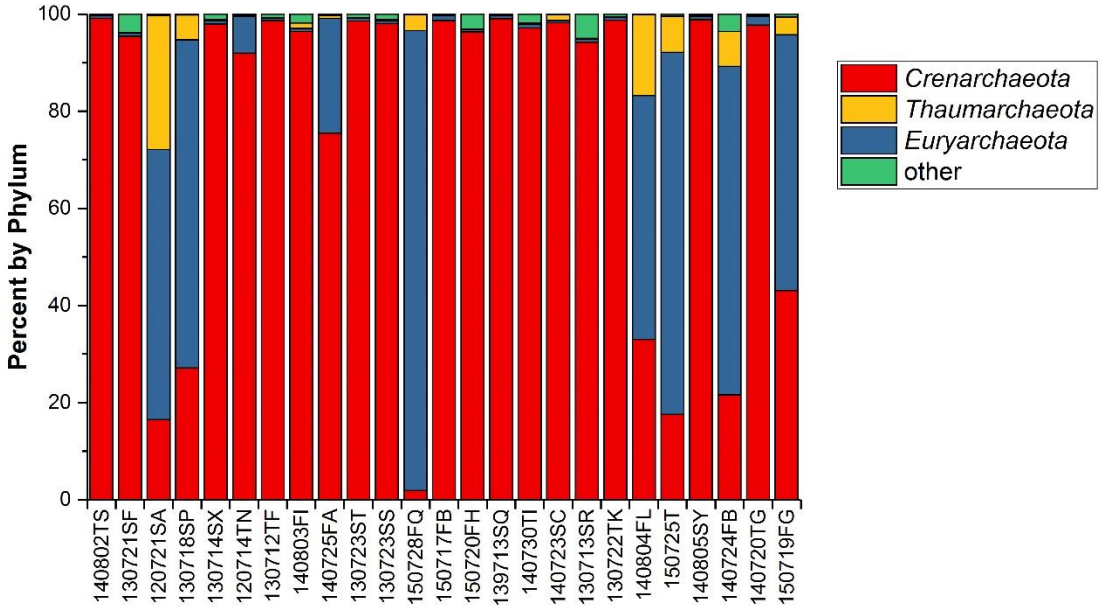

Fig 32 – Phyla of archaea present in experimental locations.

carbon. The natural abundance of both ferric minerals and organic carbon are often scarce in such systems. Regular exogenous input resulting from rain events may introduce these components to thermophilic iron reducing organisms. Thermophilic iron oxidation was detected at higher pH values than previously reported. Organisms in these locations face increased pressure from the abiotic reaction for available Fe(II). Dissolved oxygen appears to be limiting to these organisms at concentrations < 8μM. Experiments with isolates may clarify the precise role oxygen plays in determining the distribution of iron oxidation. Some community members responsible for iron oxidation or reduction were identified, but many other community members may be actively participating in iron oxidation, reduction, or both. Finally, complete redox cycling was identified in 7 locations. Continuing may confirm that redox cycling happens in most locations with large accumulations of ferric minerals. There remains much to be discovered about iron oxidation and reduction in hot spring ecosystems.

3.5Acknowledgements

The field work in support of this research took place over 4 field seasons in Yellowstone. A project of this magnitude is the result of many people's hard work over the years. Justin Pottenger was indispensable with his help running experiments over three field seasons. Alysia Cox helped with initial experiment deployment and development. Grayson Boyer, Alysia Cox, Randall Debes, Kris Fecteau, Jeff Havig, Alta Howells, and Kirt Robinson all contributed to discussions of experiments and field season planning. Dozens of undergraduates from Arizona State University accompanied the field research trip over the years, providing much of the geochemical sampling and field data. Prof Eric Boyd provided advice in the field and leant me his expertise on

molecular work. DNA extractions were performed at his laboratory at Montana State University. Kris Fecteau, Panjai Prapaipong, Kirt Robinson, Peter Canovas, Natasha Zolotov, Grayson Boyer, Randall “Vince” Debes, and many others helped analyze samples or process data. This research was supported in part by the National Science Foundation (EAR-1529963).

CHAPTER 4

THE CONSTRUCTION OF QUANTITATIVE HABITABILITY DIAGRAMS

4.1 Introduction

Two things must be true for microbes to gain chemical energy from the environment. First, there must be a source of energy. This requires the presence of compounds in differing oxidation states that are out of thermodynamic equilibrium with one another. Second, there must be mechanistic difficulties that are keeping those compounds from reacting, which means that the chemical energy cannot dissipate on its own. Using this energetic reference frame, geochemical habitability requires the combined presence of energy sources and kinetic barriers.

These barriers arise from physical-chemical phenomena, which implies that they may be mapped for individual reactions in geochemical space. The interplay of thermodynamic energy supplies and kinetic barriers for chemical reactions is illustrated schematically using just two variables, temperature and pH, in figure 33. Any other relevant geochemical variables can be used to construct complementary diagrams for examples that are inherently multidimensional. In each plot the red line indicates the equilibrium thermodynamic boundary, corresponding to the combination of pH and temperature where the overall Gibbs energy (or the chemical affinity, see below) of the reaction equals zero. Energy is available at the pH values and temperatures that plot on one side of this limit. The stippled pattern that indicates conditions where life can gain support from each reaction begins at this line and extends to the blue line, which indicates the pH and temperature combinations where the abiotic rate of the reaction is so rapid that it will preclude the biological exploitation of the reaction for energy. The

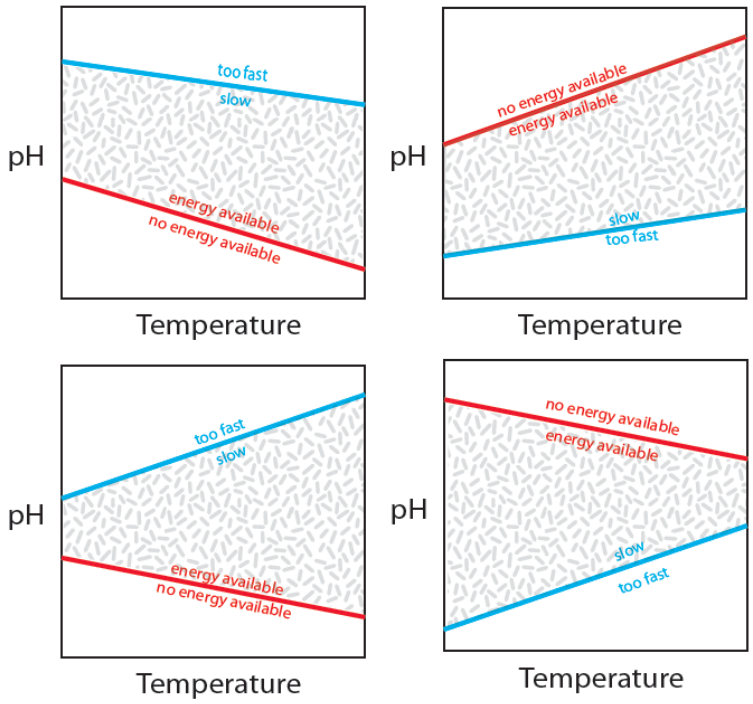

Fig 33. Schematic habitability diagrams depicting some possible combinations of thermodynamic (red) and kinetic (blue) boundaries that combine to determine regions of habitability. Each plot refers to a different hypothetical coupled oxidation-reduction reaction used by microbes as a source of energy. The stippled areas are habitable, and bounded on one side by a lack of energy and on the other by abiotic rates that are too rapid. Quantitative diagrams for individual chemical reactions will include temperature-dependent kinetic relations, complications owing to reactant availability, and constraints imposed by maintenance energy requirements.

combination of thermodynamic favorability and slow abiotic rates, involving all relevant variables, determines the ultimate boundaries of habitability for each reaction.

In the hypothetical examples shown in Figure 33 several combinations of energy and kinetic boundaries are illustrated, and each would apply to a different reaction. In each case, the support of life becomes impossible in certain pH/temperature combinations owing to thermodynamic limits or kinetic barriers. Conceptually, environments at the same temperature but varying in pH could differ radically in their ability to support certain overall metabolisms. Likewise, the same pH can have conducive or detrimental consequences at different temperatures. There are doubtlessly other possible topologies, and the straight lines should be taken to be idealized versions of curves that real diagrams of this type possess. In reality microbes would not be able to grow all the way to the thermodynamic limit of zero chemical affinity as there would be some necessary maintenance energy required simply to stay alive. Despite these caveats, these schematic habitability diagrams serve to illustrate that combinations of thermodynamic and kinetic properties of each reaction determine the geochemical conditions where that reaction can support microbial growth.

Iron oxidation by microbes – The dissimilatory oxidation of ferrous iron by microorganisms as a source of metabolic energy is found in diverse environments across the globe. Iron oxidizers have been found in cold neutral springs (Emerson and Moyer., 1997), hot springs (Inskeep et al., 2004), acid mine drainage (Colmer et al., 1950), at ocean vents (Emerson and Moyer, 2002), and in the arctic (Emerson et al 2015), among many other environments. The process is also widely distributed across the phylogenetic tree of life (Weber et al., 2006). Microbes typically couple ferrous iron to O_2 or NO_3^-, but

other inorganic oxidants have been documented as well. Most iron oxidizers are autotrophic, but some organisms grow mixotrophically (Johnson et al., 1992; Jones and Johnson, 2015) and even phototrophically (Widdel et al., 1993; Camacho et al., 2017). Iron oxidation reactions were chosen to construct habitability diagrams in this study owing to the wide geochemical distribution of iron oxidizing microbes.

Defining the reaction – The first step to make a habitability diagram is to define an explicitly stated single reaction. Environments that are not habitable for one reaction may be optimal for another reaction, even involving one or more of the same reactants or products. We have selected ferrous iron oxidation with oxygen forming ferrihydrite to construct the first diagram, as this is a process that can be inferred to occur in diverse environments (see below). The reaction can be written as:

$$Fe^{2+} + 0.25\ O_{2(aq)} + 1.5{+}x\ H_2O \rightarrow Fe(OOH) \bullet x\ H_2O + 2H^+ \qquad (1)$$

Note that FeOOH ● x H_2O is a nominal structure, in which x can range from 0-1 H_2O per Fe in the structure. Environmental samples of ferrihydrite contain significant inorganic sorption, substitutions and imperfections (*e.g.* Violante et al., 2003; Châtellier et al., 2004). Biogenic ferrihydrite also varies in composition from the abiotically derived mineral (Xu et al., 2011). Despite these sources of variability, recent measurements and thermodynamic data permit calculations for reactions involving ferrihydrite across the full range of H_2O content (Snow et al., 2012, Canovas, 2016).

We are focusing on continental aquatic environments that offer wide ranges of temperature and pH, as well as Fe(II) and dissolved oxygen concentrations. The reason for selecting the iron redox cycle is that both thermodynamic and kinetic limitations, akin to those shown in Fig 33, exist at conditions that can be found at the Earth's surface. All

reactions that support metabolism will have thermodynamic and kinetic boundaries in pH-temperature space, but some may occur at conditions well outside physiological possibilities.

There are many other reactions involving oxidation of aqueous Fe(II), including coupling to a host of other electron acceptors, like nitrate, AsO_4^{-3}, SO_4^{-2}, etc. Oxidation of Fe(II) with oxygen can also form other ferric products, such as goethite, lepidocrocite, hematite, and aqueous Fe(III) species. Separate habitability diagrams can be constructed for each of these reactions. In the case of ferrous oxidation with oxygen, the kinetic boundaries happen to be indistinguishable for each of these reactions, but the thermodynamic boundaries differ.

Thermodynamic Constraints

Calculations of Affinity - Given recent progress in theoretical geochemistry, evaluating the thermodynamic limits on diagrams of this type is no longer an obstacle (Amend & Shock, 2001; Dick, 2008; Shock et al., 2010). It is currently possible to calculate standard state thermodynamic properties for hundreds of minerals, gases, organic compounds, and organic and inorganic aqueous solutes over the range of temperatures and pressures where life is known to exist (recent contributions include: Dick et al., 2006; LaRowe & Helgeson, 2006a; 2006b; 2007; Shock, 2009; LaRowe and Dick, 2012; Canovas and Shock, 2016). With these thermodynamic data, it is possible to calculate the energy availability from thousands of coupled oxidation-reduction reactions using data from natural systems or experiments.

One approach to evaluating energy availability is to assess the chemical affinity (A_r) for a given reaction, which is evaluated from

$$A = 2.303RT \log\left(\frac{K_r}{Q_r}\right) \quad (2)$$

where R stands for the gas constant, T for temperature (in Kelvin), K_r for the equilibrium constant, which can be calculated from the standard Gibbs energy of the reaction, and Q_r for the activity product, given by

$$Q_r = \sum_i a_i^{\nu_{i,r}} \quad (3)$$

where a_i stands for activity of the ith chemical species in the reaction, and $\mathbf{v}_{i,r}$ designates the stoichiometric coefficient of the ith species in the reaction (positive for products and negative for reactants). Positive values of affinity correspond to conditions where energy would be released as the reaction proceeds.

In the case of oxidation of Fe^{+2} to yield ferrihydrite given by reaction (1), calculating the chemical affinity requires measurements of pH and concentrations of Fe^{+2} and dissolved O_2, as well as major ion concentrations that permit ionic strength determinations and allow evaluation of activities from concentrations. Concentrations of ferrous iron vs. pH, and dissolved oxygen vs. temperature are shown in Fig 34 from several environmental locations reported in the literature (Table 13) or measured in our research (chapters 2 and 3). These values permit Q_r to be evaluated, which for reaction (1) is expressed as:

$$Q_r = (a\mathrm{H}^+)^2 \times (a\mathrm{Fe}^{+2})^{-1} \times (a\mathrm{O}_2)^{-1/4} \quad , \quad (4)$$

The linear regression line in the figure leads to the prediction that the affinity will become negative at very low pH (negative values, in fact). At these conditions, this reaction can no longer be a source of metabolic energy. are plotted against pH using data

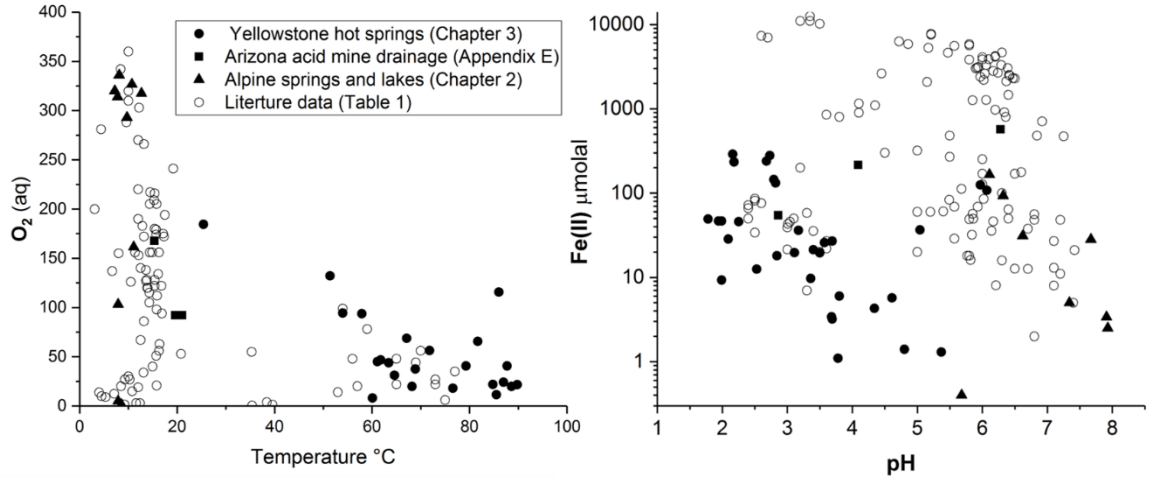

Figure 34 – Concentrations of ferrous iron vs pH and dissolved oxygen vs temperature from diverse aquatic, continental environments. These data are used, together with major ion concentrations, to evaluate activity products that can be combined with equilibrium constants to calculate chemical affinities and therefore thermodynamic boundaries on habitability diagrams.

from Yellowstone hot springs (Chapter 3) and cold springs in the Swiss Alps (Chapter 2).

Determining the boundary – To determine the boundary for our specified reaction we must find conditions where A = 0, which means $K_r = Q_r$. Since we would like to make the first diagram in pH / T space, we need to choose values for the other variables that contribute to Q_r. Ferrous iron was set to 20 μmolal, while dissolved oxygen was set to 40 μmolal. These concentrations typically support iron oxidation but are on the low side, as demonstrated by comparison with data shown in Fig 34. Altering the concentrations of Fe^{+2} and O_2(aq) across the entire ranges shown in Fig 34 varies the affinity by ~10 kJ $(mol)^{-1}$ at constant pH and temperature, as shown in Fig 35. Using these selected values allows temperature contours of affinity to be plotted against pH, and extrapolated to A=0, allowing the thermodynamic boundary to be quantified.

The resulting thermodynamic boundary for reaction (1) is depicted in figure 36. Analogous boundaries for other reactions in which ferrous iron is oxidized are shown in the Appendix. The pH at which the reaction yields no energy is slightly around pH 0, as anticipated from Fig 35. Also included in this figure are contours of affinity, calculated in a manner consistent with the A=0 line, at 10 kJ mol^{-1} increments up to 40 kJ mol^{-1}. As mentioned above, there are maintenance energy requirements that prevent organisms from growing down to A=0. Morita (1997) defined maintenance energy as "the energy required for osmotic regulation, maintenance of intracellular pH, futile cycles, turnover of macromolecules, motility, and energy dissipation by proton leak and ATP hydrolysis, exclusive of biomass production." Observations of iron oxidation in natural systems permit an estimate of the true minimum energy required to support an iron-oxidizing population (see below).

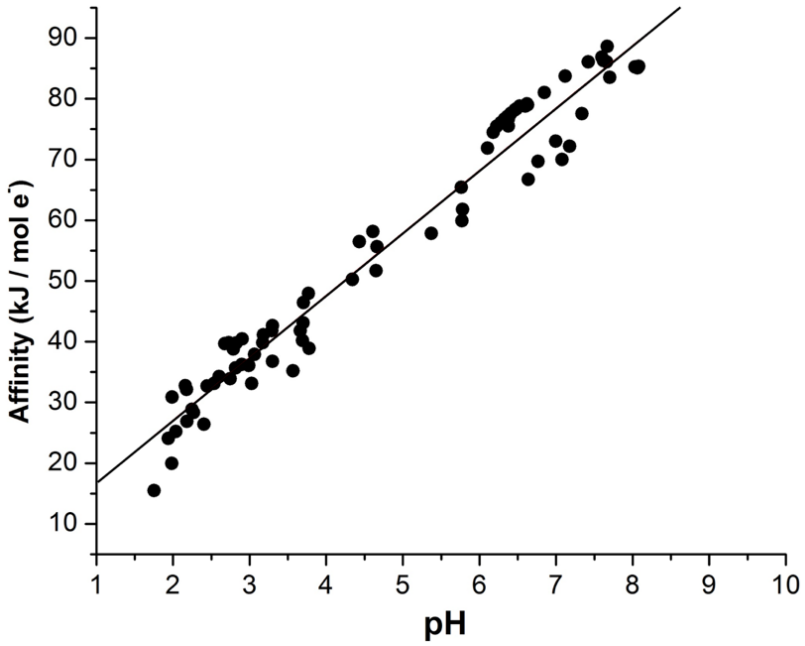

Figure 35 – Chemical affinity for the reaction (1) plotted against pH. Symbols indicate values calculated from the compositional data in Chapters 2 and 3 shown in Fig 33, together with equilibrium constants for the reaction at the temperature of each sample. The line reflects a least squares fit with a slope of 9.8 (kJ (mol e^- pH)$^{-1}$) and an intercept of 7.534 (kJ (mol e^-)$^{-1}$). Despite the range in temperature of more that 80°C, the points vary from the line by ±6 kJ mol^{-1}. This indicates the large influence that pH has on the energy yield for this reaction.

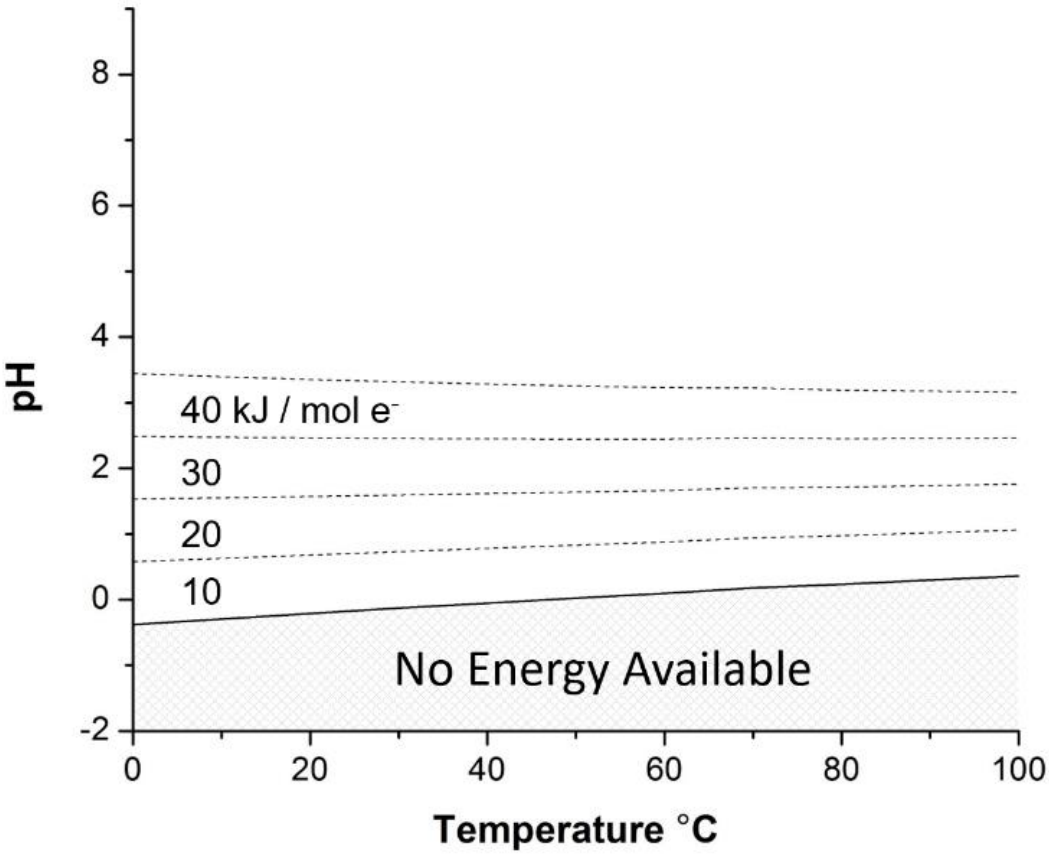

Figure 36 – Thermodynamic boundary for reactions (1) as a function of pH and temperature. The solid line represents affinity = 0, while the dashed lines are contours of affinity in 10 kJ (mol e^-)$^{-1}$ increments. Low affinities from natural environments that support iron oxidation may provide quantitative constraints on maintenance energy.

Kinetic Constraints

Defining the boundary - The kinetic boundary for habitability is dictated by the abiotic rate, consistent with one of the principles of geobiochemistry that "things that burst into flame are not good to eat" (Shock and Boyd, 2015). The fundamental determinant of the kinetic boundary is the lack of bioavailable energy resulting from rapid abiotic depletion of substrate. In this study we use field observations to draw empirical kinetic boundaries. Theoretical expressions for kinetic boundaries of habitable conditions are complicated by fluxes of substrates, differing physiologies across environmental ranges where iron oxidation can support microbial metabolism, salinity variations, the presence and abundances of complex-formating organic compounds, and other subtleties of natural systems. Kinetic boundaries based on laboratory experiments with isolates will be closely related, but not necessarily identical, to boundaries determined from observations of natural systems as used here.

Competition for available substrate by abiotic iron oxidation is widely cited as a difficulty for neutrophilic iron oxidizers. Occasionally the difference between the biotic and abiotic rate is quantified (*e.g.*, Neubauer et al., 2002). The actual geochemical conditions that completely exclude biology from taking advantage of iron oxidation are largely unexplored. Seto (2014) attempted to determine the habitability (defined as "invasibility") of iron oxidation close to the kinetic fringe by modeling the bioavailable energy. Seto's results link the rapid abiotic rate to a lack of bioavailable energy across a wide range of pH, Fe(II) and oxygen concentrations, which provides some clues to position of the boundary.

Abiotic Rates –

In contrast to the thermodynamic limits, which are relatively easily evaluated from analytical data, kinetic boundaries require experiments and observations from natural systems and in the lab. With notable exceptions (pyrite and manganese oxidation are examples) the rates of many abiotic oxidation-reduction processes are seldom measured in lab experiments at conditions where life occurs. In some cases, the abiotic rates are so slow that observing any reaction progress is a challenge (*e.g.*, methane oxidation). In other cases, there seems to have been little interest in establishing abiotic rates.

One exception is Fe^{2+} oxidation at low-temperature conditions, and many years of research have led to rates and mechanisms of abiotic iron oxidation being well described (summarized in chapter 2). As discussed by Stumm and Lee (1961), and Singer and Stumm (1970a), the abiotic rate of iron oxidation is dictated by pH. The rate expression they determined is

$$-\frac{d[\mathrm{Fe}^{2+}]}{dt} = k[\mathrm{Fe}^{2+}][\mathrm{OH}^{-}]^{2}[\mathrm{O}_{2}] \quad , \qquad (5)$$

where brackets refer to concentration. When oxygen is not limiting, and is held constant, the rate expression can be simplified to the pseudo-first-order version:

$$-\frac{d\{Fe^{2+}\}}{dt} = k_{ox}[Fe^{2+}] \quad . \qquad (6)$$

Measurements of k_{ox} at 25°C reported by Singer and Stumm (1970a) and Millero, et al., (1987), along with higher temperature measurements (chapter 3), are depicted in Fig 37.Acidic conditions with pH < 4, abiotic rate constants are slow and independent of pH

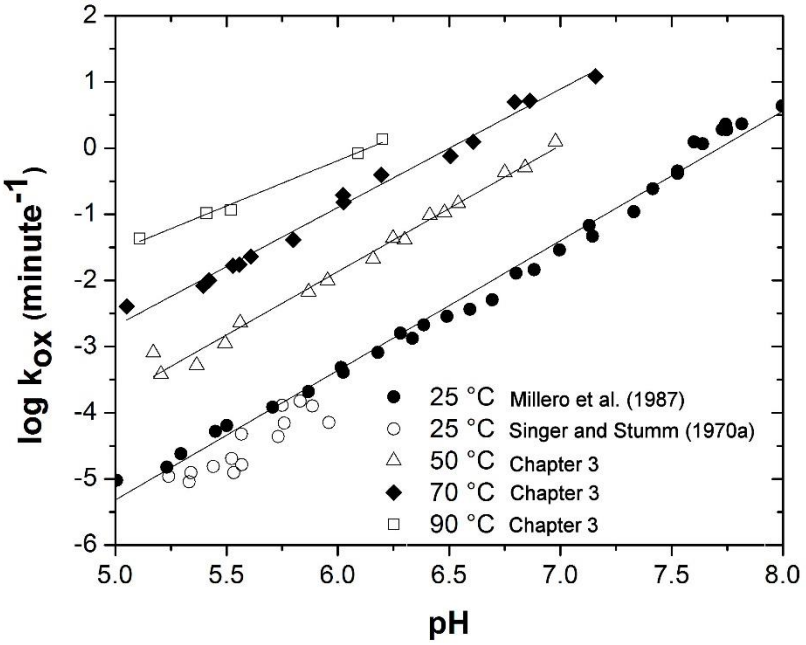

Figure 37 - Pseudo first order rate constants for Fe(II) oxidation from 25 to 90°C, as determined by laboratory experiments in dilute solution. While the higher temperature contours do not cover enough of the pH range to show the same sigmoidal shape, the parallel nature of the slopes in the pH dependent region imply the slopes will be similar. The temperature contours show that for any given value of rate constant there is a ~2 pH unit decrease from 25°C to 90°C. This suggests that the kinetic boundary will be at increasingly lower pH values at high temperatures.

(Singer and Stumm, 1970a; Lowson, 1984). At pH > 4, rate constants increase by about an order of magnitude for every pH unit increase. One consequence of this dramatic increase in rate constant is that the abiotic reaction can be so rapid that the biotic rate cannot compete as pH increases. The underlying mechanism involves the chemical speciation of Fe^{2+}, which becomes dominated by aqueous hydroxide complexes at higher pH values (Millero, 1985). These complexes react orders of magnitude more quickly than does Fe^{2+} with dissolved oxygen, and their increasing abundance with increasing pH explains the observed rate increases (Millero et al., 1987). Our experimental results shown in Fig 37 (described in chapter 3, results tabulated in appendix E) demonstrate that rates increase by about an order of magnitude between 25 and 50°C, and about another order of magnitude between 50 and 70°C, and slightly less between 70 and 90°C at constant pH. These changes of rate with temperature and pH are similar, but not identical, to estimates based on activation energies (Stumm and Morgan, 1996). If observing a constant rate while temperature is increased, it can be seen in Fig 37 that the pH that produces that rate decreases. This implies that the maximum pH where biology can compete will decrease with temperature.

The previously described data were derived from laboratory experiments performed in dilute solution. In nature many factors can influence the rate of iron oxidation, including inorganic solutes, organic compounds, and catalytic mineral surfaces. The rapid rates at high pH can be slowed slightly at higher ionic strength as quantified in experiments on seawater and electrolyte solutions (Millero et al., 1989; Trapp and Millero, 2007). Because our research takes place in fresh water (I<~0.3M), and because ionic strength has a predictable effect on the abiotic oxidation rate allowing

the change in habitability to be predicted, the effects of ionic strength on habitability can be calculated for seawater and brines. While most inorganic solutes slow the rate of oxidation, the presence of dissolved inorganic carbon (HCO_3^-, CO_3^{-2}) causes an increase in the rate (Millero et al., 1989). This results from the formation of ferrous bicarbonate and carbonate species, which have orders of magnitude faster oxidation rates than oxidation of Fe^{2+} ions (King, 1998), analogous to the ferrous hydroxide aqueous species mentioned above. Minerals can also alter the rate of reaction. As an example, the presence of ferric minerals leads to an increase in the oxidation rate owing to ferrous ion sorption lowering the activation energy (Tamura et al., 1976, 1980; Stumm and Sulzberger 1991; Park and Dempsey, 2005). This process of heterogeneous oxidation has a stronger effect at neutral pH than at acidic conditions (Jones et al., 2014). Observations about links among oxidation rates and ferrous iron sorption to minerals were extended to microbial products of iron oxidation by Rentz *et al.* (2007), and Ferris *et al.* (2016). The interaction of organic compounds with ferrous iron may also change the abiotic rate. In general, rates of reactions in the presence of various organic compounds are slower (Thies & Singer, 1974; Krishnamurti & Huang, 1991; Liang et al., 1991; Santana-Casiano et al., 2000), but increasing and negligible effects have also been recorded. As an example, phthalate slows iron oxidation while salicylate increases the rate (Santana-Casiano et al., 2004). Given the inherent complexity of abiotic rates in natural systems, abiotic Fe(II) oxidation rates in natural systems need to be measured for precise results.

Flux - The flux of reactants is a necessary consideration when determining if an abiotic rate is too fast for biology to compete. A solute may be delivered at such a high rate that even rapid abiotic dissipation does not result in complete dissipation. This is

especially the case in flowing systems, where bioavailability and habitability can decrease with distance from a point source. As an example, if a point source has a steady initial concentration 100 PPM, a delivery rate of 1 liter per minute, and a flow rate of 1 meter per minute, the first meter of outflow will likely always be habitable. Even if the abiotic dissipation half-life is 10 seconds, 1.56 PPM of solute is still available after 1 minute in that parcel of fluid. Bioavailability may not become limiting until some distance further down the outflow. It is for this reason that the kinetic boundary must be experimentally determined and constrained by solubility of the reactant. Flux is a minor consideration for iron oxidation reactions due to the solubility of Fe^{2+} at conditions where the abiotic rate is rapid. The solubility of Fe^{2+} in dilute solution at 25°C, pH 8, is around $10^{-3.5}$ molal, and is controlled by $Fe(OH)_2$ (s) (Morgan and Lahav, 2007). The solubility drops to 10^{-6} molal at the same conditions in bicarbonate medium as a result of siderite solubility (Singer and Stumm, 1970b). The maximum solubility of Fe(II) in dilute solutions at the pH values where abiotic rates are the fastest indicates that the flux will not significantly expand the pH and temperature range of habitability. When constructing habitability diagrams for other reactions, flux may be a important consideration if the solubility of reactants is high near the kinetic boundary.

Biotic and Abiotic Rates in the Field – Rates of biotic and abiotic iron oxidation have been measured in geochemically diverse natural systems ranging in temperature from 8 to 90°C and in pH from 1.8 to 9. These experimental treatments included *in situ* (unamended), maximum biotic (experimental), and abiotic rates. These experiments were performed in Yellowstone hot springs (chapter 3), acid mine drainage in southern Arizona (appendix B), and cold springs in the Swiss Alps (chapter 2). Each location

yielded an abiotic rate, while only some locations yielded a biotic rate. Results from locations that yielded a biotic rate are summarized in table 2, in which rates are presented as k_{ox} (equation 6), the pseudo-first-order rate constant. The rate constant, k_{ox}, allows normalization between differing starting concentrations of Fe^{2+}. In each case that a biotic rate constant is reported it is the faster of the measured experimental or unamend treatment. Also included in table 2 is the percent of oxidation attributable to biology, which is calculated by the difference between the abiotic rate constant and the faster of the experimental or *in situ* rate constant, divided by the biotic rate constant. A complementary suite of geochemical measurements was made at each location to permit elucidation of factors affecting rates. Selected data that affect the rate are also presented in the table. Literature reports of evidence for iron oxidation from the field are common. Rates measurements from these locations, however, remain sparse. Exceptions to this include measurements of iron oxidation rates in a neutrophilic springs and groundwater seeps (James and Ferris, 2004; Rentz et al., 2007, Ferris et al., 2016). These data are also included in table 2. Rates are reported as rate constants to permit comparison between our experiments and literature values.

Kinetic and geochemical data for locations where biological iron oxidation was not detected are summarized in table 3. These null results are necessary to determine the kinetic boundary. In some locations, the abiotic rate was too fast for biology to compete, while elsewhere other factors such as an apparent lack of dissolved oxygen (Chapter 3) produced null results. Pseudo-first-order rate constants for abiotic oxidation described by equation (6) as summarized in Table 2 are plotted in Fig 38. Rates that were too slow to detect during the experimental duration are labeled BDL (below detection limit). The

Table 14 – Rates of ferrous iron oxidation measured in microcosm experiments.

Site and ref	Sample ID	pH	T °C	Fe (II) µmolal	O_2 µmolal	Abiotic K_{ox} minutes^{-1}	Biotic K_{ox} minutes^{-1}	% Bio
Yellowstone hot springs	120721SA	2.25	64.6	45.7	31.3	0.0003 ± 0.00022	0.0027 ± 0.00048	88%
	130712TF	2.79	87.0	145.0	24.1	0.0045 ± 0.00114	0.0051 ± 0.00025	12%
Chapter 3	120714TN	2.82	67.1	132.1	68.8	0.0012 ± 0.00081	0.0074 ± 0.00082	84%
	130723SS	3.11	61.1	19.7	45.0	0.0037 ± 0.00033	0.0126 ± 0.00255	71%
	130723SV	3.69	68.9	26.9	ND	0.0057 ± 0.00122	0.0904 ± 0.04681	94%
	130722TK	3.78	86.0	1.1	115.6	0.0031 ± 0.00025	0.0102 ± 0.0023	70%
	140803FL	3.80	38.6	6.0		0.0004 ± 0.00052	0.021 ± 0.00159	98%
	140805SX	4.34	81.7	4.3	65.6	0.0005 ± 0.0002	0.0025 ± 0.00017	81%
	140730TI	3.68	85.8	3.4		0.0002 ± 0.00033	0.0124 ± 0.00373	98%
	140724TB	4.61	71.8	5.7	56.3	0.0004 ± 0.00007	0.0019 ± 0.00211	79%
	140730TG	5.04	77.0	36.5		0.001 ± 0.00003	0.0055 ± 0.0012	81%
	140724TD	4.80	61.8	1.4	46.9	0.0005 ± 0.00001	0.0039 ± 0.00204	88%
	150717FB	3.40	68.9	21.3	37.5	BDL	0.0097 ± 0.00017	100%
	150718FC	2.09	88.6	28.5	19.9	BDL	0.0013 ± 0.0008	100%
	130720TV	2.18	68.2	234.6	19.8	BDL	0.0113 ± 0.00093	100%
	130720TY	2.53	82.6	12.5	ND	BDL	0.0262 ± 0.00052	100%
	130718SP	2.68	57.9	239.9	93.8	BDL	0.0112 ± 0.0049	100%
	150728FQ	3.36	25.4	9.7	184.4	BDL	0.0009 ± 0.00016	100%
Arizona Acid Mine Drainage	130928B	4.09	15.3	215.8	167.8	0.0011 ± 0.00047	0.0134 ± 0.00042	92%
	130607F	2.86	21.0	54.6	92.2	0.0008 ± 0.0003	0.0041 ± 0.00056	81%
(Appendix B)	141122D	6.28	19.6	571.2	92.2	0.0053 ± 0.00125	0.0076 ± 0.00106	30%
Alpine springs and lakes	150906B	6.62	7.9	31.2	103.4	0.0072 ± 0.00057	0.016 ± 0.00079	55%
	150906C	6.11	8.6	166.4	1.4	0.0003 ± 0.00005	0.0014 ± 0.00017	79%
	150907F	6.32	11.1	93.2	161.6	0.0063 ± 0.00022	0.0156 ± 0.0021	60%
Chapter 2	150911T	7.34	7.9	5.0	5.0	0.0143 ± 0.0036	0.0336 ± 0.00723	58%
	150909K	5.68	9.7	0.4	293.1	0.0003 ± 0.00011	0.0027 ± 0.00046	90%
	150910O	6.98	7.2	BDL	320.0	0.0021 ± 0.00108	0.0101 ± 0.00056	80%
spring	A	NR	NR	50	6	0.056	0.947	94%
James and Ferris 2004	B	NR	NR	25	109	0.056	0.947	94%
Spring	DR Oct	6.6	21$	177	134^	0.062 ± 0.003	0.249 ± 0.042	75%
	DR Dec	6	21$	127	47^	0.058 ± 0.001	0.081 ± 0.009	28%
Rentz et al., (2007)	PWP Oct	7.1	21$	13	134^	0.016 ± 0.003	0.029 ± 0.004	45%
	PWP Dec	6.8	21$	48	47^	0.027 ± 0.001	0.072 ± 0.15	63%
Mine impacted runoff	Beaver	5.77	NR	18	160	0.0004 ± 0.001	0.036 ± 0.003	99%
	Ogilvie	6.17	NR	46	26	0.0004 ± 0.001	0.063 ± 0.003	99%
Ferris et al., 2016	Chalk A	5.93	NR	69	183	0.0004 ± 0.001	0.248 ± 0.008	100%
	Chalk B	5.93	NR	69	183	0.0004 ± 0.001	0.117 ± 0.007	100%

$Temperature values are the average of the reported range (20-22 °C). ^ Values are calculated from reported pO_2 averages during experiments using Henry's law constant at 20 °C. Standard deviations are ±19 µm for Dec and ± 90 µm for Oct.

Table 15 – Rates of abiotic oxidation in microcosm experiments.

Site	Sample ID	pH	T °C	Fe (II) µmolal	O_2 µmolal	Abiotic K_{ox} minutes^{-1}
Yellowstone hot springs	120723TM	1.78	82.2	49.2	ND	BDL
	120722SK	1.94	87.7	46.6	40.6	BDL
	130721SC	1.99	76.6	9.3	18.1	BDL
	120713SH	2.16	79.3	290.1	40.6	BDL
	130714SX	2.73	89.8	279.3	21.6	BDL
	140803FI	2.84	89.3	18.1		BDL
	130711SD	3.17	84.8	36.2	21.9	BDL
	140804FM	3.50	82.2	19.5		BDL
	130717SJ	1.99	66.3	46.6		0.0002 ± 0.00006
	130722TM	3.69	63.4	3.2	43.8	0.0011 ± 0.00013
	150720FH	3.57	85.5	25.8	11.5	0.0002 ± 0.00018
	130716SC	5.37	60.1	1.3	8.1	0.0311 ± 0.00705
	140731FG	5.97	51.4	30.4		0.1838 ± 0.03838
Alpine springs and lakes	150907G	7.91	10.7	3.4	326.9	1.3694 ± 0.03366
	150908J	7.67	12.7	28.3	317.5	0.7528 ± 0.03493
	150909M	9.04	8.1	BDL	336.0	3.3[#]
	150905A	7.93	7.8	2.5	313.8	3.9[#]
	130718SU	6.04	83.6	BDL	ND	0.3[#]
	140731FH	6.07	54.0	28.6		0.3[#]

[#]Corresponds to a minimum rate (see text)

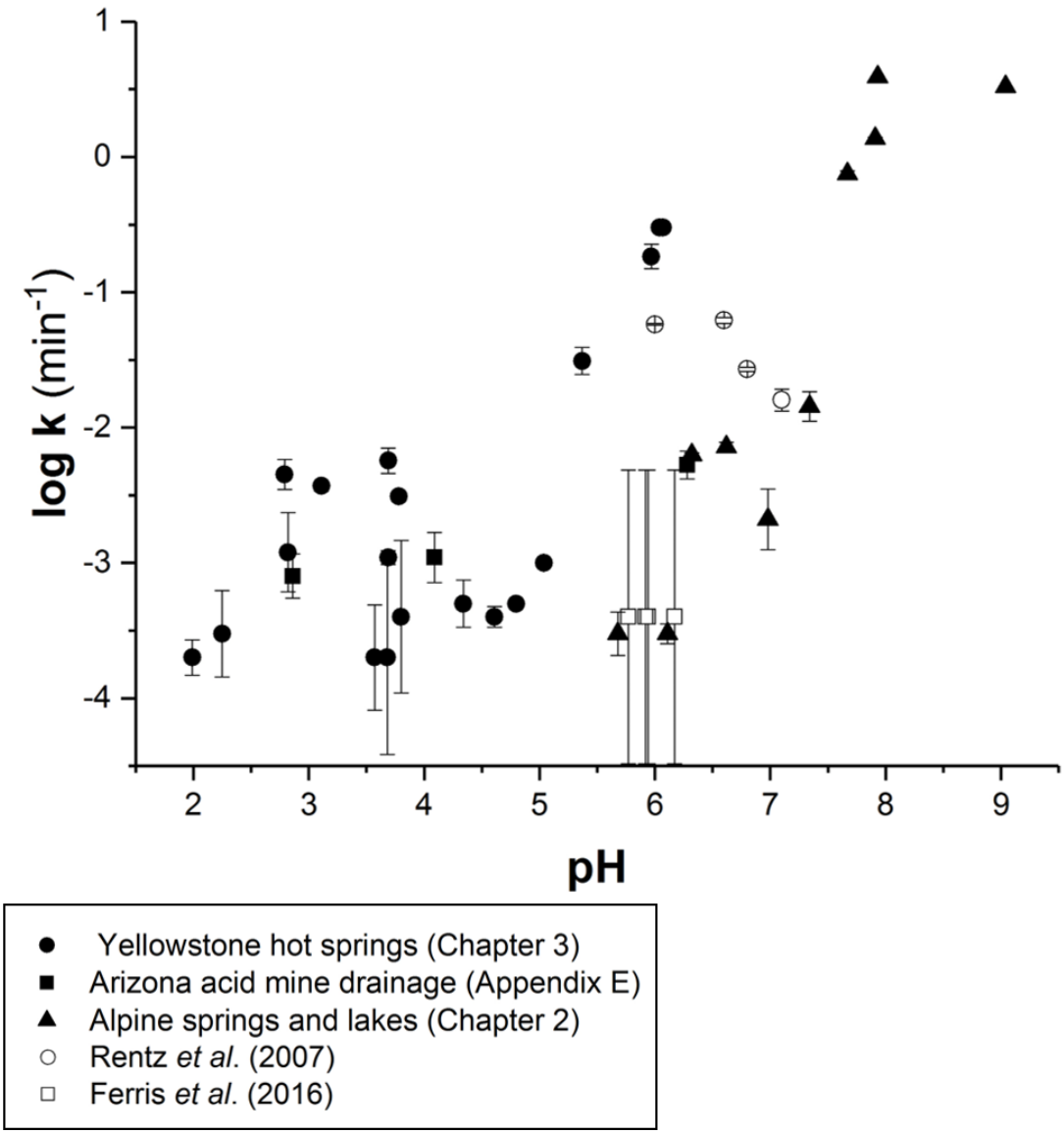

Figure 38 - Abiotic rate constants as determined from microcosm experiments in the field. The generally increasing trend with pH is anticipated based on laboratory abiotic experiments (figure 5). Measured values are depicted as circles, with error bars representing relative error of standard deviations. Rates from literature values reported in table 2 are depicted as squares, with relative error calculated from reported errors. Locations where the abiotic was rate was too slow to be determined are labelled BDL (Below Detection Limit), and are plotted with their corresponding pH as red triangles along the bottom axis. Detection limits range from a log k of -3.8 to -4.5, depending on experimental duration and replicate error. The temperature ranges from 8 °C to 90 °C. Corresponding geochemical data for each site can be found in tables 1 and 2.

actual detection limits vary slightly among experiments as a result of starting concentrations of Fe(II) and experimental duration. Acidic systems were the most likely to have slow oxidation rates. The empty circles show measurements of a minimum rate, which occurs when the microcosm is below detection after two measurements. A rate constant can still be calculated, but only the maximum time it took to be fully depleted of Fe(II) is known. This only occurred at the fastest oxidizing systems close to the kinetic boundary. Comparing field abiotic rates (Fig 38) with laboratory derived abiotic rate constants (Fig 37), reveals how the complications of natural systems necessitate *in situ* measurements.

Biological oxidation rate constants, calculated by subtracting the abiotic rates constants from biotic rate constants listed in table 2, are shown in Fig 39. Despite large variations in temperature and composition, rates vary by only ~2 orders of magnitude between all systems where biological oxidation occurs. The fastest rates are found at higher pH values close to the kinetic boundary, perhaps in response to the rapid abiotic rate. The slowest rate found to support a community of iron oxidizers is 0.0006 ± 0.00025 min^{-1}, in an acidic hot spring. This location has intermittent water flow, perhaps explaining the sluggish rate. In any case, the relatively narrow range of biological iron oxidation rates across all locations implies that the orders-of-magnitude faster abiotic rates found at the most extreme locations can dictate habitability at those conditions.

Iron Oxidation Habitability Diagram – Combining thermodynamic data from Fig 36 with results from rate experiments shown in Figs 38 and 39 permit construction of habitability diagrams for reaction (1) to be drawn. As an example, the extent of habitable pH and temperature ranges are shown in Fig 40. The habitable zone is bounded by the

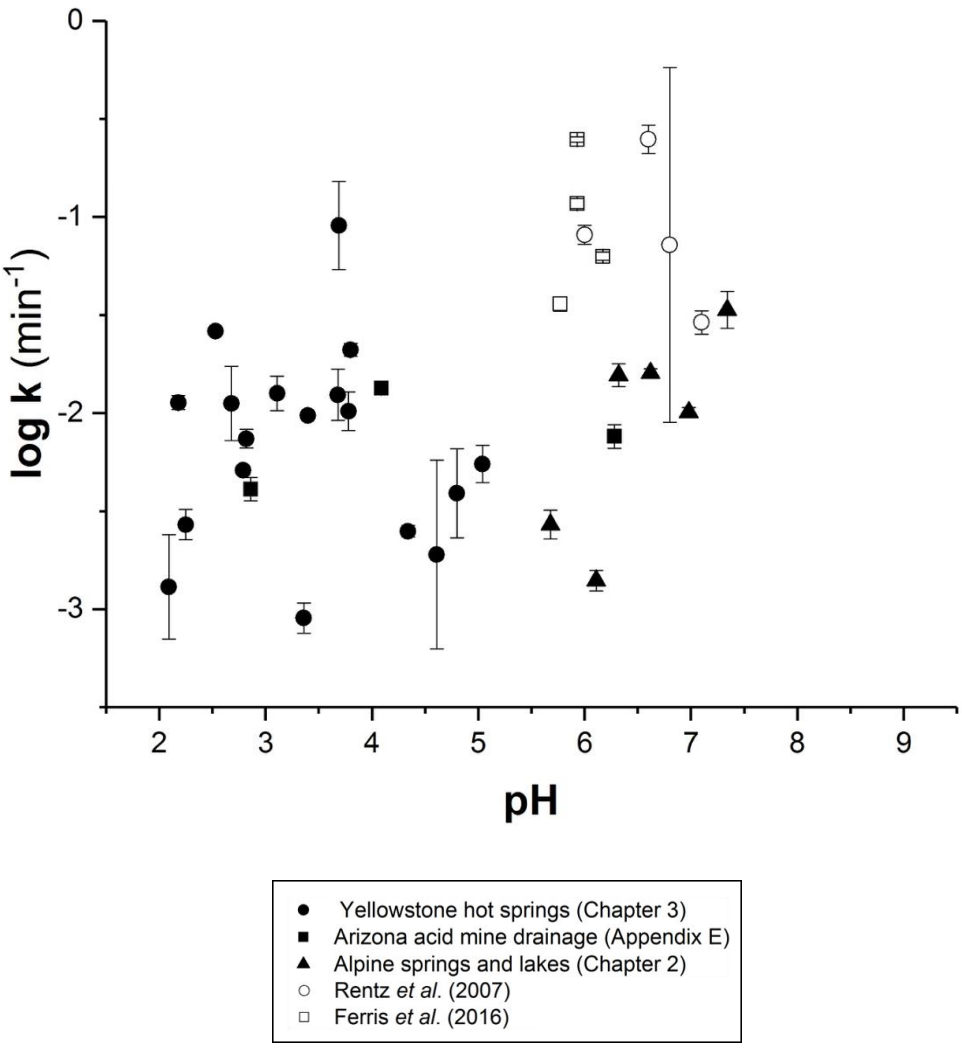

Figure 39 – Biological iron oxidation rate constants. Rate constants calculated by subtracting the azide killed abiotic rates from the biological rates in table 1. Note the log scale. Despite large geochemical variability, rate constants of biological iron oxidation vary by only ~2 orders of magnitude. The faster rates at high pH could be indicative of increased oxidation rates to compete with abiotic oxidation. Error bars represent standard deviation of 3 replicates for both biotic and abiotic rates.

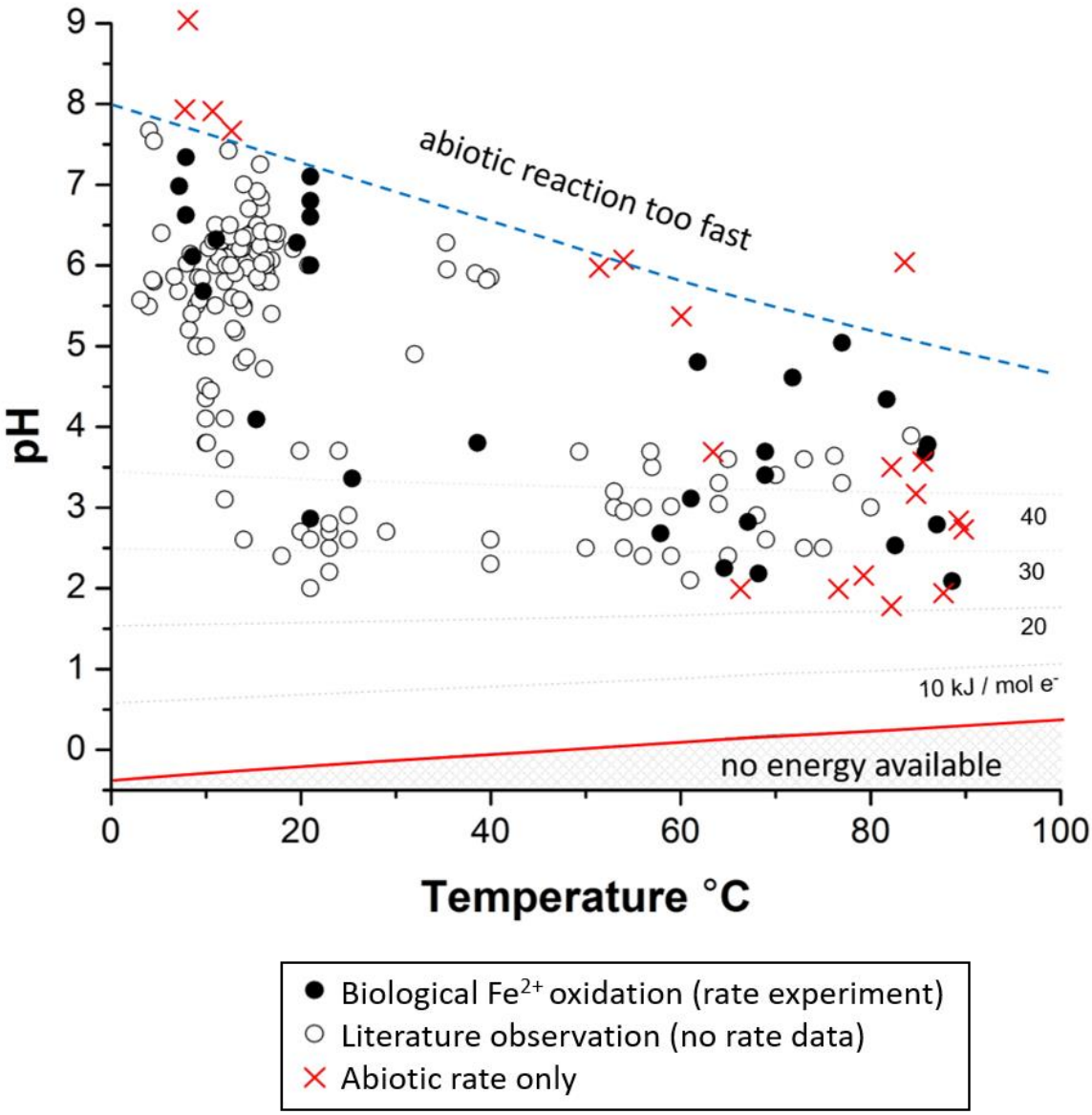

Figure 40 – Temperature-pH iron oxidation **Habitability Map** showing a kinetic (blue) boundary determined from our observations and experiments in natural systems and reports from the literature, and a thermodynamic (red) boundary based on the chemical affinity for the reaction shown in figure 4a. Also shown are affinity contours (in kJ per mole of electrons transferred) that help estimate minimum energies.

calculated thermodynamic boundary at low pH values, and the kinetic boundary determined from field measurements at higher pH values. The diagram is populated with locations where biological iron oxidation was demonstrated with rate experiments (black circles), literature observations of apparent biological iron oxidation without rate data (empty circles), and locations where only abiotic rates were measurable (red x). These null results in the habitable field underscore the multivariate effects of other relevant variables discussed below.

The thermodynamic boundary, shown by the red line, is the same as the A = 0 line from Fig 36. Neither our experiments, nor field observations from the literature indicate biotic oxidation to ferrihydrite below the 20 kJ (mol e^-)$^{-1}$ contour, which we interpret to indicate the maintenance energy across diverse natural systems, although this conclusion needs to be tested against abiotic oxidation to Fe^{3+} at lower pH values (*i.e.*, Drushel et al., 2004).

The kinetic boundary, shown as the blue line, is drawn empirically from the results of our rate experiments. The conditions where abiotic iron oxidation becomes too rapid for biology to profitably compete appear to occur at progressively lower pH values as temperature increases. This type of trend was anticipated based on increasing rates with increasing temperature at constant pH, as shown in Fig 37. Note that the kinetic boundary is drawn to include all of the biotic rate results on the habitable side of the curve, and that results showing only abiotic oxidation fall on either side. The lower frequency of data from warm (~30-55 °C) mildly acid (pH 4-5) systems results from an apparent rarity of such environments on Earth's surface. Our data over these ranges are from outflows of much hotter springs.

Literature observations - Our selection criteria for including data were to include only selected reactions and conditions. Only fresh water aquatic systems were considered. Aqueous Fe^{2+} has to be the electron donor and oxygen the electron acceptor. Reactions involving photoferrotrophy, anaerobic oxidation, or oxidation of other inorganic ions were excluded. In addition, we required some evidence of ferric mineral products, which means that oxidation to aqueous Fe (III) species was excluded. Reports of iron staining was considered adequate if other circumstances in support of iron oxidation were strong, but mineral identification or other characterization of Fe composition was strongly preferred. We found that direct evidence of iron metabolism, such as *in situ* or microcosm rate experiments, or RNA or protein data from obligate iron oxidizers, was extremely limited. We know from practical experience that these data can be difficult to obtain, but they provide the best direct evidence of iron oxidation happening in the environment. Using our selection criteria, the studies listed in table 1 report adequate information that demonstrates biological iron oxidation forming ferric minerals with high confidence. The most convincing circumstantial evidence involves isolation or enrichment of iron oxidizing organisms, combined with complete geochemical characterization of the system from which they were obtained. Other high quality evidence includes colonization of sterile substrates, and microscopy of mineral products showing distinct biogenic structures of iron minerals. The lowest standard of evidence included in this list is phylogenetic data of 16s rRNA sequencing with high counts of purported obligate iron oxidizers combined with some geochemical characterization or other circumstantial evidence. Description of new species capable of oxidizing iron were accepted if the authors reported a pH and temperature of the natural

system from which the organisms were isolated. Growth optima from such studies were not accepted values because laboratory growth conditions in synthetic media are not indicative of the conditions in the natural system. Surprisingly, few such papers reported geochemical composition of the natural system from which the organism was isolated. A handful of papers report rates measured in the field. These data are included in table 2.

Many papers were evaluated to determine the distribution of iron oxidation in natural systems. Only around thirty publications provide sufficient evidence and geochemical data to include in Fig 40 (open circles), and are listed with corresponding geochemical data in table 1. The data were pulled from papers with wide ranging topics, often not specifically focused on reporting the presence of biological iron oxidation or describing the habitats. Therefore, this list should not be considered comprehensive for all reported iron oxidation because of the wide variety of focuses, but is a relatively complete survey of environments where iron oxidation occurs. As noted by Ferris et al. (2016), interest in iron oxidation spans a wide range of topics "from early evolution of life to modern biogeochemical cycles, solid phase partitioning of contaminants, groundwater bioremediation, biofouling and corrosion." As a result, not every paper had a complete set of requisite geochemical data or sufficient evidence of biological oxidation.

Other relevant variables

Many locations where biological iron oxidation was not detected sit conspicuously in the habitable zone in Fig 40. In these systems is it not pH or temperature that prevents biological oxidation. Possible explanations include limited oxygen, competition from faster metabolizing organisms, unsuitable carbon sources or

nitrogen sources, or the presence of toxic substances. Reference to reaction (1) shows that variations in Fe^{+2} and O_2(aq) concentrations, in addition to pH and temperature, may be capable of influencing thermodynamic and kinetic constraints on habitability. The minimum amount of Fe^{2+} required to supply energy is much lower than concentrations where this metabolism is found. In contrast, many acidic hot springs release copious gas, and the flux may be sufficient to exclude atmospheric oxygen from the water, which may raise a thermodynamic problem. Geochemical sampling completed at the same time experiments were performed, along with additional sampling of related iron oxidizing systems, shows evidence of specific oxygen requirements for iron oxidation metabolism.

To determine concentrations of oxygen that are required for microbial iron oxidation, we turn to natural systems that display gradients of oxygen down outflow channels. Evidence of microbial iron oxidation can be found in hot springs throughout Yellowstone National Park, where the process is often visibly apparent as iron mats, which are communities of iron bacteria growing in macrostructures. However, at the sources of springs that support downstream iron oxidation have dissolved oxygen concentrations that are typically below the detection limit (<0.16 μM). As a result, these hot spring source regions can be devoid of iron staining. As water flows away from the source and atmospheric oxygen can infiltrate, iron oxyhydroxide staining appears abruptly permitting tests of hypotheses about oxygen minimum values. The geochemistry and development of iron mats in acidic (pH < 3.8) hot springs were initially described by Macur (2004) and Inskeep (2004), who showed a succession of inorganic substrate utilization by microbes in these systems. Our observations show that sharp boundary can be observed between host sediments and sediments rich in biogenic ferric mineral

deposits. Measurements of numerous solutes, including oxygen, sulfide, and iron, were made on outflow channels of springs containing apparent iron metabolism (See Ch 3). These data, along with literature observations (from Table 1), are shown in figure 41. It should be noted that while source compositions of these particular systems are relatively stable year to year, small variations in solute concentration and temperature may be observed across the boundary. Red X's indicate ferric mineral products were not observed. Literature measurements of oxygen concentrations (from tables 1 and 3) supporting microbial iron oxidation are also shown on the figure as open circles. Since there is abundant energy from the oxidation reaction even with dissolved oxygen as low as 1 µM, the observations can be interpreted as a physiological minimum value. Only our high temperature measurements have null results to constrain the physiological minimum. Cold natural systems have a much lower apparent physiological requirement of oxygen. Lab experiments by Druschel et al. (2008) corroborate field observations. Iron oxidizing bacteria growing at 20°C show significant declines in the biological rate below 16µm, and a biological/abiological rate maximum at the same value. Limited growth was reported down to 9 µm. Recent investigations into abiotic kinetics at low concentrations of O_2 (<0.01µM) show that reaction half-lives are still as fast as 200 minutes at pH 8 (Kanzaki and Murakami, 2013). This implies that this kinetic boundary would also apply to organisms scraping by below the amount of oxygen required to support a community.

A habitability diagram involving oxygen

As mentioned above, habitability is inherently multivariate. Given these investigations of iron oxidation at varying concentrations of oxygen we can draw provisional habitability diagrams for reaction (1) involving oxygen, pH and temperature.

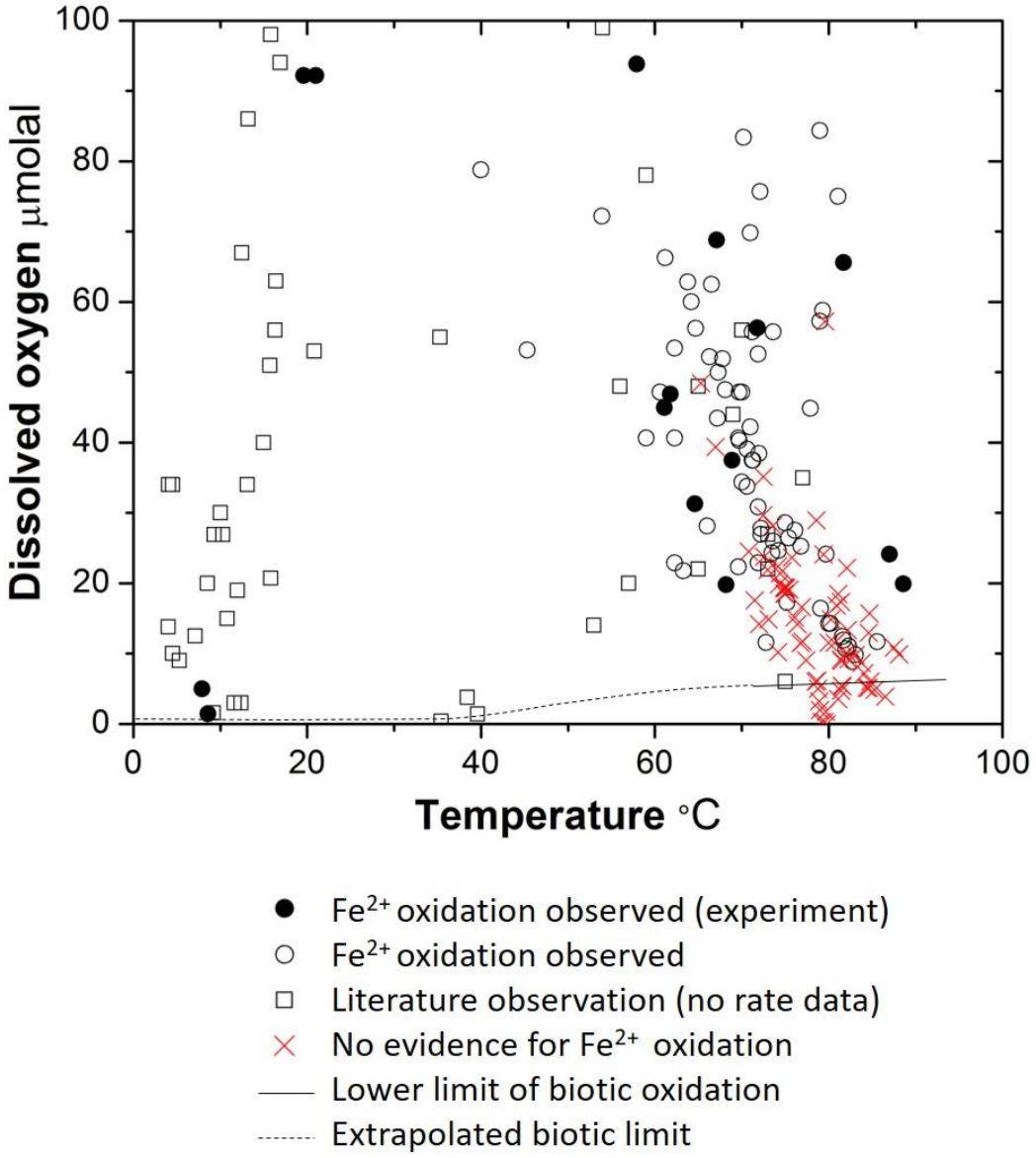

Figure 41 – Concentrations of dissolved oxygen that support microbial iron oxidation. The empty circles represent our observations of apparent biogenic iron oxides in springs with pH < 3.6 (Chapter 3). The black circles show pH and temperature of systems supported by our rate measurements (table 1). The red x's indicate locations in hot spring outflow channels upstream iron mat formation. At high temperatures, iron oxidation was not observed below 8 μm oxygen, while it was detected down to 2.5 μm in cold systems. The curve represents the lowest value of oxygen observed to support microbial iron oxidation. It is well constrained at higher temperatures, but is unconstrained at lower temperatures.

At all pH values there is a minimum amount of dissolved oxygen needed to supply energy, but this is scarcely relevant except in extremely acidic conditions (red curve in Fig 42). The temperature-dependent apparent oxygen threshold (from figure 41, black curve fig 42) falls above the no-energy curve. The kinetic boundary (in blue) is depicted as contours of temperature on the pH / O_2 habitability diagram (Fig 42, Left). The positions of the temperature contours where the curves are asymptotic are inferred from Fig 40. At extremely low concentrations of O_2, the reactant becomes limiting and allows the pH of the kinetic boundary to increase at constant T (Liang et al., 1993; Kanzaki and Murakami, 2013). Similarly, the kinetic boundary is depicted as contours of pH on the T / O_2 habitability diagram (Fig 42 right). The position of the contours is inferred from Fig 40. The trajectory is suggested by the relationship between pH and rate constants at varying temperature in Fig 37, although the trajectory is provisional. The field is populated by results from tables 1, 2 and 3, as well as observations in Fig 41. These secondary habitability diagrams permit rapid determination of habitability for reaction (1) with measurements of only oxygen, pH, and T.

Concluding Remarks

Limitations - Measurements reported here were made on bulk water and sediments, and may not be reflective of the microenvironments inhabited by microorganisms. It should be noted that the habitability field is drawn from measurements of entire communities present in the sediments of these systems. It may be that natural systems falling outside of the habitable zone contain microenvironments that permit iron oxidation to occur. There may even be systems outside the habitable zone where a negligible number of iron oxidizing organisms are dormant or performing only

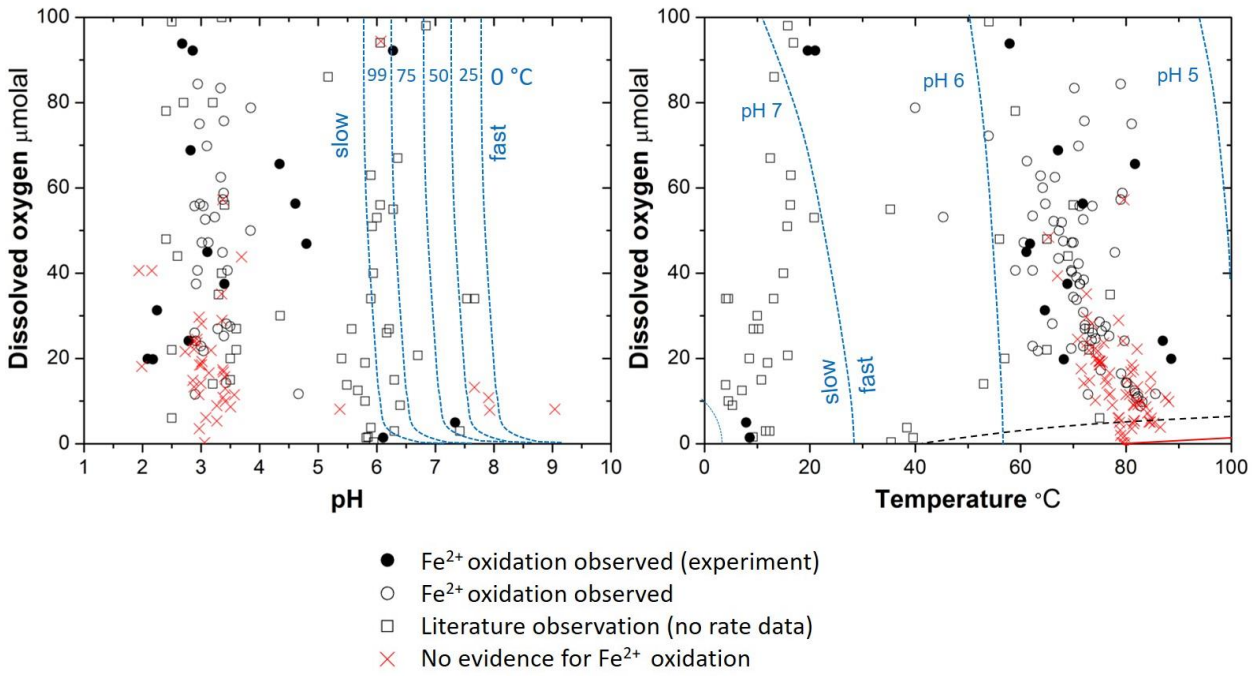

Figure 42 – Dissolved oxygen-pH and dissolved oxygen-temperature **habitability maps** showing thermodynamic (affinity = 0 curves in red and proposed physiological limits in black) and kinetic constraints (blue contours). The latter correspond to the kinetic limit shown in Fig 5. Symbols represent field data including rate experiments and observations of the iron-stained products of iron oxidation. Planned measurements at lower temperatures and higher pH values will further constrain these maps.

maintenance activities. These situations are of minor consequence to biogeochemical cycling are not the focus of the habitability diagram. Recent work by other authors (*e.g.* Hoehler et al., 2013; Lever et al., 2015) examining life in extremely energy limited environments is more appropriate for these situations.

Habitability diagrams for other reactions -

It is likely that data exist that permit habitability diagrams to be made for many other reactions involving inorganic compounds, at least as preliminary outlines, and it is our hope that habitability diagrams involving many other reactions will be generated. Thermodynamic boundaries may be drawn for thousands of reactions using the methods outlined here. Measurements of rates of biotic and abiotic processes from the field are sporadic, but analogous lab experiments permit preliminary estimates of the kinetic boundary.

Reactions coupling oxidation of organic compounds to inorganic substrates like ferric iron presents additional challenges for making field based determinations of habitability. This is because of the vast number of organic compounds present in a natural system that may be used as an oxidant, as well as determining which organic product(s) are being generated. Laboratory based rate experiments in defined media may be more conclusive for reactions involving organic compounds.

Habitability diagrams involving minerals as reactants may have an inherently different type of kinetic boundary, because the accessibility of the mineral to other reactants and to microbes becomes a necessary consideration. The surface area of the mineral can change reaction kinetics. Contours of surface area, mass %, or other deciding

factor may be necessary to incorporate into the kinetic boundary of reactions involving minerals as reactants.

As previously noted, the iron oxidation is relevant to a diverse group of topics. A remediation engineer looking to precipitate dissolved ferrous iron could use the habitability diagram to predict conditions that will be required to achieve the specified outcome. Geobiologists will be able to make rapid assessments of metabolic habitability of a system based on simple measurements. Astrobiologists will be able to infer past and present habitability of locations in our solar system and exoplanets (once the diagrams have been extended to the appropriate temperatures and pressures).

Methods –

The methods used to generate the kinetics, geochemical, and thermodynamic data that are used to construct the habitability diagrams have been previously described (Chapters 2, 3). Brief summaries of the methods are included here.

***In situ* Rate Experiments –** The experiments measuring abiotic and biotic iron oxidation rates described (Ch 2 and 3). Briefly, each assay included experimental (added $FeSO_4$), *in situ* (unamended), and killed controls ($FeSO_4$, azide), all measured in triplicate. 10 g of wet sediment and 40 mL of sample water were immediately added to each 60 mL serum vial. Reagents were added, as appropriate, and gently swirled to mix. The vial was crimp sealed, with air in the headspace. After settling for ~5 minutes, the initial concentration of Fe(II) was measured. The experimental bottles were then incubated at temperature of the sample location. Fe(II) concentrations were monitored

over 3-5 hours (10-30 minutes for locations close to the kinetic fringe) using the 1,10-phenanthroline method described next.

Samples for ferrous iron were taken directly with a 3 mL syringe and immediately filtered through a 0.2 µm into a 5 mL vial containing 100 µL of 10 g/L 1,10-phenanthroline monohydrate in 0.1M glycine/HCl buffer adjusted to pH 2.3. Laboratory development showed this method preserved ferrous iron for later measurement up to 2 months. The method did not reduce ferric ions, or oxidize ferrous iron, even in the ratios of up to 100:1 Fe^{3+}/Fe^{2+}. This method has been tested and used in several harsh natural systems, including acidic hot springs and acid mine drainage. The detection limit is 0.006 mg / L, with a total uncertainty of +/- 0.01 mg/L for a field measurement.

Geochemical Sampling and Analysis Temperature, pH, O_2, and conductivity were determined *in situ* with portable meters. Dissolved oxygen was measured using an optical method with a detection limit and precision of 5 ppb (Fibox 4 meter and optical probe, PreSens inc., Germany). Redox-sensitive solutes (Fe^{+2}, sulfide, O_2 in some locations), and aqueous silica concentrations were measured in the field using portable spectrophotometers as described for fieldwork on shallow marine hydrothermal systems (Amend et al., 2003) and Yellowstone hot springs (Shock et al., 2005; 2010; Windman et al., 2007; Havig et al., 2011; Meyer-Dombard et al., 2011; 2012; Swingley et al., 2012; Schubotz et al., 2013; 2015). Water samples were filtered to 0.2µm in the field and collected in containers appropriate for each type of analysis (acid-washed polypropylene, glass vials with septa, polycarbonate bottles, etc.) as described in the references listed above for major and trace elements, isotopes of H and O, dissolved inorganic and organic carbon, organic acids, and C isotopic analyses.

Geochemical Calculations -- Geochemical data permit assessments of chemical affinities (Eqns 2 and 3), which constrain thermodynamic limits. Equilibrium constants for numerous reactions in the microbial iron cycle were evaluated with the SUPCRT92 code (Johnson et al., 1992) in the CHNOSZ software package (Dick 2008), using an updated database containing results of recent publications of thermodynamic data (Dick et al., 2006; LaRowe and Helgeson, 2006a; 2006b; 2007; Shock, 2009; Canovas, 2016), together with earlier publications of data and parameters consistent the original SUPCRT92 code (Shock et al., 1997; Sverjensky et al., 1997), or with CHNOSZ (Dick, 2008), which is consistent with the SUPCRT92 package and offers greater versatility. Recent thermodynamic data on ferrihydrite and other iron oxyhydroxide phases (Navrotsky et al., 2008; Snow et al., 2013) have been assessed for consistency and included in these codes (Canovas 2016). Activity products (Q_r in Eqns 2 & 3) were be evaluated from the geochemical data as part of speciation calculations done with the EQ3/6 package (Wolery & Jarek, 2003), using a customized database containing equilibrium constants for dissociation and mineral hydrolysis reactions obtained from SUPCRT92 and an updated database.

Abiotic Rates in the Lab −

Abiotic oxidation experiments (reported in chapter 3) were performed analogously to those of Stumm and Lee 1961 and Sung and Morgan 1970, but in unbuffered dilute solution. 1 L of 18.2 MΩ ultra pure water was used in all experiments, with trace grade HCl or NaOH used to adjust the pH. Iron stock solutions of ferrous sulfate heptahydrate (ACS grade, Sigma-Aldrich) were made fresh daily in 0.01M HCl. The starting solution was exposed to air for 1 hour before the start of each experiment.

The reaction vessel was surrounded by a well thermostated water bath (± 0.2 °C). The pH reported is measured after Fe(II) has been added and equilibrated. Rate data are available in appendix E.

REFERENCES

Allen E. T. and Day A. L. (1935) *Hot springs of the Yellowstone National Park.* Carnegie Institution of Washington, Washington, D.C.

Amend J. and Shock E. (2001) Energetics of overall metabolic reactions of thermophilic and hyperthermophilic archaea and bacteria. *FEMS Microbiol. Rev*. **25**, 175-243.

Atkinson T., Cairns S., Cowan D. A., Danson M. J., Hough D. W., Johnson D. B., Norris P. R., Raven N., Robinson C., Robson R. and Sharp R. J. (2000) A microbiological survey of Montserrat Island hydrothermal biotopes. *Extremophiles* **4,** 305-313.

Bernstein H. C., Beam J. P., Kozubal M. A., Carlson R. P. and Inskeep W. P. (2013) *In situ* analysis of oxygen consumption and diffusive transport in high-temperature acidic iron-oxide microbial mats. *Environ. Microbiol.* **15,** 2360-2370.

Bilinski H. and Schindler P. (1982) Solubility and equilibrium constants of lead in carbonate solutions (25°C, I = 0.3 mol dm $^{-3}$). *Geochim. Cosmochim. Acta* **46,** 921-928.

Bilinski H., Huston R. and Stumm W. (1976) Determination of the stability constants of some hydroxo and carbonato complexes of Pb(II), Cu(II), Cd(II) and Zn(II) in dilute solutions by anodic stripping voltammetry and differential pulse polarography. *Anal. Chim. Acta* **84,** 157-164.

Bissig P., Goldscheider N., Mayoraz J., Surbeck H. and Vuataz F. (2006) Carbogaseous spring waters, coldwater geysers and dry CO2 exhalations in the tectonic window of the Lower Engadine Valley, Switzerland. *Eclogae Geologicae Helvetiae* **99,** 143-155.

Blöthe M. and Roden E. E. (2008) Microbial iron redox cycling in a circumneutral-ph groundwater seep. *Appl. Environ. Microbiol.* 468.

Bohorquez L. C., Delgado-Serrano L., López G., Osorio-Forero C., Klepac-Ceraj V., Kolter R., Junca H., Baena S. and Zambrano M. M. (2012) In-depth Characterization via Complementing Culture-Independent Approaches of the Microbial Community in an Acidic Hot Spring of the Colombian Andes. *Microb. Ecol.* **63,** 103-238.

Boyd E. S., Jackson R. A., Encarnacion G., Zahn J. A., Beard T., Leavitt W. D., Pi Y., Zhang C. L., Pearson A. and Geesey G. G. (2007) isolation, characterization, and ecology of sulfur-respiring crenarchaea inhabiting acid-sulfate-chloride-containing geothermal springs in Yellowstone National Park. *Appl. Environ. Microbiol.* **73,** 6669-6677.

Brantner J. S., Haake Z. J., Burwick J. E., Menge C. M., Hotchkiss S. T. and Senko J. M. (2014) Depth-dependent geochemical and microbiological gradients in Fe(III)

deposits resulting from coal mine-derived acid mine drainage. *Front. Microbiol.* **5,** 215.

Bridge TA and Johnson D. B. (1998) Reduction of soluble iron and reductive dissolution of ferric iron-containing minerals by moderately thermophilic iron-oxidizing bacteria. *Appl. Environ. Microbiol.* **64,** 2181-2186.

Brock T. D. and Gustafson J. (1976) Ferric iron reduction by sulfur- and iron-oxidizing bacteria. *Appl. Environ. Microbiol.* **32,** 567-571.

Bruno J., Wersin P. and Stumm W. (1992) On the influence of carbonate in mineral dissolution: II. The solubility of $FeCO_3$ (s) at 25°C and 1 atm total pressure. *Geochim. Cosmochim. Acta* **56,** 1149-1155.

Bruun A., Finster K., Gunnlaugsson H. P., Nørnberg P. and Friedrich M. W. (2010) A comprehensive investigation on iron cycling in a freshwater seep including microscopy, cultivation and molecular community analysis. *Geomicrobiol. J.* **27,** 15-34.

Byrne R. H. and Miller W. L. (1985) Copper(II) carbonate complexation in seawater. *Geochim. Cosmochim. Acta* **49,** 1837-1844.

Canovas P. A. (2016) Energy Transfer Between the Geosphere and Biosphere. Ph.D. thesis, Arizona State University

Canovas, P. and Shock, E.L. (in press) Geobiochemistry of metabolism: Standard state thermodynamic properties of the citric acid cycle. *Geochim. Cosmochim. Acta*

Châtellier X., West M. M., Rose J., Fortin D., Leppard G. G. and Ferris F. G. (2004) Characterization of iron-oxides formed by oxidation of ferrous ions in the presence of various bacterial species and inorganic ligands. *Geomicrobiol. J.* **21,** 99-112.

Christoffersen M. R. and Christoffersen J. (1976) The kinetics of dissolution of calcium sulphate dihydrate in water. *J. Cryst. Growth* **35,** 79-88.

Weber K. A., Achenbach L. A., and Coates J. D. (2006) Microorganisms pumping iron: anaerobic microbial iron oxidation and reduction. *Nat. Revs. Microbiol.* **4,** 752-764.

Camacho A., Walter X. A., Picazo A., and Zopfi J. (2017) Photoferrotrophy: remains of an ancient photosynthesis in modern environments. *Front. Microbiol*. **8**, 323

Cockell C. S., Kelly L. C., Summers S. and Marteinsson V. (2011) Following the kinetics: iron-oxidizing microbial mats in cold Icelandic volcanic habitats and their rock-associated carbonaceous signature. *Astrobio.* **11,** 679-694.

Colman D. R., Feyhl-Buska J., Fecteau K. M., Xu H., Shock E. L., Boyd E. S. and King G. (2016) Ecological differentiation in planktonic and sediment-associated

chemotrophic microbial populations in Yellowstone hot springs. *FEMS Microbiol. Ecol.* **92**

Colmer A. R., Temple K. L., Hinkle M. E. (1950) An iron-oxidizing bacterium from the acid drainage of some bituminous coal mines. *J. Bacteriol.* **59,** 317-328.

Debnath S., Hausner D. B., Strongin D. R. and Kubicki J. (2010) Reductive dissolution of ferrihydrite by ascorbic acid and the inhibiting effect of phospholipid. *J. Colloid Interface Sci.* **341,** 215-223.

Dick J. M. (2008) Calculation of the relative metastabilities of proteins using the CHNOSZ software package. *Geochem. Trans.* **9**, 1-17.

Dick J., LaRowe D. and Helgeson H. (2006) Temperature, pressure, and electrochemical constraints on protein speciation: Group additivity calculation of the standard molal thermodynamic properties of ionized unfolded proteins. *Biogeosci.* **3**, 311-336.

Druschel G. K., Baker B. J., Gihring T. M. and Banfield J. F. (2004) Acid mine drainage biogeochemistry at Iron Mountain, California. *Geochem. Trans.* **5,** 1-20.

Druschel G. K., Emerson D., Sutka R., Suchecki P. and Luther G. W. (2008) Low-oxygen and chemical kinetic constraints on the geochemical niche of neutrophilic iron(II) oxidizing microorganisms. *Geochim. Cosmochim. Acta* **72**, 3358-3370.

Eggerichs T., Opel O., Otte T. and Ruck W. (2014) Interdependencies between biotic and abiotic ferrous iron oxidation and influence of pH, oxygen and ferric iron deposits. *Geomicrobiol. J.* **31,** 461-472.

Elliott A. V. C., Plach J. M., Droppo I. G. and Warren L. A. (2014) Collaborative microbial Fe-redox cycling by pelagic floc bacteria across wide ranging oxygenated aquatic systems. *Chem. Geol.* **366,** 90-102.

Emerson D. and Moyer C. (1997) Isolation and characterization of novel iron-oxidizing bacteria that grow at circumneutral pH. *Appl. Environ. Microbiol.* **63,** 4784-4792.

Emerson D. and Moyer C. L. (2002) Neutrophilic Fe-oxidizing bacteria are abundant at the Loihi Seamount hydrothermal vents and play a major role in Fe oxide deposition. *Appl. Environ. Microbiol.* **68,** 3085-3093.

Emerson D., Fleming E. J. and McBeth J. M. (2010) Iron-oxidizing bacteria: an environmental and genomic perspective. *Annu. Rev. Microbiol.* **64,** 561-583.

Emerson D., Scott J. J., Benes J. and Bowden W. B. (2015) Microbial iron oxidation in the Arctic tundra and its implications for biogeochemical cycling. *Appl. Environ. Microbiol.* **81,** 8066.

Enright A. M. L. and Ferris F. G. (2016) Bacterial Fe(II) oxidation distinguished by long-range correlation in redox potential: Fluctuation Analysis of Redox Potential. *J. Geophys. Res. Biogeosci.* **121,** 1249-1257.

Fabisch M., Freyer G., Johnson C. A., Büchel G., Akob D. M., Neu T. R. and Küsel K. (2016) Dominance of '*Gallionella capsiferriformans'* and heavy metal association with *Gallionella*-like stalks in metal-rich pH 6 mine water discharge. *Geobiology* **14,** 68-90.

Fecteau K. M. (2016) Organic carbon in hydrothermal systems: from phototrophy to aldehyde transformations. Ph.D. thesis, Arizona State University.

Ferris F. G., Enright A. M. L., Fortin D. and Clark I. D. (2016) Rates of Fe(II)-oxidation and solubility of bacteriogenic iron oxides. *Geomicrobiol. J.* **33,** 237-242.

Fleischer M. (1953) Recent estimates of the abundances of the elements in the earth's crust. U.S. Dept. of the Interior, Geological Survey, Washington, D.C. **285**

Fleming E. J., Davis R. E., McAllister S. M., Chan C. S., Moyer C. L., Tebo B. M. and Emerson D. (2013) Hidden in plain sight: discovery of sheath-forming, iron-oxidizing Zetaproteobacteria at Loihi Seamount, Hawaii, USA. *FEMS Microbiol. Ecol.* **85,** 116-127.

Fleming E. J., Cetinić I., Chan C. S., Whitney King D. and Emerson D. (2014) Ecological succession among iron-oxidizing bacteria. *The ISME journal* **8,** 804-815.

Fortney N. W., He S., Converse B. J., Beard B. L., Johnson C. M., Boyd E. S. and Roden E. E. (2016) Microbial Fe(III) oxide reduction potential in Chocolate Pots hot spring, Yellowstone National Park. *Geobiology* **14,** 255-275.

Fosbøl P. L., Thomsen K. and Stenby E. H. (2010) Review and recommended thermodynamic properties of $FeCO_3$. *Corros. Eng. Sci. Techn.* **45,** 115-135.

Fouillac C. and Criaud A. (1984) Carbonate and bicarbonate trace-metal complexes - critical reevaluation of stability-constants. *Geochem. J.* **18,** 297-303.

Gardiner J. (1974) The chemistry of cadmium in natural water I - A study of cadmium complex formation using the cadmium specific-ion electrode. *Water Res.* **8,** 23-30.

Gault A. G., Langley S., Ibrahim A., Renaud R., Takahashi Y., Boothman C., Lloyd J. R., Clark I. D., Ferris F. G. and Fortin D. (2012) Seasonal changes in mineralogy, geochemistry and microbial community of bacteriogenic iron oxides (BIOS) deposited in a circumneutral wetland. *Geomicrobiol. J.* **29,** 161-172.

Hanert H. H. (2007) The Genus Gallionella. In *The Prokaryotes*. Springer New York, New York, NY. pp. 990-995.

Havig J. R., Raymond J., Meyer-Dombard D. R., Zolotova N. and Shock E. L. (2011) Merging isotopes and community genomics in a siliceous sinter-depositing hot spring. *J. Geophys. Res.* **116**

Hegler F., Lösekann-Behrens T., Hanselmann K., Behrens S. and Kappler A. (2012) Influence of seasonal and geochemical changes on the geomicrobiology of an iron carbonate mineral water spring. *Appl. Environ. Microbiol.* **78,** 7185-7196.

Helgeson H. C. (1969) Thermodynamics of hydrothermal systems at elevated temperatures and pressures. *Am. J. Sci.* **267,** 729-804.

Helgeson H. C., Kirkham D. H. and Flowers G. C. (1981) Theoretical prediction of the thermodynamic behavior of aqueous electrolytes at high pressures and temperatures: IV. Calculation of activity coefficients, osmotic coefficients, and apparent molal and standard and relative partial molal properties to 600 °C and 5 KB. *Am. J. Sci*. 281, 1249–1516.

Hinder B., Baur I., Hanselmann K. and Schanz F. (1999a) Microbial food web in an oligotrophic high mountain lake (Jöri Lake III, Switzerland). *J. Limnol.* **58,** 162-168.

Hinder B., Gabathuler M., Steiner B., Hanselmann K. And Preisig H. R. (1999b) Seasonal dynamics and phytoplankton diversity in high mountain lakes (Jöri lakes, Swiss Alps). *J. Limnol.* **58,** 152-161.

Hoehler T. M. and Jørgensen B. B. (2013) Microbial life under extreme energy limitation. *Nature Revs.Micro.* **11,** 83.

Holanda R., Hedrich S., Ňancucheo I., Oliveira G., Grail B. M. and Johnson D. B. (2016) Isolation and characterisation of mineral-oxidising "*Acidibacillus*" spp. from mine sites and geothermal environments in different global locations. *Res. Microbiol.* **167,** 613-623.

Inskeep W. P., Macur R. E., Harrison G., Bostick B. C. and Fendorf S. (2004) Biomineralization of As(V)-hydrous ferric oxyhydroxide in microbial mats of an acid-sulfate-chloride geothermal spring, Yellowstone National Park. *Geochim. Cosmochim. Acta* **68,** 3141-3155.

Isaacson L. S., Burton E. D., Bush R. T., Mitchell D. R. G., Johnston S. G., Macdonald B. C. T., Sullivan L. A. and White I. (2009) Iron(III) accumulations in inland saline waterways, Hunter Valley, Australia: Mineralogy, micromorphology and pore-water geochemistry. *Appl. Geochem.* **24,** 1825-1834.

James R. E. and Ferris F. G. (2004) Evidence for microbial-mediated iron oxidation at a neutrophilic groundwater spring. *Chem. Geol.* **212,** 301-311.

Jiang Z., Li P., Jiang D., Dai X., Zhang R., Wang Y. and Wang Y. (2016) Microbial community structure and arsenic biogeochemistry in an acid vapor-formed spring in Tengchong geothermal area, China. *PloS one* **11**.

Johnson D. B. and Bridge T. A. M. (2002) Reduction of ferric iron by acidophilic heterotrophic bacteria: evidence for constitutive and inducible enzyme systems in *Acidiphilium* spp. *J. Appl. Microbiol.* **92,** 315-321.

Johnson D. B. and McGinness S. (1991) Ferric iron reduction by acidophilic heterotrophic bacteria. *Appl. Environ. Microbiol.* **57,** 207-211.

Johnson D. B., Ghauri M. A. and Said M. F. (1992) Isolation and characterization of an acidophilic, heterotrophic bacterium capable of oxidizing ferrous iron. *Appl. Environ. Microbiol.* **58,** 1423-1428.

Johnson D. B., Okibe N. and Roberto F. F. (2003) Novel thermo-acidophilic bacteria isolated from geothermal sites in Yellowstone National Park: physiological and phylogenetic characteristics. *Arch. Microbiol.* **180,** 60-68.

Johnson J., Oelkers E. And Helgeson H. (1992) SUPCRT92 - A software package for calculating the standard molal thermodynamic properties of minerals, gases, aqueous species, and reactions from 1 bar to 5000 bar and 0°C to 1000°C. *Comput. Geosci.* **18**, 899-947.

Jones A. M., Griffin P. J., Collins R. N. and Waite T. D. (2014) Ferrous iron oxidation under acidic conditions – The effect of ferric oxide surfaces. *Geochim. Cosmochim. Acta* **145,** 1-12.

Jones R. M. and Johnson D. B. (2015) *Acidithrix ferrooxidans* gen. nov., sp. nov.; a filamentous and obligately heterotrophic, acidophilic member of the Actinobacteria that catalyzes dissimilatory oxido-reduction of iron. *Res. Microbiol.* **166,** 111.

Kanzaki, Y. and Murakami, T. (2013) Rate law of Fe(II) oxidation under low O_2 conditions. *Geochim. Cosmochim. Acta* **123,** 338-350.

Kasama T. and Murakami T. (2001) The effect of microorganisms on Fe precipitation rates at neutral pH. *Chem. Geol.* **180,** 117-128.

Kashefi K. and Lovley D. R. (2003) Extending the upper temperature limit for life. *Science* **301,** 934-934.

Kashefi K., Holmes D. E., Reysenbach A. and Lovley D. R. (2002) Use of Fe(III) as an electron acceptor to recover previously uncultured hyperthermophiles: isolation and characterization of *Geothermobacterium ferrireducens* gen. nov., sp. nov. *Appl. Environ. Microbiol.* **68,** 1735-1742.

Kato S., Chan C., Itoh T. and Ohkuma M. (2013) Functional gene analysis of freshwater iron-rich flocs at circumneutral ph and isolation of a stalk-forming microaerophilic iron-oxidizing bacterium. *Appl. Environ. Microbiol.* **79,** 5283-5290.

King D. W. (1998) Role of carbonate speciation on the oxidation rate of Fe(II) in aquatic systems. *Environ. Sci. Technol.* **32,** 2997-3003.

Kozubal M. A., Macur R. E., Jay Z. J., Beam J. P., Malfatti S. A., Tringe S. G., Kocar B. D., Borch T. and Inskeep W. P. (2012) Microbial iron cycling in acidic geothermal springs of yellowstone national park: integrating molecular surveys, geochemical processes, and isolation of novel fe-active microorganisms. *Front. Microbiol.* **3,** 109.

Kozubal M., Macur R. E., Korf S., Taylor W. P., Ackerman G. G., Nagy A. and Inskeep W. P. (2008) Isolation and distribution of a novel iron-oxidizing crenarchaeon from acidic geothermal springs in Yellowstone National Park. *Appl. Environ. Microbiol.* **74,** 942-949.

Krishnamurti G.S.R.. Huang, P.M. (1991) Influence of citrate on the kinetics of Fe(II) oxidation and the formation of iron oxyhydroxides. *Clays Clay Miner.* **39,** 28-34.

LaRowe D. E. and Dick J. M. (2012) Calculation of the standard molal thermodynamic properties of crystalline peptides. *Geochim. Cosmochim. Acta* **80**, 70-91.

LaRowe D. E. and Helgeson H. C. (2006a) Biomolecules in hydrothermal systems: Calculation of the standard molal thermodynamic properties of nucleic-acid bases, nucleosides, and nucleotides at elevated temperatures and pressures. *Geochim. Cosmochim. Acta* **70**, 4680-4724.

LaRowe D. E. and Helgeson H. C. (2006b) The energetics of metabolism in hydrothermal systems: Calculation of the standard molal thermodynamic properties of magnesium-complexed adenosine nucleotides and NAD and NADP at elevated temperatures and pressures. *Thermochim. Acta* **448**, 82-106.

LaRrowe D. and Helgeson H.C. (2007) Quantifying the energetics of metabolic reactions in diverse biogeochemical systems: electron flow and ATP synthesis. *Geobiol.* **5**, 153-168.

Larsen O. and Postma D. (2001) Kinetics of reductive bulk dissolution of lepidocrocite, ferrihydrite, and goethite. *Geochim. Cosmochim. Acta* **65,** 1367-1379.

Lemire R. J., Berner U., Musikas C., Palmer D. A., Taylor P. and Tochiyama O. (2013) *Chemical Thermodynamics of Iron, Part 1.* OECD,

Lever M. A., Rogers K. L., Lloyd K. G., Overmann J., Schink B., Thauer R. K., Hoehler T. M., Jørgensen B. B. and Giudici-Orticoni M. (2015) Life under extreme energy limitation: a synthesis of laboratory- and field-based investigations. *FEMS Microbiol. Rev.* **39,** 688-728.

Liang L., McNabb, A.J., Paulk J.M., Gu, B., McCarthy, J.F. (1993) Kinetics of iron(II) oxygenation at low partial pressure of oxygen in the presence of natural organic matter. *Environ. Sci. Technol.* **27,** 1864-1870.

Lin C., Larsen E. I., Nothdurft L. D. and Smith J. J. (2012) Neutrophilic, microaerophilic Fe(II)-oxidizing bacteria are ubiquitous in aquatic habitats of a subtropical Australian coastal catchment (ubiquitous feob in catchment aquatic habitats). *Geomicrobiol. J.* **29,** 76-87.

Lovley D. R. (1991) Dissimilatory Fe(III) and Mn(IV) reduction. *Microbiol. Rev.* **55,** 259-287.

Lovley D. R. and Elizabeth J. P. Phillips (1987) Rapid assay for microbially reducible ferric iron in aquatic sediments. *Appl. Environ. Microbiol.* **53,** 1536-1540.

Lowson R. T. (1982) Aqueous oxidation of pyrite by molecular oxygen. *Chem. Rev.* **82,** 461-497.

McAllister S. M., Davis R. E., McBeth J. M., Tebo B. M., Emerson D. and Moyer C. L. (2011) Biodiversity and emerging biogeography of the neutrophilic iron-oxidizing zetaproteobacteria. *Appl. Environ. Microbiol.* **77,** 5445-5457.

Melton E. D., Swanner E. D., Behrens S., Schmidt C. and Kappler A. (2014) The interplay of microbially mediated and abiotic reactions in the biogeochemical Fe cycle. *Nature Rev. Microbiol.* **12,** 797-808.

Meyer-Dombard D. R., Woycheese K. M., Yargıçoğlu E. N., Cardace D., Shock E. L., Güleçal-Pektas Y. and Temel M. (2014; 2015) High pH microbial ecosystems in a newly discovered, ephemeral, serpentinizing fluid seep at Yanartaş (Chimera), Turkey. *Front. Microbiol.* **5,** 723

Millero F. J. (1985) The effect of ionic interactions on the oxidation of metals in natural waters. *Geochim. Cosmochim. Acta* **49,** 547-553.

Millero F. J. and Hawke D. J. (1992) Ionic interactions of divalent metals in natural waters. *Mar. Chem.* **40,** 19-48.

Millero F. J. and Izaguirre M. (1989) Effect of ionic strength and ionic interactions on the oxidation of Fe(II). *J. Solution Chem.* **18,** 585-599.

Millero F. J., Sotolongo S. and Izaguirre M. (1987) The oxidation kinetics of Fe(II) in seawater. *Geochim. Cosmochim. Acta* **51,** 793-801.

Mitchell K. R. and Takacs-Vesbach C. D. (2008) A comparison of methods for total community DNA preservation and extraction from various thermal environments. *J. Ind. Microbiol. Biotechnol.* **35,** 1139-1147.

Mohapatra D., Singh P., Zhang W. and Pullammanappallil P. (2005) The effect of citrate, oxalate, acetate, silicate and phosphate on stability of synthetic arsenic-loaded ferrihydrite and Al-ferrihydrite. *J. Hazard. Mater.* **124,** 95-100.

Moran J. J., Whitmore L. M., Isern N. G., Romine M. F., Riha K. M., Inskeep W. P. and Kreuzer H. W. (2016) Formaldehyde as a carbon and electron shuttle between autotroph and heterotroph populations in acidic hydrothermal vents of Norris Geyser Basin, Yellowstone National Park. *Extremophiles* **20,** 291-299.

Morgan B. and Lahav O. (2007) The effect of pH on the kinetics of spontaneous Fe(II) oxidation by O_2 in aqueous solution--basic principles and a simple heuristic description. *Chemosphere* **68,** 2080-2084.

Mori J. F., Neu T. R., Lu S., Händel M., Totsche K. U. and Küsel K. (2015) Iron encrustations on filamentous algae colonized by *Gallionella*-related bacteria in a metal-polluted freshwater stream. *Biogeosci.* **12,** 5277-5289

Morita, R. (1997) Bacteria in Oligotrophic Environments, Chapman and Hall, New York.

Murphy W. M. and Shock E. L. (1999) Environmental aqueous geochemistry of actinides. *Rev. Mineral*. 38, 221–253.

Nakayama F. S. (1971) Thermodynamic functions for the dissociation of $NaHCO_3^0$, $NaCO_3^-$, H_2CO_3 and HCO_3^-. *J. Inorg. Nucl. Chem.* **33,** 1287-1291.

Nealson K. H. and Saffarini D. (1994) Iron and manganese in anaerobic respiration: environmental significance, physiology, and regulation. *Annu. Rev. Microbiol.* **48,** 311-343.

Néher-Neumann, E. (1992) Studies on metal carbonate equilibria. 24. The hydrogen carbonate and carbonate complexes of the lead(II) and cadmium(II) ions in acid solutions and a 3M (Na)ClO_4 ionic medium at 25 °C. *Acta Chem. Scand.* **46**, 231-239

Neubauer S. C., Emerson D. and Megonigal J. P. (2002) Life at the energetic edge: kinetics of circumneutral iron oxidation by lithotrophic iron-oxidizing bacteria isolated from the wetland-plant rhizosphere. *Appl. Environ. Microbiol*. **68**, 3988-3995.

Nordstrom DK, Ball JW, McCleskey RB (2005) "Ground water to surface water: chemistry of thermal outflows in Yellowstone National Park," in Geothermal Biology and Geochemistry in Yellowstone National Park, eds WP Inskeep and TR McDermott. Montana State University, Bozeman, pp. 143–162.

Park U. and Dempsey B. A. (2005) Heterogeneous oxidation of Fe(II) on ferric oxide at neutral pH and a low partial pressure of O_2. *Environ. Sci. Technol.* **39,** 6494-6500.

Poulton S. W. (2003) Sulfide oxidation and iron dissolution kinetics during the reaction of dissolved sulfide with ferrihydrite. *Chem. Geol.* **202,** 79-94.

Powell K. J., Brown P. L., Byrne R. H., Gajda T., Hefter G., Leuz A., Sjöberg S., Wanner H. (2009) Chemical speciation of environmentally significant metals with inorganic ligands. Part 3: The Pb^{2+}, OH^{-}, Cl^{-}, CO_3^{2-}, SO_4^{2-}, and PO_4^{3-} systems (IUPAC Technical Report). *Pure and Applied Chemistry* **81,** 2425-2476.

Powell K. J., Brown P. L., Byrne R. H., Gajda T., Hefter G., Leuz A., Sjoberg S. and Wanner H. (2011) Chemical speciation of environmentally significant metals with inorganic ligands. Part 4: the Cd^{2+}, OH^{-}, Cl^{-}, CO_3^{2-}, SO_4^{2-}, and PO_4^{3-} systems. *Pure and Applied Chemistry* **83,** 1163.

Powell K. J., Brown P. L., Byrne R. H., Gajda T., Hefter G., Leuz A., Sjöberg S., Wanner H. (2013) Chemical speciation of environmentally significant metals with inorganic ligands. Part 5: The Zn^{2+}, OH^{-}, Cl^{-}, CO_3^{2-}, SO_4^{2-}, and PO_4^{3-} systems (IUPAC Technical Report). *Pure and Applied Chemistry* **85,** 2249-2311.

Powell K. J., Brown P. L., Byrne R. H., Gajda T., Hefter G., Sjöberg S., Wanner H. (2007) Chemical speciation of environmentally significant metals with inorganic ligands Part 2: The Cu^{2+}, OH^{-}, Cl^{-}, CO_3^{2-}, SO_4^{2-}, and PO_4^{3-} systems (IUPAC Technical Report). *Pure and Applied Chemistry* **79,** 895-950.

Prapaipong P., Shock E. L. and Koretsky C. M. (1999) Metalorganic complexes in geochemical processes: temperature dependence of standard partial molal thermodynamic properties of aqueous complexes between metal cations and dicarboxylate ligands. *Geochim. Cosmochim. Acta* 63, 2547–2577.

Preis W. and Gamsjäger H. (2002) Critical evaluation of solubility data: enthalpy of formation of siderite. *Phys. Chem. Chem. Phys.***4,** 4014-4019.

Rentz J. A., Kraiya C., Luther G. W. and Emerson D. (2007) Control of ferrous iron oxidation within circumneutral microbial iron mats by cellular activity and autocatalysis. *Environ. Sci. Technol.* **41**, 6084-6089.

Ríos A. d. l., Bustillo M., Ascaso C. and Carvalho M. R. (2011) Bioconstructions in ochreous speleothems from lava tubes on Terceira Island (Azores). *Sediment. Geol.* **236,** 117-128.

Ryan M. P. and Bauman J. E. (1978) Thermodynamics of the zinc bicarbonate ion pair. *Inorg. Chem.* **17,** 3329-3331.

Sahl J. W., Schmidt R., Swanner E. D., Mandernack K. W., Templeton A. S., Kieft T. L., Smith R. L., Sanford W. E., Callaghan R. L., Mitton J. B. and Spear J. R. (2008; 2007) Subsurface microbial diversity in deep-granitic-fracture water in Colorado. *Appl. Environ. Microbiol.* **74,** 143-152.

Santana-Casiano J. M., Gonzalez-Daliva M., Rodrıguez M. J. and Millero F. J. (2000) The effect of organic compounds in the oxidation kinetics of Fe(II). *Mar. Chem.* **70**, 211–222.

Santana-Casiano J. M., González-Dávila M. and Millero F. J. (2004) The oxidation of Fe(II) in $NaCl^-$ HCO_3^- and seawater solutions in the presence of phthalate and salicylate ions: a kinetic model. *Mar. Chem.* **85,** 27-40.

Santana-Casiano J. M., Gonzalez-Davila M. and Millero F. J. (2005) Oxidation of nanomolar levels of Fe(II) with oxygen in natural waters. *Environ. Sci. Technol.* **39**, 2073–2079.

Schubotz F., Meyer-Dombard D. R., Bradley A. S., Fredricks H. F., Hinrichs K. -., Shock E. L. and Summons R. E. (2013) Spatial and temporal variability of biomarkers and microbial diversity reveal metabolic and community flexibility in Streamer Biofilm Communities in the Lower Geyser Basin, Yellowstone National Park. *Geobio.* **11,** 549-569.

Schwertmann U. (1991) Solubility and Dissolution of Iron Oxides. - *Plant and Soil* **130,**

Schwertmann U. and Cornell R. M. (2000) *Iron oxides in the laboratory: preparation and characterization.* VCH, Weinheim; New York.

Senko J. M., Wanjugi P., Lucas M., Bruns M. A. and Burgos W. D. (2008) Characterization of Fe(II) oxidizing bacterial activities and communities at two acidic Appalachian coalmine drainage-impacted sites. *ISME* **2,** 1134-1145.

Seto M. (2014) The gibbs free energy threshold for the invasion of a microbial population under kinetic constraints. *Geomicrobiol. J.* **31,** 645; 645-653; 653.

Shcolnick S., Summerfield T. C., Reytman L., Sherman L. A. and Keren N. (2009) The mechanism of iron homeostasis in the unicellular cyanobacterium *Synechocystis* Sp. PCC 6803 and its relationship to oxidative stress. *Plant Physiol.* **150,** 2045-2056.

Shock E. (2009) Minerals as energy sources for microorganisms. *Econ. Geol.* **104**, 1235-1248.

Shock E. L. and Boyd E. S. (2015) Principles of Geobiochemistry. *Elements* **11,** 395-401.

Shock E. L. and Helgeson H. C. (1988) Calculation of the thermodynamic and transport properties of aqueous species at high pressures and temperatures: Correlation algorithms for ionic species and equation of state predictions to 5 kb and 1000°C. *Geochim. Cosmochim. Acta* **52,** 2009-2036.

Shock E. L. and Koretsky C. M. (1995) Metal-organic complexes in geochemical processes: Estimation of standard partial molal thermodynamic properties of

aqueous complexes between metal cations and monovalent organic acid ligands at high pressures and temperatures. *Geochim. Cosmochim. Acta* **59,** 1497-1532.

Shock E. L. and McKinnon W. B. (1993) Hydrothermal processing of cometary volatiles-applications to Triton. *Icarus* **106,** 464-477.

Shock E. L., Helgeson H. C. and Sverjensky D. A. (1989) Calculation of the thermodynamic and transport properties of aqueous species at high pressures and temperatures: Standard partial molal properties of inorganic neutral species. *Geochim. Cosmochim. Acta* **53,** 2157-2183.

Shock E. L., Holland M., Meyer-Dombard D., Amend J. P., Osburn G. R. and Fischer T. P. (2010) Quantifying inorganic sources of geochemical energy in hydrothermal ecosystems, Yellowstone National Park, USA. *Geochim. Cosmochim. Acta* **74**, 4005-4043.

Shock E. L., Oelkers E. H., Johnson J. W., Sverjensky D. A. and Helgeson H. C. (1992) Calculation of the thermodynamic properties of aqueous species at high pressures and temperatures. Effective electrostatic radii, dissociation constants and standard partial molal properties to 1000 C and 5 kbar. *J. Chem. Soc. Faraday Trans.* **88,** 803.

Shock E. L., Sassani D. C., Willis M. and Sverjensky D. A. (1997) Inorganic species in geologic fluids: Correlations among standard molal thermodynamic properties of aqueous ions and hydroxide complexes. *Geochim. Cosmochim. Acta* **61,** 907-950.

Singer P. C. and Stumm W. (1970a) Acidic mine drainage: the rate-determining step. *Science* **167**, 1121-1123.

Singer P. C. and Stumm W. (1970b) The solubility of ferrous iron in carbonate-bearing waters. *American Water Works Association* **62,** 198-202.

Slobodkin AI. (2005) Thermophilic Microbial Metal Reduction. *Microbiol.* **74,** 501-514.

Slobodkin, AI. (1999).Thermoanaerobacter Siderophilus Sp. Nov., A Novel Dissimilatory Fe(III)-Reducing, Anaerobic, Thermophilic Bacterium. *Int. J. syst. bact.* 49 p. 1471.

Smith R. E. and Martell A. E. (1976) *Critical Stability Conslants.Vol. 4.Inorganic Complexes.* Plenum.

Snow C. L., Lilova K. I., Radha A. V., Shi Q., Smith S., Navrotsky A., Boerio-Goates J. and Woodfield B. F. (2013) Heat capacity and thermodynamics of a synthetic two-line ferrihydrite, $FeOOH \cdot 0.027H_2O$. *J. Chem. Thermodyn.* **58,** 307-314.

Sobolev D. and Roden E. E. (2004) Characterization of a neutrophilic, chemolithoautotrophic Fe(II)-oxidizing β -proteobacterium from freshwater wetland sediments. *Geomicrobiol. J.* **21,** 1-10.

Song W., Zhai L., Cui Y., Sun M. and Jiang Y. (2013) Carbonate-mediated Fe(II) oxidation in the air-cathode fuel cell: a kinetic model in terms of Fe(II) speciation. *J. Phys. Chem.*. **117,** 4627.

Stanley J. K. and Byrne R. H. (1990) Inorganic complexation of Zinc (II) in seawater. *Geochim. Cosmochim. Acta* **54,** 753-760.

Steiner B., Hanselmann K. W. and Krähenbühl U. (2000) Dating and heavy metal contents of sediment cores of a high-alpine, remote lake: Jörisee (Switzerland). *Int. J. Environ. Anal. Chem.* **78,** 131-148.

Stumm W. and Lee G. F. (1961) Oxygenation of ferrous iron. *Ind. Eng. Chem. Res.* **53**, 143-146.

Stumm W. and Morgan J. J. (1995) *Aquatic chemistry: chemical equilibria and rates in natural waters.* Wiley, New York.

Stumm W. and Sulzberger, B. (1992) The cycling of iron in natural environments: Considerations based on laboratory studies of heterogeneous redox processes. *Geochim. Cosmochim. Acta* **56,** 3233-3257.

Sun W., Xiao E., Krumins V., Dong Y., Xiao T., Ning Z., Chen H. and Xiao Q. (2016) Characterization of the microbial community composition and the distribution of Fe-metabolizing bacteria in a creek contaminated by acid mine drainage. *Appl. Microbiol. Biotechnol.* **100,** 8523-8535.

Sunda, W. G. and Hanson, P.J. (1979) *Chemical Speciation of Copper in River Water* in Chemical Modeling in Aqueous Systems. *ACS Symposium Series* 93, 147

Sverjensky D. A., Shock E. L. and Helgeson H. C. (1997) Prediction of the thermodynamic properties of aqueous metal complexes to 1000 °C and 5 kb. *Geochim. Cosmochim. Acta* **61,** 1359.

Swanner E. D., Mloszewska A. M., Cirpka O. A., Schoenberg R., Konhauser K. and Kappler A. (2015) Modulation of oxygen production in Archaean oceans by episodes of Fe(II) toxicity. *Nat. Geosci.* **8,** 126-130.

Tamura H., Goto K. and Nagayama M. (1976) The effect of ferric hydroxide on the oxygenation of ferrous ions in neutral solutions. *Corros. Sci.* **16,** 197-207.

Tamura H., Kawamura S. and Hagayama M. (1980) Acceleration of the oxidation of Fe^{2+} ions by Fe(III)-oxyhydroxides. *Corros. Sci.* **20,** 963-971

Theis T. L., Singer, P.C. (1974) Complexation of Iron(II) by organic matter and its effect on Iron(II) oxygenation. *Environ. Sci. Technol.* **8,** 569-573.

Trapp J. M. and Millero F. J. (2007) The oxidation of Iron(II) with oxygen in NaCl brines. *J. Solut. Chem.* **36**, 1479-1493.

Vinson M. D., Arvidson R. S. and Luttge A. (2007) Kinetic inhibition of calcite dissolution by aqueous manganese(II). *J. Cryst. Growth* **307,** 116-125.

Violante A., Ricciardella M. and Pigna M. (2003) Adsorption of Heavy Metals on Mixed Fe-Al Oxides in the Absence or Presence of Organic Ligands. *Water Air Soil Pollut.* **145,** 289-306.

Wang J., Sickinger M., Ciobota V., Herrmann M., Rasch H., Rösch P., Popp J. and Küsel K. (2014) Revealing the microbial community structure of clogging materials in dewatering wells differing in physico-chemical parameters in an open-cast mining area. *Water Res.* **63,** 222-233.

Weber K. A., Achenbach L. A. and Coates J. D. (2006) Microorganisms pumping iron: anaerobic microbial iron oxidation and reduction. *Nature Rev. Microbiol* **4,** 752-764.

Widdel F., Ehrenreich A., Heising S., Schnell S., Assmus B. and Schink B. (1993) Ferrous iron oxidation by anoxygenic phototrophic bacteria. *Nature* **362,** 834-836.

Wimberley P., Siggaardandersen O., Foghandersen N. and Boink A. (1985) Are Sodium-Bicarbonate and Potassium Bicarbonate Fully Dissociated Under Physiological Conditions. *Scand. J. Clin. Lab. Invest.* **45,** 7-10.

Windman T., Zolotova N., Schwandner F. and Shock E. (2007) Formate as an energy source for microbial metabolism in chemosynthetic zones of hydrothermal ecosystems. *Astrobio.* 7, 873–890.

Wolery T. W. and Jarek R. L. (2003) Software User's Manual EQ3/6, Version 8.0. *U.S. Department of Energy, Office of Civilian Radioactive Waste Management, Office of Repository Development* Software Document Number 10813-UM-8.0-00, 376.

Wu L., Brucker R. P., Beard B. L., Roden E. E. and Johnson C. M. (2013) Iron isotope characteristics of Hot Springs at Chocolate Pots, Yellowstone National Park. *Astrobio.* **13,** 1091.

Xu W., Hausner D. B., Harrington R., Lee P. L., Strongin D. R. and Parise J. B. (2011) Structural water in ferrihydrite and constraints this provides on possible structure models. *Am. Mineral.* **96,** 513-520.

Xu Y., Schoonen M.A., Nordstrom D.K., Cunningham K.M., Ball J.W. (1998) Sulfur geochemistry of hydrothermal waters in Yellowstone National Park. I. The origin of thiosulfate in hot spring waters. *Geochimica et Cosmochimica Acta* **62**, 3729–3743.

APPENDIX A

ESTIMATED THERMODYNAMIC PROPERTIES OF METAL CARBONATE AND BICARBONATE AQUEOUS SPECIES

Speciation of fluids in natural systems requires equilibrium constants for the formation of the species at the temperature of the system. Over the last several decades, equilibrium constants have been measured for the formation of significant number of metal carbonate and bicarbonate species at 25°C. To obtain an equilibrium constant at the correct temperature, additional thermodynamic properties of the aqueous species must be measured or estimated. Our method uses the extended Helgeson, Kirkam, Flowers (HKF) equation of state (Helgeson *et al*., (1981)) to calculate equilibrium constants at the appropriate temperature. A thorough summary of the revised HKF equation of state is found in Canovas and Shock (2016). Thermodynamic properties of the species ($\Delta\overline{G}^{\circ}_{f}$, $\Delta\overline{H}^{\circ}_{f}$, S°, $\bar{C}^{\circ}_{p}$) and HKF parameters (c1, c2, ω) were calculated or estimated to permit the calculations. Methods to calculate or estimate each property are outlined in Shock and Helgeson (1988), Shock *et al*., (1989), Shock and Koretsky (1995), Sverjenski *et al.* (1997), Murphy and Shock (1999), and Prapaipong *et al*. (1999). This appendix summarizes the methods used to generate the thermodynamic properties and HKF parameters for metal carbonate and bicarbonate complexes. The resulting parameters are listed in table A1.

Gibbs Energy of Formation ($\Delta\overline{G}^{\circ}_{f}$)

The $\Delta\overline{G}^{\circ}_{f}$ is required to determine the equilibrium constants at any temperature. Equilibrium constants derived from experimental data of the association of ions to the aqueous species are the ideal starting point for any estimation. Table A2 shows the equilibrium constants for aqueous metal carbonate and bicarbonate species used in this study. Often multiple measurements are available, with some equilibrium data having been scrutinized in reviews. The recommendations of those authors, indicated by

Table A1 - Summary of standard partial molal thermodynamic data at 25 °C and 1 bar for aqueous metal carbonate and bicarbonate species, along with equation of state parameters required to calculate the corresponding properties at high temperatures.

Species	$\Delta G_f^{\circ a}$ Cal mol^{-1}	$\Delta H_f^{\circ a}$ Cal mol^{-1}	$S^{\circ b}$ Cal mol^{-1} k^{-1}	$C^{\circ}_{p}{}^{b}$ Cal mol^{-1} k^{-1}	c1^{b} Cal mol^{-1} k^{-1}	c2^{c} ×10^{-4} Cal K mol^{-1}	ω^{a}×10^{-5} Cal mol^{-1}	Z
$FeCO_3$	-155442	-183875	-13.97	-30.00	-11.7653	-9.1456	-0.0380	0
$MnCO_3$	-187703	-213178	-2.93	-26.20	-9.5383	-8.3715	-0.0380	0
$ZnCO_3$	-167872	-197642	-15.06	-27.43	-10.2592	-8.6221	-0.0380	0
$CuCO_3$	-119725	-147820	-11.42	-27.80	-10.4760	-8.6975	-0.0380	0
$CdCO_3$	-150754	-178085	-4.39	-25.60	-9.1867	-8.2493	-0.0380	0
$PbCO_3$	-140701	-161150	21.81	-34.80	-14.5784	-10.1234	-0.0380	0
$CoCO_3$	-145208	-174468	-16.03	-29.90	-11.7067	-9.1252	-0.0380	0
$NiCO_3$	-143681	-174283	-20.64	-33.80	-13.9924	-9.9197	-0.0380	0
$Fe(CO_3)_2^{-2}$	-283939	-354507	-33.02	-56.10	7.4869	-14.4622	3.7120	-2
$Zn(CO_3)_2^{-2}$	-294950	-366798	-34.11	-53.53	9.1454	-13.9387	3.7286	-2
$Cu(CO_3)_2^{-2}$	-250760	-321123	-30.47	-53.90	8.4209	-14.0140	3.6735	-2
$Pb(CO_3)_2^{-2}$	-271913	-336371	2.76	-60.90	-0.3186	-15.4399	3.1701	-2
$NaCO_3^-$	-189567	-223464	-10.94	-8.82	-12.4895	-4.8318	-1.4638	-1
KCO_3^-	-194807	-221063	17.89	-16.12	-20.7896	-6.3182	-1.9005	-1
$LiCO_3^-$	-197222	-239041	-42.81	-3.90	-5.1587	-3.8290	-0.9812	-1
$RbCO_3^-$	-195096	-218275	31.05	-21.10	-25.5442	-7.3327	-2.0998	-1
$NH_4CO_3^-$	-146442	-191478	24.74	-2.36	-13.6810	-3.5153	-2.0042	-1
$Fe(HCO_3)+$	-164158	-184997	11.50	55.02	41.8870	8.1736	0.3770	1
$Mn(HCO_3)+$	-197142	-214597	23.97	63.57	45.1584	9.9153	0.1882	1
$Zn(HCO_3)+$	-177692	-199910	10.27	60.81	45.4479	9.3515	0.3957	1
$Cu(HCO_3)+$	-127117	-147520	14.38	59.97	44.3866	9.1819	0.3334	1
$Cd(HCO_3)+$	-161571	-180938	22.33	64.92	46.1790	10.1903	0.2131	1
$Pb(HCO_3)+$	-148530	-160004	51.92	44.22	29.9188	5.9737	-0.2350	1
$Co(HCO_3)+$	-156284	-178030	9.17	55.25	42.3438	8.2195	0.4123	1
$Ni(HCO_3)+$	-154211	-176473	7.33	46.47	37.4577	6.4320	0.4401	1
$Na(HCO_3)_{aq}$	-203093	-222193	38.69	47.88	33.9093	6.7192	-0.0347	0
$K(HCO_3)_{aq}$	-207437	-223501	52.08	31.95	22.7051	3.4743	-0.2375	0
$FeSO_4^0$	-203784	-238961	-5.8	-28.40	-10.8255	-8.8190	-0.0380	0

a. cal mol^{-1}
b. cal mol^{-1} K^{-1}
c. cal K mol^{-1}

Table A2 – Equilibrium constants used to determine thermodynamic. Discussion Reference refers to a critical review of available equilibrium constants that were used to select the value in the table. A review was not found for species that do not list a discussion reference. In this case selection was made based on the most apparently reliable or only available data.

Ion	Species	Log K*	Data Reference	Discussion Reference
Fe^{2+}	$FeCO_3$ aq	5.45	Bruno *et al.* 1992	Fosbol *et al.* 2010 and Lemire *et al.* 2014
	$FeHCO_3$+	1.47	Bruno *et al.* 1992	Fosbol *et al.* 2010 and Lemire *et al.* 2014
	$Fe(CO_3)_2^{-2}$	7.1	Preis and Gamsjager 2002	Fosbol *et al.* 2010 and Lemire *et al.* 2014
Cu^{2+}	$CuHCO_3$+	1.84	Byrne and Miller 1985	Powell *et al.* 2007
	$CuCO_3$ aq	6.75	Sunda and Hanson 1979	Powell *et al.* 2007
	$Cu(CO_3)_2^{-2}$	10.3	Sunda and Hanson 1979	Powell *et al.* 2007
Cd^{2+}	CdCO3	4.4	Gardiner 1974	Powell *et al.* 2011
	$CdHCO_3^+$	2	Fouillac and Criaud 1984	Powell *et al.* 2011
Zn^{2+}	ZnCO3	4.75	Bilinski *et al.* 1976	Powell *et al.* 2013
	$Zn(CO_3)_2^{-2}$	5.4	Stanley *et al.* 1990	Powell *et al.* 2013
	ZnHCO3+	1.62	Ryan and Bauman 1978	Powell *et al.* 2013
Pb^{2+}	PbCO3	6.45	Bilinksi and Schindler 1982	Powell *et al.* 2009
	$Pb(CO_3)_2^{-2}$	10.13	Bilinksi and Schindler 1982	Powell *et al.* 2009
	PbHCO3+	1.86	Néher-Neumann 1992	Powell *et al.* 2009
Co^{2+}	CoCO3	4.41	Fouillac and Criaud 1984	-
	CoHCO3+	2.2	Fouillac and Criaud 1984	-
Ni^{2+}	NiCO3	4.83	Fouillac and Criaud 1984	-
	NiHCO3+	2.22	Fouillac and Criaud 1984	-
Mn^{2+}	$MnCO_3$ aq	4.7	Vinson *et al.* 2007	-
	MnHCO3+	1.29	Vinson *et al.* 2007	-
Na^+	$NaCO_3^-$	0.575	Nakayama 1971	-
	$NaHCO_3^0$	0.161	Nakayama 1971	-
K^+	KCO_3^-		estimated#	-
	$KHCO_3^0$	-0.26	Wimberly *et al.* 1985	-
Li^+	$LiCO_3^-$		estimated#	--
Rb^+	$RbCO_3^-$		estimated#	-
NH_4^+	$NH_4CO_3^-$		estimated#	-

*log k is for the reaction $xM^{+x} + y(HCO_3^- \text{ or } CO_3^{-2}) \rightarrow$ species at 25°C and ionic strength of 0.

discussion reference in table A2, are adopted unless otherwise noted. Experimental equilibrium data for some species is much more limited. The most reliable experimental data are chosen based on experimental procedure and error.

The equilibrium constants for most monovalent carbonates are currently unknown. While they are likely to be only feebly associated in conditions common in natural systems on earth's surface, their potentially high abundance means they cannot be left out of speciation calculations. Correlations are required to estimate the $\Delta G°_f$ of these species. Similarities exist between the gibbs energy of formation for metal carbonates and metal oxalate species. Figure A1 shows ΔG_f of divalent cations plotted against $\Delta G°_r$ for the formation of aqueous divalent carbonate (filled circles) and divalent oxalate (empty circles) species. The similarity of the slopes and intercepts of divalent cations suggests that the monovalent carbonate species have similar $\Delta G°_f$ to the monovalent oxalate species. Indeed when ΔG_f of the monovalent cations plotted against $\Delta G°_r$ for the formation of aqueous monovalent oxalate species, the $\Delta G°_r$ for $NaCO_3^{-1}$ lies close to the oxalate line. Note that experimental error in equilibrium constants typically translates to $\Delta G°_r$ error of several hundred calories per mole. The resulting values give small equilibrium constants as expected, that will not significantly alter the speciation of carbonates except at extreme concentrations of the monovalent cations. Experiments will ultimately reveal the accuracy of these estimations.

$\Delta_r\overline{S}°$ and $\Delta_r\overline{C}_P^\circ$

Methods for estimating standard partial molal entropies and heat capacities of aqueous carbonate complexes at the reference conditions exist but are poorly documented. Sverjensky et al. (1997) obtained standard partial molal entropy values at

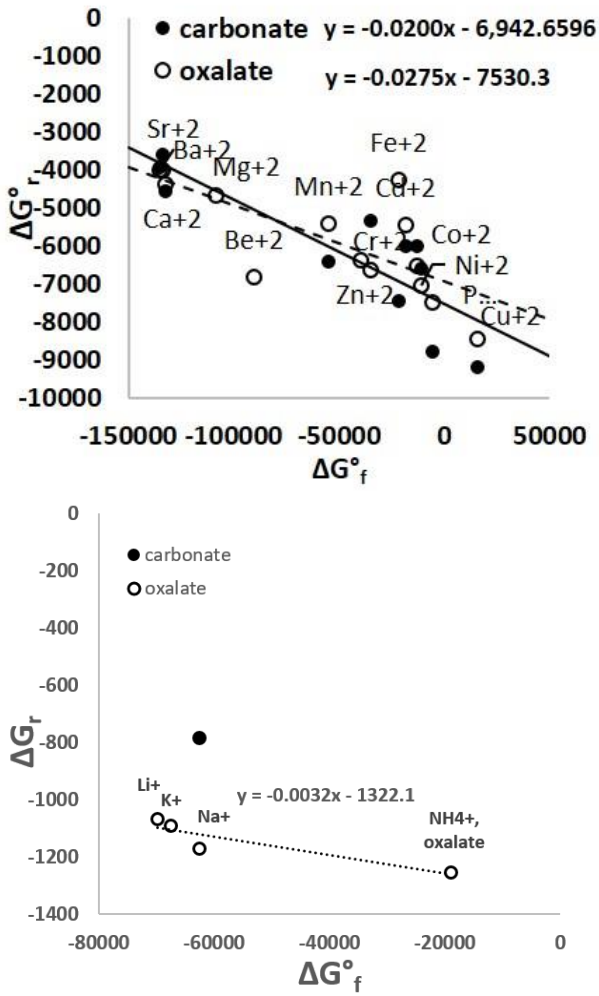

Figure A1 - $\Delta\overline{G}°_f$ of the cations plotted against $\Delta G_r°$ of the reaction forming the aqueous species of the metal with carbonate (filled circles) and oxalate (empty circles). The similarity of the resulting slopes for both carbonate and oxalate divalent species (top figure) suggests that monovalent oxalate and carbonate monovalent species will have similar values of $\Delta G_r°$ (bottom figure).

25°C and 1 bar for several aqueous carbonate complexes through regression of experimental equilibrium dissociation constants available over various temperature ranges. They also provided correlations of standard partial molal entropies of association ($\Delta_r\bar{S}°$) with the standard partial molal entropies ($\bar{S}°$) of monovalent and divalent cations. Expressions for these correlations are given by

$$\Delta_r\bar{S}° = 1.83\bar{S}° - 38.5 \qquad (1)$$

for monovalent and

$$\Delta_r\bar{S}° = 0.213\bar{S}° + 28.67 \qquad (2)$$

for divalent cations, which were used in the present study. Murphy and Shock (1999) estimated $\bar{S}°$ for the carbonate complex of Am^{+3} and reference methods provided by Sverjensky et al. (1997), which offers no correlation for trivalent cations. What Murphy and Shock (1999) did was construct a provisional correlation for trivalent cations based on the slopes and intercepts of the monovalent and divalent correlations from Sverjensky et al. (1997) given by Eqns. (1) and (2), inspired by the existence of correlations for sulfate complexes for all three cation charges, and the observation by Sverjensky et al. (1997) that correlations of slope with cation charge and intercept with cation charge exist for the three sulfate complex correlations. The resulting predicted correlation for trivalent cation complexes of carbonate is

$$\Delta_r\bar{S}° = -1.4\bar{S}° + 95.8 \quad . \qquad (3)$$

Murphy and Shock (1999) also made an estimate of $\bar{S}°$ of the second carbonate complex of Am^{+3}, leaving only the cryptic message in a footnote that the value was "estimated with methods developed in this study based on those described by Sverjensky et al. (1997)…" without elaborating further. Sverjensky et al. (1997) obtained reference

state values of the $\bar{S}°$ of the first (0 cal mol^{-1} K^{-1}) and second (-19 cal mol^{-1} K^{-1}) carbonate complexes of Ag^+ by regression of equilibrium constant data. These values can be combined with $\bar{S}°$ of the carbonate ion (-11.95 cal mol^{-1} K^{-1}; Shock et al., 1997) to calculate the standard entropy of the reaction

$$AgCO_3^- + CO_3^{-2} = Ag(CO_3)_2^{-3} \quad , \qquad (4)$$

giving -7.1 cal mol^{-1} K^{-1}. Murphy and Shock (1999) used this value and their data for Am^{+3} and $AmCO_3^+$ to estimate $\bar{S}°$ of $Am(CO_3)_2^-$. This strategy was adopted in the present study to estimate reference state values of $\bar{S}°$ for second carbonate complexes.

Regression of accurate standard partial molal heat capacity ($\bar{C}_P^\circ$) values at the reference conditions for aqueous complexes from equilibrium dissociation constants requires data at temperatures > 100°C. Sverjensky et al. (1997) found that experimentally determined equilibrium constants in this temperature range for inorganic complexes involving divalent ligands were extremely rare, and obtained $\bar{C}_P^\circ$ values for only two sulfate complexes, KSO_4^+ and $CaSO_4°$, via regression. They used these values to calculate standard partial molal heat capacities of association ($\Delta_r\bar{C}_P^\circ$) for the two complexes from

$$\Delta_r\bar{C}_P^\circ = \bar{C}_{P,complex}^\circ - \bar{C}_{P,cation}^\circ - \bar{C}_{P,ligand}^\circ \qquad (5)$$

and used the resulting $\Delta_r\bar{C}_P^\circ$ values for sulfate complexes of monovalent (51.4 cal mol^{-1} K^{-1}) and divalent (47.4 cal mol^{-1} K^{-1}) cations to make estimates. On the one hand they estimated $\bar{C}_P^\circ$ for $MnSO_4°$ and used the estimate together with experimental dissociation

constants to obtain a value of $\bar{S}°$ for this complex. On the other, they also used these values of $\Delta_r\bar{C}_P^\circ$ to estimate values of $\bar{C}_P^\circ$ for *carbonate* complexes, citing the relatively small difference in the values of $\bar{C}_P^\circ$ for sulfate (-64.38 cal mol^{-1} K^{-1}) and carbonate (-69.5 cal mol^{-1} K^{-1}) as justification for this estimation strategy, and cautioning that equilibrium constants obtained above 100°C using this strategy should be considered "provisional estimates". Because we adopted this same estimation strategy for carbonate complexes, that same caution should be applied to using the results of the present study at temperatures >100°C.

Murphy and Shock (1999) extended this estimation strategy to divalent-ligand complexes of trivalent cations with a cryptic footnote about "methods deduced from Sverjensky et al. (1997)". What they did was take the difference between the two $\Delta_r\bar{C}_P^\circ$ values calculated with Eqn (5) for monovalent and divalent cations (4 cal mol^{-1} K^{-1}) and estimated 43.4 cal mol^{-1} K^{-1} for $\Delta_r\bar{C}_P^\circ$ for the association reaction forming sulfate complexes of trivalent cations, which they used to estimate $\bar{C}_P^\circ$ for $AmSO_4^+$ and $AmCO_3^+$. Their estimates of $\bar{C}_P^\circ$ for the second sulfate and carbonate complexes were obtained by using the same value of $\Delta_r\bar{C}_P^\circ$ a second time. In effect, using 43.4 cal mol^{-1} K^{-1} as $\Delta_r\bar{C}_P^\circ$ in the relation

$$\Delta_r\bar{C}_P^\circ = \bar{C}_{P,2nd\ complex}^\circ - \bar{C}_{P,1st\ complex}^\circ - \bar{C}_{P,ligand}^\circ, \qquad (6)$$

and solving for $\bar{C}_{P,2nd\ complex}^\circ$. In the case of Am^{+3} complexes this yields -77.8 cal mol^{-1} K^{-1} for $Am(SO_4)_2^-$ and -88.0 cal mol^{-1} K^{-1} for $Am(CO_3)_2^-$. The latter value is opposite in sign to the value reported by Murphy and Shock (1999), which we have determined is a typographical error. The justification for Eqn (6) is unclear, although it should be noted

that Sverjensky et al. (1997) used the same approach to estimate $\bar{C}_P^\circ$ for $Ag(CO_3)_2^{-3}$, using the monovalent cation value of 51.4 cal mol^{-1} K^{-1}, which was then used to regress low-temperature equilibrium constants to obtain $\bar{S}°$ for that complex. In this context, it is worth noting that in section 5 of Sverjensky et al. (1997) there is a subsection 5.1 about monovalent ligands, but no corresponding subsection 5.2 that may have, in the original manuscript, explained some of these estimation strategies for divalent ligands, and offered a justification for using Eqn (6) the way it was used. It is odd to have a stand-alone subsection 5.1 with no other subsections. In any event, in the present study we used the methods outlined above to estimate values of $\bar{C}_P^\circ$ for second carbonate complexes, and repeat the caution from Sverjensky et al. (1997) that resulting equilibrium constants calculated above 100°C should be considered provisional estimates.

$\Delta\bar{H}°_f$, c1, c2, ω

Other parameters were calculated by well-established methods. The equations used to calculate them can be found in table A3, along with a summary of equations used to calculate each thermodynamic property or HKF parameter.

Table A3 – A summary of equations used to determine thermodynamic properties and HKF parameters.

	species	log k / ΔG	ΔS	ΔH	Cp	ω	c1	c2
Divalent carbonates and sulfate	$FeCO_3^0$ $MnCO_3^0$ $ZnCO_3^0$ $CuCO_3^0$ $CdCO_3^0$ $PbCO_3^0$ $CoCO_3^0$ $NiCO_3^0$ $FeSO_4^0$	See table A2	correlation in Sverjensky *et al* 1997 $\Delta S_r^\circ = 0.213 * S_{M^{++}}^\circ + 28.637$	$\Delta H_r = \Delta G_r + (298.15 * \Delta S_r)$ $\Delta \bar{H}^\circ_f = \Delta H_r + H_{Cation} + H_{Ligand}$	$\bar{C}^\circ_p = \Delta C_p^\circ + C_p cation + C_p ligand$ ΔC_p° is set to 47.4, see text	set to -0.038 for neutral species	$c1 = Cpn - \frac{c2}{(298.15 \times \theta)^2}$ Cpn = Cp – Cps Cps= ω_{con} * 298.15 * X X = -3.09×10^{7}, Θ = 228.0	c2 = 0.2037× C_p - 3.0346
Divalent Carbonates Second association	$Fe(CO_3)_2^{2}$ $Zn(CO_3)_2^{2}$ $Cu(CO_3)_2^{2}$ $Pb(CO_3)_2^{2}$ $Fe(SO_4)_2^{2}$	See table A2	$S^\circ = \Delta S^\circ_r + SL + SC$ ΔS°_r is estimated to be -7.1 cal $mol^{1} K^{1}$ (see text)	$\Delta H_r = \Delta G_r + (298.15 * \Delta S_r)$ $\Delta \bar{H}^\circ_f = \Delta H_r + H_{Cation} + 2(H_{Ligand})$	$\bar{C}^\circ_p = \Delta C_p^\circ + C_p cation + C_p ligand$ ΔC_p^0 is set to 47.4, see text	$\omega_{P_rT_r} = -1514.4 \times \bar{S}^0_{PrTr} + \beta_z$ βz ($x10^{5}$) = 3.2120 for Z =-2	$c1 = Cpn - \frac{c2}{(298.15 \times \theta)^2}$ Cpn = Cp – Cps Cps= ω_{con} * 298.15 * X X = -3.09×10^{7}, Θ = 228.0	c2 = 0.2037× C_p - 3.0346
Monovalent Carbonates	$NaCO_3$- KCO_3- NH_4CO_3- $LiCO_3$-	NaCO3- in table A2. All other values estimated from oxalate correlations (see text)	Correlation in Sverjensky *et al* 1997 $\Delta S_r^\circ = 1.83 * S_{M^{++}}^\circ - 38.5$	$\Delta H_r = \Delta G_r + (298.15 * \Delta S_r)$ $\Delta \bar{H}^\circ_f = \Delta H_r + H_{Cation} + H_{Ligand}$	dz = 0.856*C_pL - 2.1 + 45.3*Z_C ΔC_p^0 = 1.25*C_pC + dz $C_p^0 = \Delta C_p 1 + C_p C + C_p L$	$\omega_{P_rT_r} = -1514.4 \times \bar{S}^0_{PrTr} + \beta_z$ βz ($x10^{5}$) = -1.6295 for Z =-1	$c1 = Cpn - \frac{c2}{(298.15 \times \theta)^2}$ Cpn = Cp – Cps Cps= ω_{con} * 298.15 * X X = -3.09×10^{7}, Θ = 228.0	c2 = 0.2037× C_p - 3.0346
Divalent Bicarbonates	$Fe(HCO_3)^+$ $Mn(HCO_3)^+$ $Zn(HCO_3)^+$ $Cu(HCO_3)^+$ $Cd(HCO_3)^+$ $Pb(HCO_3)^+$ $Co(HCO_3)^+$ $Ni(HCO_3)^+$	See table A2	ΔS°_r =0.37 $SM^{++\circ}_{abs}$ +26 (Shock and Koretsky 1995)	$\Delta H_r = \Delta G_r + (298.15 * \Delta S_r)$ $\Delta \bar{H}^\circ_f = \Delta H_r + H_{Cation} + H_{Ligand}$	dz = 0.856*C_pL - 2.1 + 45.3*Z_C ΔC_p^0 = 1.25*C_pC + dz $C_p^0 = \Delta C_p 1 + C_p C + C_p L$	$\omega_{P_rT_r} = -1514.4 \times \bar{S}^0_{PrTr} + \beta_z$ βz ($x10^{5}$) = 0.5512 for Z = 1	$c1 = Cpn - \frac{c2}{(298.15 \times \theta)^2}$ Cpn = Cp – Cps Cps= ω_{con} * 298.15 * X X = -3.09×10^{7}, Θ = 228.0	c2 = 0.2037× C_p - 3.0346
Monovalent Bicarbonates	$NaHCO_3$ $KHCO_3$	See table A2	ΔS°_r =0.31 $SM^{+\circ}_{abs}$ 3.1 Shock and Koretski (1995) equation 11	$\Delta H_r = \Delta G_r + (298.15 * \Delta S_r)$ $\Delta \bar{H}^\circ_f = \Delta H_r + H_{Cation} + H_{Ligand}$	dz = 0.856*CPL - 2.1 + 45.3*ZC ΔC_p^0 = 1.25*C_pC + dz $C_p^0 = \Delta C_p 1 + C_p C + C_p L$	set to -0.038 for neutral species	$c1 = Cpn - \frac{c2}{(298.15 \times \theta)^2}$ Cpn = Cp – Cps Cps= ω_{con} * 298.15 * X X = -3.09×10^{7}, Θ = 228.0	c2 = 0.2037× C_p - 3.0346

Table A4 - Log k for the formation of divalent metal carbonate species from 0 – 350 °C. Log k is for the reaction $M^{++} + CO_3^{-2} \rightarrow MCO_3$ aq

species	Experimental Log k (25°C)	0° C	50° C	100° C	150° C	200° C	250° C	300° C	350° C
$FeCO_3^0$	5.41	5.528	5.450	5.578	5.848	6.277	6.923	7.930	9.572
$MnCO_3^0$	4.7	4.672	4.792	5.071	5.461	5.986	6.712	7.786	9.495
$ZnCO_3^0$	4.75	4.772	4.803	5.022	5.364	5.851	6.546	7.593	9.265
$CuCO_3^0$	6.75	6.936	6.655	6.622	6.760	7.076	7.625	8.546	10.103
$CdCO_3^0$	4.4	4.350	4.511	4.821	5.231	5.769	6.501	7.574	9.304
$PbCO_3^0$	6.45	6.492	6.478	6.642	6.929	7.357	7.988	8.966	10.634
$CoCO_3^0$	4.41	4.400	4.484	4.732	5.094	5.595	6.302	7.360	9.037
$NiCO_3^0$	4.83	4.873	4.857	5.024	5.321	5.769	6.429	7.447	9.081

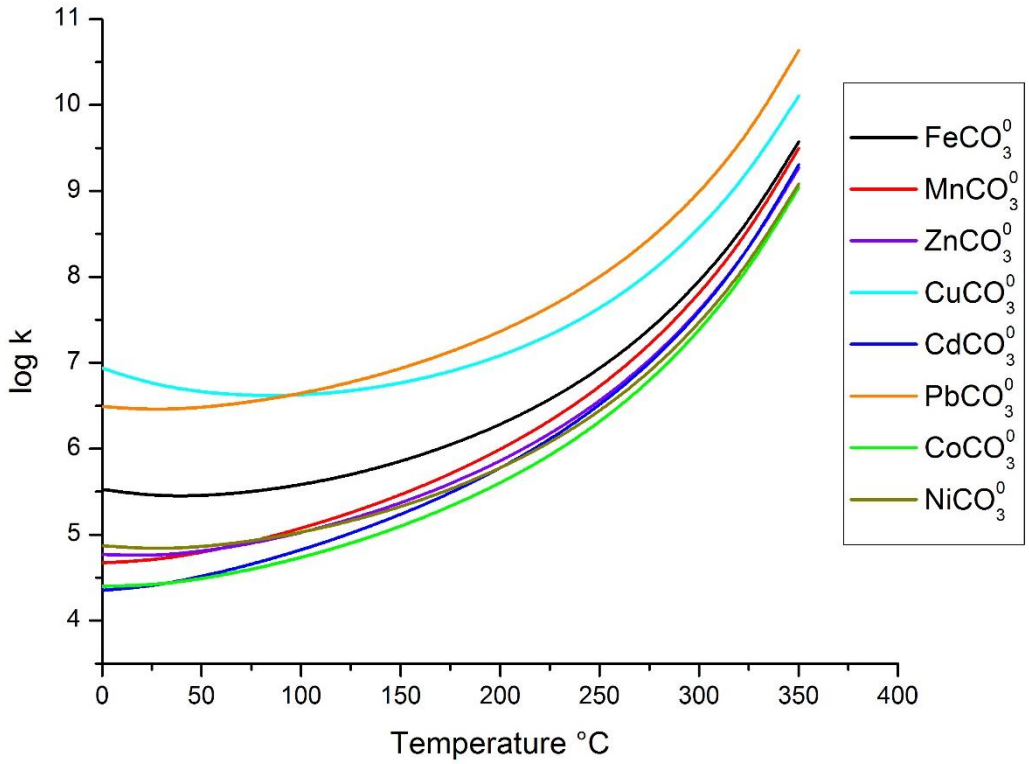

Figure A2 – Log k for the formation of divalent metal carbonate species from 0 – 350 °C. Log k is for the reaction $M^{++} + CO_3^{-2} \rightarrow MCO_3$ aq

Table A5 - Log k for the formation of divalent metal carbonate (second association) species from 0 – 350 °C. Log k is for the reaction $M^{++} + 2\ CO_3^{-2} \rightarrow M(CO_3)^{-2}$

species	Experimental Log k (25°C)	0°C	50°C	100°C	150°C	200°C	250°C	300°C	350°C
$Fe(CO_3)_2^{-2}$	7.17	7.949	6.696	6.266	6.277	6.612	7.259	8.326	10.184
$Zn(CO_3)_2^{-2}$	5.4	6.034	5.053	4.826	4.992	5.447	6.190	7.334	9.259
$Cu(CO_3)_2^{-2}$	10.3	11.332	9.611	8.829	8.563	8.675	9.139	10.051	11.751
$Pb(CO_3)_2^{-2}$	10.13	10.718	9.813	9.625	9.819	10.303	11.082	12.266	14.131

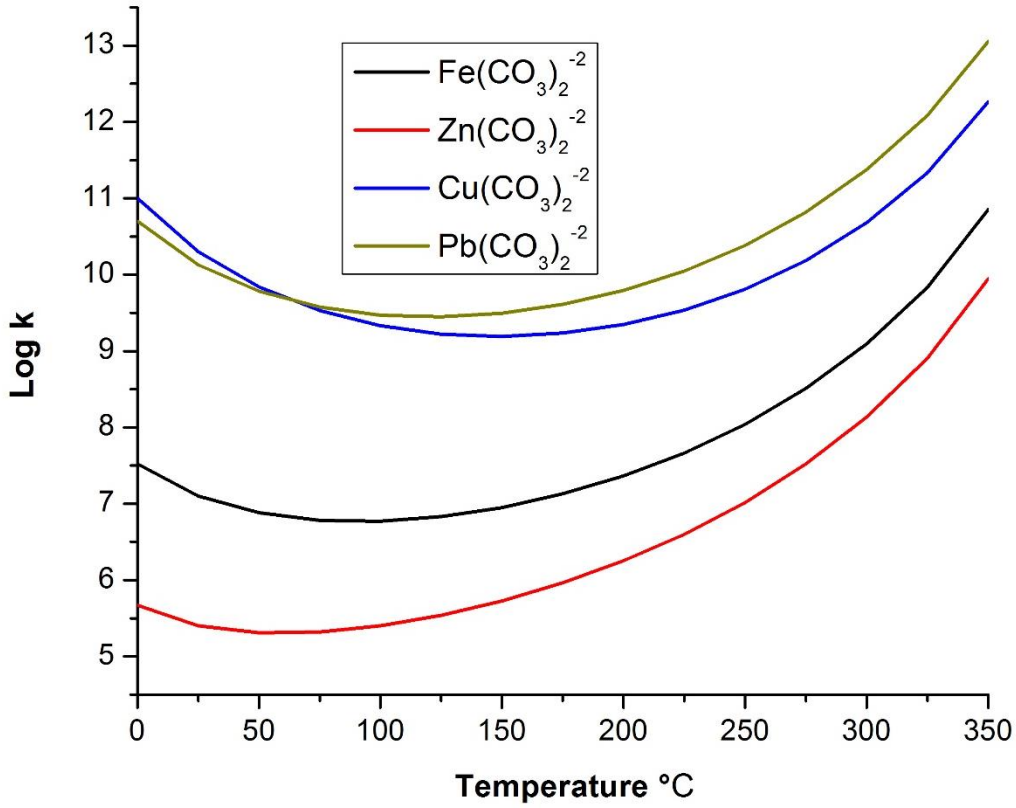

Figure A3 - Log k for the formation of divalent metal carbonate (second association) species from 0 – 350 °C. Log k is for the reaction $M^{++} + 2\ CO_3^{-2} \rightarrow M(CO_3)^{-2}$

Table A6 - Log k for the formation of divalent metal carbonate (second association) species from 0 – 350 °C. Log k is for the reaction $M^+ + CO_3^{-2} \rightarrow M(CO_3)^-$. Log k at 25 °C for $NaCO_3^-$ is experimental, but all others are estimated (see text)

species	Log k 25 °C	0.1	50	100	150	200	250	300	350
$NaCO_3^-$	0.575	0.940	0.344	0.118	0.136	0.405	1.032	2.360	6.014
KCO_3^-	0.81	0.820	0.875	1.124	1.517	2.107	3.049	4.782	9.439
$LiCO_3^-$	0.81	1.604	0.209	-0.588	-0.999	-1.074	-0.764	0.176	2.875
$RbCO_3^-$	0.81	0.652	1.020	1.508	2.088	2.837	3.934	5.865	11.017
$NH_4CO_3^-$	0.67	0.737	0.953	1.340	1.848	2.539	3.579	5.432	10.359

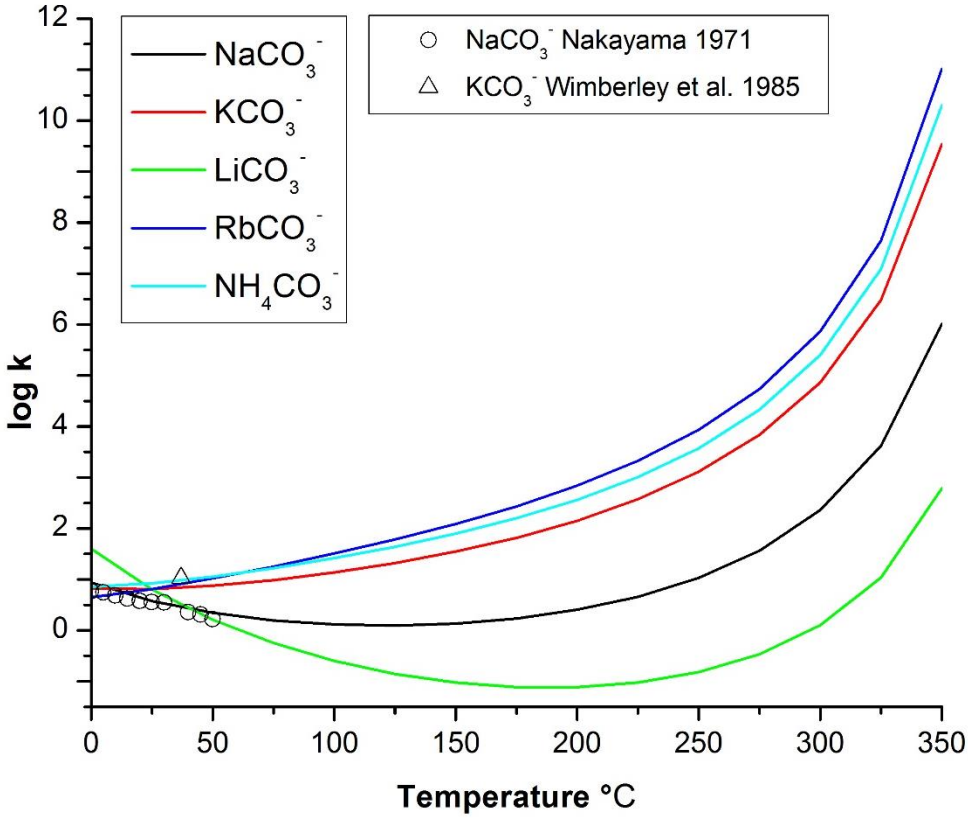

Figure A4 - Log k for the formation of monovalent metal carbonate species from 0 – 350 °C. Log k is for the reaction $M^+ + CO_3^{-2} \rightarrow M(CO_3)^-$. Our estimates for $NaCO_3^-$ are in good agreement with Nakayama 1971 (empty circles) from 5-50 °C. Likewise, our estimate for KCO_3^- is close to that measured by Wimberley et al. (1985) at 37 °C.

Table A7 - Log k for the formation of divalent metal bicarbonate species from 0 – 350 °C. Log k is for the reaction $M^{++} + HCO_3^- \rightarrow MHCO_3^+$

species	Experimental Log k (25°C)	0.1	50	100	150	200	250	300	350
$Fe(HCO_3)^+$	1.47	1.411	1.626	2.063	2.593	3.196	3.893	4.746	5.876
$Mn(HCO_3)^+$	1.29	1.152	1.520	2.088	2.733	3.440	4.235	5.188	6.422
$Zn(HCO_3)^+$	2.2	2.219	2.296	2.642	3.104	3.655	4.308	5.125	6.220
$Cu(HCO_3)^+$	1.84	1.799	1.980	2.387	2.888	3.466	4.139	4.973	6.076
$Cd(HCO_3)^+$	2	1.936	2.168	2.638	3.207	3.850	4.588	5.487	6.696
$Pb(HCO_3)^+$	1.86	1.613	2.166	2.830	3.523	4.254	5.064	6.047	7.425
$Co(HCO_3)^+$	2.2	2.220	2.289	2.619	3.068	3.607	4.252	5.062	6.147
$Ni(HCO_3)^+$	2.22	2.199	2.337	2.699	3.160	3.700	4.338	5.134	6.197

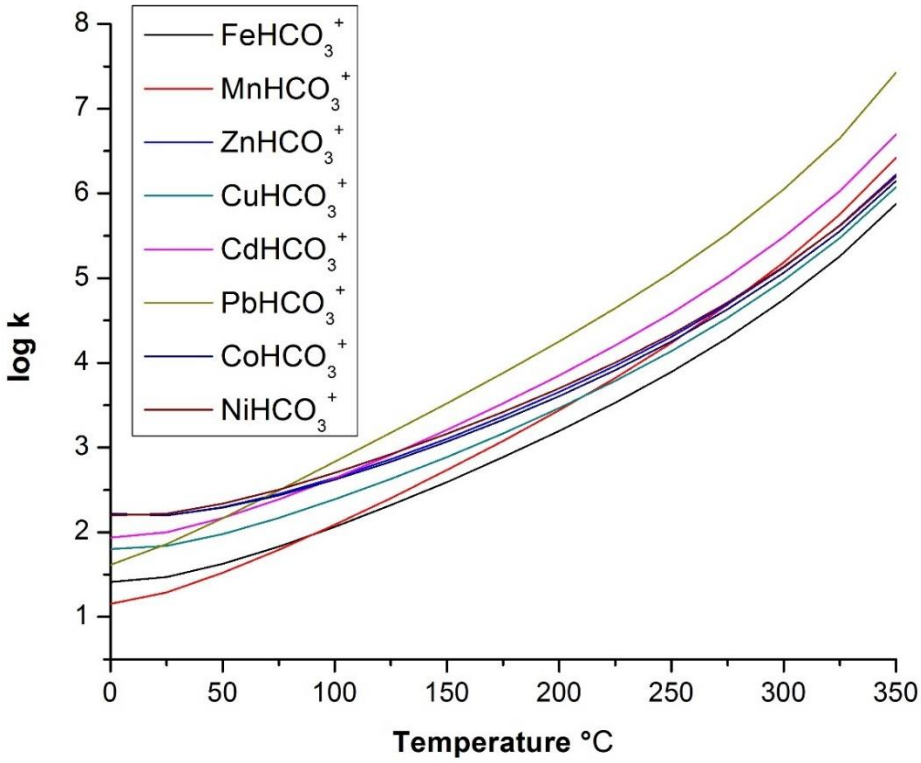

Figure A5 - Log k for the formation of divalent metal bicarbonate species from 0 – 350 °C for the the reaction $M^{++} + HCO_3^- \rightarrow MHCO_3$

Table A8 - Log k for the formation of divalent metal bicarbonate species from 0 – 350 °C. Log k is for the reaction $M^+ + HCO_3^- \rightarrow MHCO_3^0$

species	Experimental Log k (25°C)	0.1	50	100	150	200	250	300	350
$NaHCO_3^0$	0.161	0.20	0.20	0.37	0.62	0.94	1.34	1.89	2.82
$KHCO_3^0$	-0.26	-0.33	-0.14	0.15	0.48	0.87	1.33	1.95	3.03

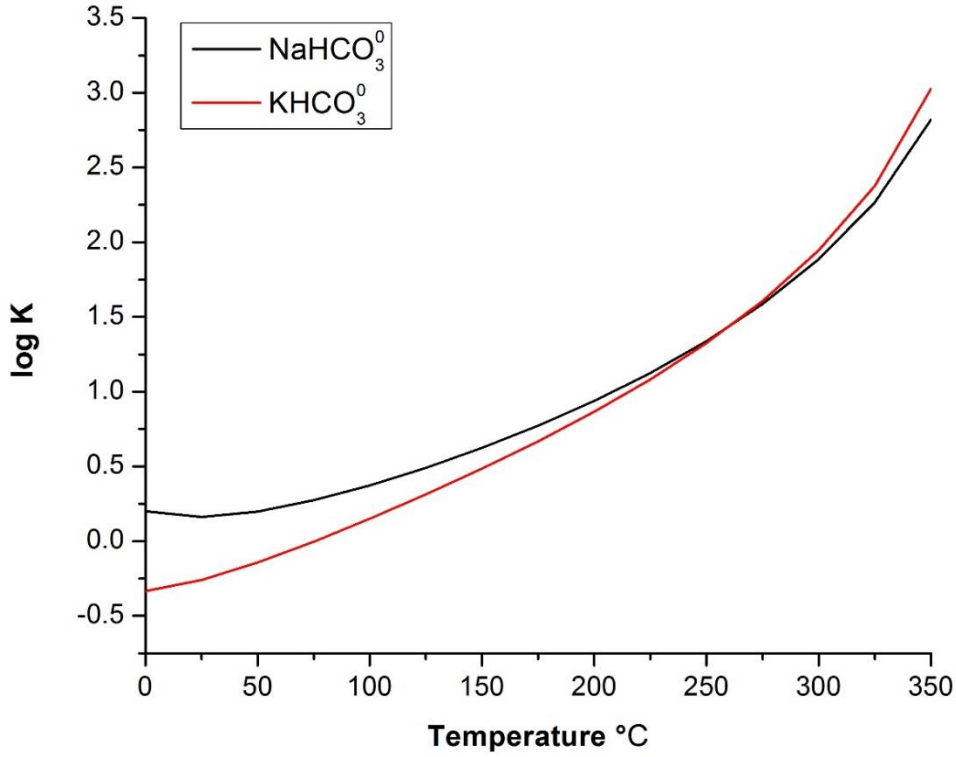

Figure A6 - Log k for the formation of divalent metal bicarbonate species from 0 – 350 °C for the reaction $M^+ + HCO_3^- \rightarrow MHCO_3^0$

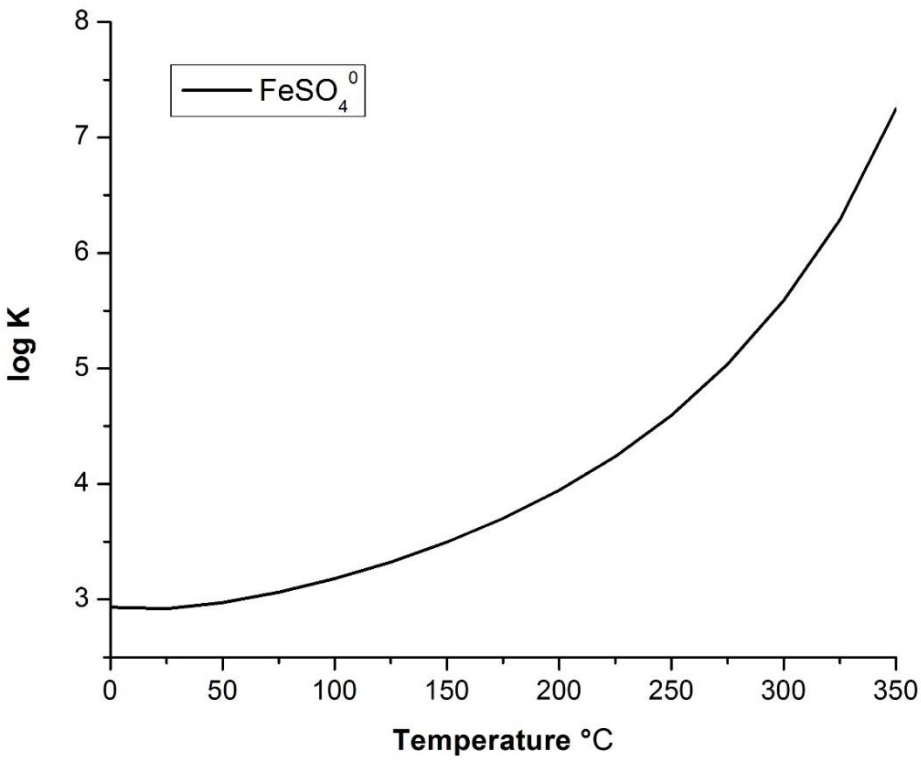

Figure A7 - Log k for the reaction $Fe^{+2} + SO_4^{-2} \rightarrow FeSO_4$ aq from 0-350 °C. Ferrous sulfate thermodynamic properties and HKF paramters were calculated using the same methods as ferrous carbonates, except $\Delta S°_r$ determined by Smith and Martell (1976) was used to calculate S°.

APPENDIX B

FIELD RATE EXPERIMENTS

This appendix contains data from rate experiments used throughout this Dissertation. The tables report the time, in either minutes or seconds, and concentration of Fe^{2+}.

Table B1 – Rate data from 150906 B, Conradins spring

Type	Replicate	#	**Time** minutes	**Fe^{2+}** mg/L	**Fe^{2+}** molal
Experimental	A	1	0	1.39	7.75E-05
		2	143	0.47	2.60E-05
		3	217	0.06	3.38E-06
		4	257	0.03	1.52E-06
	B	1	0	1.47	8.20E-05
		2	142	0.50	2.79E-05
		3	217	0.15	8.26E-06
		4	257	0.10	3.16E-06
	C	1	0	1.32	7.37E-05
		2	141	0.43	2.43E-05
		3	216	0.13	7.21E-06
		4	257	0.10	3.06E-06
In situ	A	1	0	0.32	1.78E-05
		2	141	0.04	2.30E-06
		3	216	0.01	5.62E-07
		4	257	BDL	BDL
	B	1	0	0.26	1.45E-05
		2	140	0.02	1.00E-06
		3	215	0.01	3.90E-07
		4	257	BDL	BDL
	C	1	0	0.24	1.35E-05
		2	150	0.02	1.05E-06
		3	214	0.01	4.67E-07
		4	257	0.01	3.24E-07
Killed	A	1	0	0.80	4.49E-05
		2	142	0.87	4.84E-05
		3	220	0.31	1.75E-05
		4	258	0.13	7.05E-06
	B	1	0	0.86	4.83E-05
		2	142	0.53	2.94E-05
		3	215	0.20	1.10E-05
		4	259	0.14	7.57E-06
	C	1	0	1.09	6.07E-05
		2	141	0.49	2.75E-05
		3	217	0.20	1.10E-05
		4	259	0.15	8.20E-06

Table B2 – Rate data from 150906C, Trap door spring at Val Sinestra

Type	Replicate	#	**Time** minutes	**Fe^{2+}** mg/L	**Fe^{2+}** molal
Experimental	A	1	0	5.39	3.05E-04
		2	70	4.92	2.75E-04
		3	110	4.56	2.54E-04
	B	1	0	5.52	3.08E-04
		2	71	5.25	2.93E-04
		3	111	4.79	2.68E-04
	C	1	0	6.24	3.49E-04
		2	70	5.85	3.27E-04
		3	112	5.32	2.97E-04
In situ	A	1	0	3.14	1.75E-04
		2	68	3.08	1.72E-04
		3	116	2.87	1.60E-04
	B	1	0	3.08	1.72E-04
		2	67	2.96	1.65E-04
		3	117	2.82	1.57E-04
	C	1	0	3.04	1.70E-04
		2	66	2.94	1.64E-04
		3	117	2.84	1.59E-04
Killed	A	1	0	5.43	3.03E-04
		2	66	5.66	3.16E-04
		3	120	5.26	2.94E-04
	B	1	0	5.31	2.97E-04
		2	66	5.21	2.91E-04
		3	122	4.83	2.70E-04
	C	1	0	5.10	2.85E-04
		2	67	5.25	2.93E-04
		3	123	4.87	2.72E-04

Table B3 – Rate data from 150907E, Rablönche Source. See figure 7 in the full text

Type	Replicate	#	**Time** minutes	**Fe^{2+}** mg/L	**Fe^{2+}** molal
Experimental	A	1	0	2.34	1.31E-04
		2	96	1.04	5.79E-05
		3	286	0.23	1.27E-05
	B	1	0	2.27	1.27E-04
		2	96	0.84	4.66E-05
		3	286	0.11	6.10E-06
	C	1	0	2.51	1.40E-04
		2	96	0.89	4.96E-05
		3	287	0.21	1.15E-05
In situ	A	1	0	1.04	5.80E-05
		2	96	0.31	1.75E-05
		3	287	0.02	1.21E-06
	B	1	0	1.08	6.04E-05
		2	96	0.31	1.74E-05
		3	287	0.02	8.95E-07
	C	1	0	1.00	5.59E-05
		2	96	0.28	1.57E-05
		3	287	0.01	3.05E-07
Killed	A	1	0	2.23	1.24E-04
		2	96	1.13	6.30E-05
		3	287	0.37	2.08E-05
	B	1	0	2.32	1.30E-04
		2	96	1.29	7.20E-05
		3	287	0.35	1.96E-05
	C	1	0	2.23	1.25E-04
		2	96	1.11	6.18E-05
		3	288	0.38	2.11E-05

Table B4 – Rate data from 150909K, Jori Lake XIII

Type	Replicate	#	**Time** minutes	**Fe^{2+}** mg/L	**Fe^{2+}** molal
Experimental	A	1	0	0.96	5.39E-05
		2	231	0.72	4.02E-05
		3	526	0.60	3.33E-05
		4	1217	0.02	1.18E-06
	B	1	0	0.98	5.45E-05
		2	230	0.92	5.16E-05
		3	525	0.53	2.98E-05
		4	1217	0.09	4.85E-06
	C	1	0	1.10	6.16E-05
		2	230	0.85	4.74E-05
		3	525	0.80	4.47E-05
		4	1218	0.05	2.62E-06
In situ	A	1	0	0.13	7.33E-06
		2	225	0.14	7.75E-06
		3	520	0.21	1.16E-05
		4	1211	0.03	1.59E-06
	B	1	0	0.31	1.73E-05
		2	203	0.16	8.86E-06
		3	490	0.13	7.05E-06
		4	1188	0.02	9.62E-07
	C	1	0	0.13	7.18E-06
		2	202	0.04	2.11E-06
		3	1188	BDL	BDL
		4		BDL	BDL
Killed	A	1	0	0.90	5.01E-05
		2	199	0.70	3.89E-05
		3	494	0.57	3.19E-05
		4	1183	0.56	3.81E-05
	B	1	0	1.11	8.28E-05
		2	200	0.85	4.75E-05
		3	487	0.67	3.72E-05
		4	1182	0.57	4.86E-05
	C	1	0	1.01	5.65E-05
		2	201	0.65	3.65E-05
		3	1181	0.63	4.82E-05

Table B5 – Rate data from 150911T, Eisenquelle

Type	Replicate	#	**Time** minutes	**Fe^{2+}** mg/L	**Fe^{2+}** molal
Experimental	A	1	0.0	0.83	4.61E-05
		2	2.7	0.69	3.84E-05
		3	17.8	0.57	3.16E-05
		4	50.7	0.19	1.04E-05
		5	81.2	0.02	1.12E-06
		6	110.9	0.01	3.62E-07
	B	1	0.0	0.58	3.21E-05
		2	40.5	0.16	9.17E-06
		3	70.9	0.06	3.22E-06
		4	101.1	0.01	6.86E-07
		5	126.3	0.01	2.86E-07
	C	1	0.0	0.70	3.92E-05
		2	38.0	0.28	1.56E-05
		3	68.6	0.15	8.14E-06
		4	99.0	0.1	3.00E-06
		5	123.6	0.0	4.48E-07
In situ	A	1	0	0.10	1.83E-06
		2	28	0.05	9.81E-07
		3	53	BDL	BDL
	B	1	0	0.09	1.54E-06
		2	27	0.04	6.29E-07
		3	53	BDL	BDL
	C	1	0	0.11	1.94E-06
		2	28	BDL	BDL
		3	54	BDL	BDL
Killed	A	1	0.0	0.72	4.01E-05
		2	53.7	0.40	2.23E-05
		3	84.2	0.31	1.73E-05
		4	110.1	0.21	1.19E-05
		5	143.7	0.16	8.70E-06
	B	1	0.0	1.19	6.66E-05
		2	46.6	0.72	4.01E-05
		3	72.0	0.45	2.49E-05
		4	98.4	0.35	1.94E-05
	C	1	0.0	1.23	6.89E-05
		2	48.3	0.52	2.91E-05
		3	73.1	0.33	1.84E-05
		4	100.0	0.24	1.34E-05
		5	132.9	0.09	4.79E-06

Table B6 – Rate data from 150910O, Jöri lake II

Type	Replicate	#	**Time** minutes	**Fe^{2+}** mg/L	**Fe^{2+}** molal
Experimental	A	1	0	0.51	2.86E-05
		2	121.0	0.35	1.97E-05
		3	251.0	0.05	2.62E-06
	B	1	0	0.62	3.48E-05
		2	120.0	0.42	2.33E-05
		3	249.0	0.48	2.66E-05
	C	1	0	0.71	3.97E-05
		2	119.0	0.20	1.11E-05
		3	0	0.12	6.75E-06
In situ	A	1	118.0	0.01	7.52E-07
		2	251.0	0.01	7.90E-07
		3	0	0.03	1.44E-06
	B	1	117.0	0.01	5.43E-07
		2	247.0	0.01	3.52E-07
		3	0	0.03	1.76E-06
	C	1	116.0	0.02	1.20E-06
		2	246.0	0.00	4.76E-08
		3	0	0.88	4.92E-05
Killed	A	1	115.0	0.52	2.93E-05
		2	245.0	0.47	2.62E-05
		3	0	0.98	5.47E-05
	B	1	114.0	0.73	4.09E-05
		2	244.0	0.47	2.60E-05
		3	0	0.92	5.11E-05
	C	1	114.0	0.86	4.80E-05
		2	233.0	0.80	4.47E-05
		3	0	0.51	2.86E-05

Table B7 – Rate data from 150908J, Rablönche OF 5

Type	Replicate	#	**Time** seconds	**Fe^{2+}** mg/L	**Fe^{2+}** molal
Experimental	A	1	21	1.23	6.86E-05
		2	70	0.87	4.85E-05
		3	131	0.38	2.10E-05
		4	207	0.20	1.12E-05
		5	302	0.08	4.68E-06
	B	1	32	0.59	3.29E-05
		2	77	0.40	2.24E-05
		3	132	0.18	9.80E-06
		4	192	0.09	4.79E-06
		5	264	0.04	2.34E-06
	C	1	24	0.44	2.48E-05
		2	82	0.22	1.24E-05
		3	131	0.13	7.30E-06
		4	197	0.1	2.89E-06
		5	256	BDL	BDL
Filtered spring water	A	1	21	1.23	6.85E-05
		2	74	0.60	3.33E-05
		3	144	0.24	1.34E-05
		4	196	0.13	7.36E-06
		5	250	0.07	3.70E-06
	B	1	30	1.07	5.96E-05
		2	81	0.49	2.74E-05
		3	162	0.17	9.77E-06
		4	224	0.08	4.52E-06
	C	1	26	1.13	6.32E-05
		2	93	0.49	2.74E-05
		3	145	0.20	1.09E-05
		4	255	0.07	4.13E-06
		5	318	0.03	1.91E-06

Table B8 – Rate data from 150907G, Rablönche OF 6. See Figure 8 in the full text of this paper for plots of these data.

Type	Replicate	#	**Time** seconds	**Fe^{2+}** mg/L	**Fe^{2+}** molal
Experimental	A	1	30	0.67	3.74E-05
		2	123	0.14	7.96E-06
		3	235	0.03	1.70E-06
	B	1	20	0.63	3.54E-05
		2	60	0.22	1.24E-05
		3	122	0.10	5.40E-06
		4	170	0.05	3.05E-06
	C	1	16	1.07	5.96E-05
		2	52	0.48	2.70E-05
		3	107	0.15	8.50E-06
		4	147	0.08	4.38E-06
		5	193	0.05	2.95E-06
Filtered spring water	A	1	16	0.83	4.66E-05
		2	43	0.48	2.67E-05
		3	72	0.25	1.40E-05
		4	112	0.10	5.58E-06
		5	148	0.04	2.05E-06
	B	1	14	1.01	5.63E-05
		2	49	0.38	2.10E-05
		3	80	0.20	1.12E-05
		4	115	0.08	4.70E-06
		5	150	0.05	2.54E-06
	C	1	12	1.01	5.62E-05
		2	48	0.42	2.33E-05
		3	93	0.15	8.58E-06
		4	130	0.06	3.30E-06
		5	164	0.04	2.09E-06

Table B9 – Rate data from 150909M, Jori Lake 20. Fe^{2+} measurements in this experiment are all at or below the detection limit by the second measurement point. The rates calculated in table 4 are minimum rates determined by assuming the 0.5 mg / L ferrous iron is all depleted in 30 seconds.

Type	Replicate	#	**Time** seconds	**Fe^{2+}** mg/L	**Fe^{2+}** molal
Filtered spring water	Experimental				Not determined
	A	1	0	0.5[#]	8.95E-06[#]
		2	15	0.02	3.14E-07
		3	26	BDL	BDL
	B	1	0	0.5[#]	8.95E-06[#]
		2	13	0.04	7.90E-07
		3	27	BDL	BDL
	C	1	0	0.5[#]	8.95E-06[#]
		2	15	0.02	3.14E-07
		3	25	BDL	BDL

[#] indicates the concentration of added Fe(II) at T=0, which assumes all Fe(II) is from added reagents.

Table B10 – Rate data from Arvadi 150905A

Type	Replicate	#	**Time** seconds	**Fe^{2+}** mg/L	**Fe^{2+}** molal
Experimental	A	1	15	1.22	2.18E-05
		2	45	0.75	1.34E-05
		3	90	0.34	6.09E-06
		4	121	0.29	5.19E-06
		5	153	0.19	3.40E-06
	B	1	17	1.20	2.15E-05
		2	44	0.89	1.59E-05
		3	88	0.37	6.62E-06
		4	136	0.15	2.69E-06
		5	165	BDL	BDL
	C	1	15	1.08	1.93E-05
		2	51	0.74	1.32E-05
		3	82	0.31	5.55E-06
		4	114	0.05	8.95E-07
		5	141	BDL	BDL
Filtered spring water	A	1	14	1.20	2.15E-05
		2	38	0.66	1.18E-05
		3	65	0.37	6.68E-06
		4	85	0.30	5.30E-06
		5	104	0.29	5.19E-06
		6	165	0.01	2.19E-07
	B	1	17	1.11	1.98E-05
		2	42	0.61	1.09E-05
		3	69	0.40	7.08E-06
		4	99	0.31	5.48E-06
		5	121	0.25	4.50E-06
	C	1	15	0.63	1.13E-05
		2	50	0.22	3.87E-06
		3	82	0.13	2.31E-06
		4	135	0.02	2.76E-07

Table B11 – Rate data from Ferrous Spa 130928B

Type	Replicate	#	**Time** seconds	**Fe^{2+}** µmolal
Experimental	A	1	0	434
		2	123	320
		3	218	188
	B	1	0	446
		2	124	294
		3	218	174
	C	1	0	437
		2	125	268
		3	218	73
In situ	A	1	0	231
		2	126	43
		3	218	0
	B	1	0	220
		2	129	80
		3	219	9
	C	1	0	224
		2	129	66
		3	219	12
killed	A	1	0	389
		2	130	339
		3	219	341
	B	1	0	383
		2	131	335
		3	220	308
	C	1	0	437
		2	131	376
		3	221	292

Table B12 – Rate data from Ferrous Spa 130929G

Type	Replicate	#	**Time** seconds	**Fe^{2+}** µmolal
Experimental	A	1	0	355
		2	123	376
		3	218	221
	B	1	0	496
		2	124	321
		3	218	269
	C	1	0	496
		2	125	326
		3	218	254
In situ	A	1	0	84
		2	126	55
		3	218	BDL
	B	1	0	93
		2	129	56
		3	219	36
	C	1	0	102
		2	129	66
		3	219	36
killed	A	1	0	489
		2	130	508
		3	219	420
	B	1	0	586
		2	131	496
		3	220	446
	C	1	0	505
		2	131	497
		3	221	446

Table B13 – Rate data from Bamboozled 141122D

Type	Replicate	#	**Time** minutes	**Fe^{2+}** µmolal
Experimental	A	1	0	456
		2	45	330
		3	78	265
		4	134	228
		5	187	170
	B	1	0	379
		2	45	311
		3	71	284
		4	126	213
		5	177	102
	C	1	0	212
		2	56	163
		3	106	139
Filtered spring water	A	1	44	515
		2	95	471
		3	152	463
		4	206	470
	B	1	0	502
		2	46	483
		3	90	458
		4	146	447
		5	200	444
	C	1	0	544
		2	48	490
		3	83	475
		4	139	474
		5	194	473

APPENDIX C

ADDITIONAL SUPPORTING DATA FOR CHAPTER 1

Table C1 – UTM coordinates of sample sites in this Chapter 1

Area	**Sample ID**	**Sample name**	**latitude** UTM 32T	**longitude** UTM	**elevation** meters
Alvaneu	150905A	Arvadi Spring	548'783	5'168'030	929
	150911T	Eisenquelle	551'098	5'168'699	961
Val Sinestra	150906B	Conradins Spring	601'934	5'189'515	1477
	150906C	Trap Door	601'935	5'189'513	1477
	150906D	Back Fountain	601'928	5'189'517	1477
	150908H	Pipe outlet riverbed	601'964	5'189'509	1470
	150908I	La Brancha River	601'965	5'189'513	1470
Rablönche	150907F	Rablönche OF4	600'889	5'184'393	1190
	150907G	Rablönche OF6	600'896	5'184'374	1183
	150908J	Rablönche OF5	600'893	5'184'375	1183
Jöri Lakes	150909K	Jöri Lake XIII	573'286	5'180'755	2639
	150909N	Jöri Lake XII 10m Depth	573'337	5'180'800	2629
	150909L	Jöri Lake XIII OF	573'337	5'180'800	2639
	150909M	Jöri Lake XX	573'334	5'180'422	2668
	150910O	Jöri Lake II	574'139	5'181'021	2491
	150910P	Snow above Jöri XIII	573'268	5'180'598	2648
	150910Q	Lake XIX	573'423	5'180'059	2720
	150910R	Lake XVIII	573'512	5'180'001	2731
	150910S	Lake XXII (new)	573'568	5'179'889	2737

Table C2 - Rablönche outflow profile (from figure 2)

Distance meters	**pH**	**Temperature** °C	**Conductivity** µS / cm	**oxygen** µmolal	**Fe (II)** µmolal
0 (150907F)	6.32	11.1	1674	162	93.2
2	6.38	11.0	1600	198	89.0
4	6.60	11.0	1560	228	77.2
6	6.63	11.0	1668	245	72.5
8	6.85	11.6	1675	274	56.5
10	7.12	12.1	1685	298	48.1
12	7.42	11.3	1628	313	35.3
14	7.60	11.3	1315	315	21.2
16	7.62	11.0	1350	315	15.7
18	7.66	11.0	1408	318	12.0
20	7.70	10.7	1386	318	3.4

Table C3 – Val Sinestra outflow profile (from figure 4)

Distance meters	**pH**	**Temperature** °C	**Conductivity** µS / cm	**oxygen** µmolal	**Fe (II)** µmolal
0 (150906C)	6.11	8.6	2886	1.4	166
21	6.179	8.5	2895	43	154.7
23	6.2239	8.4	2889	91	159.0
25	6.33	8.4	2886	124	152.5
27	6.368	8.4	2852	135	148.9
29	6.412	8.5	2836	161	145.2
31	6.463	8.5	2841	179	141.9
33	6.483	8.4	2780	184	139.4
35	6.528	8.2	2860	200	136.2

Table C4 - Arvadi Outflow profile

Distance Meters	**pH**	**Temperature** °C	**Conductivity** µS / cm	**oxygen** µmolal	**Fe (II)** µmolal
0 (150905A)	7.93	7.8	1118	314	2.5
5	8.033	7.8	1116	313	2.0
8	8.048	7.8	1118	313	1.8
11	8.051	7.8	1117	313	1.8
14	8.068	7.9	1118	314	1.6
17	8.066	7.8	1118	314	1.6
20	8.082	7.9	959	316	1.6

Table C5 – Speciation of Fe(II) in springs and lakes. All units are mol / L

Sample ID	Name	Fe^{+2}	$FeCO_3$ (aq)	$FeHCO_3^+$	$Fe(CO_3)_2^{-2}$	$FeSO_4$ (aq)	$FeOH^+$	$Fe(OH)_2$	$FeCl^+$	FeF^+
150905A	Arvadi Spring	8.48E-07	1.20E-06	4.71E-08	1.46E-09	4.0E-07	6.24E-09	$<10^{-12}$	5.12E-12	1.03E-09
150911T	Eisenquelle	2.72E-06	4.75E-07	7.47E-08	8.59E-11	1.74E-06	4.84E-09	$<10^{-12}$	1.99E-11	2.66E-09
150906B	Conradins	6.00E-05	3.55E-05	3.10E-05	3.33E-08	7.29E-06	1.78E-08	$<10^{-12}$	4.56E-07	1.82E-08
150906C	Trap Door	1.14E-04	1.11E-05	2.91E-05	1.06E-09	1.14E-05	1.28E-08	$<10^{-12}$	4.93E-07	3.35E-08
150906D	Back Fountain	4.47E-07	6.65E-07	2.48E-07	1.75E-09	6.63E-08	3.20E-10	$<10^{-12}$	4.43E-09	1.96E-10
150908H	River Outlet	7.95E-05	3.59E-05	2.92E-05	1.83E-08	7.04E-06	2.79E-08	1.83E-08	3.27E-07	2.03E-08
150907F	Rablönche OF4	5.97E-05	1.36E-05	2.10E-05	2.62E-09	1.44E-06	1.34E-08	$<10^{-12}$	1.93E-08	7.44E-09
150907G	Rablönche OF6	2.28E-07	1.83E-06	7.21E-08	1.19E-08	5.97E-09	1.99E-09	$<10^{-12}$	**8.21E-11**	5.33E-11
150908J	Rablönche OF5	4.34E-06	2.23E-05	1.49E-06	9.25E-08	1.05E-07	2.49E-08	$<10^{-12}$	1.52E-09	4.82E-10
150909N	Jöri Lake XIII 10m Depth	1.55E-05	4.63E-08	3.62E-08	$<10^{-12}$	2.98E-08	6.98E-09	$<10^{-12}$	2.43E-11	2.90E-09

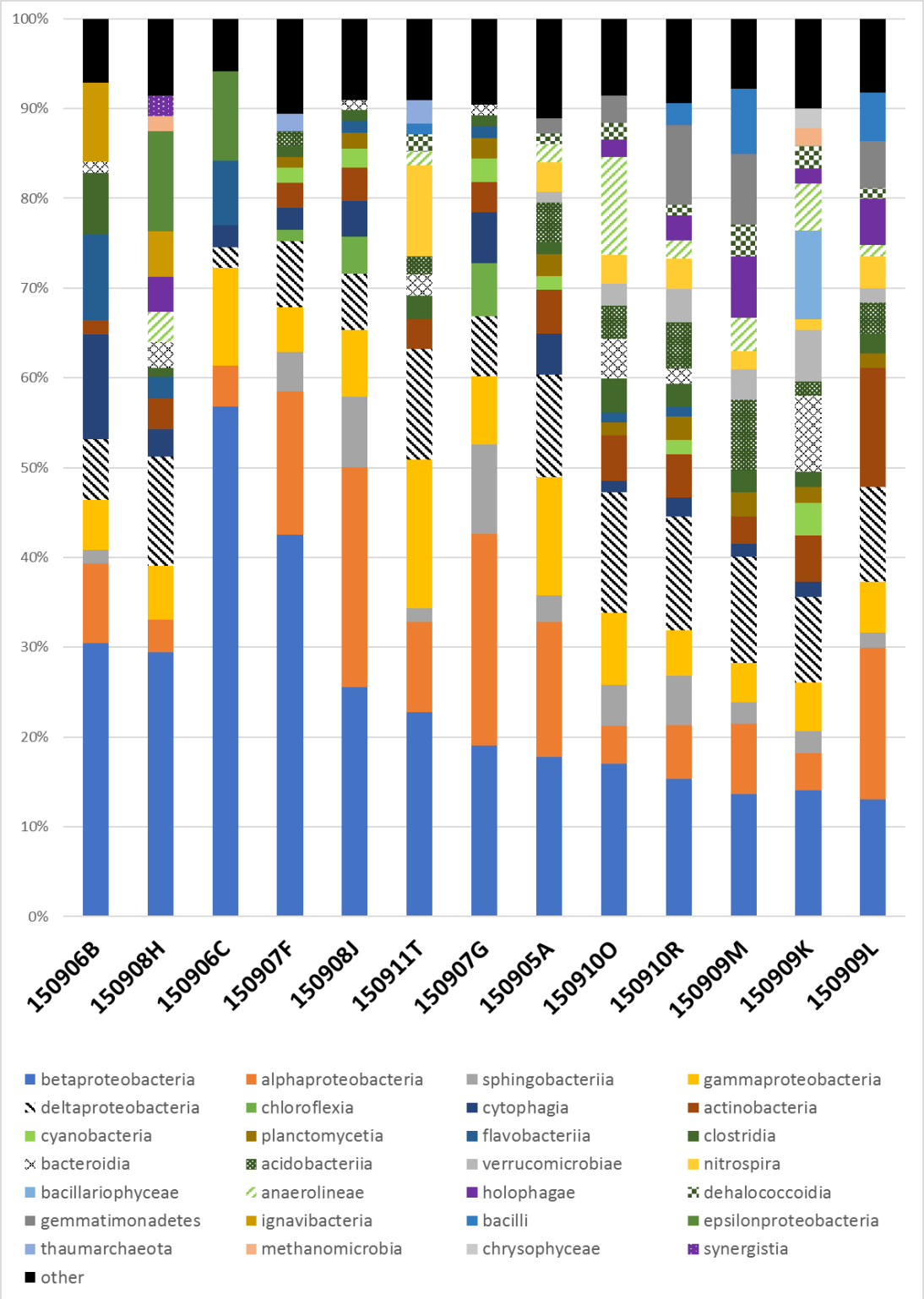

Figure C1 – Family level phylogenetic data for Swiss springs and lakes.

Table C6 – Organic acid abundances for swiss springs and lakes

Sample	name	formate ppb	stdev	Lactate ppb	stdev	acetate ppb	stdev
150905A	Arvadi Spring	55.6	0.0	BDL		BDL	
150911T	Eisenquelle Source	BDL		BDL		BDL	
150906B	Conradins/Val Sin	BDL		37.9	4.2	BDL	
150906C	Trap Door	BDL		BDL		BDL	
150906D	Back Fountain	9.3	0.0	29.5	0.0	BDL	
150908H	River Outlet	BDL		BDL		BDL	
150907F	Rablonche OF4	8.9	1.1	BDL		BDL	
150907G	Rablonche OF6	BDL		10.5	2.1	BDL	
150908J	Rablonche OF5	BDL		BDL		BDL	
150909K	Jori Lake 13	BDL		BDL		BDL	
150909L	Jori Lake 13 OF	BDL		BDL		BDL	
150909M	Jori Lake 20	BDL		BDL		BDL	
150909N	Jori Lake 13 10m Depth	BDL		16.8	4.2	10.5	3.5
150910O	Jori Lake 2	39.7	7.7	BDL		BDL	
150910P	Snow above Jori 13	BDL		BDL		BDL	
150910Q	Jori lake 19	BDL		BDL		BDL	
150910R	Jori Lake 18	BDL		BDL		BDL	
150910S	Jori lake emphemeral	BDL		BDL		BDL	

APPENDIX D

MICROBIAL COMMUNITY COMPOSITION OF EXPERIMENTAL LOCATIONS

This section contains species level phylogenetic data for each experimental locations in support of chapters 2,3,4. Only species with 1% or greater relative abundance are reported here. Switzerland samples were amplified with universal primers (see methods) and have one list of species per sampling location. Yellowstone samples were amplified with bacterial and archaeal specific primers and have those domains listed separately. Percentage for YNP samples is indicative of the relative percentage of each species in each domain.

Table D1 – Species level community composition of springs and lakes in the Swiss Alps. Community members that are only reported at the genus level indicate that only the closest genus could be determined for the sequences.

Sample ID	**Species**	**% Abundance**
150905A	*Thiobacillus spp.*	6.26
	Acidobacterium spp.	4.17
	Nitrospira spp.	3.20
	Cytophaga spp.	2.34
	Geobacter spp.	1.75
	Gemmatimonas spp.	1.69
	Nordella spp.	1.57
	Mesorhizobium spp.	1.47
	Cyanobacterium spp.	1.41
	Anaeromyxobacter spp.	1.39
	Beggiatoa spp.	1.39
	Hyphomicrobium spp.	1.36
	Thiorhodospira spp.	1.33
	Ohtaekwangia spp.	1.29
	Pseudoxanthomonas koreensis	1.22
	Dehalococcoides spp.	1.13
	Gallionella spp.	1.10
	Other	65.92
150906B	*Cytophaga spp.*	11.36
	Nitrosomonas spp.	9.34
	Gallionella spp.	6.90
	Clostridium spp.	6.25
	Maribacter sp.	6.17
	Ignavibacterium spp.	5.77
	Propionivibrio spp.	4.05
	Ignavibacterium album	2.34
	Pseudorhodobacter sp.	2.27
	Anaeromyxobacter dehalogenans	2.22
	Flavobacterium sp.	1.99
	Xanthomonas sp.	1.77
	Sphingomonas arctic sea	1.56
	Algisphaera agarilytica	1.35
	Geobacter spp.	1.33
	Sideroxydans spp.	1.11
	Thiohalomonas denitrificans	1.11
	Roseovarius sp.	1.07
	Other	32.02
150906C	*Gallionella spp.*	44.31
	Sulfuricurvum spp.	9.73
	Xanthomonas sp.	3.83
	Luteimonas spp.	2.95
	Fluviicola spp.	2.87
	Flavobacterium sp.	2.37
	Cytophaga spp.	2.36
	Acidovorax delafieldii	1.97
	Sphingomonas arctic sea	1.82
	Silanimonas mangrovi	1.60
	Geobacter spp.	1.00
	Other	25.19
150908H	*Sulfuricurvum spp.*	10.75
	Gallionella spp.	9.80
	Geobacter spp.	5.02
	Thiobacillus spp.	4.89
	Ignavibacterium spp.	4.38
	Holophaga spp.	3.78

	Cytophaga spp.	2.93
	Longilinea spp.	2.86
	Thermanaerovibrio spp.	2.26
	Acidovorax delafieldii	2.26
	Pelobacter spp.	1.88
	Anaeromyxobacter spp.	1.85
	Rhodoferax spp.	1.54
	Gallionella sp.	1.53
	Prolixibacter spp.	1.48
	Luteimonas spp.	1.37
	Streptomyces spp.	1.22
	Thioalkalivibrio spp.	1.11
	Other	39.08
150911T	*Crenothrix polyspora*	10.49
	Nitrospira spp.	8.16
	Sideroxydans spp.	5.62
	Gallionella spp.	4.20
	Geobacter spp.	4.08
	Mesorhizobium spp.	2.20
	Pelobacter spp.	1.87
	Acidobacterium spp.	1.81
	Thermodesulfovibrio spp.	1.79
	Dehalococcoides spp.	1.70
	Anaeromyxobacter spp.	1.31
	Azonexus spp.	1.18
	Petrimonas spp.	1.11
	Cupriavidus spp.	1.02
	Other	53.46
150907G	*Leadbetterella sp.*	3.12
	Oscillochloris spp.	2.14
	Chloroflexus spp.	2.02
	Chitinophaga spp.	1.98
	Paucibacter toxinivorans	1.82
	Novosphingobium stygium	1.61
	Terrimonas spp.	1.56
	Cytophaga spp.	1.48
	Gallionella spp.	1.47
	Phormidium autumnale	1.36
	Rhodobacter spp.	1.30
	Thiobacillus spp.	1.28
	Leptothrix spp.	1.17
	Lewinella spp.	1.09
	Haliscomenobacter spp.	1.08
	Rhodoferax spp.	1.05
	Sediminibacterium spp.	1.01
	Other	73.46
150908J	*Gallionella spp.*	3.31
	Oscillochloris spp.	2.27
	Leadbetterella sp.	2.10
	Paucibacter toxinivorans	1.97
	Curvibacter spp.	1.82
	Thiobacillus spp.	1.65
	Rhodobacter spp.	1.61
	Novosphingobium stygium	1.59
	Rhodoferax spp.	1.58
	Rhodobacter katedanii	1.38
	Rhodoferax ferrireducens	1.35
	Leptothrix spp.	1.34
	Phormidium autumnale	1.29
	Frigoribacterium sp.	1.28
	Chitinophaga spp.	1.24

	Rhodobacter capsulatus	1.23
	Terrimonas spp.	1.20
	Hyphomonas spp.	1.15
	Methylibium spp.	1.14
	Chloroflexus spp.	1.10
	Cytophaga spp.	1.05
	Pseudorhodobacter sp.	1.01
	Beijerinckia spp.	1.00
	Other	65.34
150907F	*Gallionella spp.*	23.89
	Bdellovibrio sp.	2.32
	Paucibacter toxinivorans	1.58
	Acidobacterium spp.	1.56
	Geobacter spp.	1.28
	Rhodobacter spp.	1.28
	Acidovorax delafieldii	1.28
	Porphyrobacter spp.	1.23
	Sideroxydans spp.	1.20
	Curvibacter spp.	1.16
	Methylibium spp.	1.06
	Other	62.16
150909K	*Alkaliflexus spp.*	7.84
	Levilinea spp.	3.73
	Cyanobacterium spp.	3.45
	Massilia spp.	3.28
	Verrucomicrobium spp.	2.86
	Dehalococcoides spp.	2.51
	Methylobacter spp.	2.38
	Burkholderia spp.	2.13
	Pedosphaera spp.	1.98
	Anaeromyxobacter spp.	1.98
	Holophaga spp.	1.77
	Geobacter spp.	1.71
	Longilinea spp.	1.63
	Nitrosovibrio spp.	1.54
	Cytophaga spp.	1.51
	Acidobacterium spp.	1.49
	Nitrospina spp.	1.42
	Solirubrobacter spp.	1.25
	Nitrospira spp.	1.20
	Steroidobacter spp.	1.19
	Anaeromyxobacter dehalogenans	1.19
	Prolixibacter spp.	1.19
	Gallionella spp.	1.09
	Ferrithrix spp.	1.01
	Other	48.68
150909L	*Bradyrhizobium spp.*	6.84
	Rhodococcus spp.	5.74
	Gemmatimonas spp.	5.34
	Thermoflavimicrobium spp.	5.28
	Holophaga spp.	5.12
	Nitrospira spp.	3.43
	Geobacter spp.	3.25
	Anaeromyxobacter spp.	3.22
	Steroidobacter spp.	2.68
	Acidobacterium spp.	2.38
	Pseudonocardia halophobica	1.63
	Nitrosovibrio spp.	1.61
	Thiobacillus spp.	1.58
	Ktedonobacter spp.	1.46
	Hyphomicrobium spp.	1.33

	Dehalococcoides spp.	1.14
	Rhodocista spp.	1.11
	Other	46.85
150909M	*Gemmatimonas spp.*	7.81
	Holophaga spp.	6.75
	Acidobacterium spp.	6.72
	Thermoflavimicrobium spp.	6.67
	Geobacter spp.	4.22
	Dehalococcoides spp.	3.14
	Nitrosospira spp.	1.97
	Nitrospira spp.	1.87
	Levilinea spp.	1.63
	Anaeromyxobacter spp.	1.61
	Nitrosovibrio spp.	1.59
	Janthinobacterium lividum	1.40
	Verrucomicrobium spp.	1.22
	Rhodocista spp.	1.22
	Other	52.18
150910O	*Levilinea spp.*	5.54
	Geobacter spp.	3.78
	Acidobacterium spp.	3.41
	Nitrospira spp.	3.09
	Gemmatimonas spp.	3.04
	Bellilinea spp.	2.69
	Alkaliflexus spp.	2.66
	Burkholderia spp.	2.47
	Methylobacter spp.	2.45
	Massilia spp.	2.40
	Steroidobacter spp.	1.94
	Dehalococcoides spp.	1.77
	Solitalea canadensis	1.65
	Longilinea spp.	1.56
	Thermaerobacter spp.	1.53
	Holophaga spp.	1.34
	Gallionella spp.	1.20
	Nitrosospira spp.	1.06
	Desulfobacterium spp.	1.06
	Other	55.38
150910R	*Gemmatimonas spp.*	9.09
	Geobacter spp.	6.44
	Nitrospira spp.	3.24
	Acidobacterium spp.	3.04
	Holophaga spp.	2.49
	Chitinophaga spp.	2.44
	Thermoflavimicrobium spp.	2.23
	Nitrosospira spp.	1.76
	Janthinobacterium lividum	1.47
	Ohtaekwangia spp.	1.36
	Cyanobacterium spp.	1.30
	Zavarzinella spp.	1.20
	Burkholderia spp.	1.12
	Prosthecobacter spp.	1.11
	Gallionella spp.	1.07
	Dehalococcoides spp.	1.05
	Levilinea spp.	1.04
	Anaeromyxobacter spp.	1.02
	Verrucomicrobium spp.	1.01
	Other	56.51

Table D2 – Species level community composition of hot springs at Yellowstone National Park. Community members that are only reported at the genus level indicate that only the closest genus could be determined for the sequences.

	Archaea		**Bacteria**	
Sample ID	**Species**	**%**	**Species**	**%**
150717FB	*Thermofilum*	80.20	*Myxosarcina sp.*	29.01
	Sulfolobus islandicus	5.36	*Ralstonia* spp.	15.13
	Sulfolobus	4.25	*Carboxydocella manganica*	13.53
	Thermogladius cellulolyticus	2.34	*Ralstonia sp.*	7.52
	Sulfolobus beitou	1.36	*Acidithiobacillus caldus*	2.43
	Vulcanisaeta	1.26	*Streptococcus thermophilus*	2.26
	Stygiolobus	1.06	*Pseudomonas veronii*	2.20
	Other	4.16	*Sediminibacterium* spp.	2.16
			Hydrogenobaculum sp.	2.04
			Ferrimicrobium spp.	1.75
			Terrimonas pekingensis	1.60
			Niastella spp.	1.34
			Delftia spp.	1.13
			Burkholderia sp.	1.04
			Other	16.83
150718FC	*Stygiolobus sp.*	51.13	*Nd*	
	Vulcanisaeta spp.	29.81		
	Stygiolobus spp.	8.26		
	Sulfolobus thuringiensis	1.95		
	Sulfolobus tokodaii	1.93		
	Sulfolobus sp.	1.19		
	Acidianus infernus	0.98		
	Other	4.75		
150719FG	*Methanobacterium sp.*	37.17	*Desulfovirga adipica*	31.18
	Unclutured candidatus nitrosocaldus sp.	26.06	*Desulfuromonas* spp.	13.15
	Thermofilum sp.	13.10	*Leptospirillum ferrodiazotrophum*	12.04
	Methanomassiliicoccus sp.	5.16	*Cyanobacterium* spp.	11.19
	Aciduliprofundum sp.	4.05	*Acidobacterium* spp.	5.05
	Candidatus caldiarchaeum subterraneum	3.46	*Desulfurella kamchatkensis*	3.40
	Candidatus nitrosocaldus yellowstonii	2.50	*Desulfomonile tiedjei*	3.03
	Methanocella sp.	1.18	*Ignavibacterium* spp.	1.87
	Other	7.32	*Thiomonas sp.*	1.60
			Steroidobacter spp.	1.27
			Pelobacter spp.	1.21
			Desulfomonile spp.	1.10
			Other	13.91
150720FH	*Vulcanisaeta* spp.	93.37	*Hydrogenobaculum sp.*	52.22
	Caldococcus sp.	2.62	*Propionibacterium acnes*	19.96
	Stygiolobus sp.	1.33	*Acidisphaera* spp.	11.18
		2.69	*Streptococcus thermophilus*	7.24
			Staphylococcus spp.	2.29
			Lactococcus lactis	1.58
			Other	5.53
150725T	*Aciduliprofundum sp.*	39.87	*Pseudomonas veronii*	32.88
	Thermoplasma sp.	32.63	*Delftia* spp.	10.29
	Candidatus nitrososphaera gargensis	7.51	*Ralstonia* spp.	7.21
	Sulfolobus islandicus	6.91	*Pseudomonas trivialis*	4.85
	Caldisphaera draconis	4.42	*Anaerococcus sp.*	4.72
	Thermocladium sp.	2.04	*Carboxydocella manganica*	4.55
	Thermogymnomonas acidicola	1.93	*Sphingobacterium sp.*	3.49
	Sulfolobus sp.	1.15	*Propionibacterium acnes*	3.38

	Other	3.54	*Ralstonia sp.*	3.28
			Sphingobacterium spp.	2.50
			Sediminibacterium salmoneum	2.32
			Hydrogenobaculum sp.	2.02
			Sediminibacterium spp.	1.50
			Planomicrobium okeanokoites	1.21
			Other	15.79
150728FQ	*Aciduliprofundum sp.*	73.94	*Acidobacterium* spp.	44.44
	Thermoplasma sp.	18.91	*Caldisericum exile*	11.34
	Candidatus nitrososphaera gargensis	3.31	*Nitrospira* spp.	6.09
	Thermogymnomonas acidicola	1.46	*Chlorogloeopsis sp.*	2.91
	Other	2.38	*Planifilum fulgidum*	2.85
			Lutispora spp.	2.39
			Desulfuromonas spp.	2.33
			Thermanaerothrix daxensis	2.23
			Vibrio sp.	1.79
			*Geobacillus stear*Other*mophilus*	1.53
			Thermodesulfobacterium geofontis	1.12
			Other	20.98
140804FL	*Aciduliprofundum sp.*	49.82	*Propionibacterium acnes*	46.16
	Candidatus nitrososphaera gargensis	16.62	*Streptococcus thermophilus*	24.21
	Sulfolobus islandicus	13.02	*Staphylococcus* spp.	8.08
	Caldisphaera draconis	8.40	*Ralstonia* spp.	3.01
	Thermocladium sp.	4.47	*Carboxydocella manganica*	1.88
	Sulfolobus sp.	2.21	*Pseudomonas veronii*	1.61
	Vulcanisaeta spp.	1.96	*Streptococcus oralis*	1.59
	Other	3.50	*Ralstonia sp.*	1.58
			Streptococcus spp.	1.38
			Anaerococcus sp.	1.21
			Other	9.29
130714SX	*Vulcanisaeta* spp.	91.35	*Hydrogenobaculum sp.*	96.65
	Caldococcus sp.	2.94	Other	3.35
	Sulfolobus sp.	1.45		
	Other	4.26		
130718SP	*Acidiplasma ferroplasma cyprexacervatum*	44.91	*Hydrogenobaculum sp.*	41.39
	Thermoplasma acidophilum	13.32	*Acidithiobacillus caldus*	36.10
	Sulfolobus sp.	11.76	*Desulfurella kamchatkensis*	14.15
	Aciduliprofundum sp.	7.25	*Acidisphaera* spp.	2.03
	Candidatus nitrososphaera gargensis	5.09	*Hydrogenobaculum* spp.	1.90
	Acidianus brierleyi	4.81	*Myxosarcina sp.*	1.20
	Thermofilum sp.	4.57	Other	3.24
	Ferroplasma sp.	1.96		
	Caldisphaera draconis	1.31		
	Vulcanisaeta spp.	1.04		
	Other	3.99		
130721SF	*Vulcanisaeta* spp.	83.43	*Pseudomonas veronii*	34.24
	Stygiolobus sp.	8.01	*Propionibacterium acnes*	12.00
	Sulfolobus tokodaii	1.71	*Delftia* spp.	9.18
	Stygiolobus spp.	1.63	*Anaerococcus sp.*	6.43
	Other	5.22	*Pseudomonas trivialis*	5.73
			Ralstonia spp.	3.00
			Streptococcus spp.	2.78
			Curvibacter spp.	2.72
			Propionibacterium sp.	2.44
			Carboxydocella manganica	2.43
			Moheibacter sediminis	2.35

			Ralstonia sp.	1.89
			Other	14.81
140803FI	*Stygiolobus sp.*	86.71	*Hydrogenobaculum sp.*	63.99
	Vulcanisaeta spp.	3.84	*Propionibacterium acnes*	7.25
	Stygiolobus spp.	2.60	*Pseudomonas veronii*	6.88
	Candidatus nitrososphaera gargensis	1.14	*Ralstonia* spp.	5.97
	Caldococcus sp.	1.02	*Delftia* spp.	3.31
	Other	4.70	*Carboxydocella manganica*	3.00
			Ralstonia sp.	2.98
			Pseudomonas trivialis	1.66
			Other	4.96
140723SC	*Thermofilum sp.*	85.64	*Nd*	
	Vulcanisaeta spp.	6.12		
	Sulfolobus islandicus	1.87		
	Thermogladius cellulolyticus	1.26		
	Candidatus nitrososphaera gargensis	1.21		
	Vulcanisaeta sp.	1.06		
	Other	2.84		
140725FA	*Thermofilum sp.*	62.11	*Thermaerobacter subterraneus*	35.88
	Aciduliprofundum sp.	23.50	*Caldisericum exile*	15.92
	Thermogladius cellulolyticus	3.03	*Sulfurihydrogenibium* spp.	12.84
	Sulfolobus islandicus	2.74	*Thermodesulforhabdus* spp.	10.56
	Sulfolobus sp.	2.52	*Hippea sp.*	10.55
	Vulcanisaeta spp.	1.54	*Sulfurihydrogenibium sp.*	7.47
	Other	4.57	*Nitrospira sp.*	1.06
			Other	5.73
140724TB	*Aciduliprofundum sp.*	60.35	*Propionibacterium acnes*	27.86
	Candidatus nitrosocaldus yellowstonii	11.66	*Delftia* spp.	19.48
	Methanobacterium sp.	8.14	*Pseudomonas veronii*	18.70
	Candidatus nitrososphaera gargensis	7.42	*Pseudomonas trivialis*	3.84
	Thermofilum sp.	3.42	*Anaerococcus sp.*	3.50
	Unclutured candidatus nitrosocaldus sp.	2.57	*Streptococcus thermophilus*	3.36
	Caldisphaera draconis	1.37	*Ralstonia* spp.	3.04
	Vulcanisaeta spp.	1.31	*Sphingobacterium sp.*	3.04
	Other	3.77	*Ralstonia sp.*	2.12
			Staphylococcus spp.	1.92
			Klebsiella oxytoca	1.77
			Massilia spp.	1.62
			Propionibacterium sp.	1.27
			Other	8.48
130713SR	*Vulcanisaeta* spp.	92.94	*Nd*	
	Vulcanisaeta distributa	1.75		
	Other	5.31		
140725FB	*Vulcanisaeta* spp.	75.34	*Nd*	
	Sulfolobus tokodaii	9.39		
	Sulfolobus sp.	5.56		
	Vulcanisaeta distributa	2.12		
	Stygiolobus sp.	1.83		
	Caldococcus sp.	1.44		
	Other	4.31		
130722TK	*Vulcanisaeta* spp.	83.81	*Pseudomonas veronii*	14.65
	Sulfolobus sp.	8.59	*Carboxydocella manganica*	14.60
	Stygiolobus sp.	2.01	*Propionibacterium acnes*	12.34
	Thermofilum sp.	1.62	*Ralstonia* spp.	11.19
	Other	3.97	*Thermus sp.*	9.87

			Delftia spp.	6.94
			Ralstonia sp.	6.52
			Pseudomonas trivialis	3.61
			Hydrogenobaculum sp.	3.16
			Spirosoma sp.	2.62
			Streptococcus thermophilus	2.23
			Candidatus rhabdochlamydia rhabdochlamydia crassificans	1.60
			Other	10.67
120714TN	*Sulfolobus sp.*	46.36	*Hydrogenobaculum sp.*	55.64
	Thermofilum sp.	22.85	*Mei*Other*mus timidus*	31.65
	Sulfolobus islandicus	8.04	*Thermoflavimicrobium* spp.	2.27
	Aciduliprofundum sp.	7.45	*Streptococcus thermophilus*	1.30
	*Staphyl*Other*mus marinus*	3.12	*Ralstonia* spp.	1.30
	*Staphyl*Other*mus sp.*	2.37	Other	7.84
	Sulfolobus beitou	2.13		
	Vulcanisaeta spp.	1.82		
	Thermocladium sp.	1.64		
	Stygiolobus sp.	1.26		
139713SQ	*Vulcanisaeta* spp.	68.54	*Sulfurihydrogenibium* spp.	32.70
	Stygiolobus sp.	8.06	*Ralstonia* spp.	13.21
	Sulfolobus sp.	8.00	*Carboxydocella manganica*	12.70
	Thermofilum sp.	6.12	*Ralstonia sp.*	7.35
	Stygiolobus spp.	3.28	*Delftia* spp.	6.68
	Sulfolobus islandicus	1.55	*Pseudomonas veronii*	6.16
	Other	4.45	*Streptococcus thermophilus*	2.29
			Pseudomonas trivialis	2.11
			Hydrogenobaculum sp.	1.46
			Sediminibacterium spp.	1.29
			Propionibacterium acnes	1.20
			Staphylococcus spp.	1.17
			Other	11.68
130723SS	*Vulcanisaeta* spp.	71.04	*Hydrogenobaculum sp.*	73.32
	Stygiolobus sp.	7.34	*Methylacidiphilum infernorum*	23.63
	Sulfolobus sp.	5.56	*Thermoflavimicrobium* spp.	1.83
	Thermofilum sp.	4.99	Other	1.21
	Sulfolobus islandicus	4.30		
	Stygiolobus spp.	1.64		
	Other	5.12		
140720TG	*Ignisphaera sp.*	21.10	*Sulfurihydrogenibium* spp.	92.17
	Thermofilum sp.	16.74	*Hippea sp.*	2.67
	Caldococcus sp.	15.21	*Thermaerobacter subterraneus*	1.20
	Desulfurococcus sp.	10.43	Other	3.96
	Thermogladius cellulolyticus	9.22		
	Thermosphaera aggregans	5.69		
	Ignisphaera aggregans	4.45		
	Vulcanisaeta spp.	3.72		
	Thermogladius shockii	3.61		
	Caldisphaera draconis	1.71		
	Thermoproteus sp.	1.40		
	Stygiolobus sp.	1.18		
	Methanobacterium sp.	1.08		
	Other	4.46		
120721SA	*Aciduliprofundum sp.*	55.30	*Hydrogenobaculum sp.*	91.29
	Candidatus nitrososphaera gargensis	27.70	*Mei*Other*mus timidus*	5.52
	Sulfolobus sp.	5.20	Other	3.19
	Thermofilum sp.	4.37		
	Caldisphaera draconis	1.55		
	Vulcanisaeta spp.	1.32		

	Unclutured candidatus nitrosocaldus sp.	1.13		
	Thermocladium sp.	1.01		
	Other	2.43		
140805SY	*Thermofilum sp.*	78.72	*Pseudomonas veronii*	28.41
	Vulcanisaeta spp.	10.24	*Propionibacterium acnes*	15.91
	Vulcanisaeta sp.	3.06	*Delftia* spp.	10.38
	Sulfolobus islandicus	1.45	*Thermocrinis* spp.	8.70
	Unclutured candidatus nitrosocaldus sp.	1.13	*Pseudomonas trivialis*	4.43
	Other	5.41	*Ralstonia* spp.	4.19
			Ralstonia sp.	2.04
			Propionibacterium sp.	1.70
			Carboxydocella manganica	1.57
			Staphylococcus spp.	1.52
			Peptoniphilus asaccharolyticus	1.26
			Anaerococcus sp.	1.15
			Hymenobacter spp.	1.14
			Faecalibacterium prausnitzii	1.12
			Hydrogenobaculum sp.	1.03
			Other	15.46
140730TI	*Vulcanisaeta* spp.	54.13	*Streptococcus thermophilus*	63.39
	Stygiolobus sp.	15.35	*Lactococcus lactis*	17.82
	Sulfolobus sp.	9.24	*Ralstonia* spp.	3.05
	Thermofilum sp.	8.33	*Streptococcus macedonicus*	2.19
	Sulfolobus islandicus	3.90	*Ralstonia sp.*	1.45
	Stygiolobus spp.	3.48	*Carboxydocella manganica*	1.25
	Other	5.57	*Bacillus mycoides*	1.21
			Other	9.64
130723ST	*Stygiolobus sp.*	51.32	*Ralstonia* spp.	24.07
	Sulfolobus sp.	30.94	*Carboxydocella manganica*	22.90
	Sulfolobus beitou	3.90	*Propionibacterium acnes*	22.38
	Vulcanisaeta spp.	3.24	*Ralstonia sp.*	10.49
	Sulfolobus islandicus	2.63	*Terrimonas* spp.	1.87
	Sulfolobus tokodaii	1.76	*Staphylococcus* spp.	1.35
	Stygiolobus spp.	1.72	*Pseudomonas veronii*	1.25
	Sulfolobus thuringiensis	1.18	*Burkholderia sp.*	1.16
	Other	3.31	*Pelomonas* spp.	1.00
			Other	13.53
140802TS	*Stygiolobus sp.*	72.06	*Hydrogenobaculum sp.*	98.44
	Acidianus ambivilens	13.15	Other	1.56
	Acidianus infernus	7.93		
	Stygiolobus spp.	2.43		
	Vulcanisaeta spp.	1.52		
	Other	2.91		

APPENDIX E

ADDITIONAL SUPPORTING DATA FOR CHAPTER 3

Table E1– Psuedo-first-order rate constants for the reaction $Fe^{2+} + O_2 \rightarrow$ products. These data appear in Figs 23 and 37

25 °C[a]		25 °C[b]		50 °C		70 °C		90 °C	
pH	log k	pH	log k	pH	log k	pH	log k	pH	log k
5.96	-4.15	8.87	1.07	6.98	1.26	7.16	1.09	5.11	-1.37
5.89	-3.90	8.69	0.98	6.84	0.51	6.86	0.72	5.41	-0.98
5.83	-3.83	8.39	0.92	6.75	0.43	6.79	0.70	6.09	-0.08
5.76	-4.16	8.35	0.87	6.54	0.15	6.61	0.09	6.20	0.13
5.75	-3.89	8.20	0.70	6.48	0.11	6.51	-0.12	5.52	-0.94
5.73	-4.36	8.09	0.71	6.41	0.10	6.20	-0.41		
5.57	-4.79	8.00	0.64	6.30	0.04	6.02	-0.71		
5.57	-4.32	7.82	0.36	6.25	0.04	6.03	-0.82		
5.53	-4.91	7.75	0.28	6.16	0.02	5.80	-1.39		
5.52	-4.69	7.74	0.36	5.95	0.01	5.61	-1.64		
5.44	-4.81	7.73	0.28	5.87	0.01	5.56	-1.76		
5.34	-4.91	7.64	0.07	5.56	0.00	5.53	-1.78		
5.33	-5.04	7.60	0.09	5.49	0.00	5.42	-2.00		
5.24	-4.96	7.53	-0.38	5.17	0.00	5.40	-2.08		
4.90	-5.93	7.53	-0.35	5.37	0.00	5.05	-2.39		
4.89	-5.32	7.42	-0.62	5.21	0.00	4.75	-2.97		
4.79	-5.76	7.33	-0.96			4.43	-3.29		
4.66	-6.02	7.14	-1.33			3.39	-3.68		
4.60	-5.87	7.13	-1.17						
4.31	-6.51	7.00	-1.54						
4.12	-5.91	6.88	-1.84						
4.10	-6.52	6.80	-1.89						
3.14	-6.93	6.69	-2.29						
2.66	-6.94	6.59	-2.44						
2.16	-7.01	6.49	-2.54						
1.20	-7.07	6.39	-2.67						
		6.34	-2.88						
		6.28	-2.80						
		6.18	-3.09						
		6.03	-3.39						
		6.02	-3.31						
		5.87	-3.68						
		5.71	-3.92						
		5.50	-4.20						
		5.45	-4.28						
		5.30	-4.62						
		5.23	-4.82						
		5.01	-5.02						
		4.97	-4.94						

[a.] Data from Singer and Stumm (1970a). [b.] Data from Millero *et al*. (1987)

Table E2 – Hot spring outflow locations without visible ferric minerals. These data appear in Figs 28, 29, 40, 41.

Sample ID	sediment color	pH	T °C	DO µ*m*	Fe^{+2} µ*m*	ΣS^{-2} µ*m*
130712TJ	gray	--	80.7	11.5	--	14.0
130712TJ-1	yellow	--	74.9	19.4	--	8.6
130712TJ-2	yellow	--	73	21.9	--	7.9
130723SU-1	white	2.88	82.1	22.2	25.2	0.5
130723SU-2	white	2.87	79.4	24.1	25.9	0.3
140725FB	gray	2.83	87.0	--	--	--
140725FC-1	gray	--	74.2	22.4	--	--
140725FC-2	gray	--	74.9	18.5	--	--
140725FC-3	gray	--	75.5	19.1	--	--
140725FC-4	gray	--	73.1	14.8	--	--
140725FC-5	gray	--	74.2	10.2	--	--
140725FC-6	gray	--	79.8	0.0	--	--
140725FC-7	gray	--	79.5	0.3	--	--
140725FC-8	white	3.13	74.1	--	33.2	3.8
140725FC-9	yellow	3.02	74.9	19.3	130.6	2.4
140725FC-10	yellow	3.01	73.6	28.1	32.7	3.7
140725FC-11	yellow	3.02	75.1	19.3	32.0	6.7
140725FC-12	yellow	3.13	76.9	16.6	32.2	9.5
140725FC-13	yellow	--	74.7	21.8	--	--
140725FC-14	yellow	--	76.1	15.2	--	--
140725FC-15	yellow	--	76.4	14.2	--	--
140725FC-16	yellow	--	78.5	6.0	--	--
140725FC-17	yellow	--	79	1.9	--	--
140725FC-18	yellow	--	78.9	3.2	--	--
140725FC-19	gray	3.08	78.7	6.1	33.0	11.2
140727FD-1	gray	--	71.5	17.6	--	--
140727FD-2	gray	--	79.7	1.8	--	--
140727FD-3	gray	2.97	72.5	29.7	29.2	7.2
140727FD-4	gray	2.97	81.1	3.6	27.7	80.0
140727FD-5	gray	2.97	81.1	18.4	29.2	73.3
140727FD-6	yellow	2.93	70.8	24.5	29.9	11.9
140727FD-7	yellow	2.96	80	11.6	27.6	73.1
140727FD-8	yellow	2.93	75.8	23.7	29.3	50.4
140727FD-9	yellow	--	74.4	21.4	--	--
140727FD-10	yellow	--	77	11.7	--	--
140727FD-11	yellow	--	77.4	9.1	--	--
140727FD-12	yellow	--	65.3	48.4	--	--
140727FD-13	yellow	--	67	39.4	--	--
140727FD-14	yellow	--	72.6	23.8	--	--
140727FD-15	yellow	--	74.3	19.8	--	--
140727FD-16	yellow	--	76.8	11.5	--	--
140727FD-17	yellow	--	78.8	5.0	--	--
140727FE	gray	3.27	81.5	8.9	36.0	109.5
140727FE-1	gray	3.27	81.6	5.4	--	--
140727FF	gray	2.88	82.2	13.3	--	--
140727FF-1	gray	--	84.1	7.2	--	--
140727FF-2	gray	--	84.6	5.1	--	--
140727FF-3	gray	--	86.5	3.9	--	--
140727FF-4	gray	--	84.8	6.0	--	--
140727FF-5	gray	--	85.3	4.8	--	--
140803FI	gray	2.84	89.3	--	--	--
140803FJ-1	gray	3.38	87.5	10.9	19.3	5.5
140803FJ-2	yellow	3.35	72.5	35.2	18.2	0.5
140803FJ-3	yellow	3.36	78.6	28.9	19.8	3.4
140803FJ-4	yellow	3.37	81.4	17.3	19.4	5.2
140803FK	gray	3.37	79.6	57.2	23.0	1.0

140803FK-1	gray	3.38	80.9	16.8	18.4	3.1
140803FK-2	gray	3.40	84.7	15.7	17.0	3.0
140803FK-3	gray	3.42	88.1	9.9	16.5	4.6
140803FN-1	gray edge	--	82.1	10.1	--	--
140803FN-2	gray	3.50	83.8	8.6	31.0	15.1
140803FN-3	gray	--	84.4	5.1	--	--
140803FN-4	gray	--	81.5	5.4	--	--
140803FN-5	gray	--	81.4	4.7	--	--
140803FN-6	gray	--	81.4	9.2	--	--
140803FN-7	gray	--	**82.3**	9.2	--	--
150722FKMR1	gray	3.06	79.2	0.3	--	--
150722FKMR2	yellow	3.00	72	14.2	--	--
150722FKMR3	yellow	3.01	75	18.5	--	--
150724FM	gray	--	83.1	9.8	23.6	0.6
150728C-1	gray	2.86	80.3	14.8	24.7	0.4
150728Y	gray	3.41	84.6	12.9	32.9	4.6

Table E3 – Hot spring outflow locations with apparent ferric mineral staining. These data appear in Figs 28, 29, 40, 41.

Sample ID	sediment color	pH	T °C	DO µ*m*	Fe^{+2} µ*m*	ΣS^{-2} µ*m*
140725FA	red	2.89	73.6	55.7	135.8	1.1
140725FC	red	2.89	73.6	26.0	33.1	2.2
140725FC	red	3.04	71.2	55.7	33.3	1.1
140725FC	red	3.07	71.9	52.6	32.6	1.6
140725FC	red	3.10	71	69.8	32.5	2.4
140725FC	red	--	69	--	--	3.3
140725FC	red	--	70	34.4	--	4.4
140725FC	red	3.22	72.4	162.0	32.0	1.8
140727FD	red	2.92	71.2	37.5	29.8	1.5
140727FD	red	2.94	62.3	40.6	27.4	0.8
140727FD	red	2.98	64.7	56.3	24.6	0.5
140727FD	red	2.97	81.1	75.0	29.1	0.8
140727FD	red	3.34	66.5	62.5	34.4	0.4
140727FD	red	2.92	71.3	37.5	40.5	1.5
140727FE	red and yellow	3.28	72.2	26.9	35.4	10.9
140727FF	red	2.91	79.7	24.1	28.0	0.2
140727FF	red	2.94	79	84.4	30.9	0.0
140727FF	red	3.39	72.1	75.7	19.4	0.4
140727FF	red	--	82.7	8.8	--	--
140729TC	red	3.50	76.1	27.5	12.7	1.6
140729TY	red	4.67	85.6	11.7	9.0	1.9
140803FJ	red	3.39	76.8	25.2	26.5	0.4
140803FJ	red spots	3.33	70.2	83.4	18.8	0.5
140803FK	red	3.37	79	57.2	16.9	1.0
140803FK	red	3.37	77.9	44.9	17.5	2.0
140803FK	red	3.39	79.3	58.8	17.7	1.1
150720FI	red and yellow	3.43	66	28.1	21.3	8.6
150720FJ	red and yellow	3.24	45.3	53.1	21.8	16.2
150722FK	red	3.13	70	47.2	74.8	4.1
150722FK	red	--	69.7	47.2	--	--
150722FK	red	--	66.3	52.2	--	--
150722FK	red	--	70.6	39.1	--	--
150722FK	red	--	69.7	40.3	--	--
150722FK	red	--	71.9	22.9	--	--
150722FK	red	--	63.8	62.8	--	--
150722FK	red	--	70.6	33.8	--	--
150722FK	red	--	67.2	43.4	--	--
150722FK	red	--	73.5	24.3	--	--
150722FK	red	--	72.2	27.8	--	--
150722FK	red	--	74.2	24.7	--	--
150722FK	red	--	71.9	30.8	--	--
150722FK	red	--	69.6	40.6	--	--
150722FK	red	--	75.2	17.3	--	--
150722FK	red	--	69.6	22.3	--	--
150722FKMR4	red	3.04	63.3	21.8	--	--
150722FKMR5	red	3.00	62.3	22.9	--	--
150722FKMR6	red	3.01	60.6	47.2	--	--

150722FL	red	3.43	80.2	14.3	--	0.9
150724FM	red	--	83.1	9.8	--	--
150724FM	red	--	81.6	12.4	--	--
150724FM	red	--	81.7	11.9	--	--
150724FM	red	--	75	28.6	--	--
150724FM	red	--	82.3	11.0	--	--
150724FM	red	--	82	10.7	--	--
150724FN	red	--	62.3	53.4	--	--
150724FN	red	--	53.9	72.2	--	--
150724FN	red	--	61.2	66.3	--	--
150725FQ	red	3.85	40	78.8	108.8	0.01
150728B	red	3.85	67.3	50.0	39.0	--
150728FQ	red	3.36	25.4	184.4	9.7	0.4
150728Y	red	--	64.2	60.0	--	--
150728Y	red	--	67.8	51.9	--	--
150728Y	red	--	72	38.4	--	--
150728Y	red	--	68.1	47.5	--	--
150728Y	red	--	75.4	26.4	--	--
150728Y	red	--	71	42.2	--	--
150728Y	red	--	79.1	16.4	--	--
150728Y	red	--	80	14.3	--	--
150728Z	red	3.45	59	40.6	16.7	1.4
	red	2.90	72.8	11.6	154.2	0.2

APPENDIX F

ADDIOTNAL SUPPORTING INFORMATION FOR CHAPTER 4

Table 15 – Literature reports of biological iron oxidation in field locations. Blank numbers for geochemistry means the value was not reported.

Environment Type	Evidnece of biological iron oxidation	pH	T °C	Fe(II) µmolal	Oxygen µmolal	Reference
iron mat	**rate experiment**	6.17		46	26	Ferris *et al.* 2016
		5.77		18	160	
		5.93		69	183	
mine seep	**rate experiment**	7.42	12.4	21	3	Enright *et al.* 2016
tundra submerged soils	16s, slide colonization, O_2 profiles	5.5	9	270		Emerson *et al.* 2016
		5.5	11	480		
		5.2	8.2	60		
		NR	9	20		
		6.5	11	170		
		5	9	320		
		5	10	60		
		5	10	20		
		6	11	170		
mine adit and outflow	16s, microscopy, mineral characterization	2.6		7341		Sun *et al.* 2016
hot springs	16s, geochemistry	3.89	84.3			Zhou *et al.* 2016
		3.64	76.2			
		3.69	56.8			
		3.69	49.3			
mining and geothermal	isolation and rate experiments	2.9	25			Holanda *et al.* 2016 and references therein
		3	80			
		4.9	32			
		7	14			
		2.8	23			
mine contaminated creek	16s, geochemistry	5.9	16.4	3014	63	Mori *et al.* 2015
		5.94	15	3134	40	
		5.92	15.7	3074	51	
		6.06	16.9	3307	94	
		6.41	14.9	2515	156	
		6.04	14.3	2602	115	
		6.17	15.4	2808	122	
		6.29	17.3	3298	172	
		6.47	15.3	2304	209	
		5.97	14.4	2387	156	
		6.24	15.7	2663	179	
		6.39	17.5	3039	194	
		6.5	15.4	2289	216	
		6.37	14.4	2114	205	
		6.42	15.8	2481	205	
mine	16s, microscopy, mineral characterization	5.8	12	5640	19	Fabisch *et al.* 2015
		6.2	13.8	4220	128	
		5.9	13.1		34	
		6.2	19.2	4150	241	
		5.8	16	5850		
		6.3	13.2	4640	266	
		6.2	13.2	4140	172	
		6.1	12.2		303	
		6	16.3	4100	156	
		5.8	15.7	3830		
		6.1	11.4	3880	156	
		6	12.1	3850	153	
		6.2	13.6		138	
		3.7	19.9			
		4.8	13.8	187000		
		3.8	10.1			
		5.4	16.9			
		5.6	12.8	137000		
		6	12.6			
wells in mining area	16s	5.47	14	4610	120	Wang *et al.* 2014
		5.17	13.2	5270	86	

		5.57	13.6	5570	127	
		5.15		2080	118	
		4.86	14.3	5860	105	
		5.21	12.9	7750	183	
		5.21	12.9	7550	183	
		5.85	15.4	1260	128	
		6.06	16.3	1270	56	
		4.72	16.1	6300	134	
		6.02	15.9	2200	112	
		6.84	15.8	480	98	
		7.25	15.7	470	174	
		6.92	15.4	710	180	
		4.45	10.5	2620	126	
		6.36	12.5	800	67	
		6.34	13.9	910	120	
acid mine drainage sediment	FeOB enumeration and enrichment, 16s, geochemical and mineral characterization	3.5		10200	15	Brantner *et al.* 2014
		2.7		7000	80	
		3.2		11000	80	
		3.35		12500	100	
		3.35		11000	40	
iron floc	enrichment, 16s, apparent biogenic minerals	6.3	11.6	100	3	Elliot *et al.* 2013
		6.4	5.3	64	9	
iron floc	isolate, 16s	6.7	15.8	37.6	20.7	Kato *et al.* 2013
iron mat	enrichment	6.4	17.1	50	175	Lin *et al.* 2012
		5.8	16.8	18	122	
spring	16s	5.8	4.5	48.9	10	Gault *et al.* 2012
	16s	6.02	8	85.1	155	
	16s	5.85	9.2	56.6	1.56	
	16s	5.57	9.3	68.7	26.9	
	16s	5.49	4	83.1	13.8	
	16s	5.68	7.1	112	12.5	
	16s	5.82	4.4	16.1	281	
	16s	6.14	8.4	35.8	342	
	16s	6.21	10.3	8.06	26.9	
	16s	5.84	9.6	31.9	288	
	16s	5.57	3.1	28.8	200	
	16s	5.86	6.7	49.6	137	
Hot Springs and outflows	isolates, enrichments, slides, 16s	3.3	77	58	35	Kozubal *et al.* 2012
		3.6	73	27	27	
		3.6	65	22	22	
		3.5	57	20	20	
		3.3	64	7		
		3.4	70	35.5	56	
		2.5	75	86	6	
		2.4	65	66	48	
		2.4	59	50	78	
		2.4	56	72	48	
		2.5	73	81	22	
		2.6	69	76	44	
		2.5	54	34	99	
		3.2	53	200	14	
iron spring and mat	16s, MPN, geochemistry, microscopy	6.3	10.8	15.9	15	Hegler *et al.* 2012
		6.5	12.5	12.7	140	
		6.7	14.5	12.6	217	
iron seep	16s, microscopy	7.67	4.05		<34	Cockell *et al.* 2011
	16s, microscopy	7.54	4.5		<34	
stalagtite	microscopy	5.5	14			De Los Rios *et al.* 2011
warm spring	16s	2.7	29			Bohorquez *et al.* 2011
seep	16s	5.4	8.5	60.5	20	Bruun *et al.* 2009
pore water	microscopy, geochemistry	7.1		13		Isaacson *et al.* 2009
		7.1		27		
		6.8		2		
		7.2		48		
		6.8		2		
		7.4		5		

		6.8 6.2 6.4 7.2		56 974 1461 11		
coal mine drainage	microcosms experiments, enrichment and isolation, 16s	4.1 3.6 3.1 4.35 4.1 3.8 4.5	12 12 12 10 10 10 10	900 850 50 1100 1150 800 300	190 220 270 30 320 360 310	Senko *et al.* 2008
iron mat	**rate experiment**	*6.6* 6 7.1 6.8		177 127 13 48		Rentz *et al.* 2007
deep mine borehole water	16s, chemical analysis	5.85 5.9 6.28 5.82 5.95	40 38.4 35.3 39.6 35.4		3.75 55 1.4 0.4	Sahl *et al.* 2007
hot spring OF	16s, microscopy	3.04 3 3.01 3	64 53 59 56	45.57 21.4 43.2 39.2		Inskeep *et al.* 2004
cave stalactite	enrichment experiment	6	20.8	252	53	Kasama and Murikami 2001
hot springs	enrichment and isolation, 16s	3.7 2.95	24 54			Atkinson *et al.* 2000
groundwater in drain	isolate	7.1	10	8		Emerson and Moyer 1997

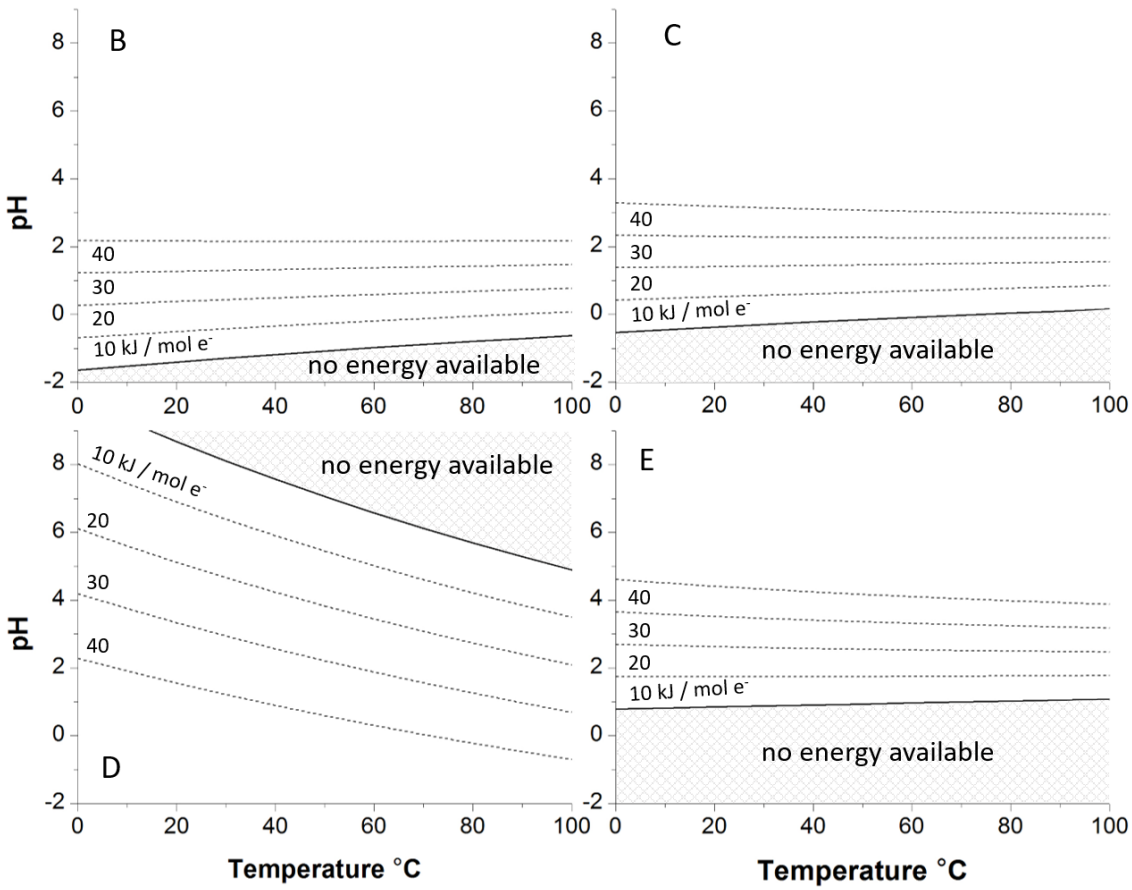

Fig F1 – Thermodynamic boundaries for additional iron oxidation reactions.The reactions that correspond to each plot are:

B $Fe^{2+} + 0.25\ O_2 + 1.5\ H_2O \rightarrow \alpha FeOOH$ (goethite) $+ 2H^+$
C $Fe^{2+} + 0.25\ O_2 + 1.5\ H_2O \rightarrow \gamma FeOOH$ (lepidocrocite) $+ 2H^+$
D $Fe^{2+} + 0.25\ O_2 + H^+ \rightarrow Fe^{3+} + 0.5\ H_2O$
E $Fe^{2+} + 0.25\ O_2 + 1.5\ H_2O \rightarrow FeOOH$ (ferrihydrite core)$+ 2H^+$
The solid lines represent affinity = 0, while the dashed lines are contours of affinity in 10 kJ / mol e^- increments. The thermodynamic boundary for the formation of ferric minerals (B,C,E) occurs at low pH values, with energy increasing pH increases. The opposite is true for the formation of ferric ions (D).